



governmentattic.org

"Rummaging in the government's attic"

Description of document: Joint Department of Defense (DoD) / Department of Energy (DOE) Munitions Technology Development Program Progress Report FY 1998, March 15, 1999

Requested date: 29-June-2017

Release date: 16-May-2019

Posted date: 19-August-2019

Source of document: FOIA/PA Officer
NNSA/Office of the General Counsel
P.O. Box 5400
Albuquerque, NM 87185-5400
Fax: (505) 284-7512
Email: FOIOfficer@nnsa.doe.gov

The governmentattic.org web site ("the site") is a First Amendment free speech web site, and is noncommercial and free to the public. The site and materials made available on the site, such as this file, are for reference only. The governmentattic.org web site and its principals have made every effort to make this information as complete and as accurate as possible, however, there may be mistakes and omissions, both typographical and in content. The governmentattic.org web site and its principals shall have neither liability nor responsibility to any person or entity with respect to any loss or damage caused, or alleged to have been caused, directly or indirectly, by the information provided on the governmentattic.org web site or in this file. The public records published on the site were obtained from government agencies using proper legal channels. Each document is identified as to the source. Any concerns about the contents of the site should be directed to the agency originating the document in question. GovernmentAttic.org is not responsible for the contents of documents published on the website.



Department of Energy
National Nuclear Security Administration
Office of the General Counsel
P. O. Box 5400
Albuquerque, NM 87185



May 16, 2019

SENT VIA EMAIL

This letter is the final response to your June 29, 2017 Freedom of Information Act (FOIA) request. You requested the following:

“The Joint DOD/DOE Munitions Technology Development Program, Progress Report for FY98.”

Your request was received in this office on July 5, 2017. We contacted the National Nuclear Security Administration’s Office of Defense Programs (NA-10) and the Livermore Field Office (NA-LL), which has oversight responsibility for the Lawrence Livermore National Laboratory (LLNL), about your request. NA-10 and NA-LL searched and located one document entitled “1998_UCRL-ID-103482-98, which is being provided with deletions pursuant to 5 USC § 552 (b)(3) (Exemptions 3 of the FOIA).

Exemption 3 prohibits the release of information specifically exempted from disclosure by statute (other than section 552(b) of this title), provided that such statute (A) requires that the matters be withheld from the public in such a manner as to leave no discretion on the issue, or (B) establishes particular criteria for withholding or refers to particular types of matters to be withheld. The international Traffic in Arms Regulations (ITAR), 22 CFR § 120 -130, implements the Arms Export Control Act (AECA), 22 U.S.C §2778, which provides authority to control the export of defense articles and defense services covered by the United States Munitions List (USML). In general, any items, information, or software covered under the USML is prohibited from release to any foreign nationals without prior government authorization. The USML includes 21 categories of defense articles and is included in the ITAR. In this case, information withheld pursuant to Exemption 3, falls under Category III “Ammunition/Ordinance” and Category V “Explosives, and Energetic Materials, Propellants, Incendiary Agents, and their Constituents.”

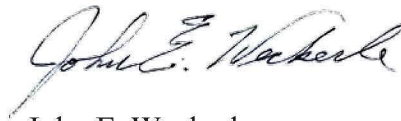
To the extent permitted by law, the DOE pursuant to 10 CFR § 1004.1, will make available records it is authorized to withhold under the Freedom of Information Act (FOIA) whenever it determines that such disclosure is in the public interest. With respect to the information withheld from disclosure pursuant to Exemption 3, the DOE has no further discretion under the FOIA or DOE regulations to release information currently and properly classified pursuant to the ITAR, as amended.

Pursuant to 10 CFR § 1004.7(b)(2), I am the individual responsible for the withholding of the information pursuant to Exemption 3 of the FOIA.

You may appeal our withholding of Exemption 3 information pursuant to 10 CFR 1004.8. Such an appeal must be made in writing within 90 calendar days from receipt of this letter. Appeals should be addressed to the Director, Office of Hearings and Appeals, HG-1, U.S. Department of Energy, 1000 Independence Avenue SW, L'Enfant building, Washington, DC 20585. Your appeal must contain a concise statement of the grounds for the appeal and a description of the relief sought. Please submit a copy of this letter with the appeal. Clearly mark both the envelope and the letter "Freedom of Information Appeal." You may also submit your appeal by e-mail to OHA.filings@hq.doe.gov, including the phrase "Freedom of Information Appeal" in the subject line (this is the method preferred by the Office of Hearings and Appeals). Thereafter, judicial review will be available to you in the Federal District Court either: 1) in the district where you reside; 2) where you have your principal place of business; 3) where DOE's records are situated; or 4) in the District of Columbia.

There are no fees chargeable to you for processing this request. If you have questions, please contact Ms. Delilah Perez by e-mail at Delilah.Perez@nnsa.doe.gov, or write to the address above. Please reference Control Number FOIA 17-00156-M in your communication.

Sincerely,



John E. Weckerle
Authorizing and Denying Official

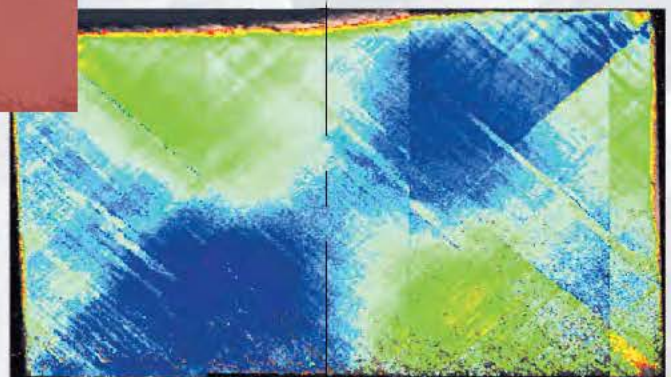
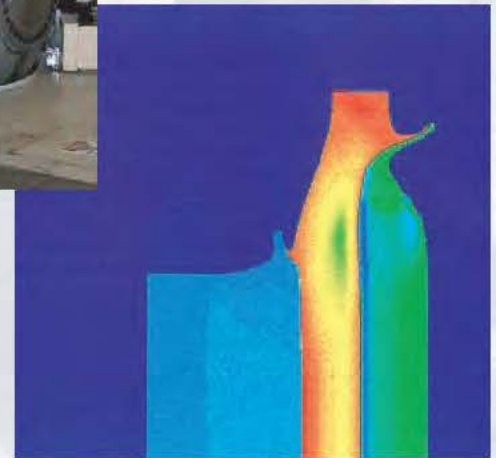
Enclosure

Joint DoD/DOE

Munitions Technology Development Program

Progress Report

FY98



DISCLAIMER

This document was prepared as an account of work sponsored by an agency of the United States Government. Neither the United States Government nor the University of California nor any of their employees, makes any warranty, express or implied, or assumes any legal liability or responsibility for the accuracy, completeness, or usefulness of any information, apparatus, product, or process disclosed, or represents that its use would not infringe privately owned rights. Reference herein to any specific commercial product, process, or service by trade name, trademark, manufacturer, or otherwise, does not necessarily constitute or imply its endorsement, recommendation, or favoring by the United States Government or the University of California. The views and opinions of authors expressed herein do not necessarily state or reflect those of the United States Government or the University of California, and shall not be used for advertising or product endorsement purposes.

Joint DoD/DOE

Munitions Technology Development Program

Progress Report
March 15, 1999

FY98

Dennis W. Baum

Program Manager
(925) 423-2236, email: baum1@llnl.gov

Pamela D. Howard

Program Financial Manager
(925) 423-6099, email: howard8@llnl.gov

Table of Contents

Foreword.....	iii
I. Warhead Technology	
Overview.....	I-1
Warhead Design Optimization.....	I-3
<i>Michael J. Murphy</i>	
Diagnostics for Jets and Material Properties.....	I-15
<i>Peter Poulsen</i>	
Hard Target Response.....	I-19
<i>S. Christian Simonson, III</i>	
Liner Processing/Microstructural Effects.....	I-37
<i>Adam J. Schwartz</i>	
Advanced Composites Technology.....	I-49
<i>S. J. DeTeresa, R. M. Christensen, S. E. Groves, S. McCarvill, and R. J. Sanchez</i>	
II. Energetic Materials	
Overview.....	II-1
Synthesis and Scale-up of New Explosives.....	II-3
<i>Philip F. Pagoria, Alexander R. Mitchell, Robert D. Schmidt, Glenn A. Fox, Theodore F. Baumann, and Laurence E. Fried</i>	
New Formulations and Material Characterization.....	II-15
<i>R. L. Simpson, R. W. Swansiger, J.W. Forbes, R. S. Lee, J. Cutting, T. M. Tillotson, and L. W. Hrubesh</i>	
Equations of State for High Explosives.....	II-37
<i>Choong-Shik Yoo and Hyunchae Cynn</i>	
Kinetic Modeling of Non-Ideal Explosives with CHEETAH.....	II-45
<i>Laurence E. Fried and W. Michael Howard</i>	
Ignition and Initiation Phenomena: Cookoff Violence Prediction.....	II-61
<i>Jon L. Maienschein and Albert L. Nichols III</i>	
Gun Propellants.....	II-93
<i>John E. Reaugh</i>	

Metastable Solid Phase High Energy Density Materials	II-101
<i>Hector E. Lorenzana and William Evans</i>	

III. Life Cycle Technology

Overview.....	III-1
Femtosecond Laser Cutting of Energetic Materials.....	III-3
<i>Frank Roeske, Paul Banks, Rick Cross, Ron Lee, and Brent Stuart, LLNL Ed Roos, Allied Signal, Inc.</i>	
Characterization of NO _x Emission from Molten Salt Destruction of Explosives.....	III-13
<i>Henrik Wallman, Martyn Adamson, Peter Hsu, César Pruneda, and Bruce Watkins</i>	
Resource Recovery and Reuse (R ³) of Explosives by Conversion to Higher Value Products	III-19
<i>Alexander R. Mitchell</i>	

IV. Fuzing

Overview.....	IV-1
Safe, Arm, and Fuze Technology	IV-3
<i>R. S. Lee, J. L. Cutting, R. Druce, A. M. Frank, C. Gillespie, F. Roeske, and P. Watts</i>	

V. Simulation

Overview.....	V-1
ALE Hydrocode Development.....	V-3
<i>Richard Couch, Richard Sharp, Ivan Otero, Juliana Hsu, Rob Neely, Scott Futral, Evi Dube, Tim Pierce, Rose McCallen, John Dolaghan, Brad Wallin, and Albert Nichols</i>	
Electron-Beam Heated Dynamic Tensile Experiments	V-11
<i>David H. Lassila and Mary M. LeBlanc</i>	
Shock Induced Plastic Deformation of Tantalum.....	V-21
<i>Peter S. Fiske, Neil Holmes and David H. Lassila</i>	
Mechanical Behavior of Orientated, Single Crystal Tantalum.....	V-25
<i>Adam J. Schwartz, W. E. King, G. H. Campbell, Mary M. LeBlanc, and David H. Lassila</i>	

Foreword

The Department of Defense (DoD) and the Department of Energy (DOE), through a memorandum of understanding (MOU), have agreed to use the unique facilities and capabilities of DOE weapons laboratories to explore and apply advanced technologies of mutual interest and identified importance to the Armed Services.

The MOU Program has been in place for more than twelve years and has proved to be of great benefit to both the DoD and DOE. The program has contributed to the development of base technologies of critical importance in the life cycles of the nation's nuclear and conventional weapons. It provides the national weapons laboratories an opportunity to contribute significantly to a wide range of challenging defense problems. In addition, as the DoD gains new technologies to apply to its problems, the synergistic nature of the work has permitted DOE to benefit in many areas of its mission program. Moreover, the comprehensive management and review process established for the program has yielded unexpected benefits. For example, collaborations have developed between the DOE scientists performing the work and their DoD counterparts who review the projects. This synergistic activity has benefited both agencies. In addition, the increased coordination of research and development activities has served to avoid duplication of effort between and within the two departments.

The MOU Program has moved forward to meet the new challenges of modern defense requirements that are evolving as DoD and DOE adjust to the post-Cold War environment. For example, life cycle technology is a relatively new area of work. In addition to demilitarization, it encompasses the study of accelerated aging of explosives and its effect on their mechanical properties. This is an area of great interest to both DoD and DOE as their weapons remain in the stockpile for ever-increasing lengths of time.

This publication contains the annual progress reports of the MOU Program projects at the Lawrence Livermore National Laboratory for FY98. Our projects contribute mainly in the areas of numerical simulation and modeling, warhead technology, energetic materials, fuzing, and life cycle technology. The work on simulation technology can be utilized both in warhead design and weapon safety improvements.

Here are some highlights from the 1998 work:

- The respective roles of impurity levels and grain size on the ductility of metals under rapid dynamic deformation conditions were explained for the first time on a fundamental microstructural basis, consistent with observed experimental results.
- The new insensitive molecule LLM-105 was scaled to 500-gram quantities for sensitivity testing. It was found to be very insensitive to one-dimensional shock loading, approaching that of the very insensitive explosive TATB.
- A new diagnostic technique was applied to thermal cook-off tests, in which the violence of the explosive reaction as well as the time to reaction was measured. These data are

very important to the material response modeling capability being developed under the Accelerated Strategic Computing Initiative (ASCI).

- ALE3D is a computational code being developed to simulate coupled thermal, mechanical, chemical, and hydrodynamic phenomena. The cook-off experiments described above are being accurately modeled by ALE3D.
- Our thermochemistry code CHEETAH now incorporates a kinetic detonation model that allows prediction of detonation velocities to within a few percent in ideal and non-ideal composite energetic materials.
- The Molten Salt Destruction (MSD) technology has been transitioned to Eglin AFB in the form of a pilot unit currently installed at Eglin. A larger unit was built for Blue Grass Army Depot. Industrial partners are currently engaged in discussions for further MSD transition efforts.
- A new project, Femtosecond Laser Cutting, was initiated that has demonstrated the capability to cut explosives, explosives components, and munitions with negligible heat transfer to the cut surface and minimal waste.
- Experiments on high heating rates of copper combined with high strain rates have shown that the tensile failure mode can abruptly change as a function of the heating rate and temperature to which the sample is heated. This is an important effect to understand in the development of a failure model that can be used over a wide range of conditions.

The reader is encouraged to learn the details of this work from the following project descriptions and to contact the Principal Investigators directly for additional details.

All reports in this document are unclassified.

I. Warhead Technology Overview

Our warhead technology effort includes a coordinated suite of projects that are closely related to advanced warhead design issues. Modern conventional warhead design has much in common with nuclear warhead design. This commonality enables us to work on problems of interest to the DoD service laboratories and technology centers, while maintaining and improving our nuclear design competencies. Current areas of interest for both DoD and DOE include understanding the influence of material properties on warhead performance and advanced design techniques. The projects in this section address both of these needs.

The Warhead Design Optimization project effort was focused on two areas during FY98. One endeavor was working with DoD and DoD contractors in applying GLO, the Global Local Optimizer software package, to their specific problems of interest. The other was applying GLO to optimize warhead design for the defeat of concrete targets. Both these efforts are expected to continue over the next several years.

The issue of understanding and relating material properties to warhead performance requires knowledge of dynamic material properties, which in turn requires an ability to measure and quantify dynamic material properties. The objective of the Diagnostics for Jets and Material Properties project is to develop and utilize diagnostics to measure useful material properties and munitions characteristics for comparison and calibration of material models and hydrocodes. The focus of the project remains the accurate determination of the surface temperature of shocked metals, in particular materials such tantalum and copper. During FY98, the infrared diagnostic was upgraded to improve sensitivity. The bandwidth of each infrared channel was increased, fiber optics cables replaced mirrors in the optical transport system, and the experiments were moved to the LLNL gas gun facility; all these changes were designed to improve signal sensitivity and reduce background noise associated with experiments.

Hard Target Response experiments and calculations were continued in the attempt to understand penetration and the response of concrete targets to attack. (b)(3)

(b)(3)

Liner Processing/Microstructural Effects is a new project within Warhead Technology. The overall goal of this project is to systematically identify and then make progress in understanding the microstructural and chemistry issues that influence material performance under extreme deformation conditions, which routinely occur during warhead function. During FY98, significant progress was made in understanding the respective roles of impurity levels and grain size as they affect material behavior in shaped-charge liners.

Fiber composite components play an ever-increasing role in modern munitions; the Advanced Fiber Composites project is characterizing the failure of advanced fiber composites under multiaxial stress in order to evaluate three-dimensional (3D) failure models and develop improved ones as necessary. Specific results this year included the effect of superimposed pressure on multiaxial stress states in laminates, the effect of fiber waviness on loss of strength of thermoplastic matrix composites, and the effect of moisture on the fatigue of laminated composites.

The activities conducted in the final project in this technical area—the High Speed Jet—are reported in a separate volume.

Warhead Design Optimization

Michael J. Murphy
Lawrence Livermore National Laboratory
(925) 423-7049
mjmurphy@llnl.gov

Abstract

The Global Local Optimizer (GLO) software package has been successfully applied to the design of a shaped-charge warhead for penetration in concrete. Typical shaped-charge holes drilled in concrete are tapered with a bottom hole diameter that is as small as half of the entrance borehole diameter. GLO was first used to calibrate material property parameters for the jet and target to match the tapered hole profiles from tests at various charge diameter (CD) standoffs. GLO was then used to redesign the warhead to create a different hole profile in the concrete. The new warhead design was verified experimentally.

Introduction

During FY98, we focused our effort in two project areas of research. Our primary activity was using GLO for advanced warhead design. We also continued with the development of GLO, including the technology transition to the Department of Energy (DOE), Department of Defense (DoD), and contractors. In the first area of research—utilization of GLO to optimize warhead designs—we worked on the design of warheads for the defeat of concrete targets. The objective of this effort is to develop a fundamental understanding of concrete target damage derived from directed chemical energy warheads, i.e., shaped charges, explosively formed penetrator (efp) charges, and platter charges, and then use this information to optimize warheads for the desired target damage effect. Liner material and warhead configuration issues will be studied and evaluated. Other potential issues include target damage versus energy deposition, penetrator disruption, penetration hydrodynamics, chemistry/kinetics, and standoff/hole-volume/hole profile.

We are also working on the further development and refinement of GLO. This effort includes modifications to the global and local optimization modules, the implementation and evaluation of the package on new hardware platforms, and the addition of new features as requested by users. Our current effort is focused on developing a response surface model (RSM) optimization module [1-3]. With this analysis approach, we will first conduct a global sampling of the parameters. Then we will define an interpolation function that fits the data (locally quadratic) along with a basis function that merges the interpolation functions. This closed form mathematical model can then be quickly optimized with other global modules to define interesting locations for local optimization.

Concrete Target Damage from Shaped-charge Jet Penetration

The first objective of this effort was to develop a fundamental understanding of concrete target damage derived from directed chemical energy warheads (primarily from shaped charges and efp charges). The second objective of this effort was to apply the fundamental technology to the optimization of warheads that create a desired target damage effect.

In our work last year, we conducted a background review of previous studies and experiments on shaped-charge penetration into concrete [4]. Several fundamental relationships between target damage and warhead design, liner material, jet energy, and standoff distance were discussed. Several of these relationships are summarized below.

In our current year's work, we emphasized the development of a warhead that creates a specific target damage effect in concrete. In the first part of the year, we conducted additional research into the areas of liner materials and charge standoff. Then we used GLO to optimize a warhead that creates the desired hole in a high strength concrete target.

Fundamental Relationships

As a first order relationship, the depth of target penetration is a function of the density of the jet and target materials. From the fundamental theory of shaped-charge jet penetration, we know that a higher density jet will penetrate deeper in the target and have a smaller borehole diameter than will a lower density jet, which does not penetrate as far into the target but has a larger borehole diameter. These effects are consistent with the square root of the density penetration relation and the jet energy/target hole volume relation assuming the total hole volume does not change.

Another first order relationship of interest in the current effort is the effect of charge standoff distance. The standoff distance effects the amount of time the jet can stretch before either breaking up or impacting the target. Most of the jet will penetrate the target prior to breakup at a short standoff distance; whereas, at a long standoff distance, most of the jet will break up prior to penetrating the target. During the stretching process prior to breakup, the jet is elongated and the diameter is reduced. An increase in standoff results in a longer jet that produces more penetration with a smaller borehole diameter. Assuming the jet energy delivered to the target is constant (constant borehole volume), then increasing the standoff produces deeper, narrower holes. Decreasing the standoff produces a shorter, wider hole.

The last relationship of interest in this effort is that the hole volume created in a target is proportional to the kinetic energy of the jet that drills the hole. The hole profile (hole diameter versus depth) in the target is proportional to the jet energy deposited along the penetration path in the target as the jet penetrates. For example, to get a cylindrical hole in the target, the jet should have a constant energy deposition rate into the target. Thus, it must deliver a constant kinetic energy to the bottom of the hole during the penetration process.

In order to develop an efficient (i.e., large target hole volume per unit mass of explosive) warhead for drilling specific shaped holes in a high strength concrete target, all of these relationships must be fully understood and utilized in the optimization process.

Liner Material Issues

The experimental results summarized in last year's report show that target holes from aluminum jets have a larger borehole volume than holes from copper jets with the same jet energy. It is not fully understood why the aluminum jets appear to be more efficient. It seems to violate the fundamental relationship that the target hole volume is proportional to the jet kinetic energy. A numerical study was conducted to determine whether this observation could be duplicated with the CALE hydrocode [5]. An initial simulation was conducted in Eulerian mode with a L/D 10 copper rod penetrating into a thick concrete target. A standard Steinberg material model [6] was used for the copper rod while the concrete target material model was from Sinz [7]. The CALE boundary plot of the 20-mm-diam, 200-mm-long copper rod and concrete target are shown in Fig. 1(a). The final target hole profile from the penetration of the copper rod with initial velocity of 5.0 km/s is shown in Fig. 1(b).

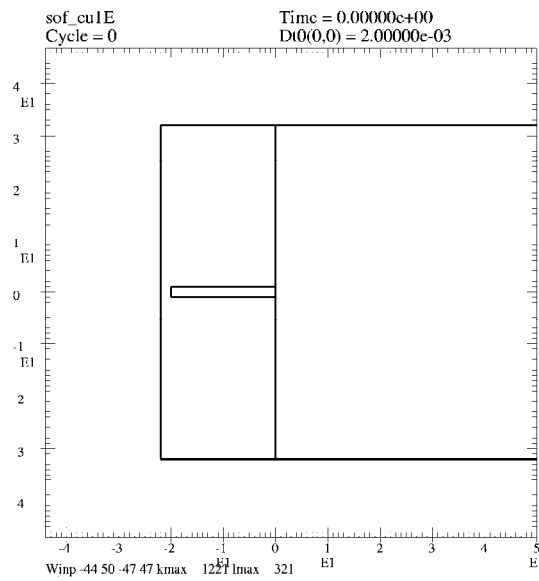


Figure 1(a). Description of CALE setup for a Copper rod impacting the concrete target.

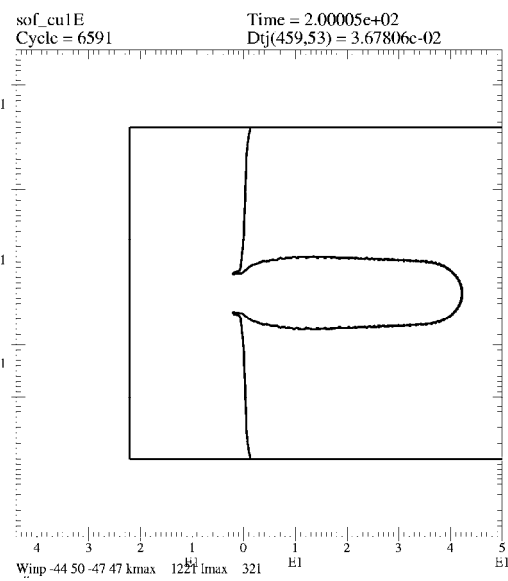


Figure 1(b). Hole profile from copper rod calculated by CALE in Eulerian mode.

Several additional simulations were then conducted using an aluminum rod with the same mass and velocity as the copper rod. In these simulations, the length and diameter of the aluminum rod were varied, while keeping the mass constant, until the penetration depth in the concrete target was the same as for the copper rod. The resulting aluminum rod had a diameter of 25.1 mm and a length of 420 mm (same mass, velocity, and energy as the copper rod). The CALE boundary plot of this geometry is shown in Fig. 2(a). The final target hole profile from this penetration simulation is shown in Fig. 2(b). A general comparison shows that the hole profiles for the two simulations are about the same. Thus, with CALE in Eulerian mode, we get about the same hole profile with copper as with aluminum.

We then ran the copper and aluminum rod simulations with CALE in the arbitrary Lagrangian-Eulerian mode (ALE). The copper rod hole profile is shown in Fig. 3(a) while the aluminum rod hole profile is shown in Fig. 3(b). As with the Eulerian simulations, a general comparison shows that the hole profiles for the two ALE simulations are about the

same. In fact, the copper hole may be slightly larger than the aluminum hole. We observe that the greatest difference in hole profile comes from the mode of analysis (Eulerian versus ALE) not the rod material (copper versus aluminum). Our conclusion is that for L/D 10 rods, copper and aluminum have about the same efficiency in damaging a concrete target. We have still not ruled out the possibility that aluminum jets are more efficient than copper jets. It may be that the lower penetration and larger diameter hole allows more of the aluminum jet to reach the bottom of the hole.

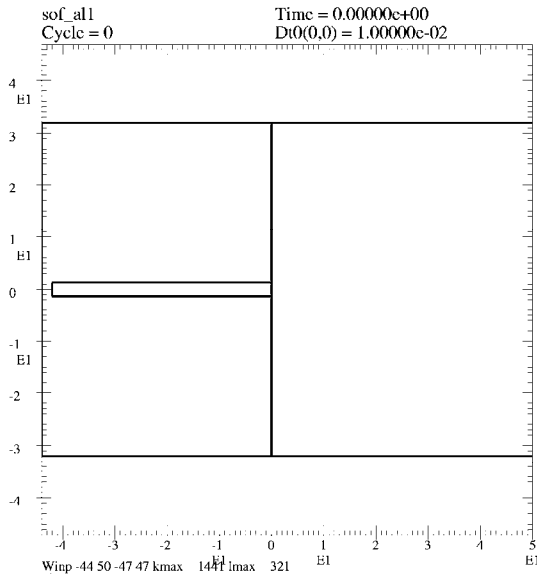


Figure 2(a). Description of CALE setup for an aluminum rod impacting the concrete target.

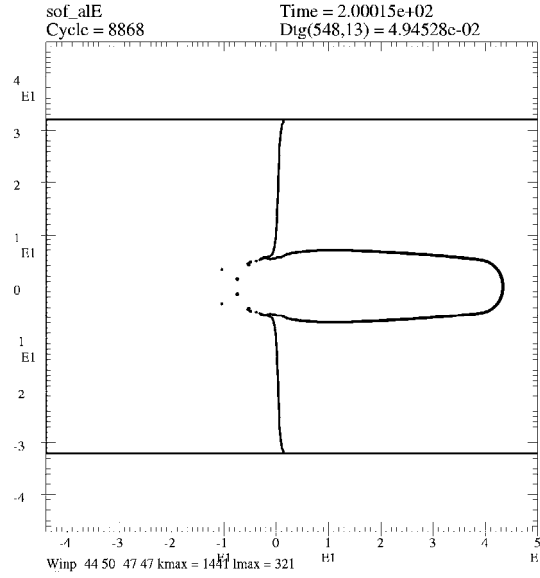


Figure 2(b). Hole profile from aluminum rod calculated by CALE in Eulerian mode.

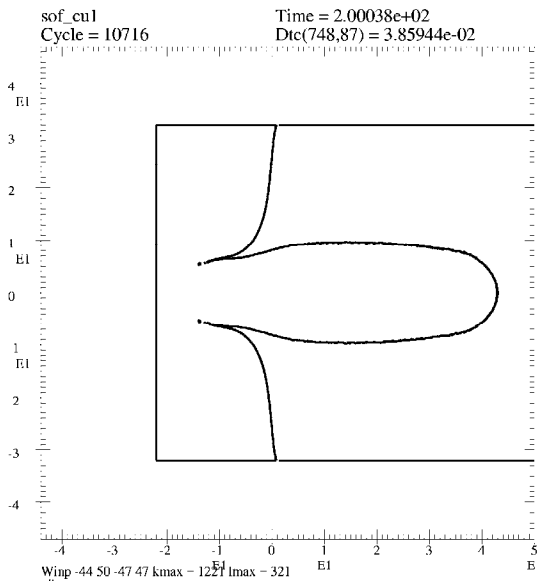


Figure 3(a). Hole profile from copper rod calculated by CALE in ALE mode.

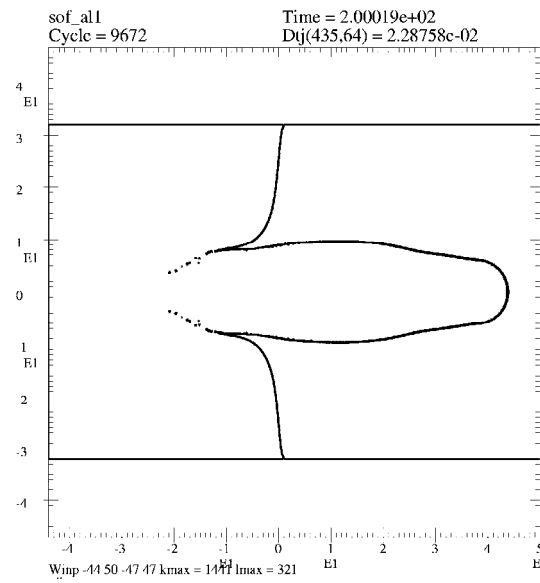


Figure 3(b). Hole profile from aluminum rod calculated by CALE in ALE mode.

Charge Standoff Issues

The standoff distance effects the amount of time the jet can stretch before either breaking up or impacting the target. During the stretching process, the jet increases in length while decreasing in diameter (conservation of mass). Once breakup occurs, we assume the length and diameter of the jet particles do not change. Since the depth of penetration is proportional to the length of the jet, the penetration depth increases with increasing standoff, up to the point of jet breakup. However, since the diameter of the jet decreases with increasing standoff, the hole diameter decreases with increasing standoff. Proper balancing of the standoff, jet stretching, and breakup are required to obtain the desired hole profile.

A description of a shaped charge developed in the early 1980s for the velocity augmented munition (VAM) program is shown in Fig. 4. This charge was designed to maximize hole volume with a minimum warhead weight. Its key characteristics are the LX-14 explosive fill, wave shaper, wide angle, and aluminum liner. This charge was selected as a baseline charge for testing in the Memorandum of Understanding (MOU) program. It was tested at various standoff distances to determine its capability to drill large volume holes in high strength, heavily reinforced concrete.

This charge was tested against high strength concrete at various standoff distances. Based on these test results, GLO was used to calibrate material property parameters for the jet and target. The material properties were optimized to match the penetration depth and hole profiles from each of the tests.



(b)(3)

Charge Optimization for Desired Hole Profiles with GLO

Charge Design Parameters

The initial step in the design optimization process was to develop a baseline CALE input deck with embedded parameters that allowed for the definition of a wide range of charge sizes and geometries. (b)(3)

(b)(3)

Charge Design Optimization

The next step in the numerical design process involved running the GLO (Global Local Optimizer) optimization code coupled to the CALE and HIPEN codes for optimizing the charge design. The Latin Hypercube Sampling (LHS) and LOCAL optimization modules

of GLO were used to specify values of the seven parameters that defined the explosive and liner geometries. The CALE hydrocode was run to determine the jet mass and velocity distribution for each charge design based on the GLO-defined values of the seven parameters. The HIPEN analytic penetration code was then used to calculate the jet penetration and target hole profile based on the CALE defined jet configuration. In a typical overnight optimization run on a four-processor SGI R-10000 workstation, the GLO code could execute 250 CALE/HIPEN simulations with 250 different sets of parameters that define the HE and liner geometry. Several optimization runs were conducted before selection of the optimum configuration for experimental evaluation.

In our first optimization series, we used the LOCAL optimization module to determine the "best" set of parameters for creating the desired hole profile in the target. Unfortunately, it became apparent that the figure-of-merit surface was riddled with local minima and we could not get very far in the optimization process.



(b)(3)

(b)(3)

(b)(3)

Conclusions

The GLO code has been used previously to design warheads that create jets with specific mass and velocity characteristics. By creating a warhead that creates a desired hole profile in the target, we have extended this design capability. This was achieved by coupling GLO to the CALE and HIPEN codes for optimizing the charge design. The CALE hydrocode was run to determine the jet mass and velocity distribution for each charge design based on the GLO-defined values of the optimization parameters. The HIPEN analytic penetration code was then used to calculate the jet penetration and target hole profile based on the CALE-defined jet configuration. The final optimized design was experimentally verified with eight shaped-charge experiments fired into concrete targets.

References

1. R. Unal, R. D. Braun, A. A. Moore, and R. A. Lepsch, "Response Surface Model Building Using Orthogonal Arrays for Computer Experiments," 19th Annual International Conference of the International Society of Parametric Analysis, No. ASA-STI 66, New Orleans, Louisiana, May 27-30, 1997.
2. G. E. P. Box and N. R. Draper, *Empirical Model-Building and Response Surfaces*, John Wiley & Sons, New York, NY, 1987.
3. C. Joyner and J. Sabatella, "Launch Vehicle Propulsion Optimization Using Response Surface Methodology," AIAA/SAE/ASME/ASEE 26th Joint Propulsion Conference, Orlando, FL, USA, 16-18 July, AIAA 90-2433, 1990.
4. M. J. Murphy in *Joint DoD/DOE Munitions Technology Development Program—FY97 Progress Report*, D.W. Baum, Program Manager, Lawrence Livermore National Laboratory, UCRL-ID-103482-97, 1998.
5. R. E. Tipton, "CALE Users Manual—Version 980201," Lawrence Livermore National Laboratory, February 1998.
6. D. J. Steinberg, "Equation of State and Strength Properties of Selected Metals," Lawrence Livermore National Laboratory, UCRL-MA-106439, 1991.
7. K. H. Sinz, "Toward a Universal Model for Concrete," *Joint DoD/DOE Munitions Technology Development Program—FY93 Progress Report*, UCRL-ID-103482-93, January 1994.

Publications

1. L. E. Fried, M. J. Murphy, P.C. Souers, B. J. Wu, S. R. Anderson, E. M. McGuire, and D. E. Maiden, "Detonation Modeling with an In-Line Thermochemical Equation of State," *11th International Symposium on Detonation*, Snowmass, CO, September 1998.
2. M. J. Murphy, D. W. Baum, R. L. Simpson, J. Monolo, L. Montesi, K. Newman, D. Tuerpe, and J. Osborn, "Demonstration of Enhanced Warhead Performance With More Powerful Explosives," UCRL-JC-127575, Ballistics '98, *17th International Symposium on Ballistics*, South Africa, March 1998.
3. M. J. Murphy, R. P. Matzke, I. R. Corey, "The Optimizing Hydrocode: A Coupling of GLO with our Numerical Modeling Codes," *Second Biennial Tri-Laboratory Engineering Conference on Modeling and Simulation*, Los Alamos, NM, November 1997.
4. M. J. Murphy, R. L. Simpson, D. W. Baum, and S. Karlsson, "Effect of High Explosive Properties on Shaped Charge Jet Characteristics," presented at the *First International Seminar on Cumulation Effect*, St. Petersburg, Russia, July, 1997.

This page intentionally left blank

Diagnostics for Jets and Material Properties

Peter Poulsen
Lawrence Livermore National Laboratory
(925) 422-6692
poulsen1@llnl.gov

Abstract

We used the powder gun at the LLNL High Explosives Applications Facility (HEAF) to conduct a number of experiments where we measure the emitted infrared radiation from the surface of a shocked plate. The gun is limited in the velocity it can attain without blow-by of luminous gases that interfere with the detection of the infrared radiation from the target. We found that our present diagnostic did not have adequate sensitivity for the temperatures obtained at the velocities where blow-by was not an issue. The experiment is being redesigned and moved to the gas gun facility, which has a greater speed and therefore a greater accessible temperature range. The diagnostic is being redesigned for greater temperature sensitivity and less response to the presence of stray light. The gas gun experiments are being designed with the aid of hydrocode modeling of the impact process.

Temperature Measurement

The temperature ranges available for the shocked plate experiments using the powder gun at the HEAF facility were found to be too limited for experiments where a range of parameters are of interest. We attempted to obtain temperature data at lower velocities than the 2.4-mm/ μ s impact velocity that had been used previously. Six gun experiments were conducted, which all resulted in inadequate data. Apparently, at low speeds, we did not have adequate shock strength to produce detectable radiation on the surface of the target plate. At higher speeds, the signal was contaminated by light due to blow-by from the gun. We have therefore decided to move the experiment to the two-stage gas gun facility at LLNL. This facility has been employed previously for shocked surface temperature experiments in the visible range of wavelengths. The maximum speed at this facility is approximately 8 mm/ μ s compared to the 2.4 mm/ μ s speed available at the HEAF powder gun. To further increase the sensitivity and the capability to reach lower surface temperatures, the wavelength bands of each channel will be widened to 1 to 2 μ m. Instead of using mirrors to transport the light from the surface to the detectors, we will use fiber-optic cables. Fiber-optic cable has a number of advantages, including less sensitivity to surface movement, and it is easily replaced after each shot. We expect that the initial experiments, which will use tantalum plates, will be conducted in January and February of 1999. The experiments will investigate the effect of shock strength by varying the incident sabot speed. LiF windows will be employed to increase the pressure at the Ta surface and to eliminate the problem of ejecta that might otherwise obscure the surface.

Modeling of the Experiment

We used our hydrocode to model the experiment that we are planning to do in the two-stage gas gun. We have employed a zoning of 0.01 cm/zone. The expected sheet thickness is 2 or 3 mm, resulting in 20 or 30 zones across the sheet. We have explored various experimental geometries, in part to assess the magnitude of the expected signal, but also to investigate the behavior of the flow of the material where it is two- or three-dimensional. Shear flow at the edges are often sources of light because large internal energies can be generated. It is also important to assess the limits to the one-dimensional behavior of the target (i. e., the maximum area that is uniform and can be viewed by the detector). A typical result is shown in Fig. 1 for the case where a sheet of 0.3-cm tantalum is impacted by a copper flyer. The anvil in this case is lithium fluoride, which is used to prevent release of the tantalum and formation of ejecta. It shows shear flow at the junction of the LiF and the rarefaction coming in from the edges to set the limit of the maximum uniform area that can be viewed by a detector through the LiF. This can be alleviated by enclosing the lithium fluoride with a ring of aluminum (Fig. 2); because the aluminum is a good density match to the LiF, the radial variation in the diagnostic region is less severe, and nearly the whole diameter of the LiF radiates uniformly. The radial variation of the pressure at the Ta-LiF interface is shown in Fig. 3 for the cases with and without the aluminum sleeve.

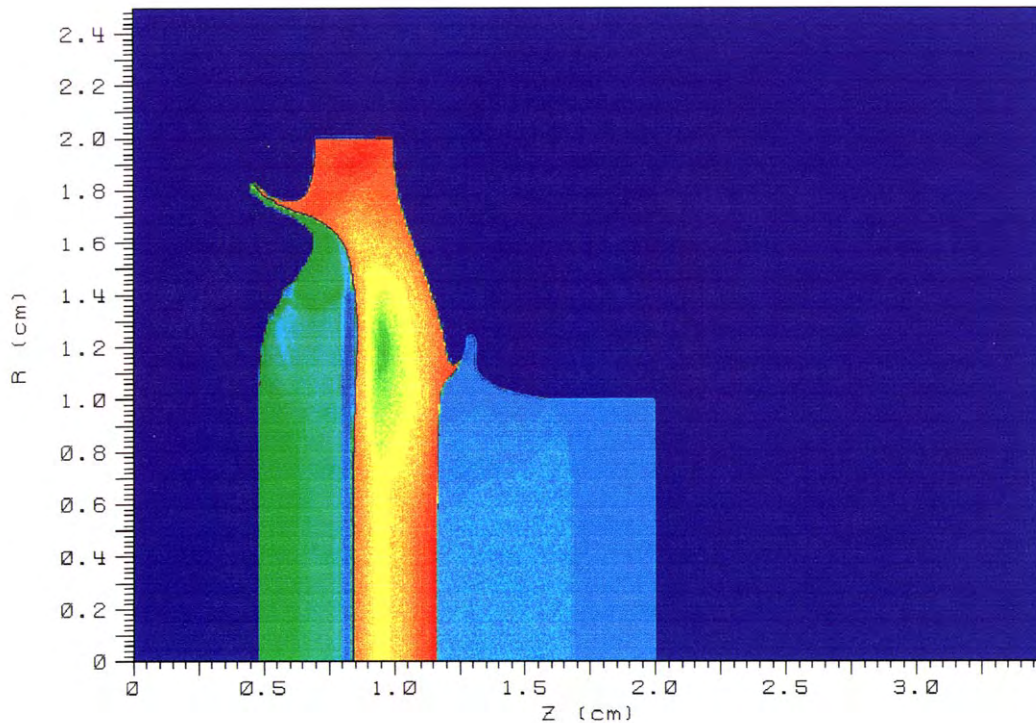


Figure 1. The flow of material when a Ta target is impacted by a Cu flyer from the left. The target is backed by a LiF anvil to provide optical access to the high-pressure, high-temperature Ta surface.

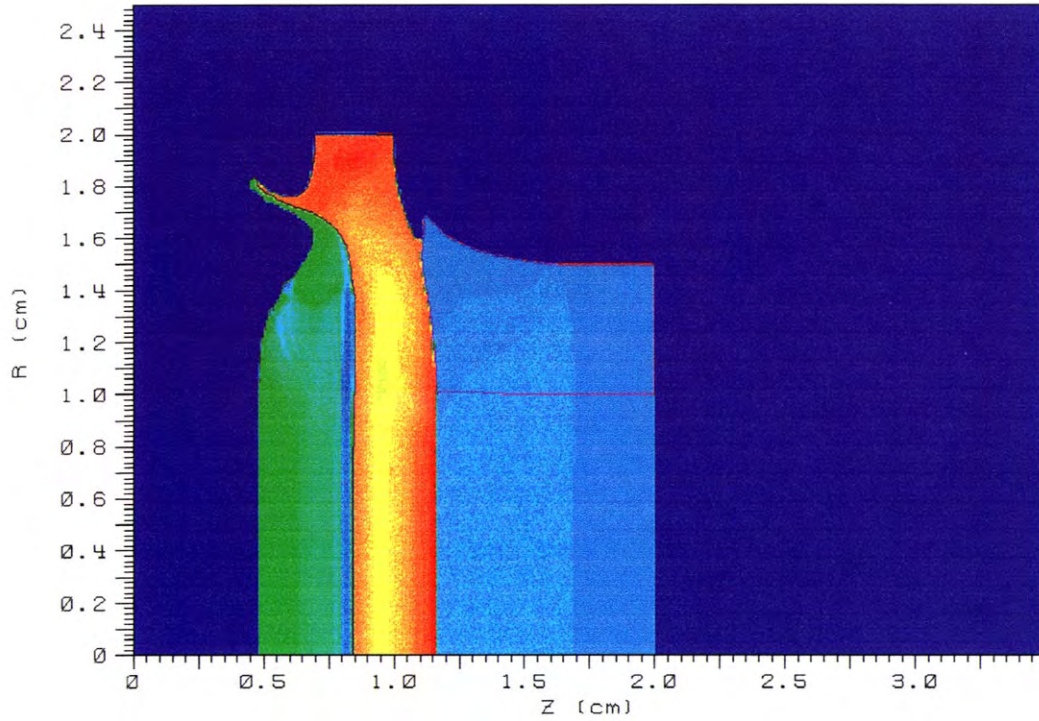


Figure 2. A more one-dimensional flow is achieved in the diagnostic region when the LiF is surrounded by an Al sleeve.

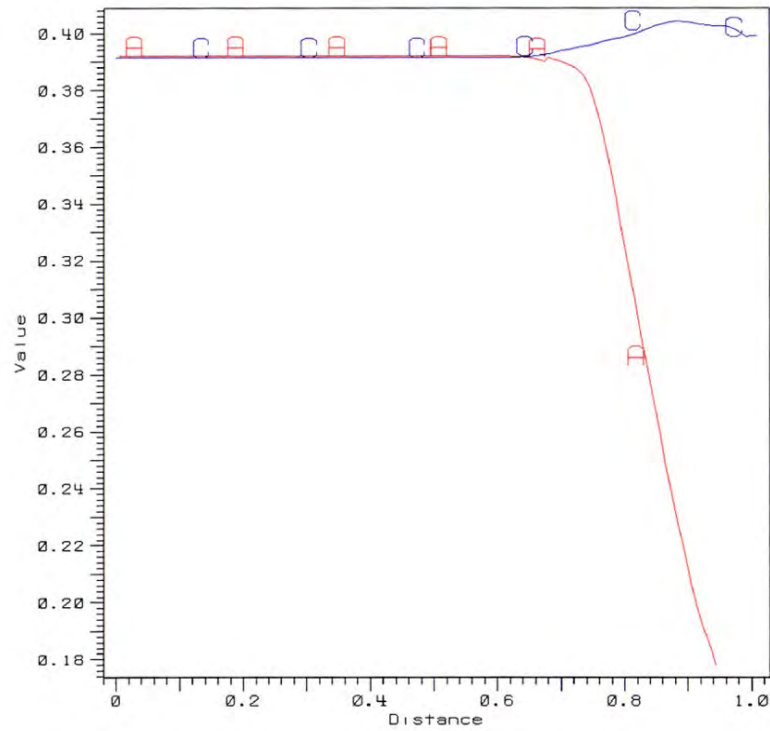


Figure 3. The radial variation in material properties is significantly reduced by the addition of the Al sleeve, as illustrated by the pressure variation (in Mbar) along the Ta-LiF interface: (A) without sleeve, (C) with sleeve.

It is essential to shield the detectors and fiber optics from extraneous light. The modeling shows that the target has not sheared due to the impact of the copper flyer, and that it is possible to shield the luminous driving gases upstream of the target from the detectors downstream of the target. The jetting that occurred under the conditions of Fig. 1 at the target–LiF interface is removed from the problem by the aluminum ring. In addition, the aluminum ring serves as a shield for other possible sources of light that could enter the lithium fluoride and hence the detectors. The fiber-optic cables are placed so they abut the lithium fluoride, with the holder and the aluminum ring completely enclosing the LiF so the only source of radiation for the detectors is the luminous shocked surface and the small radiation from the volume of the lithium fluoride.

It is clear from the computations that a temperature difference is generated between the lithium fluoride and the shocked target surface. We are evaluating the effect of this gradient on the observed radiation and the inferred temperature of the shocked target surface.

Jet Particulation (with Adam Schwartz, LLNL)

We will use the available LLNL diagnostics, including the high-resolution IC camera, to investigate the break-up of shaped-charge jets. In particular, the IC camera exposures will be used to relate the surface perturbations on the jet as it is initially formed to the later growth of jet diameter variations and eventual break-up.

Hard Target Response

S. Christian Simonson, III
Lawrence Livermore National Laboratory
(925) 422-6569
simonson2@llnl.gov

Abstract

In FY98, the Hard Target Response project, which investigates mechanisms for increasing the penetration capability of munitions against buried and/or hardened targets, has primarily been devoted to advanced time-resolved diagnostics with some attention being directed toward enhanced penetration.

The advanced diagnostics work concentrated on the application of micropower-impulse radar (MIR) to measure projectile penetration into concrete and rock, based on experiments done in fall 1997. The measurements were complicated by lossy target material and by motions of the target blocks after impact. We obtained parameters for the range over which MIR can be applied, and laid out directions for possible improvements.

The enhanced penetration work focused on understanding the efficiencies of extended crater formation resulting from simultaneous multiple shaped-charge impact. In follow-on experiments to a previous triple impact on a concrete cylinder by Viper shaped-charge jets, steel projectiles were launched at the preconditioned target and at comparison targets. In the preconditioned target, the effect of the triple impact was to create an enlarged Y-shaped crater that resulted from tensile stresses caused by the interaction of the overlapping pressure waves from the jets. Penetration was increased by an amount corresponding to the depth of this crater. Calculations were begun, using 2D and 3D codes, to look at efficiencies in terms of simultaneity requirements and in jet mass and velocity distributions to give more effective interacting pressure distributions.

Introduction

(b)(3)

Advanced Diagnostics

The main purpose of providing time-resolved, non-intrusive diagnostic techniques is intended to be the validation of continuum mechanics simulation codes and material models, which can then be used in the design of penetrator weapons and the analysis of experiments. In previous years, this project developed three types of diagnostics for measuring penetrator trajectories and material response—fiber optic arrays, Fabry-Perot velocimetry, and MIR. Fiber optic arrays give the time and location of a projectile or jet and its bow shock. Fabry-Perot velocimetry provides the timing and magnitude of particle velocity in concrete, which is a direct measurement of the pressure. MIR provides detailed tracking of a metallic penetrator in a dielectric target.

One reason for the current emphasis on MIR is that it is readily transportable to remote locations, unlike the other two techniques. Thus it has the potential to be employed in measuring projectile trajectories in target interaction experiments at other Department of Defense (DoD) and Department of Energy (DOE) sites. The Hard Target Response project in FY98 included radar upgrades, target and projectile surveys, and application to experiments.

(b)(3)

The 1997 series of experiments consisted of eight shots at LLNL Site 300 in October-December 1997. MIR was set up to detect projectiles fired with a 90-mm powder gun at concrete and sandstone targets. The projectiles were 70 mm in diameter by 50 cm in length, ballasted with sand to a mass of 6.7 kg, representing 1/5-scale BLU-109s. They were launched at velocities of 335-365 m/s.

During preliminary shots, we discovered that the transmittivity of the concrete was much lower than had been expected, based on experiments using sand in the previous year. An investigation by researchers in the LLNL Earth Sciences department revealed the presence of iron-bearing inclusions in the locally obtained aggregate, which appeared to be responsible for this result. Since the radar was unable to penetrate the concrete from the back, the remaining shots into concrete were viewed from the front (i.e., from beside the muzzle) as this configuration is also of interest to projectile penetration diagnostics.

There were two other differences between the 1996 sand experiments and the current series. First, in sand the deceleration event lasted 5 ms, while these experiments were over in about 2 ms. The depth of penetration was also smaller. This meant we could expect a smaller number of data points, since the pulse repetition frequency (PRF) remained at 2 MHz and the number of signal points was typically 511 (i.e., 0.1 ms per sweep through all the range points) or 1023 (0.2 ms per sweep).

A characteristic of MIR in these experiments is that the return signal from the moving projectile is typically much smaller than that from other objects in the field of view, notably the concrete or rock target. Successful detection depends upon the effectiveness of the background subtraction over the duration of the event. This also requires stationary antennas that are isolated from any source of motion, such as the muzzle blast from the gun. While this was successfully achieved, and clear traces were made of the projectile approaching the target through the muzzle blast gases, it was hard to discern the deceleration phase owing to confusion with motions of the face of the target upon impact by the projectile.



(b)(3)

The radar record of the experiment is shown in Fig. 1(c). The vertical coordinate is range-bin number, in this case 1-1023, and the horizontal coordinate is the sweep number, with 100 μ s between sweeps. The projectile is clearly seen as it enters the figure from the upper left. Its raw velocity value is 420 m/s, which does not take account of the projection angle. When it strikes the target, bulk motion of the target obscures the remainder of the penetration event.

Radar transmittivity measurements were also made of typical materials. A limestone block was provided by Sandia National Laboratory, and it turned out to have favorably low losses. Low losses were also found for items such as locally obtained pea gravel and loam, even when wet. The radar was also taken to Socorro, New Mexico, to investigate conditions for experiments involving a gun-fired projectile into sand at that location.

(b)(3)

In order to estimate the range of experimental conditions in which the MIR can operate, the microwave loss was measured for several materials (Table 1).

Table 1. Microwave loss for several materials.

Material	Loss (dB/m)	Total Loss (dB)
Granite	9	
Sandstone	14	28
Concrete with wire mesh	58	
Concrete, SAC 5, sample no. 1	138	360
Concrete, SAC 5, sample no. 2	106	276
Water	267	
		ϵ_r
Top sand	20	6.2
3/8" pea gravel	8	5.1
Olympia sand #1	10	9.2

One problem is that MIR does not currently have a 28-dB signal-to-noise (S/N) ratio to spare. MIR currently has $S/N = \sim 100$ dB. Figure 2 shows where it is used. First of all, there is the range loss in air. At each target interface there is a reflection loss, and within the target there is bulk material loss. The radar cross section (RCS) of the projectile may be small, particularly in the case of an ogive nose. Clutter also reduces detection.

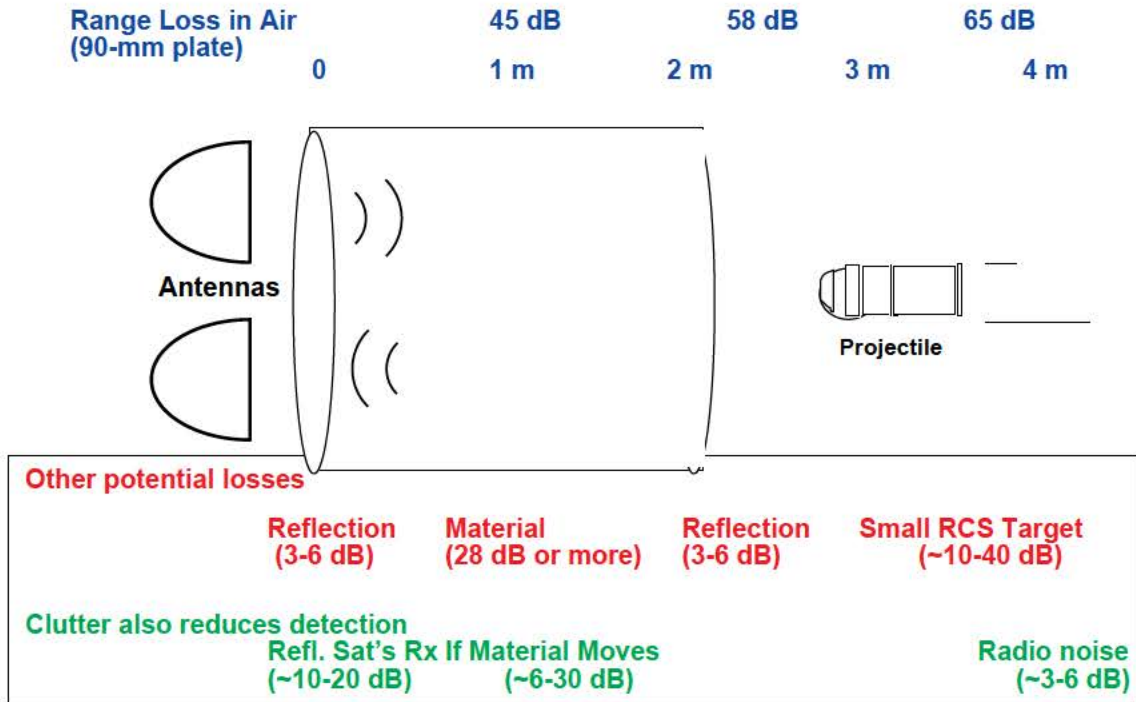


Figure 2. MIR currently has ~100-dB signal-to-noise ratio; here is where it is used.

Another type of problem is illustrated in Fig. 3 for the first experiment in which the antennas were moved to locations near the muzzle. The target is shown in Fig. 3(a), and the layout is shown in Fig. 3(b). For protection, the antennas were placed behind a plywood blast shield. In the record shown in Fig. 3(c), the blast shield began to move just after sweep number 60, and the motion of the projectile was not detected. After seeing these results, it was decided to move the antennas out from behind the plywood barrier, which resulted in the clearer signals shown earlier in Fig. 1, despite suffering some damage to the antennas.

In a final attempt to view through less lossy material than the concrete, three sandstone blocks were stacked together, and the radar viewed the projectile through them. A photograph of the setup is shown in Fig. 4(a), taken from the direction of the gun. The layout is shown in Fig. 4(b). In an attempt to reduce the target motion, two large iron weights were placed in contact with the back of the target on either side. The radar antennas were coupled to the back of the target in the center through a 1-in. Teflon sheet.

The results are shown in Fig. 4(c). There was insufficient signal transmitted through the sandstone to detect the projectile motion. The signals seen between sweep numbers 400–500 are the result of the motion of the sandstone blocks.

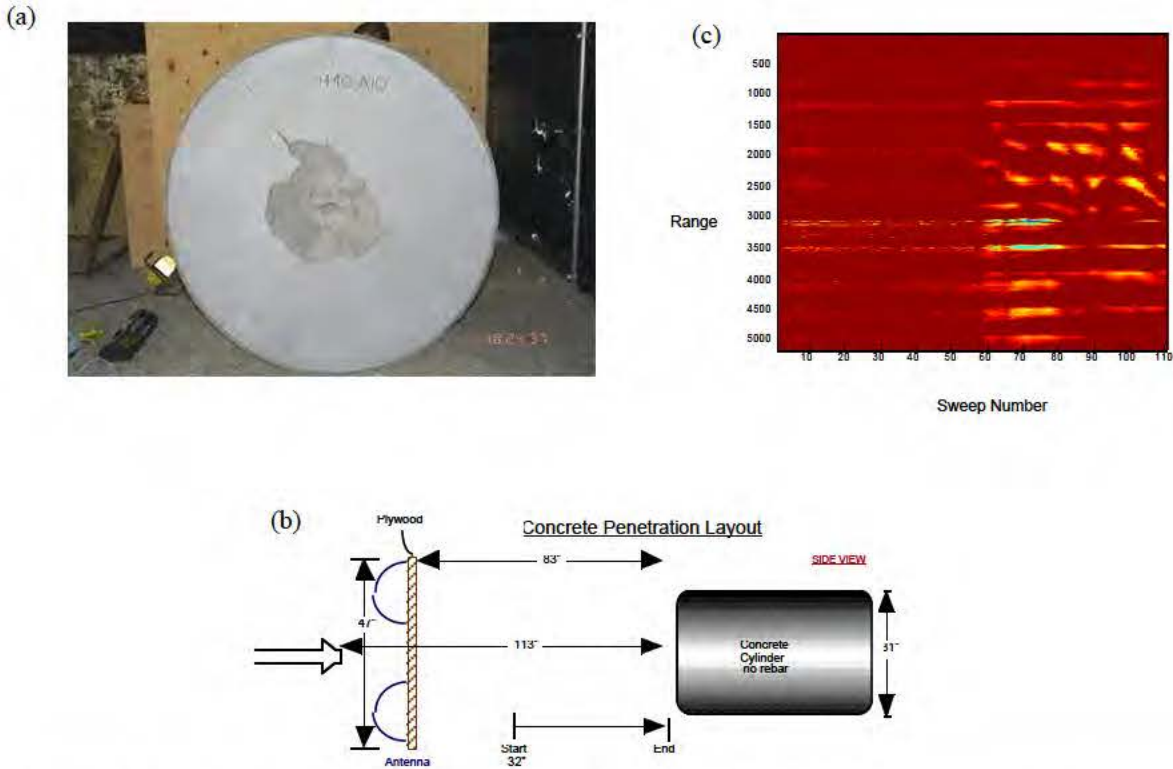


Figure 3. (a) Concrete target (upper left); (b) schematic layout of experiment setup (bottom); (c) motion of plywood blast shield masks signal from projectile (upper right).

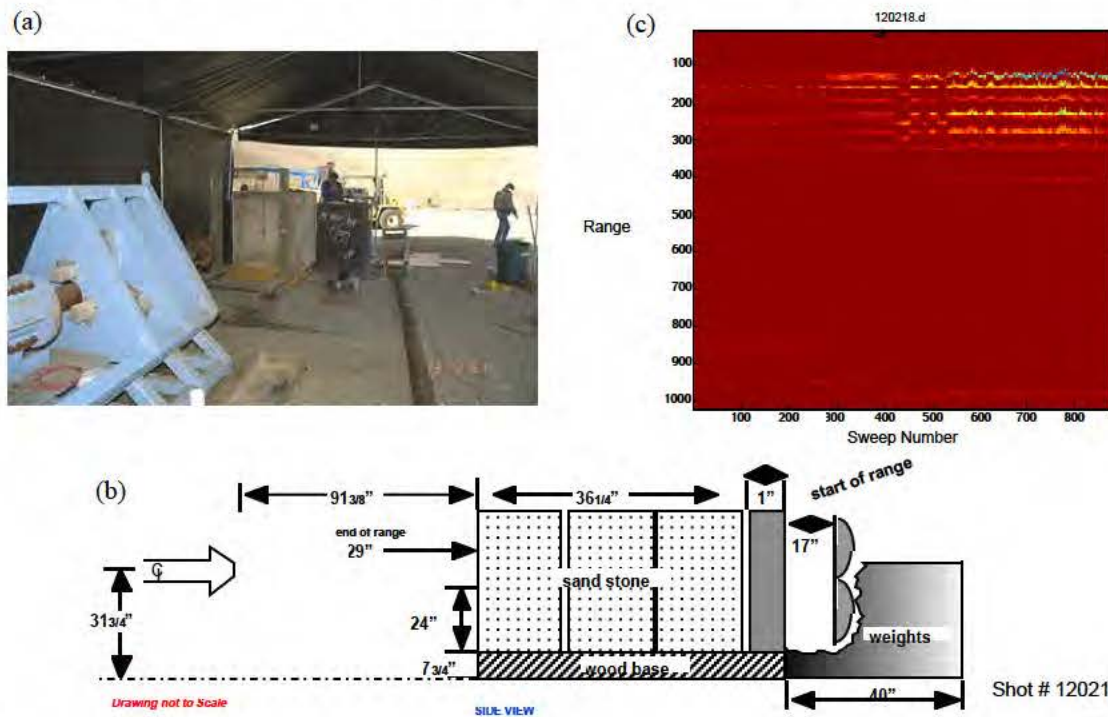


Figure 4. (a) View of sandstone experiment from beside gun (upper left); (b) schematic layout (bottom); (c) insufficient signal was transmitted through the sandstone to detect projectile motion (upper right).

Two major factors affecting detectability are projectile diameter and material loss in the target. The tradeoff between these two factors is shown in Fig. 5 with effective diameter in centimeters and one-way microwave loss in dB.

Radar cross sections of typical projectiles were measured in the laboratory. As might be expected, ogive noses gave very small RCS values when viewed from the front. Also, while the 70-mm diameter, 1/5-scale BLU-109 projectiles used in the experiments with the 90-mm gun were reasonably visible, particularly from the back, smaller scale projectiles (25-mm or 12.5-mm diameter) gave only marginal returns.

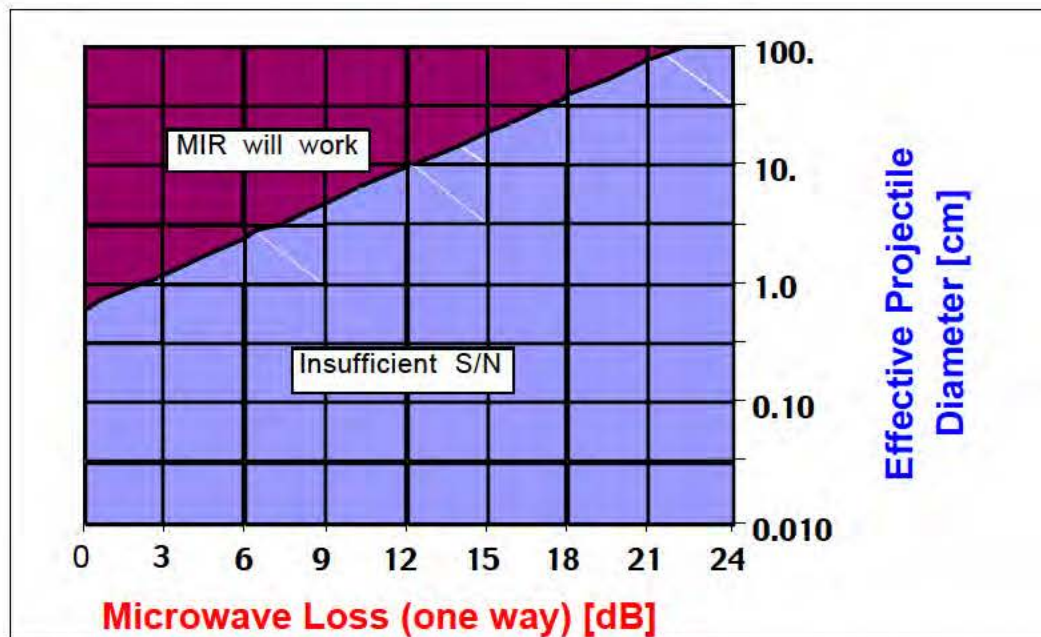
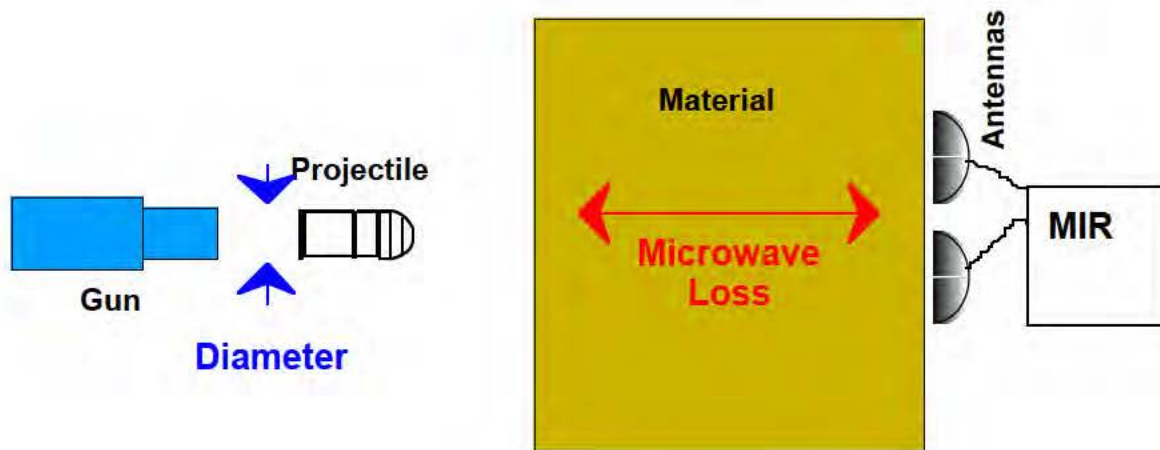


Figure 5. The two major factors affecting detectability are projectile diameter and material loss.

Improvements

In order to improve the situation, one approach would be to use a larger antenna. Or, one may employ an array of radars. For an array of nine radars, the detectability diagram is shown in Fig. 6. Another approach is to increase the transmit power in the impulses. A radar now operating with 1-kV pulses gives a range of 100 m or more, but the PRF is 10 kHz rather than 2 MHz. There are also possibilities in improved detector design.

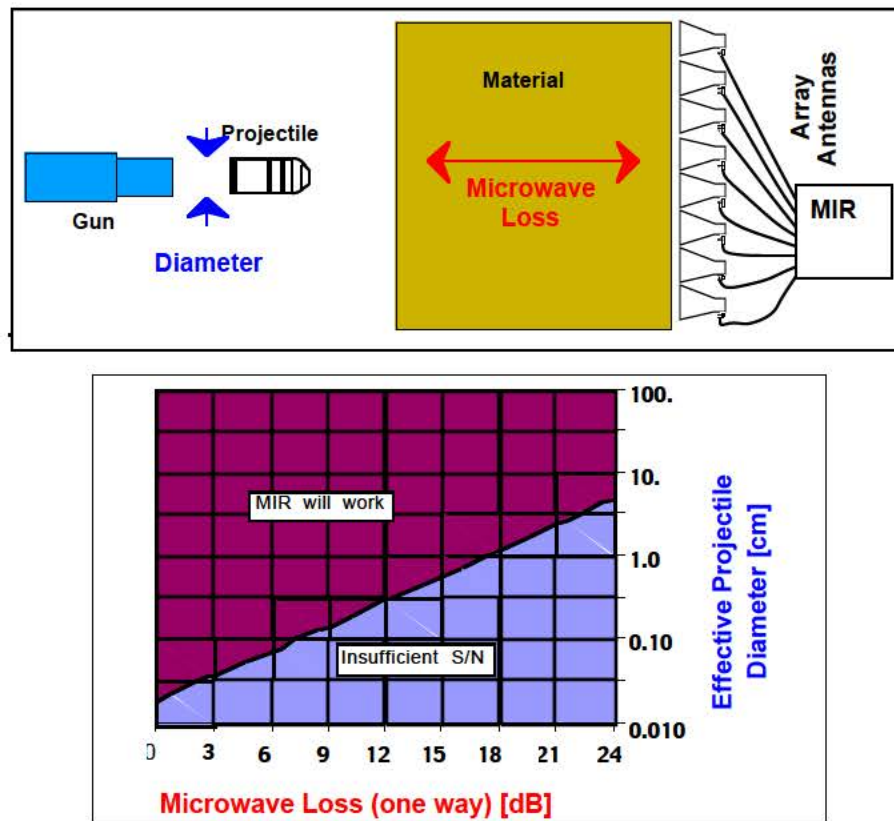


Figure 6. An array of radars could improve detection.

Part of the problem with the background has to do with the amount of the target in the radar beam. When this starts to move, the projectile signal can get overwhelmed. This may be addressable by redesign of the antenna feed to provide sum and difference of the main beam and principal side lobes. The difficulty here is the characteristically large bandwidth of the impulse radar. Another approach may be to cover the target and surrounding surfaces with absorptive cloth, except for a hole through which the projectile can pass.

In order to be able to obtain greater time resolution for penetration events that last only a few milliseconds, the radar is being upgraded to a PRF of 10 MHz under a separate project. A disadvantage is that unambiguous range data is only available to the equivalent distance of 30 m in air, but this is unlikely to pose a problem in target penetration applications.

A set of three radars has been fabricated so as to allow several radars to be applied in succession along a long target or, alternatively, allow the investigation of 3D effects. The first application of these radars was in a high explosive cook-off experiment, where the radar viewed a heated cylinder for many hours, recording its scans on a data loop, until an energetic event occurred and the motion of the cylinder walls was captured.

In the meantime, lessons learned in these experiments include the importance of measuring a sample of the target material for losses, using the actual radar, prior to conducting field tests. Similarly, it is important to measure the radar cross section of the projectile.

Enhanced Penetration with Preconditioned Targets



(b)(3)

(b)(3)

Three hydrocode approaches are under way. These use, respectively: (1) CALE, a 2D code running in a planar mode; (2) ALE3D, a 3D code running on a single processor; and (3) ALEC, a 3D code running on massively parallel processors. CALE has been used to investigate the tensile stress patterns that lead to crater enlargement, and it is being used to study the effect of time displacement of multiple impacts. ALE3D has been used to calculate the impact of a stretching jet at an oblique angle in concrete. ALEC is currently under development, and the impact of a stretching jet is currently being tested. An up-to-date concrete model has been installed, including the Brittle Fracture Kinetics model. The advantage of ALEC is not only in its concrete model but also in its potential speed, as multiple processors (typically 32-128) can be applied.

(b)(3)

(b)(3)

(b)(3)

(b)(3)

(b)(3)

(b)(3)

(b)(3)

(b)(3)

Acknowledgments

The radar work was directed by Tom Rosenbury, with the assistance of Doug Poland, George Governo, Aaron Jones, and Bob Simpson. Bob Kuklo carried out the gun shots, with the assistance of the Site 300 Bunker 851 crew. Annemarie Meike characterized the concrete conglomerate.

References

1. *Science and Technology Review*, Lawrence Livermore National Laboratory, UCRL-52000-96-1, (January/February 1996), p. 17.
2. Tipton, R. E., "CALE User's Manual," private communication (1997).

Liner Processing/Microstructural Effects

Adam J. Schwartz
Lawrence Livermore National Laboratory
(925) 423-3454
ajschwartz@llnl.gov

Abstract

The overall goal of this project is to systematically identify and then make progress in understanding the specific microstructural and chemistry issues that influence material performance under extreme deformation conditions. The diagnostics available to evaluate these applications are well established; they allow critical investigation of specific microstructural influences on the deformation behavior. Specifically, it is of great interest to differentiate between the design, fabrication, and materials effects on the performance of materials under these extreme deformation conditions.

During this year, we made significant progress in understanding the fundamental relationships between grain size, bulk impurity concentration, and material performance under extreme deformation conditions as observed in shaped-charge liners. A geometrical analysis based on an assumed tetrakaidecahedron grain shape is applied to determine the relationship among grain size, bulk impurity content, and breakup time in sulfur-doped, high-precision, 81-mm, oxygen-free electronic (ofe) copper shaped-charge liners. The calculations determine the number of impurity atoms as a function of grain size, the number of available sites at the intercrystalline defects, and the intercrystalline impurity concentration. Recent experiments have shown that some larger grain size liners with low impurity contents exhibit better ductility than smaller grain size liners with higher impurity concentrations. Within the range of grain sizes and bulk impurity contents in this study, the analysis suggests that the quadruple nodes and triple lines are saturated with impurities. Over this same range of impurities and grain sizes, only partial filling of a monolayer of impurities exists at the grain boundaries. The analysis suggests that breakup time is fundamentally related to grain boundary impurity concentration.

Introduction

There has been significant discussion in the shaped-charge literature regarding the importance of grain size and impurity content on the ductility of shaped-charge jets. In the majority of these investigations, one of these parameters was held constant, while the other was varied. Duffy and Golaski found that at constant impurity content, jet ductility increases as the grain size decreases [1]. An additional observation has been that at constant grain size, jet ductility improves as the bulk impurity content decreases [2,3]. Lichtenberger has proposed a criterion for the selection of shaped-charge liner materials based on the

recrystallization temperature [4,5], which indirectly takes into account the relationship between grain size and impurity content. Despite these general trends in the experimental observations of jet ductility, there have been no systematic studies aimed at determining the combined effects of grain size and impurity content on breakup behavior. The purpose of this investigation is to examine the relationship among grain size, overall impurity content, and shaped-charge jet ductility in sulfur-doped ofe copper. The analysis was motivated by experiments that indicate that large grain size liners sometimes exhibit better ductility than small grain size liners. Similarly, longer breakup times have been observed in some lower purity materials than in higher purity materials.

It is well known that impurities such as oxygen [6], sulfur [7], and bismuth [8] cause embrittlement in copper. In order to evaluate the influence of impurity content on the behavior of shaped-charge jets, knowledge of the spatial distribution of impurities is necessary. In a two-dimensional representation of the microstructure, i.e., a micrograph, grain boundaries are observed as lines, and triple lines as points. In an actual material, grain boundaries are surfaces separating two misoriented grains; triple lines are linear defects occurring at the intersection of three grains; and quadruple nodes are the point intersection of four triple lines. Depending on a number of factors, however, each of these microstructural features can be assumed to occupy some volume. For example, the grain boundary can be assumed to have some width, and triple lines a length times a cross-sectional area. The intersection of four triple lines at a quadruple node would then lead to a volume for the quadruple node, as discussed by Palumbo et al. [9] and Wang et al. [10]. The critical assumption of this analysis is that all impurity atoms diffuse along, and remain at, the grain boundaries, triple lines, and/or quadruple nodes.

Experimental Procedures

The copper shaped-charge liners were produced from ofe 99.99% copper, Hitachi C10100 bar stock with the measured impurity concentration obtained by chemical analysis listed in Table 1 [11]. The liners were back extruded using a standard cold-forge process into the shape of hollow cones (base inner diameter = 81 mm, apex angle = 42°). After forging, the liners were annealed at 315°C for one hour or 400°C for 10 minutes or 100 hours in order to stabilize the microstructure for subsequent sulfur doping. After the recrystallization anneal, several of the liner cones were doped with sulfur as described in Chan and in Lassila [2,3]. The grain size of the liners was measured using standard metallographic techniques, and the breakup times determined from the flash x-ray radiographs of the jets. Shot data for high impurity content liners (10–15 ppm S) is also reported.

Table 1. Measured impurity concentrations in ofe copper, Hitachi C10100 stock. All other elements had concentrations <0.1 ppm.

Impurity	Concentration (ppm)	Impurity	Concentration (ppm)
H	0.9	Ni	1.0
C	5.0	As	0.4
N	< 0.1	Se	0.3
O	6.0	Ag	6.4
Si	0.2	Sb	0.3
P	0.4	Pb	0.2
S	4.0	Bi	0.2
Fe	2.0	—	—

Simulation of the Microstructure

To simulate the microstructure for analysis, a number of approaches may be taken. The basic methods would be to approximate the grains as cubes or spheres. Cubic grains represent the simplest of approaches, but real materials rarely have grain morphologies that can be approximated as cubes. An advantage of using spheres to approximate the grain morphologies is that a grain size distribution can be incorporated. In this case, the distribution of sphere sizes can be made to touch, thus leaving a small amount of free volume, or made to overlap, leading to an overestimate of the volume giving rise to upper and lower bounds of surface area to volume ratios. A disadvantage of the spherical approach is the difficulty in calculating grain boundary area and “triple line” lengths.

The approach used in this analysis is to approximate the shape of the grains by truncated octahedra, or Kelvin tetrakaidecahedra as shown in Fig. 1. A tetrakaidecahedron is a 14-sided polyhedra of which the faces consist of 6 squares and 8 hexagons formed by truncating two opposing pyramids. Each face (hexagon and square) has one full-facing neighbor of the same configuration in the adjacent grain, while each line of length λ is the boundary between three tetrakaidecahedron grains. The advantages of using tetrakaidecahedra are that the objects fill space entirely and come close to minimizing the surface area to volume ratio. A disadvantage of this approach is that a grain size distribution cannot be considered.

It is necessary to relate the characteristic length of the tetrakaidecahedron, λ , to the diameter of the grains, d , in the material. A lower value would be to use the diameter of an inscribed sphere; however, for this analysis, an upper limit is applied. The diameter of the tetrakaidecahedron is calculated at the maximum spanning length in the cell. From vertex to vertex:

$$d = \sqrt{10}\lambda \quad (1)$$

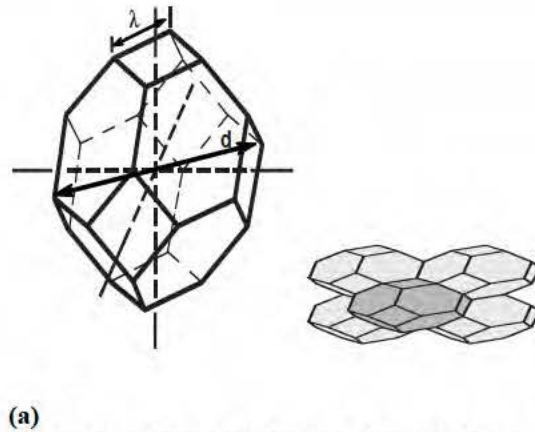


Figure 1. (a) Isolated tetrakaidecahedron; this 14-sided polyhedra has a characteristic length, λ , and consists of 6 square and 8 hexagonal faces. (b) Assembly of tetrakaidecahedra; each individual tetrakaidecahedron has 14 neighbors, each sharing one face with the opposing grain.

When the individual tetrakaidecahedra are assembled to entirely fill space in a “body-centered cubic like” packing arrangement as shown in Fig. 1(b), the equations for volume, surface area, triple line length, and number of quadruple nodes must be modified to allow for the “sharing” of microstructural features between the grains. The volume of the grain remains unchanged, but since each face of the tetrakaidecahedron is shared with another, the surface area per grain in the assembly is reduced by a factor of two. Similarly, since each triple line represents the linear boundary between three grains, the length of triple lines per grain in the assembly is reduced by a factor of three. Each quadruple node is shared by four grains; thus the individual tetrakaidecahedron submits six quadruple nodes per grain to the entire assembly. The volume, surface area, and length of triple lines for an assembly of tetrakaidecahedra in terms of the characteristic length, λ , and the grain size, d , is as follows:

$$V = 8\sqrt{2}\lambda^3 = \frac{4\sqrt{5}}{25}d^3 \quad (2)$$

$$A = (3 + 6\sqrt{3})\lambda^2 = \frac{(3 + 6\sqrt{3})d^2}{10} \quad (3)$$

$$L = 12\lambda = \frac{12d}{\sqrt{10}} \quad (4)$$

Intergranular Impurity Concentration

The method used to determine the “effective” concentration of impurities at the grain boundaries, triple lines, and quadruple nodes begins by calculating the total number of available atomic sites at these intercrystalline defects. The impurity concentration at each location then equals the total number of impurities (in each grain), N_i , divided by the total number of available sites as a function of grain size. Taking the lattice parameter of fcc copper as: $a_o = 0.362$ nm, the volume per atom, V_a is calculated as:

$$V_a = a_o^3 / 4. \quad (5)$$

The total number of atoms in this volume, N_a , is equal to volume of the grain (grain size, d) divided by the volume per atom:

$$N_a = \frac{V_g}{V_a} = \frac{16d^3}{5\sqrt{5}a_o^3}, \quad (6)$$

The total number of impurity atoms equals the concentration of impurities, C_s , times the total number of atoms,

$$N_i = C_s N_a = \frac{C_s V_g}{V_a} = \frac{16C_s d^3}{5\sqrt{5}a_o^3}. \quad (7)$$

Grain Boundary Impurity Concentration: The concentration of impurities at the grain boundaries is determined by distributing a monolayer of impurities over the entire grain boundary area: assuming the impurity atoms are arranged in a hexagonal packing arrangement. The calculation for the area per atom uses the atomic radius of sulfur, $r_s = 0.127$ nm.

$$A_{\text{atom}} = 2\sqrt{3}r_s^2 \quad (8)$$

Thus, the total number of sites at the grain boundary is given by:

$$\text{Sites}_{\text{gb}} = \frac{A_{\text{gb}}}{A_{\text{atom}}} = \frac{(3 + 6\sqrt{3})d^2}{20\sqrt{3}r_s^2}. \quad (9)$$

The possible concentration of impurities at the grain boundary is:

$$C_{\text{gb}} = \frac{N_i}{\text{Sites}_{\text{gb}}} = \frac{64\sqrt{6}r_s^2 C_s d}{(3 + 6\sqrt{3})\sqrt{10}a_o^3}. \quad (10)$$

Figure 2 represents the concentration of impurities at the grain boundaries (as a fraction of one monolayer coverage) as a function of grain size, for differing levels of bulk impurity content as derived in Eq. (10). To calculate the grain size at which the concentration of impurities at the grain boundaries saturates at 1 ppm bulk impurity content, set $C_{gb} = 1.0$ and $C_s = 1 \text{ ppm}$ (1×10^{-6}). At 1 ppm bulk impurity content, the grain boundaries will saturate with impurities for $d > 794.54 \mu\text{m}$. At 10 ppm, the grain boundaries saturate at $d > 79.45 \mu\text{m}$.

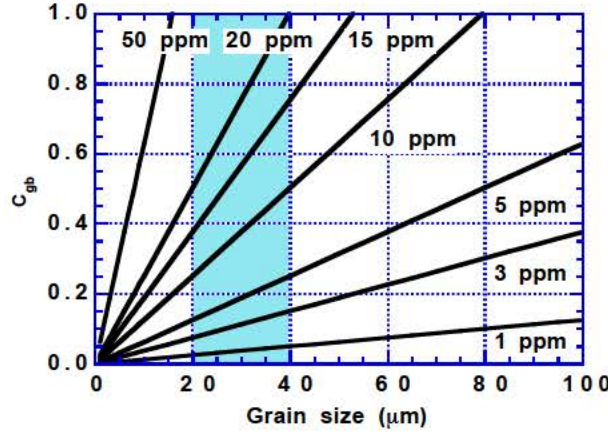


Figure 2. Calculated concentration of impurities at the grain boundary as a function of grain size. Different levels of bulk impurity content are plotted. The shaded area represents the region of interest of grain size and impurity content for the liners in this investigation.

Triple Line Impurity Concentration: The calculation is performed by determining the number of impurity atoms per unit length times the total length of triple lines. As three grain boundaries intersect at a triple line, it is assumed that each contributes one atom per length of triple line. The number of atoms per length equals $3/2 r_s$, and the total number of triple line sites equals the total length of triple lines times the number of atoms per length. Therefore,

$$\text{Sites}_{tl} = 12\lambda \cdot 3/2r_s = \frac{18d}{\sqrt{10}r_s}, \text{ and} \quad (11)$$

$$C_{tl} = \frac{N_i}{\text{Sites}_{tl}} = \frac{8\sqrt{2}r_s C_s d^2}{45a_o^3}. \quad (12)$$

The triple lines will saturate with impurities when $C_{tl} = 1.0$ and $C_s = 1 \times 10^{-6}$ for Eq. (12). The saturation grain size equals $1.22 \mu\text{m}$ at 1 ppm based on the calculations above, and $0.39 \mu\text{m}$ at 10 ppm.

Quadruple Node Impurity Concentration: Four triple lines come together at a quadruple node. Each triple line contributes 3 impurity atoms. Therefore, at each quadruple node, there are 12 impurity sites times 6 quadruple nodes per tetrakaidecahedron, for a total of 72 impurity sites.

$$C_{\text{qn}} = \frac{N_i}{\text{Sites}_{\text{qn}}} = \frac{2C_s d^3}{45\sqrt{5}a_o^3} \quad (13)$$

To calculate the grain size at which the concentration of impurities at the quadruple nodes saturates at 1 ppm bulk impurity content, set $C_{\text{qn}} = 1.0$ and $C_s = 1 \text{ ppm}$ (1×10^{-6}). Thus, saturation at the quadruple nodes occurs for grain sizes greater than 133.64 nm at 1 ppm bulk impurity concentration.

Application to Shaped-charge Experimental Data

This section evaluates the experimental shaped-charge data in terms of the analysis described above. Using the two experimentally determined parameters, grain size and bulk impurity content, the analysis examines the correlation between the grain boundary impurity concentration and the jet ductility as measured by breakup time. Table 2 lists the breakup time as a function of impurity content and grain size, where the grain size is the average value measured by Chan [2].

Table 2. Bulk sulfur content, grain size, breakup time, and grain boundary impurity content for the liners shot in this investigation.

Sulfur concentration (ppm)	Grain size, d (μm)	Breakup time (μsec)	C_{gb}
3	40	186	0.151
4	40	185	0.201
7	40	147	0.353
8	40	148	0.403
9	40	152	0.453
10	20	193	0.252
15	20	160	0.378
15	20	161	0.378

The breakup time of sulfur-doped ofe copper is plotted as a function of grain size and bulk sulfur content in Fig. 3(a and b). There does not appear to exist a straightforward correlation between the breakup time and the sulfur content or grain size. Figure 3(a) reveals a somewhat counter-intuitive behavior; i.e., within the band of higher breakup times, the higher sulfur content liner (10 ppm) had better jet ductility than the lower sulfur content liners (3 and 4 ppm). Similarly, in the collection of data with lower breakup times, the higher sulfur liners (15 ppm) had better breakup times than the lower sulfur liners (7–9 ppm).

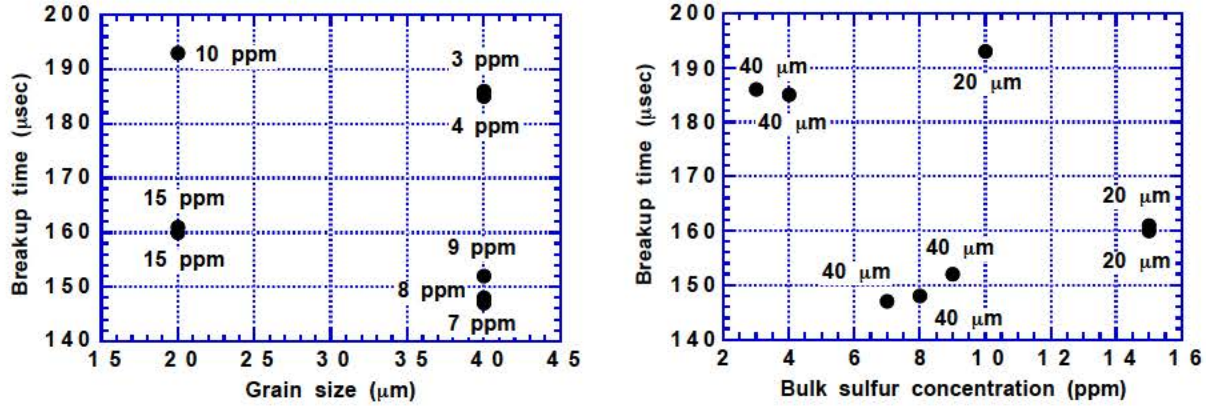


Figure 3. (a) Plot of breakup time as a function of grain size. (b) Breakup time as a function of bulk sulfur content. These two plots reveal no systematic relationship among breakup time, sulfur content, and grain size.

The relationship among the breakup time, grain size, and bulk impurity content of the liners in Table 2 is now analyzed in terms of Eq. (10). Substitution of the experimentally determined grain size and impurity concentration allows the breakup time to be plotted in Fig. 4 as a function of the sulfur content at the grain boundaries. The figure indicates that the concentration spans the range from approximately 15% coverage to nearly 45% coverage of the boundaries in the monolayer geometry described previously.

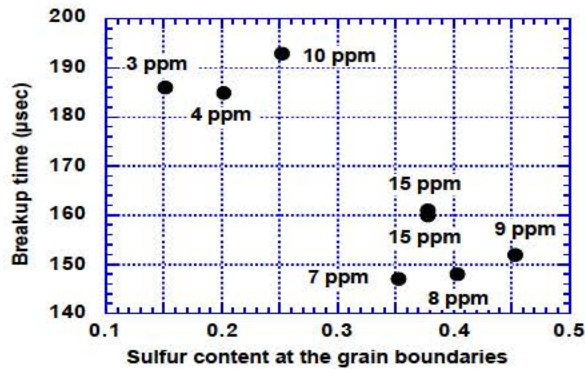


Figure 4. Plot of breakup time as a function of sulfur content at the grain boundaries for 40 μm and 20 μm grain sizes (1.0 represents a full monolayer of coverage). The breakup time decreases with increasing grain boundary impurity concentration.

X-ray radiographs of four shaped-charge liner shots are shown in Fig. 5. Figure 5(a, b) are 40-μm grain size liners with 3 and 7 ppm sulfur levels. Figure 5(c, d) represent 20-μm liners with 10 ppm and 15 ppm sulfur, respectively.

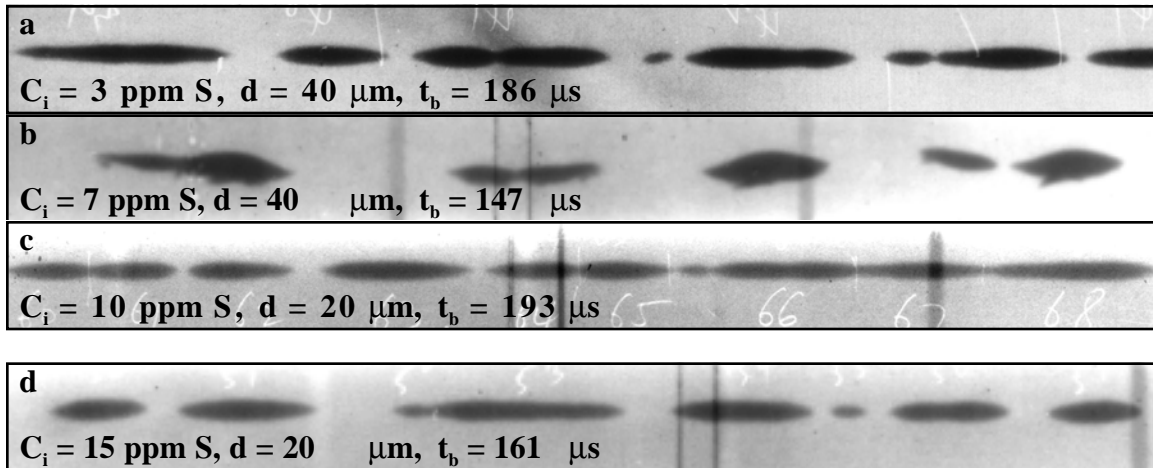


Figure 5. X-ray radiographs of sulfur-doped ofe Cu liners. (a) 3 ppm S, 40- μm grain size, (b) 7 ppm, 40- μm grain size, (c) 10 ppm, 20- μm grain size, and (d) 15 ppm, 20- μm grain size.

Discussion

Viewed outside the context of a combined influence of grain size and bulk impurity content, the interpretation of the radiographs in Fig. 5 would be misleading. Impurity content, examined independently, cannot explain the more ductile behavior of the 10- and 15-ppm sulfur jets compared with the 7-ppm S radiograph. An independent examination of the grain size alone would also present misleading information. Both the 3- and 7-ppm S liners have the same grain size, but dramatically different breakup times and jet characteristics. This variability in jet behavior is revealed clearly in Fig. 3, which suggests no straightforward interpretation of the correlation between breakup time, grain size, and bulk impurity content. However, when the breakup times and radiographs are examined in light of Eq. (10), a reasonable hypothesis can be presented. The application of Eq. (10) to the grain size and bulk impurity content of the liners given in Table 2 indicates that the grain boundaries have impurity coverages between 0.15 and 0.45 of a monolayer, a significant enough level to expect an influence on jet ductility. The plot of breakup time as a function of grain boundary impurity concentration in Fig. 4 as well as the radiographs in Fig. 5 demonstrate that there exists a combined influence of grain size and bulk impurity content on the jet ductility. Thus, the analysis strongly suggests that the grain boundary impurity content is a reliable predictor of the shaped-charge jet ductility.

Despite predicting decreasing ductility with increasing grain boundary impurity content, the analysis above implies that the jet ductility (breakup time) would continue to decrease with the C_{gb} . This behavior over the entire spectrum of grain boundary impurity concentrations does not appear physically likely in light of the transition from ductile, to semi-brittle or brittle jet behavior, to liner particulation. A more likely scenario may be as follows:

- (i) At low C_{gb} , the jet behavior is ductile with high aspect ratio particles.

- (ii) At medium C_{gb} , the behavior transitions to relatively high aspect ratio particles with some evidence of brittle fracture. Void nucleation likely occurs at the quadruple nodes, triple lines, and grain boundaries.
- (iii) As C_{gb} continues to increase, the majority of the particles appear to break up in a semi-brittle, or brittle fashion. Void nucleation occurs readily at the grain boundaries.
- (iv) As C_{gb} approaches one, there likely exists a critical C_{gb} at which the jet behavior transitions from brittle jet breakup to jet particulation. At this stage, it is possible that second phase particles occur at the grain boundaries.

This scenario assumes a homogeneous distribution of impurity atoms at every grain boundary, and that every grain boundary behaves similarly under high strain rate, rapid temperature rise deformation. This is not likely an accurate assumption in that impurity atoms are more prone to segregate to random and high Σ boundaries than to low angle and low Σ boundaries. The coincident site lattice (CSL) model has been used to categorize the misorientations of grain boundaries [12]. In this model, the Σ value corresponds to the inverse of the number of lattice sites in the coincident site lattice. Small Σ s correspond to high coincidence, low mismatch boundaries such as twins, and other low energy boundaries. The analysis above should then be modified to assume that some high Σ boundaries may approach saturation (depending on the overall value of C_{gb}), whereas low Σ boundaries remain less concentrated. To validate this argument, a detailed understanding of the location of the impurity atoms at different types of boundaries is required, in addition to the grain boundary character distribution which describes the relative fractions of high and low Σ boundaries.

Summary

1. Tetraikadehedron grain shapes were used as an approximation of copper microstructures. The use of tetraikadehedra allows for straightforward calculations of grain volume, surface area, triple line length, and number of quadruple nodes.
2. By assuming that all the impurity atoms segregate to, and remain at, the quadruple nodes, triple lines, and grain boundaries, the intercrystalline impurity concentrations at these locations can be calculated. The concentration of impurity atoms at quadruple nodes is proportional to (grain size)³, triple lines proportional to (grain size)², and the concentration of impurity atoms at grain boundaries is proportional to (grain size)¹.
3. Quadruple nodes and triple lines are saturated at grain sizes of interest in conventionally processed shaped-charge liner materials. Grain boundaries are only partially filled with impurity atoms.
4. The breakup time of copper shaped-charge liners doped with sulfur is observed to decrease with the grain boundary impurity content.

The results of this study suggest that the transition from semi-brittle or brittle breakup to particulation may be due to some critical concentration of impurities at the grain boundaries, possibly near saturation. The analysis also suggests that the distribution of impurities at special versus random boundaries in conjunction with the grain boundary character distribution may play an important role in the breakup behavior.

References

1. M. L. Duffy and S. T. Golaski, "Effect of Liner Grain Size on Shaped Charge Jet Performance and Characteristics," U.S. Army Ballistic Research Laboratory Technical Report No. BRL-TR-2800 (1987).
2. D. K. Chan, D. H. Lassila, W. E. King, and E. L. Baker, "MRS Proceedings on Fracture — Instability Dynamics, Scaling and Ductile/Brittle Behavior," R. L. Blumberg Selinger, J. J. Mecholsky, A. E. Carlsson, and E. R. Fuller, Eds., *Mater. Res. Soc.*, 195–200 (1996).
3. D. H. Lassila, E. L. Baker, D. K. Chan, W. E. King and A. J. Schwartz, "Effect of Sulfur on the Ductility of Copper Shaped-Charge Jets," *Proc. 16th Int'l Ballistics Symposium*, San Francisco, CA, 31–38 (1996).
4. A. Lichtenberger, "Some Criteria for the Choice of Shaped Charge Copper Liners," *Proc. 11th Int'l Ballistics Symposium*, Brussels, Belgium, 5–11 (1989).
5. A. Lichtenberger, "The Influence of Grain size and Quality of Nickel-Based Liners on the Ductility of Shaped Charge Jets," *13th Int'l Ballistics Symposium*, Stockholm, Sweden, 337–384 (1992).
6. T. G. Nieh and W. D. Nix, "Embrittlement of Copper Due to Segregation of Oxygen to Grain Boundaries," *Met. Trans. A*, **12A**, 893–901 (1981).
7. D. H. Lassila, "Correlations Between Shaped Charge Jet Breakup and Grain Boundary Impurity Concentrations," *13th Int'l Ballistics Symposium*, Stockholm, Sweden, 549–556 (1992).
8. A. Fraczkiewicz and M. Biscondi, "Intergranular Segregation of Bismuth in Copper Bicrystals," *Journal de Physique*, **C4, S4**, 497–503 (1985).
9. G. Palumbo, S. J. Thorpe, and K. T. Aust, "On the Contribution of Triple Junctions to the Structure and Properties of Nanocrystalline Materials," *Scripta Mat.*, **24**, 1347 (1990).
10. N. Wang, G. Palumbo, Z. Wang, U. Erb, K. T. Aust, "On the Persistence of Four-Fold Triple Line Nodes in Nanostructured Materials," *Scripta Met et Mat*, **28**, 253–256 (1993).
11. Interstitial impurities were measured by Luvak Inc. Metallic impurities were measured by Northern Analytical Laboratory Inc. using glow discharge mass spectrometry.
12. H. Grimmer, W. Bollmann, and D.H. Warrington, "Coincidence-Site Lattices and Complete Pattern-Shift Lattices in Cubic Crystals," *Acta Cryst.* **30A**, 197–207 (1974).

Publications

1. Adam J. Schwartz, David H. Lassila, and Ernest L. Baker, "Analysis of Intergranular Impurity Concentration and the Effects on the Ductility of Copper Shaped Charge Jets," *Proceedings of the 17th International Symposium on Ballistics*, Midrand, South Africa, March 23–27, 1998, Edited by C. Van Niekerk, International Ballistics Committee, Vol. 2, pg. 439–446, 1998.
2. Adam J. Schwartz, David H. Lassila, and Mary M. LeBlanc, "The Effects of Tungsten Addition on the Microtexture and Mechanical Behavior of Tantalum Plate," *Materials Science and Engineering, A*, Vol. A244, (1998) 178–190.

Awards

Neill Griffiths Memorial Award for the most significant contribution to shaped-charge technology; received at the 17th International Symposium on Ballistics.

Meetings

1. Technical Coordination Group TCG-I on Simulation (Lawrence Livermore National Laboratory, Livermore, CA, December 2-3, 1997).
2. Technical Coordination Group TCG-IV on Warhead Mechanisms (Lawrence Livermore National Laboratory, Livermore, CA, January 29, 1998).
3. 17th International Symposium on Ballistics, Midrand, South Africa, March 23–27, 1998.
4. Technical Coordination Group TCG-IV on Warhead Mechanisms (U.S. Army, ARDEC, Picatinny, NJ, June 4, 1998).

Advanced Composites Technology

S. J. DeTeresa, R. M. Christensen, S. E. Groves, S. McCarvill, and R. J. Sanchez
Lawrence Livermore National Laboratory
(925) 422-6466
deteresa1@llnl.gov

Abstract

The development of fiber composite components in next-generation munitions relies on design trade-off studies using validated material models in computer code simulations. In support of this goal, we are characterizing the failure of advanced fiber composites under multiaxial stresses in order to evaluate three-dimensional (3D) failure models and develop new ones if necessary. A critical series of tests for existing fiber composite failure models are for the effects of superimposed hydrostatic pressure on failure. These were conducted using a high-pressure testing system that incorporates several unique features for composites testing. Results for both lamina and laminate failure are reported. Studies were also conducted to evaluate the impact of fiber waviness on the tensile performance of thermoplastic matrix composites. These defects arise from processing. We show that they lead to a significant degradation in strength, which can be predicted using a notch-insensitive analysis. Additionally, the presence of fiber misalignment leads to new damage initiation mechanisms at low thresholds of tensile strain. New results are also given for the effect of moisture on the fatigue of laminated composite under combined interlaminar stresses.

Introduction

We are studying the mechanics of failure in thick-section composites for application to sabots for long-rod, kinetic energy penetrators, advanced artillery projectiles, lightweight gun barrels, and flywheel rotors as power sources for electromagnetic guns. A common need in these and other applications of advanced composites are validated 3D failure models that are suitable for implementation into continuum computer codes. We are developing unique experimental capabilities for thick-section composites and failure models to address this need.

As a means to critically evaluate composite failure criteria and also to provide data for thick-section composite applications, we continue to investigate the effects of superimposed pressure on the matrix- and fiber-dominated failure of unidirectional and laminated composites. Additional improvements were made this year to the internal load cell and the specially adapted test hardware for fiber composites testing.

A common problem in the fabrication of thick-section composites is the increased likelihood of processing-induced defects. For the particular case of local fiber misalignment,

previous theoretical and experimental work by others and by us have shown that small misalignment angles lead to severe reductions in compression strength [1-3]. However, we show in this report that fiber waviness can cause an equally significant reduction in tensile performance.

For laminated fiber composites, there is a paucity of results for failure under combined interlaminar stresses. These stress states arise in several common locations in composite structures, such as at free edges, in bonded and bolted joints, and under lateral impact loads. The failure modes under these stresses are matrix-dominated and thus can be the weak link in any design. We have developed a test method for characterizing the combined stress effects on failure and fatigue. The method was used this year to examine the significant contributions of normal stress and moisture content to fatigue life.

Experimental Studies

Failure under Superimposed Hydrostatic Pressure

Despite the modifications made to the internal load cell in the previous year, uncertainty due to the effect of pressure on the measured axial load (stress difference) was still significant for some samples. This problem was overcome using internally bonded, foil strain gages to give pressure compensation in a manner similar to that used to compensate for thermal output. An outside firm (StrainSert, West Conshohocken, PA) was found that could bond the biaxial gages onto the inside wall of the bore of the load cell as shown in Fig. 1. Since pure hydrostatic pressure yields negative axial and transverse (circumferential) strains in the active region of the load cell, then the appropriate linear combination of these two yields a null output. Conversely, under pure uniaxial load, the two strains are of opposite sign and the same linear combination enhances the output. An example of this load cell's ability to compensate for pure pressure effects and augment the load signal is also shown in Fig. 1. All test results described herein were obtained using this pressure-compensating load-cell.

Additional precautionary measures were applied to the test hardware after estimating the dimensional changes in the specimens and pressure vessel at the highest pressures. Under 100 ksi pressure, the tabbed specimen is compressed in thickness approximately 0.015 in., which is likely enough to eliminate the clamping preload applied through the set screws at atmospheric pressure. We incorporated a stack of Belleville washers under the set screws to maintain a clamping force even at the highest pressures. Also, the bore diameter of the pressure vessel will expand by 0.006 in. at 100 ksi pressure, which could allow some misalignment of the fixtures under compression. To avoid this problem, the brass guide rings were removed from the fixtures and the entire assembly was fit into a brass guide tube, which sits inside the vessel. Since there is no pressure difference acting on this guide, the precise slip-fit tolerance between its inner diameter and the outer diameter of the steel fixtures is maintained at all test pressures.

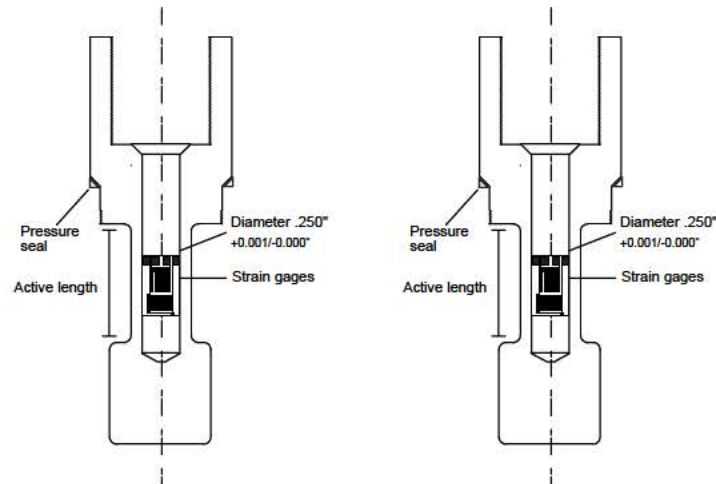


Figure 1. Schematic of load cell that utilizes internal biaxial strain gages and a typical response curve showing its ability to compensate for pressure loads.

Results for the matrix-dominated transverse compression failure of a carbon fiber/epoxy composite (IM7/8551-7) under superimposed hydrostatic pressure are shown in Fig. 2. Pressure is shown to significantly improve both the stress and strain at failure. This behavior is similar to what has been observed for pure polymers under similar loading conditions [4]. The failure envelope is quadratic in nature, which is predicted only by interactive failure criteria.

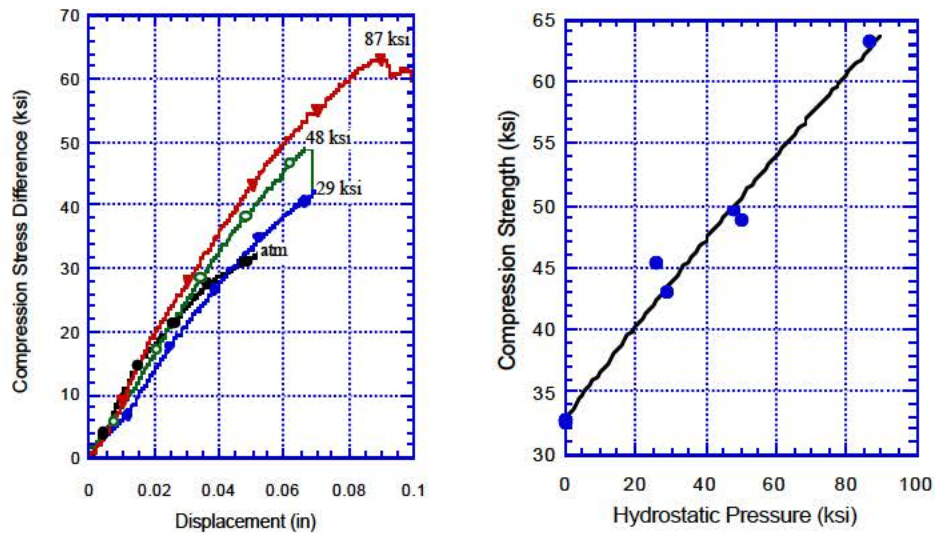


Figure 2. Effect of pressure on transverse compression failure of IM7/8551-7.

The effects of superimposed pressure on the fiber-direction compression strength (stress difference) of IM7/8551-7 are shown in Fig. 3. The two sets of data are for tabbed specimens that have release tape in the bondline near the gage section (stress-relieved) or

pure adhesive throughout (no relief of stress). The purpose of the tape is to reduce the stress concentration at the tab end, which may initiate premature failure. Although the stress-relieved specimen exhibits higher strength at atmospheric pressure, as expected, the strengths of the two types of specimens at elevated pressure are identical. Also included in this figure are results by Wronski and Parry for a different carbon fiber/epoxy system [5]. Clearly their results depart significantly, at moderate pressure levels, from what we have measured.

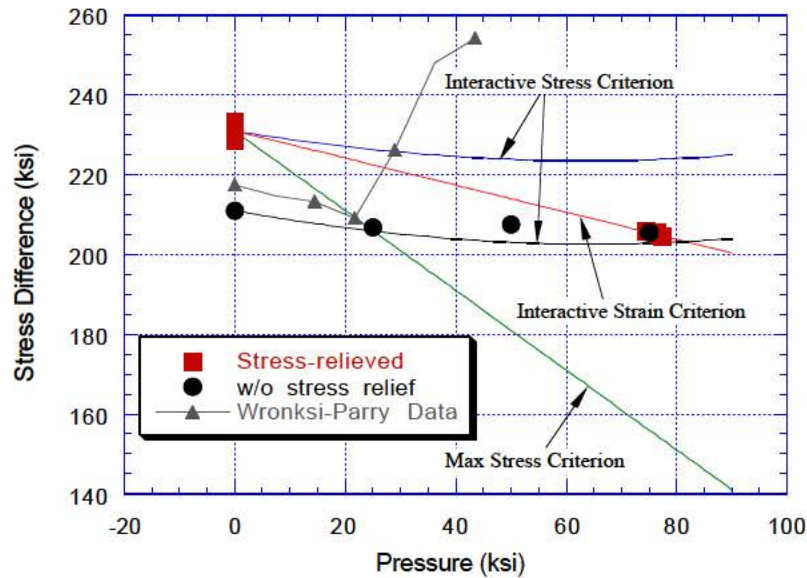


Figure 3. Effect of pressure on the longitudinal compression strength of IM7/8551-7.

Also shown in Fig. 3 are predictions based on some of the proposed failure models for fiber composites. For all three sets of data, the popular maximum stress theory severely underpredicts strength as a function of pressure. A recently proposed interactive stress criterion [6] matches well with the data for IM7/8851-7 specimens having no stress relief and with the initial portion of the Wronski-Parry data. In this case, the predicted effect of pressure on compressive strength is slight over a wide range of pressures. Considering normal experimental uncertainty, this behavior is not very different from that expected for a Mises-type material (strength independent of pressure). The failure envelope for specimens having stress-relief, which is perhaps the most reliable, is well described by interactive, strain-based criteria [7,8].

These results raise more questions concerning the effects of pressure on fiber-dominated lamina strength. Although the Wronski-Parry data have to date been considered the most dependable, when examined in terms of *strength* vs. pressure, the reversal in the pressure-effect is disconcerting. This behavior can not be captured with simple failure models and could possibly represent a change in failure mode, which the authors did observe. The disparity in our results between tabbed specimens with and without stress relief is enough to favor one type of failure model vs. another. Current studies with untabbed specimens and other composite materials are expected to resolve these issues.

Since most composite failure theories are lamina-based, tests for failure of a lamina under multiaxial stresses are the most straightforward means to evaluate these models. However, the unique lamina-level stress states present in some laminates also offers a route to validating failure models. Additionally, there is the practical need to understand laminate failure since most structures are, by necessity, laminated. To this end, we are currently working with the Army Research Laboratory (ARL) to evaluate the family of $[0_2/\pm\theta]$ laminates under uniaxial compression with and without superimposed pressure.

We have reported on the strength at atmospheric pressure and found that with the exception of the $\pm 30^\circ$ variant, all of the $[0_2/\pm\theta]$ laminates failed due to compression of the 0° ply at an *in-situ* stress level of 255 ± 17 ksi. The $\pm 30^\circ$ laminate failed at a much lower stress due to, apparently, a Poisson's effect initiating a premature failure by transverse cracking of the 0° plies. Failure of these laminates was also different in that fracture occurred along the 30° fiber orientation as shown in Fig. 4. This particular laminate is of interest in sabot applications, where a significant mean hydrostatic stress exists. Without testing under a similar stress state, which may suppress the premature failure mode, strength estimates may be too conservative.

Our results for the effect of 75-ksi hydrostatic pressure on the compression strength and failure surface of the $[30/0/-30/0]_{2S}$ laminate are shown in Fig. 4. These indicate that this level of pressure does indeed suppress the weak failure mode and improves both strength and ultimate strain. The fracture surface is typical for a failure due to compression of the 0° plies. Analysis for the stress state in each ply (which is not simply axial stress plus pressure), shows that the stress in the 0° ply at failure is 242 ksi, which is within the range of *in-situ* strengths calculated for the 0° plies in all the other laminates.

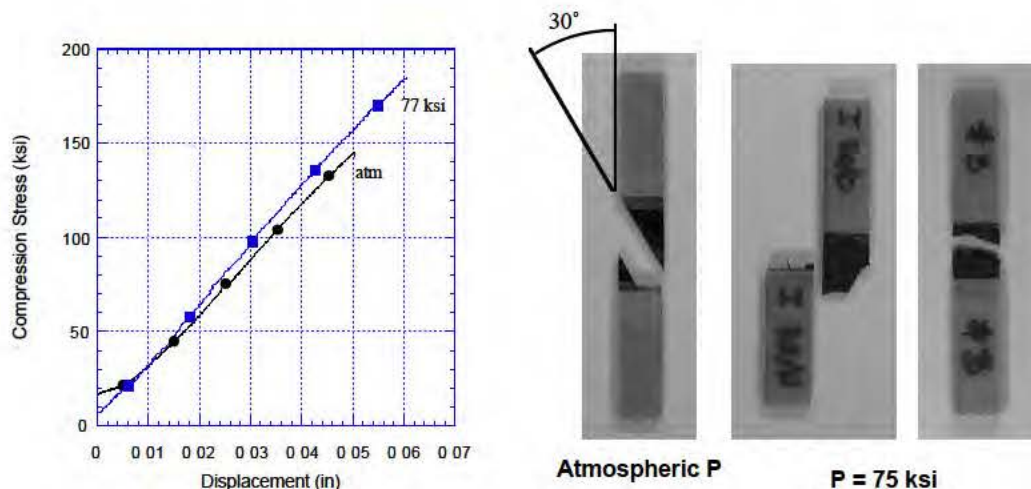


Figure 4. Change in strength and failure mode of a $[30/0/-30/0]_{2S}$ laminate of IM7/8551-7 under superimposed pressure.

Fiber Waviness and Tensile Performance

A common and potentially deleterious defect in fiber composites is the local misalignment of the reinforcing fiber. These defects are typically observed in thermoplastic matrix composites that are processed against tooling material that exhibits a different thermal expansion behavior from the fiber. Since the fiber has a relatively low coefficient of thermal expansion (CTE), most tooling materials impose a compression on the composite during cool-down from processing temperatures. Until the polymeric matrix hardens, this compression can induce local microbuckling in the poorly supported fiber. Examples of these fiber waviness defects in two material systems are shown in Fig. 5. Since the forces that compress the fiber are transferred via shear at the interface between composite and tooling, the severity of these defects is greatest on the surface and diminishes with depth into the composite laminate.

Several studies have been conducted to examine and predict the significant effect of fiber misalignment on compression performance of a lamina [1–3]. However, essentially nothing has been reported for the effect of these defects on tensile behavior. We have produced unidirectional and cross-ply laminates of IM7/K3B composite, with and without defects, in order to ascertain these effects. To produce the defect-free control materials, composites were processed on monolithic carbon tooling, which matches the CTE of the fiber.

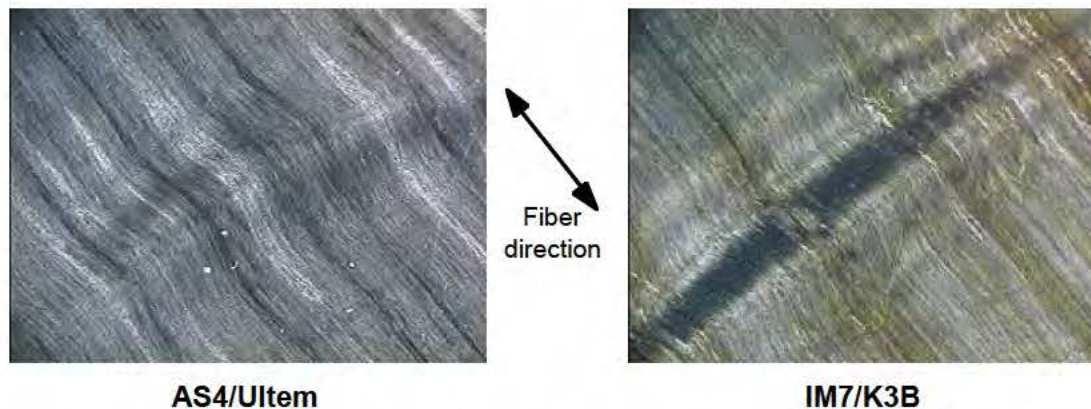


Figure 5. Fiber waviness defects on the surface of thermoplastic matrix composites.

The static tensile properties of the unidirectional (0_4) and cross-ply ($0/90_2/0$) laminates are summarized in Fig. 6 and Table 1. The loss in strength is the only noticeable difference between control and defect-containing materials, but the strength loss is significant. Attempts to detect the onset of damage during these tests using acoustic emission techniques proved unsuccessful.

The failure modes were also affected by the fiber waviness. Normal failure of the unidirectional composite involves significant longitudinal splitting, making it nearly impossible to determine an initiation point. With the fiber waviness, fracture invariably occurred at a defect site in both types of laminates and propagated at 90° to the load axis.

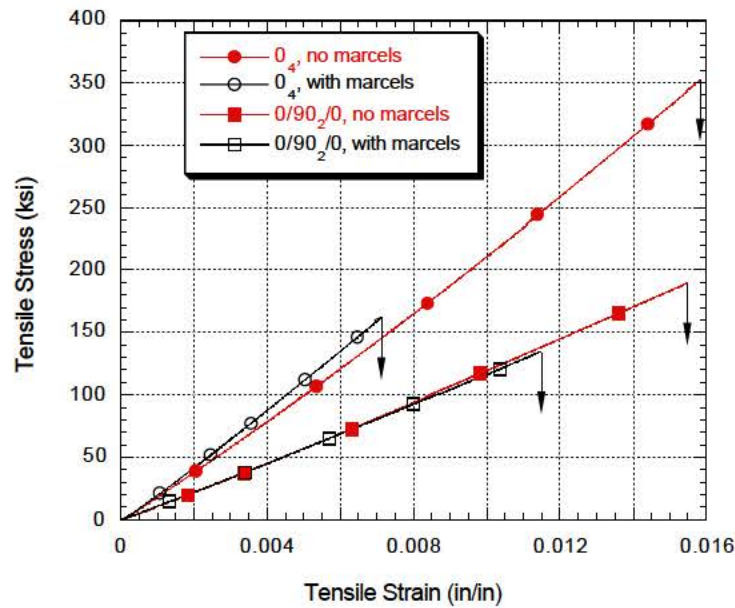


Figure 6. Effects of local fiber waviness on the tensile performance of unidirectional and cross-ply IM7/K3B composites.

Table 1. Effect of fiber waviness on tensile properties of unidirectional and cross-ply laminates.

Specimen	Tensile Strength (ksi)	Tensile Modulus (Msi)	Elongation (%)
0 ₄ -no defects	367	21.1	1.56
0 ₄ -with defects	211	23.5	0.85
<i>Percent Reduction:</i>	<i>43</i>		<i>46</i>
0/90 ₂ /0-no defects	197	12.1	1.55
0/90 ₂ /0-with defects	141	12.0	1.14
<i>Percent Reduction:</i>	<i>29</i>		<i>26</i>

We found that the magnitude of strength reduction in the unidirectional laminates was correlated with the defect width. The predominant characteristics of the fiber waviness defect are the maximum misalignment angle and the size of the region having misaligned fiber. For a particular processing condition, the maximum angle is relatively constant, but the size of the defect is variable. The overall shape of the defect zone is roughly elliptical, with the major axis oriented perpendicular to the nominal fiber axis. We have treated the defect zones as regions of highly compliant material or, essentially, holes in the laminate and applied

notch sensitivity analysis to the degradation of tensile strength. With loading in the fiber direction, the width of this zone is the critical dimension since it represents the percentage of fiber that cannot contribute to bearing load. This assumption is reasonably valid for highly anisotropic fiber composite materials.

The effect of a hole or notch on tensile strength is described by two extremes in behavior, which are shown schematically in Fig. 7. Brittle, elastic materials develop a large stress concentration at the notch, which causes premature failure. Tougher materials can undergo local yielding that mitigates the stress concentration and, in the limiting case of notch insensitivity, exhibit a reduction in strength that is simply proportional to the fractional width (width of notch divided by width of specimen) of the defect.

Data for the strength reduction in the unidirectional composites are plotted in Fig. 7. The observed linear decrease in strength is a clear indication that the IM7/K3B composite is notch-insensitive. It is interesting to note that the fully extended defect (fractional width = 1) still retains about 45% of the virgin tensile strength. This is due to the reduced severity of the defect in the subsurface plies of the laminate. Since we have found the material to be notch insensitive, it is expected that the strength degradation in structures, where the defect may be localized, should not be severe. The magnitude of this degradation can be easily estimated from the size of the defects.

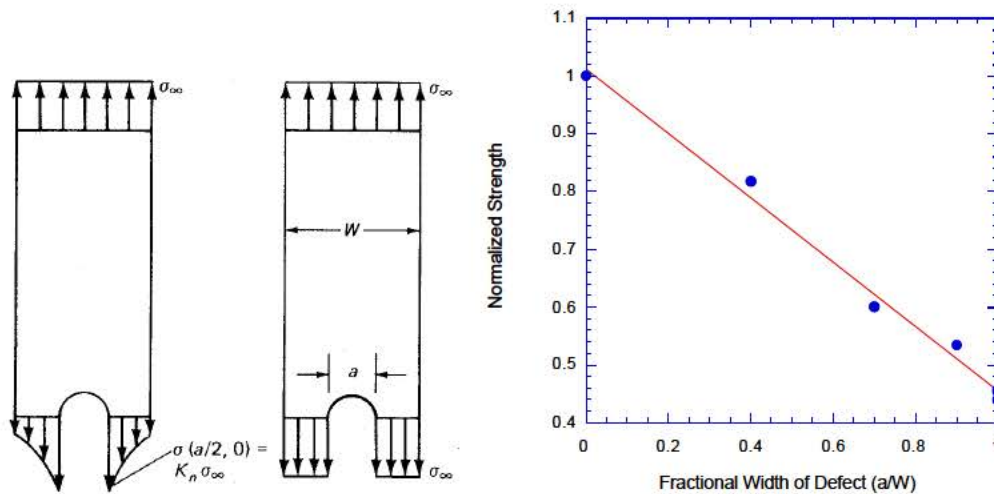


Figure 7. Quantitative relationship between size of defect and tensile strength reduction in IM7/K3B unidirectional composites.

For long-term applications of composites, the initiation and accumulation of damage is of higher concern than ultimate properties. The concentration of stress in the vicinity of a fiber waviness defect can possibly lead to initiation of damage prior to ultimate failure. Using high-magnification video, we examined both unidirectional and cross-ply laminates under tensile loads to determine what were the contributions of the defects to damage mechanisms and threshold levels.

In unidirectional composites, a combined state of shear plus tension causes microcracking to occur in the most misaligned region of the defect. An example of this is shown in Fig. 8. These cracks were readily visible at strain levels of about 0.5%, but estimates for the failure in a region having a 25° misalignment angle suggest that failure occurred at less than half of this strain. Depending on how these cracks propagate under fatigue loads, this very low threshold level could severely reduce safety margins.

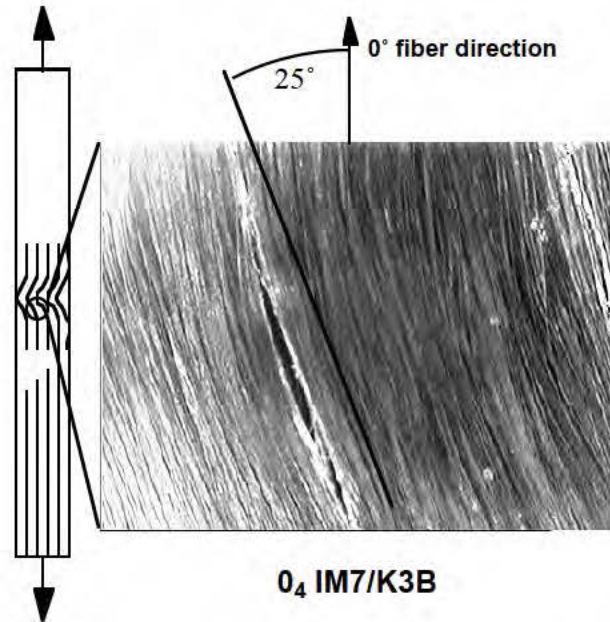


Figure 8. Microcracking within fiber waviness zone on the surface of a unidirectional composite.

In defect-free cross-ply composites, the weaker transverse ply cracks first in random locations, but the entire laminate remains intact since most of the load is borne by the higher strength longitudinal ply. We found that the presence of the fiber waviness defect lowers the threshold for this transverse microcracking and causes it to form in pairs that are adjacent to the defects as shown schematically in Fig. 9. The threshold for cracking of the transverse ply is reduced from 1.25% to 0.67% due to the presence of the defects. The reason for the paired pattern of these microcracks is that the 0° ply cracks first in the most misaligned region at strains less than 0.5%. This cracking makes the defect even more compliant, allowing a magnification of strain in the adjacent transverse ply. Despite the cracking, which occurs first in the 0° ply and then, second, in the 90° ply, ultimate failure of the laminate doesn't occur until it reaches a strain of 1.14%. Since the unidirectional composite containing defects fails at a lower average strain of 0.85%, it is apparent that there is a synergy between the two crossed-ply, which acts to reinforce the locally damaged regions in the $0/90_2/0$ laminate.

We are currently extending this work to examine the propagation of damage under tensile fatigue loads.

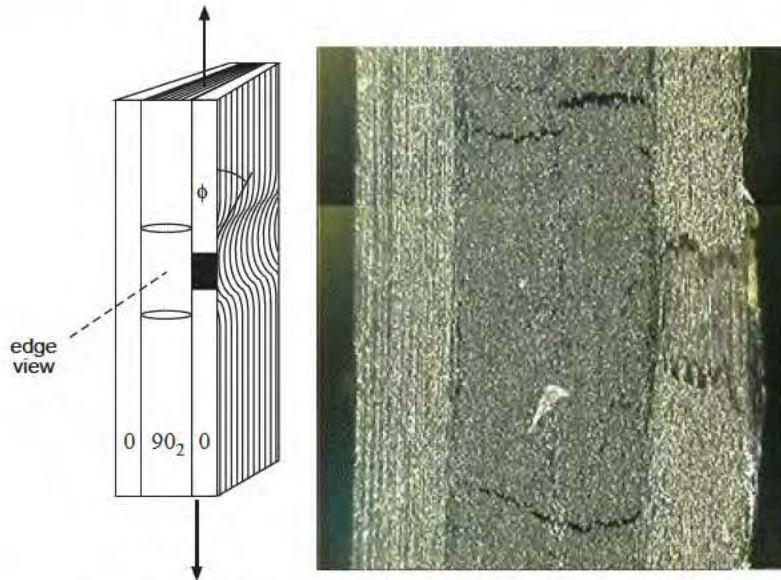


Figure 9. Microcracking initiation in the vicinity of a fiber waviness defect in IM7/K3B cross-ply composite.

Failure and Fatigue under Combined Interlaminar Stresses

Previously we have described a method for investigating the mechanical performance of thick-section composites under combined interlaminar stresses [9]. Results for shear fatigue of IM7/8551-7 were presented and it appeared that a single characteristic fatigue curve could be used to describe the effects of temperature and compression stress on fatigue life. Additional results for the effect of moisture are reported here and compared with predictions based on a simple fit to data collected under one condition.

In the course of our fatigue studies we discovered that specimens that had been stored for about one year at ambient conditions exhibited a significant loss in performance at elevated temperature (200°F). Strength measurements of these specimens at 200°F revealed a 15% drop from previously measured values. A plausible explanation for this apparent “aging” effect was the absorption of water into the matrix of the composite material. While it is well-known that water is a plasticizer for many polymeric materials and therefore can lower the glass transition temperature, it wasn’t expected that water absorbed at ambient conditions would be sufficient to cause the observed changes in mechanical properties. Nevertheless, specimens were subjected to vacuum drying at 155°F and 20 mTorr to see if water absorption was contributing to the reduced performance. After 190 hours of drying, the weights of the specimens had stabilized at a value that was only 0.34 wt% lower than the predried condition. However, the dried specimens did indeed show a recovery of the original strength at 200°F.

This finding is reported for two reasons. First, this material has been selected as a candidate for composite-wrapped gun barrels in the Navy Firebox ship-defense system. Considering both the exposure to water and the heating of the barrel during firing, our results show that there could be severe degradation in performance of the composite in this environment. The second reason for describing the water effect is to compare interlaminar

shear fatigue lifetimes of moisture-containing specimens with the original, presumably dry specimens. Data for three series of tests at 200°F are plotted in Fig. 10.

The observation that a single relationship could describe life for various conditions of temperature and combined stress implies that the failure mode is identical for the different test conditions. More importantly, it suggests that fatigue lifetimes for a variety of loading conditions can be predicted using this relationship. The general shape of the curve is adequately captured using the form:

$$\frac{\sigma}{\sigma_0}(\%) = A + (100 - A)e^{-BN^C} \quad (1)$$

where σ is the maximum fatigue stress, σ_0 is the quasi-static strength at each test condition, N is the number of cycles to failure, A is the fractional run-out value, and B and C are material constants. The constants A , B , and C are independent of temperature, combined stress and moisture content.

It is important to note that the large increases in quasi-static strength, achieved with out-of-plane compression stress, translate into significant improvements in fatigue life at a particular maximum shear stress. This effect is demonstrated graphically in Fig. 10. For this particular case, the superposition of 15 ksi compression stress improves fatigue life to an extent that “run-out” is achieved at a shear stress level equal to the interlaminar shear strength measured under pure shear.

The solid lines in Fig. 10 are predictions based on using Eq. (1) and constants obtained from a fit to the data obtained for dry specimens under 0 psi compression. The effects of both 15 ksi compression and the absorption of small quantities of water are predicted with reasonable accuracy by this characteristic curve.

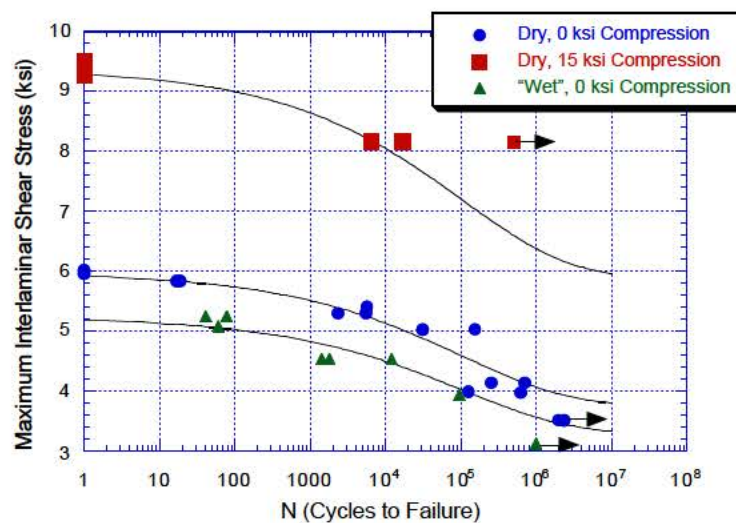


Figure 10. Predicted and measured shear fatigue lifetime changes at 200°F due to interlaminar compression and moisture absorption.

Conclusions

Results for the effect of superimposed pressure on the failure of unidirectional composites show that interactive failure criteria are required for both matrix- and fiber-dominated failure modes. Pressure causes a large increase in matrix-dominated strength, but decreases fiber-direction compression strength. The multiaxial stress state generated in $[30/0/-30/0]_{25}$ laminates under combined pressure and axial compression was shown to suppress a premature failure mode and improve performance.

Processing-induced fiber waviness defects were found to significantly reduce the tensile strength of unidirectional and cross-ply laminates. By analogy to notch strength analysis, we found that the composites examined herein exhibit a notch-insensitive relationship between defect dimensions and tensile strength loss. However, new damage mechanisms were found to initiate at relatively low strain thresholds at the defect sites, which may limit tensile fatigue life.

We found that interlaminar shear fatigue life was limited by a single failure mechanism, which allows prediction of life under various conditions of temperature, combined stress, and moisture content.

Acknowledgments

We are grateful to the contributions made by others to this work. Our thanks to Will Andrade and Jeff Petersen for their help in designing and machining improvements to the test systems and specimens and to Greg Larsen for his help with the tensile tests of composite with fiber waviness defects. The discussions with Chris Hoppel and Jerome Tzeng of ARL have provided important guidance to this project.

References

1. R. M. Christensen and S. J. DeTeresa, "The Kink Band Mechanism for the Compressive Failure of Fiber Composites," *J. Appl. Mech.* **64**(1) 1, 1997.
2. A. L. Highsmith, J. J. Davis, and K. L. E. Helms, "The influence of fiber waviness on the compressive behavior of unidirectional continuous fiber composites," *Composite Materials: Testing and Design (Tenth Volume)*, ASTM STP 1120, Glenn C. Grimes, Ed., ASTM, Philadelphia, pp. 20–36, 1992.
3. B. P. Rice and A. S. Crasto, "The influence of tooling CTE on the properties and microstructure of T650-42/Radel 8320 Composites," *40th International SAMPE Symposium*, pp. 1572–1583, May 8–11, 1995.
4. W. A. Spitzig and O. Richmond, "Effect of Hydrostatic Pressure on the Deformation Behavior of Polyethylene and Polycarbonate in Tension and Compression," *Polym. Eng. Sci.* **19**(16) 1129–1139, 1979.

5. T. V. Parry and A. S. Wronski, "Kinking and compressive failure in uniaxially aligned carbon fibre composite tested under superposed hydrostatic pressure," *J. Mater. Sci.*, **17** 893-900, 1982.
6. R. M. Christensen, "Stress based yield/failure criteria for fiber composites," *Int. J. Solids Struct.* **34**(5) 529–543, 1997.
7. R. M. Christensen, "Tensor Transformations and Failure Criteria for the Analysis of Fiber Composite Materials," *J. Comp. Mater.*, **24**(8) 796–800, 1990.
8. W. W. Feng, "A Failure Criterion for Composite Materials," *J. Comp. Mater.*, **25**(1) 88–100 (1991).
9. S. J. DeTeresa, D. C. Freeman, and S. E. Groves, "Durability of Fiber Composites for Munitions Applications," *Joint DoD/DOE Munitions Technology Development Program FY97 Progress Report*, LLNL UCRL-ID-103482-97, January 15, 1998.

Publications

1. S. J. DeTeresa, D. C. Freeman, and S. E. Groves, "Fatigue and Fracture of Fiber Composites under Combined Interlaminar Stresses," *Proceedings of the American Society for Composites, 13th Technical Conference on Composite Materials*, Baltimore, MD, September 21–23, 1998.
2. S. J. DeTeresa, S. E. Groves, and R. J. Sanchez, "Advanced Composites Technology," ARL Technical Report, 1998.

This page intentionally left blank

II. Energetic Materials Overview

The energetic materials effort focuses on the storage of chemical energy and its precise release in applications involving metal acceleration, blast, and the generation of gas at high pressure and temperature. To do so in a precise, efficient, safe, and predictable manner, we need to develop a scientific understanding of the chemical and physical properties at conditions ranging from ambient pressures up to 500,000 atmospheres, temperatures to 5000°C, and times as short as one nanosecond. To design advanced weapons and other devices, we must be able to synthesize and formulate very high-energy–high-power materials that are precise, safe, and affordable. Our main thrust is in high explosives but technical challenges in gun and rocket propellants are also addressed.

A majority of energetic materials projects are managed as the High Explosives and Initiation Systems Thrust Program, which coordinates the efforts in this area to meet the needs of both the Department of Defense (DoD) and the Department of Energy (DOE). Both agencies desire energetic materials with increased or tailored performance, decreased sensitivity with reliable initiation systems, processing technologies consistent with new and anticipated environmental safety and health regulations, and a fundamental understanding of safety and vulnerability hazards.

The work in this program is a particularly good example of the synergy that has developed within the Memorandum of Understanding program. Both agencies' missions have directly benefited far beyond the investment made by each. In recent years, the goals of the DoD and the DOE have become even more similar as a relatively small number of moderate to high cost, smart convention munitions whose energetic materials specifications are similar to those in nuclear devices begin to replace traditional mass-use munitions.

Our FY98 effort ranges from basic materials research and development to the characterization of new and existing materials and development of the capability to predict the response of munitions in abnormal environments. During this past year, the synthesis effort scaled the insensitive molecule LLM-105 to 500-gram quantities. Our Formulations and Characterization Project began testing on the material and found it to be very insensitive to one-dimensional shock loading. The insensitivity to shock is approaching that of the extremely insensitive explosive TATB. Another synthesis was successfully carried out on diaminodinitroethylene (DADE). This explosive was first synthesized by the Russians. It is also being looked at by the Swedes as a high power, less sensitive explosive. Our preliminary work indicates that DADE will have similar explosive performance to RDX. DADE has been found to have a complex thermal decomposition that must be understood to determine its hazard properties. As development of LLM-105 and DADE continues, we have started discussion with NSWC, Indian Head, concerning a joint development program.

New munitions designs and safety analyses require the ability to predict highly coupled thermal-mechanical-chemical-hydrodynamic processes. The Ignition and Initiation Project is developing the capability to predict the violence of the cook-off and the response to mechanical insult of energetic materials and their systems. This year, we applied

microimpulse radar (MIR) to measuring the violence of explosive reactions. We initiated a series of highly designed thermal cookoff experiments using the radar as one of the diagnostics. These tests should provide the DoD and the DOE with data needed for model development in computational simulations. The effort is taking advantage of DOE's Accelerated Strategic Computing Initiative (ASCI), which is providing the software and hardware infrastructure from which practical simulation of munitions may be made. Models of explosives response are being developed and implemented in the three-dimensional code ALE. This code is able to simulate coupled thermal, mechanical, chemical, and hydrodynamic phenomena.

Our CHEETAH thermochemistry effort has several accomplishments. We developed a kinetic detonation model based on multi-species equations of state and multiple reaction rate laws. This allows us to model a wide range of ideal and non-ideal composite energetic materials. Detonation velocities are accurate to within a few per cent and there is generally good agreement with estimated reaction zone lengths. CHEETAH Version 1.40 was released to over 300 users. CHEETAH Version 2.0 is just going through review and release; version 2.0 includes expanded gun and rocket propulsion capabilities.

In the Gun Propellant effort, we have begun to investigate the effects of processing variables on the laminar burn rates, using our high-pressure strand burner to measure these rates at pressures exceeding 700 MPa. We burned JA2 and M43 propellant samples, provided by the Army, from propellant lots previously used in round-robin tests. We received more recently formulated EX-99 propellant, similar to M43, from NSWC Indian Head, and have begun preparation for burn-rate testing with that material. Data obtained will enable us to determine the impact of processing variables on burn rates. This information is not only of critical importance to propellants but also provides data relevant to explosives safety.

Major limitations remain in our modeling capability. This study will obtain the equations of state for high explosives and detonation products in an extended range of high pressures and temperatures. In FY98, we determined the isotherms of unreacted HMX, RDX, and PETN at quasi-hydrostatic high pressures below 45 GPa by using a diamond-anvil cell, angle-resolved synchrotron x-ray diffraction method. The equation-of-state parameters (bulk modulus B_0 and its derivatives B') are presented for the 3rd-order Birch-Murnaghan formula based on the measured isotherms. We also present the evidence of shear-induced chemistry of HMX in non-hydrostatic conditions. In this report, we also briefly describe the experimental plan for FY99.

Synthesis and Scale-up of New Explosives

Philip F. Pagoria, Alexander R. Mitchell, Robert D. Schmidt, Glenn A. Fox,
Theodore F. Baumann, and Laurence E. Fried
Lawrence Livermore National Laboratory
(925) 423-0747
pagoria1@llnl.gov

Abstract

We are investigating the synthesis of new energetic materials comprised of nitro- and amino-substituted heterocycles. We anticipate this class of compounds will provide target molecules for both our main areas of research. These research areas were selected in response to the needs of the Department of Defense (DoD) for (1) insensitive energetic materials that approach HMX in energy and (2) new energetic materials that are calculated to have more energy than CL-20. In the first area of research, in FY98, we synthesized 500 g of 2,6-diamino-3,5-dinitropyrazine-1-oxide (LLM-105), 400 g of 1,1-diamino-2,2-dinitroethylene (DADE) 20 g of 3,6-dinitropyrazolo[4,3-d]pyrazole (DNPP), and 10 g of 4-amino-3,5-dinitropyrazole (ADNP), all with 80 to 85% of the energy of HMX and excellent thermal stability. We have also synthesized 5 g of 1,4-diamino-3,6-dinitropyrazolo[4,3-d]pyrazole (DAPP) a new energetic material with a crystal density of 1.84 g/cc and a predicted performance of 104% of HMX. In the second area of research, we synthesized a series of nitro-substituted, heterocyclic intermediates to target molecules that are calculated to have more energy than CL-20. The structure, predicted performance, and synthetic scheme for each of the target molecules was a result of a collaborative effort between the synthesis and the theoretical modeling groups. Finally, the synthesis of insensitive energetic materials by the Vicarious Nucleophilic Substitution (VNS) of hydrogen, which incorporates 1,1,1-trimethylhydrazinium iodide (TMHI) as an aminating reagent for nitro-substituted aromatic and heterocyclic compounds, is a continuing effort in our program.

Introduction

The Synthesis Group of the Energetic Materials Section is dedicated to the development of new energetic materials while being responsive to both the Department of Energy (DOE) and DoD needs. Our efforts over the years may be summarized into several different areas of interest: (1) new, insensitive compounds that perform better than 2,4,6-trinitrotoluene (TNT); (2) new energetic compounds that possess more energy than 1,3,5,7-tetranitro-1,3,5,7-tetraazacyclooctane (HMX) or CL-20; (3) synthesis of new oxidizers for propellant application; and (4) new energetic polymer ingredients.

Our group has the capability to synthesize and perform process and development work on new compounds from the milligram to the multi-kilogram scale. In addition, our group is closely coupled with the LLNL theoretical modeling and experimental testing groups, providing the capability to quickly obtain performance measurements and equation-of-state information on new compounds with as little as 50 g of material.

The areas of interest we identified address the need for improvement in the safety and performance of current and future weapon systems. As an example, the development of new energetic materials possessing more energy than HMX has been of critical importance to weapon designers for some time. Although HMX has very good performance and safety characteristics, it has been found lacking in some applications where energy per unit volume is critical. The development of a more energetic high explosive would provide alternatives in these applications. The development of new oxidizers for propellant application will lead to an increase in Isp (specific impulse) and range of new weapon systems while new polymer ingredients for thermoplastic elastomers will aid in the demilitarization of weapons. Finally, with the growing concern for safety, the development of a more insensitive and energetic replacement for TNT and RDX has also been a critical area of research in recent years. We believe this area of interest to be especially important to meet the insensitive munitions (IM) requirements for future weapon systems.

Many of our projects are done in collaboration or discussion with groups in the DoD community, including NavAir-China Lake, NavSea-Indian Head, and Eglin Air Force Base. A current project in our group is the synthesis of 1,1-diamino-2,2-dinitroethylene (DADE), a new insensitive energetic material which is calculated to have 85–90% the energy of HMX. This synthesis will be done in collaboration with NavSea-Indian Head, which shares an interest in the synthesis and performance measurements on this compound. In the future, the synthesis will be scaled up to the pilot plant scale at Indian Head.

The nature of our synthetic research program demands that the synthesis and characterization of the performance of a new energetic material be considered a payoff. We will provide performance and sensitivity information of the new energetic material to the DoD and DOE for their evaluation of its usefulness. Additionally, information gained on new materials will help improve predictive capabilities, point out anomalies due to structural features, and assist in guiding the design of future generation target materials in our collaborative effort with our theoretical modeling group.

Summary of Work and Milestones

Our synthetic work in the past year was divided into two main thrust areas: (1) synthesis of new energetic compounds which are predicted to be more energetic than CL-20; and (2) synthesis of new insensitive energetic explosives (IHEs) with more energy than TNT. From this latter effort we have synthesized 2,6-diamino-3,5-dinitropyrazine-1-oxide (LLM-105) [1,2], an insensitive energetic material with 30% more energy than TNT. The synthesis of LLM-105 through the oxidation of 2,6-diamino-3,5-dinitropyrazine with trifluoroacetic peracid at room temperature was first reported by us in 1995 [1]. The synthesis of the

immediate precursor to LLM-105, 2,6-diamino-3,5-dinitropyrazine (ANPZ), was first reported by D.S. Donald at DuPont [2] and repeated in our laboratories in the initial synthesis of LLM-105. The DuPont [2] synthesis involved the condensation of diaminomaleonitrile with diiminosuccinonitrile in trifluoroacetic acid to give tetracyanopyrazine, which when reacted with ammonia gives 2,6-diamino-3,5-dicyanopyrazine. This was hydrolyzed to the dicarboxylic acid and then nitratively decarboxylated with a nitric/sulfuric acid mixture to give ANPZ. Our first synthesis of 10 g of LLM-105 provided enough material to perform small-scale safety tests and characterization of the physical properties of LLM-105. It was found to be a dense ($\rho = 1.913 \text{ g/cc}$), thermally stable ($\text{DSC} = 347^\circ\text{C}$), relatively insensitive energetic material ($\text{Dh}_{50} = 117\text{cm}$) with 81% the energy of HMX.

Recently we scaled up the synthesis of LLM-105 to produce 900 g using a procedure described in a Russian patent [3] for the synthesis of ANPZ (Fig. 1). This provided enough material for shock sensitivity and ODTX (One-Dimensional-Time-to-Explosion) measurements with the remaining amount of material to be used in a 1-in. cylinder shot near the end of the calendar year. The DuPont [2] synthesis of ANPZ was determined to be too difficult for scale-up so this new procedure was employed. We made significant improvements during our research and development to scale up the process to the yields and ease of work-up of the Russian procedure. The scale-up was performed in a batch process with energetic intermediates synthesized at a scale of 100 g or less. The final oxidation step involved treatment of 2,6-diamino-3,5-dinitropyrazine with a mixture of trifluoroacetic acid and 30% hydrogen peroxide at room temperature overnight. This is a heterogeneous reaction and the product is easily filtered from the reaction mixture and washed with water to give LLM-105 as a brilliant yellow powder in 95% yield. Recrystallization of LLM-105 to remove acid impurities was accomplished by dissolving LLM-105 in hot DMSO (120°C) and adding an equivalent amount of hot water to yield LLM-105 as fine needles. We are currently investigating other solvents of recrystallization in order to improve the crystal morphology of the product.

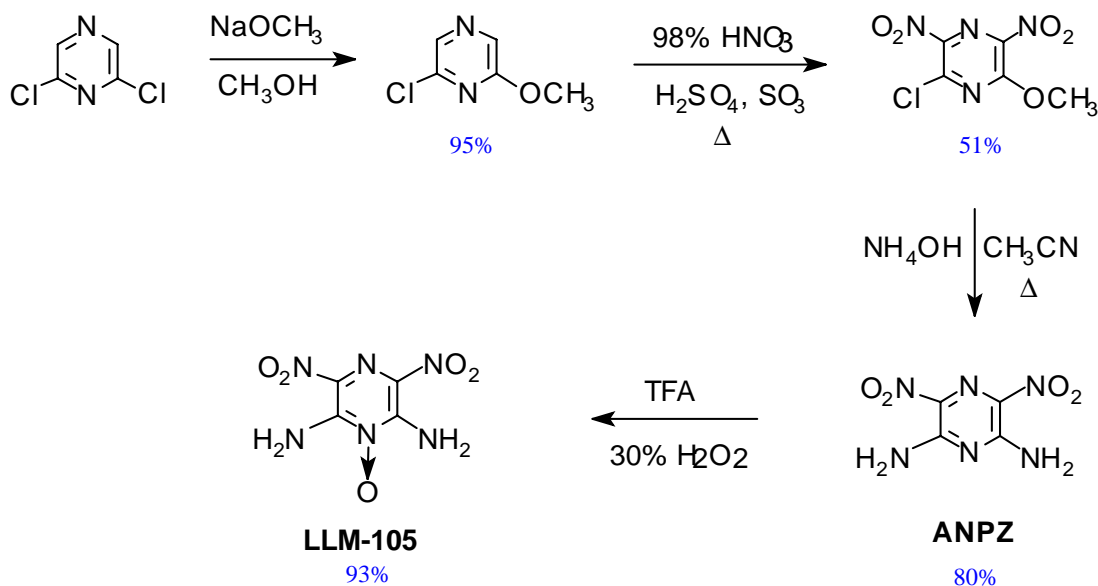


Figure 1. Synthesis of LLM-105. [3]

LLM-105 Shock Sensitivity and ODTX Experiments

Approximately 400 g of LLM-105 was formulated with Kel-F (92.4% LLM-105, 7.4% Kel-F) using a traditional slurry coating process, hydrostatically pressed into parts, and the explosive parts used in a series of shock sensitivity experiments. As mentioned earlier, our recrystallization process yielded LLM-105 as fine needles with a high aspect ratio. These were difficult to formulate and press into high-density parts. Therefore, the explosive parts could be pressed to only 92.4% TMD, but still encouraging results from the shock sensitivity experiments were obtained. Three experiments were performed at 30, 42 and 58 Kbar shock loading pressures, respectively. At 30 Kbar pressure, no reaction was observed, while at 42 Kbar, some reaction occurred but transition to full detonation did not occur at the maximum measured travel distance of 19.7 mm. At 58 Kbar, LLM-105 rapidly transitioned to full detonation. These results are encouraging for a material with 7.5% porosity. In comparison to other materials (including TATB) with similar pressing densities, LLM-105 approaches TATB in shock sensitivity and is superior to HMX and HNS.

ODTX experiments were also performed on LLM-105. The results indicate LLM-105 has essentially the same thermal stability as TNT, and is intermediate between HMX and TATB. These experiments placed the critical temperature of LLM-105 at 190–214°C. Another observation made during ODTX experiments is the violence of reaction. The violence of reaction observed for LLM-105 was mild with little damage to the hemispherical anvils used in the experiment. This contrasts with the fairly violent reaction and substantial damage to the anvils caused by HMX or RDX in ODTX experiments.

The remaining LLM-105 will be formulated and pressed into parts for a 1-in. cylinder shot. This will provide a measurement of the detonation velocity and performance and also allow the development of an equation-of-state model for LLM-105, which is invaluable to the weapon designers.

1,1-Diamino-2,2-dinitroethylene (DADE) and 3,6-dinitropyrazolo[4,3-c]pyrazole (DNPP)

We have recently scaled-up the synthesis of two new, insensitive energetic materials whose performance is predicted at 85–90% of HMX (Fig. 2). A total of 400 g of 1,1-diamino-2,2-dinitroethylene (DADE) was synthesized using two methods described to us by FOA-Sweden [4] (Fig. 3).

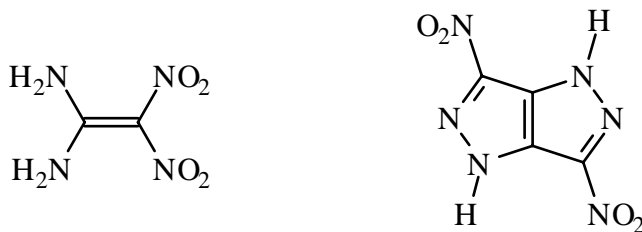


Figure 2. 1,1-Diamino-2,2-dinitroethylene (DADE) and 3,6-dinitropyrazolo[4,3,-c]pyrazole (DNPP).

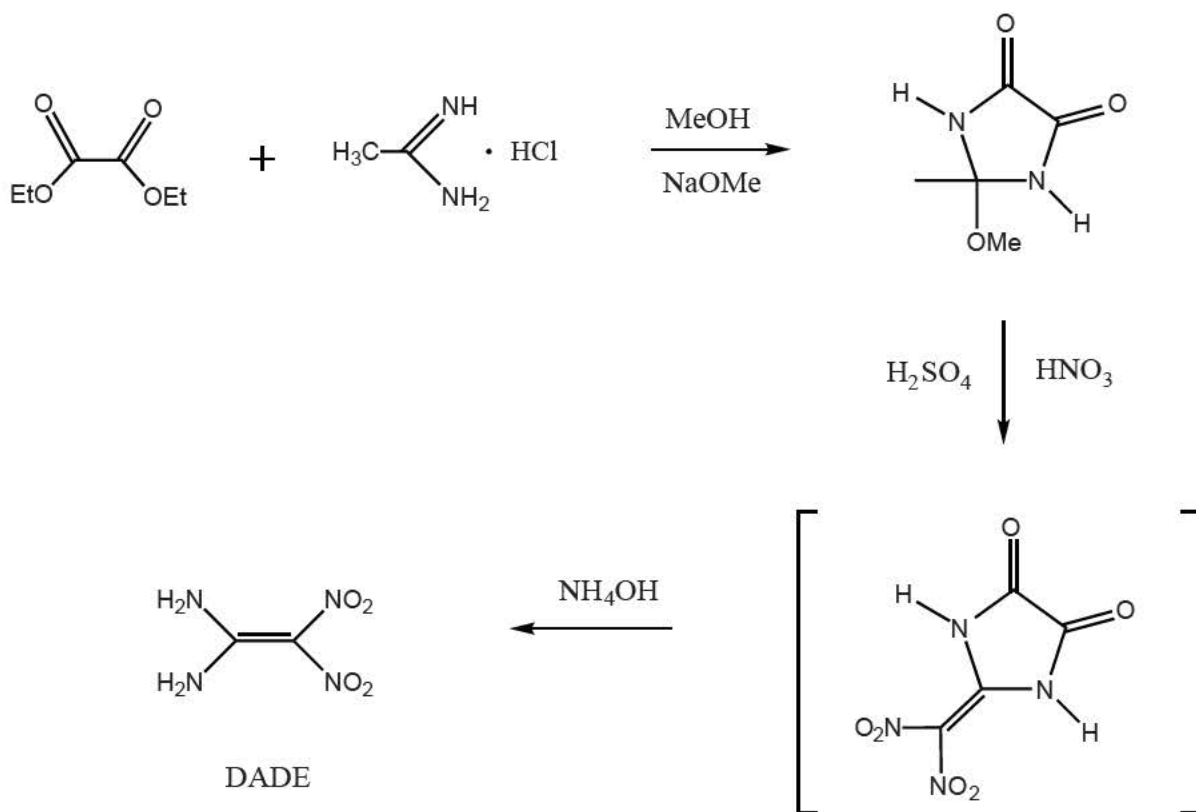


Figure 3. Synthesis of DADE.

(b)(3)

(b)(3)

Approximately 60 g of DADE was formulated and pressed into parts for ODTX measurements, and the remainder will be used in shock sensitivity experiments in the near future. The ODTX experiments showed DADE has thermal stability similar to TNT with a fairly mild reaction, as determined by the damage done to the anvils used in the experiment. The remainder of the DADE will be

used in shock sensitivity measurements similar to those performed on LLM-105. If the shock sensitivity measurements are also encouraging, a second scale-up will be completed and a 1-in. cylinder shot will be performed.

We have synthesized 40 g of 3,6-dinitropyrazolo[4,3-c]pyrazole (DNPP), using a method similar to that reported by Shevelev and coworkers [6] (Fig. 4). We made several significant improvements to the original synthesis resulting in higher yields and easier isolation of the intermediate products. We improved the first step by using a higher acid concentration, a shorter reaction time, and lower sodium nitrite concentration while improving the yield and purity of the product. The most significant improvement was to combine two steps into a single decarboxylative nitration step. Thus, 3-carboxy-6-nitropyrazolo[4,3-c]pyrazole was converted in one step in 60% yield by heating in a mixed acid solution for 4 hours at 45°C. This eliminated a low-yield, high-temperature, decarboxylation step. DNPP is thermally stable with a peak exotherm of 330°C, as determined by DSC, and a density of 1.865 g/cc, as determined by x-ray crystallography [5]. It has a $Dh_{50} = 68$ cm and is spark and friction insensitive. Predictive codes show it has 80–85% the energy of HMX. This compound is very promising in its own right but it is also being investigated as a precursor to two other target molecules: 1,3,4,6-tetranitropyrazolo[4,3-c]pyrazole and 1,4-diamino-3,6-dinitropyrazolo[4,3-c]pyrazole.

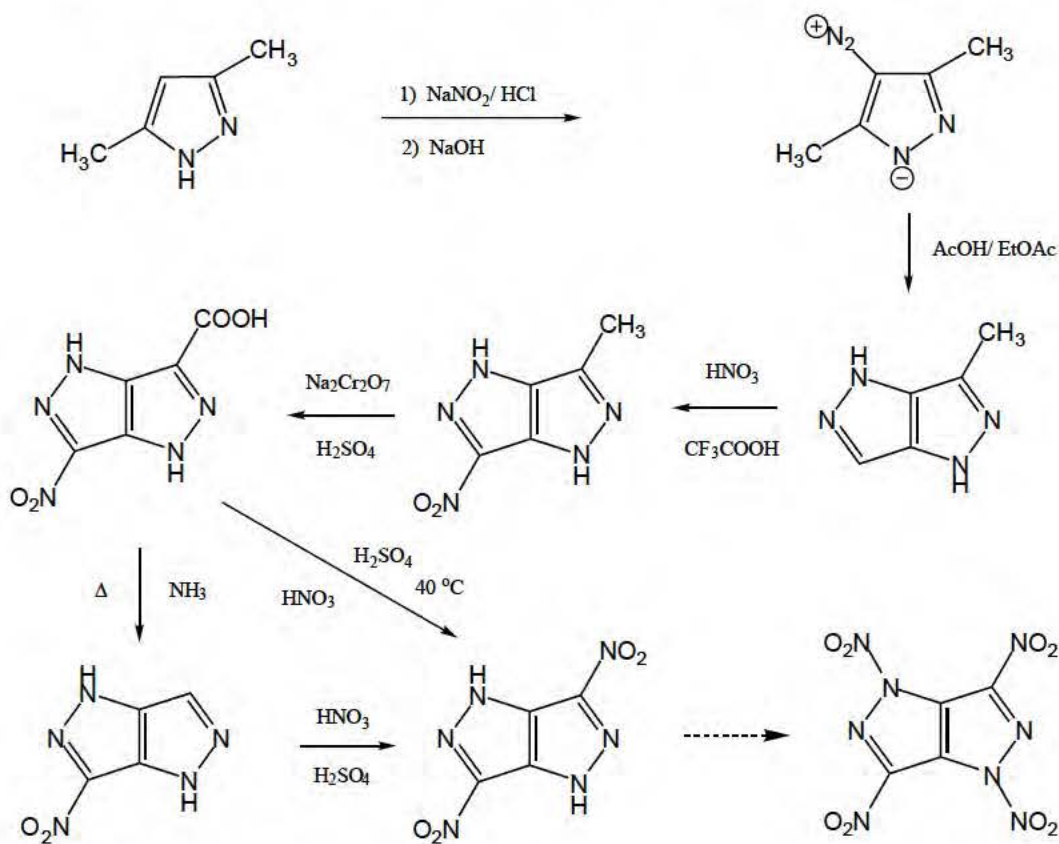


Figure 4. Synthesis of DNPP.

1,4-Diamino-3,6-dinitropyrazolo[4,3-c]pyrazole (DAPP)(LLM-119) was synthesized by amination of DNPP using either hydroxylamine-O-sulfonic acid in aqueous base [7] or O-mesitylenhydroxylamine in THF with NaH as the base [7] (Fig. 5). The latter method gives the best yields and product purity. LLM-119 has a density of 1.845g/cc as determined by x-ray crystallography [7], significantly lower than predicted. The low density may be attributed to the fact that the crystal structure shows the amino groups are orthogonal to the plane of the molecule. We predicted that the amino groups would be in the same plane as the rest of the molecule to maximize the delocalization of their lone pair of electrons with the heterocyclic π -electron system and maximize hydrogen bonding with the nitro- groups. The predicted geometry was that of a planar molecule, similar to TATB. In actuality, the repulsion energy between the lone pair of electrons of the amino-nitrogen and the ring nitrogen must be significantly greater than the energy gained by delocalization of the amino-nitrogen lone pair of electrons into the heterocyclic ring system and in maximizing hydrogen bonding. Dr. Richard Gilardi [5] noted that other compounds possessing an N-amino moiety, of which he determined the crystal structure, have similar crystal structures with the amino group orthogonal to the plane of the molecule. Even with the lower than anticipated density, LLM-119 still has a predicted performance 104% that of HMX. We are currently performing small-scale safety tests on LLM-119. This material has a peak exotherm at 253°C as determined by DSC, suggesting fairly good thermal stability.

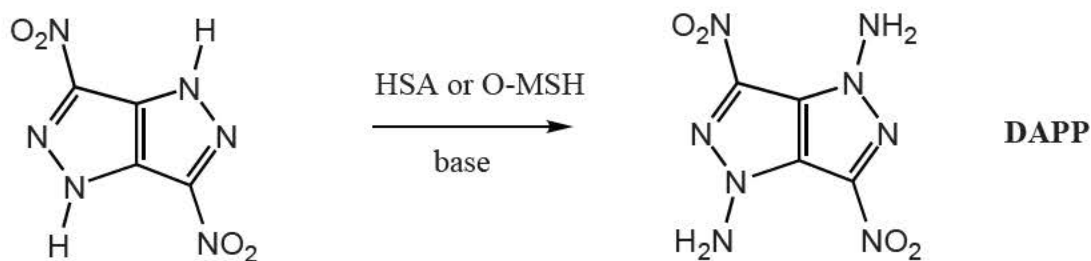


Figure 5. Synthesis of LLM-119.

(b)(3)

(b)(3)

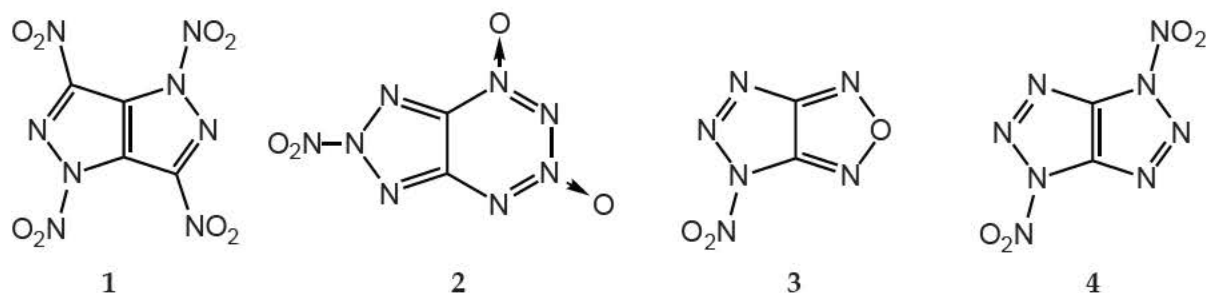


Figure 6. Target Highly Energetic Heterocycles.

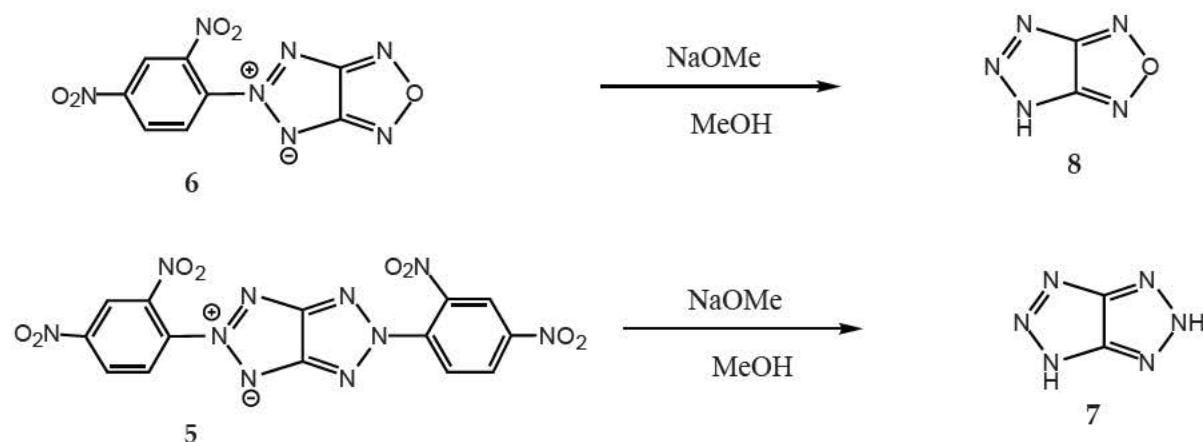


Figure 7. Reaction of 2,5-bis-(2,4-dinitrophenyl)triazolo[4,5-d]triazole (5) with NaOMe.

The synthesis of 4-amino-5-nitro-2-phenyl[1,2,3]triazole (9), using the method described by Nikitin and coworkers [8] was completed at the 15-g scale (Fig. 8). This compound is of interest as an intermediate to the triazolo[4,5-d]triazole target material and also to 4-amino-5-nitro-[1,2,3]-triazole (10), a potential higher energy, insensitive molecule. We have nitrated 9 using mixed acid at 90°C, yielding a mixture of products. The ¹H-nmr spectrum of the crude product suggests the desired 2,4-dinitrophenyl derivative was synthesized, but there also seems to be a substantial amount of the 4-nitro- and 2,4,6-trinitro-derivatives. We attempted to remove the 2,4-dinitrophenyl and 2,4,6-trinitrophenyl protecting groups from this mixture but have thus far been unsuccessful. Again, we are encouraged by this method because we were able to isolate 2,4-dinitroanisole, the expected product from the removal of the dinitrophenyl protecting group from 9. This investigation will continue and the various nitrated derivatives will be separated by chromatography before further attempts at the removal of their protecting groups. In addition, the nitration will be investigated more carefully in the hope that the synthesis of the 2,4-dinitrophenyl derivative can be optimized.

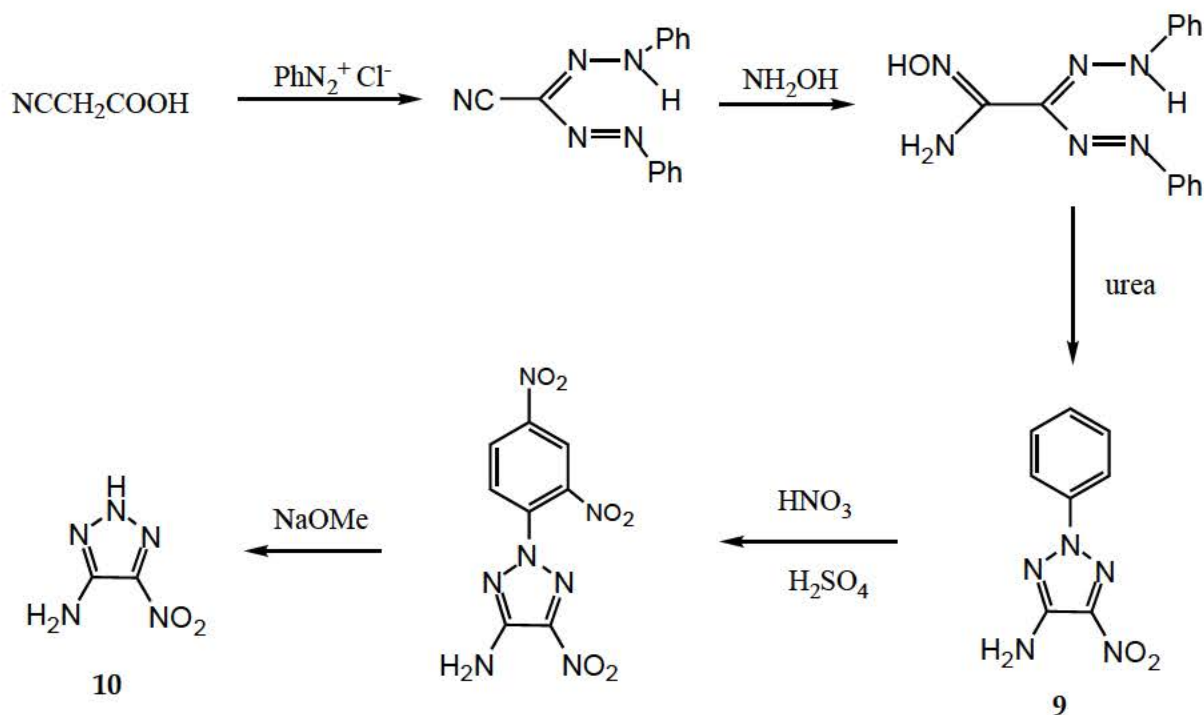


Figure 8. Nitration of 4-amino-5-nitro-2-phenyl[1,2,3]triazole (9).

The synthesis of 4-amino-5-formamido[1,2,3]triazole (**11**) [9] was completed at the 10-g scale. This compound may be an important intermediate to the bistriazole target molecule. The synthesis of **11** involved the condensation of hydroxylamine with thioamide in an equal molar ratio to yield thiocarbonylformamide oxime, followed by cyclization to 3-thiocarbamoyl-1,2,4-oxadiazole and condensation with hydrazine. We have made several attempts at the condensation of **11** with NaNO₂ to yield the triazolo[4,5-d]triazole ring system but thus far have been unsuccessful (Fig. 9). This investigation is continuing using alternative methods for forming the triazolo[4,5-d]triazole ring system.

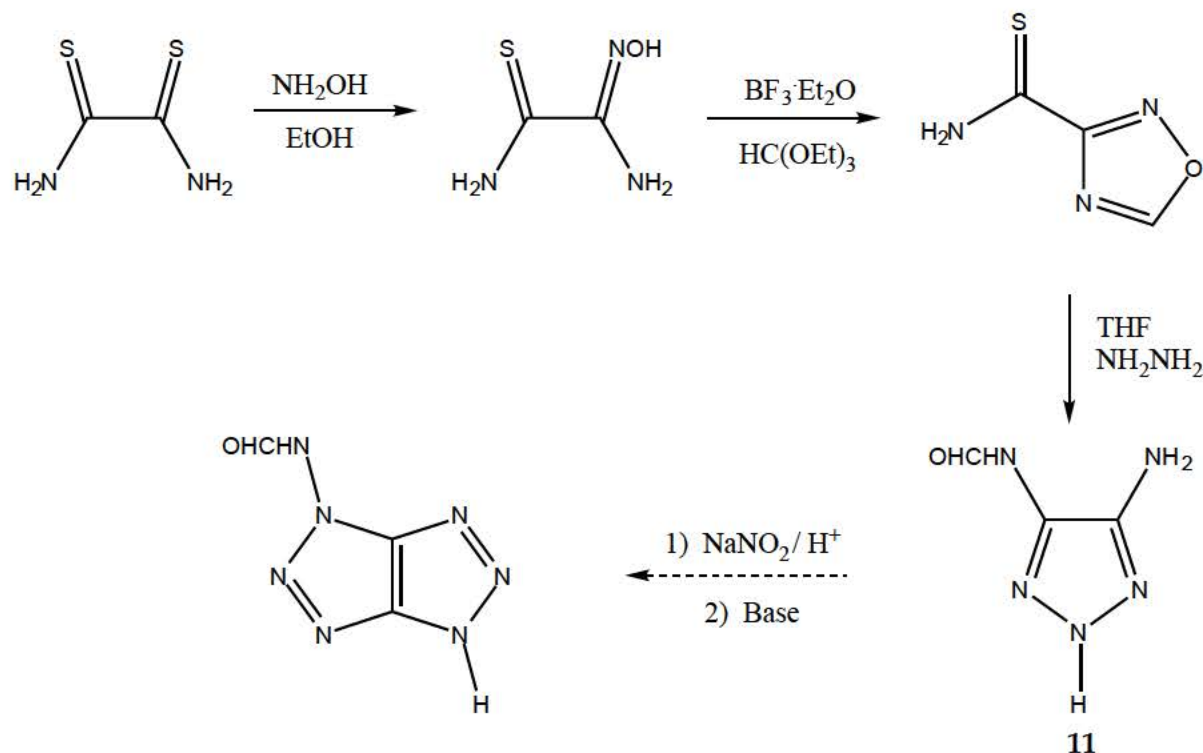


Figure 9. Synthesis of 4-amino-5-formamido[1,2,3]triazole (11).

Summary

The synthesis of LLM-105 was scaled up to 900 g and shock sensitivity and ODTX experiments were performed on the formulated material. These experiments indicated that LLM-105 approaches TATB in both thermal stability and shock sensitivity and surpasses both HMX and HNS. They suggest LLM-105 may have applications in both insensitive booster and main charge applications. We also reported the synthesis and small-scale safety testing of DNPP, an interesting new insensitive energetic material, with predicted performance 80–85% of HMX. We have synthesized 400 g of DADE and performed small-scale safety tests and ODTX experiments on the material. The ODTX experiments were encouraging with DADE exhibiting similar thermal response to TNT. The synthesis of DADE will be further scaled up in FY99 to produce enough material for shock sensitivity and performance measurement, and the results reported at a later date. We have also synthesized the new compound 1,4-diamino-3,6-dinitropyrazolo[4,3-c]pyrazole (LLM-119), predicted to have 104% the energy of HMX.

References

1. P.F. Pagoria, *Propell. Explosiv. Pyrotechn.*, submitted for publication.
2. D.S. Donald, U.S. Patent 3,808,209, Apr. 30, 1974.
3. Russian Patent SU 1703645A1. Cheeseman, Goodwin, *J. Chem. Soc.*, 1971, 2973.
4. N. Latypov, J. Bergman, A. Langlet, U. Wellmar, U. Bemm, *Tetrahedron.*, **54**, 11525-36, 1998.
5. X-ray crystallographic analysis performed by Richard Gilardi, Naval Research.
6. S.A. Shevelev, I.L. Dalinger, T.K. Shkineva, B.I. Ugrak, V.I. Gulevskaya, M.I. Kanishchev, *Russ. Chem. Bull.*, **42**, 1063, 1993.
7. Y. Tamura, J. Minamikawa, K. Sumoto, S. Fujii, M. Ikeda, *J. Org. Chem.*, **38**, 1239-41. 1993, V.M. Vinogradov, I.L. Dalinger, V.I. Guleskaya, S.A. Shevelev, *Russ. Chem. Bull.*, **42**, 1369-71, 1993.
8. V.I. Nikitin, A.V. Zavodov, A.L. Vereshchagin, L.I. Vereshchagin, *Zh. Org. Khim.*, **28**, 1885, 1992.
9. V.G. Anriyanov V.G. Semenikhina, A.V. Ereemeev, *Chem. Heterocycl. Cmpds.*, **28**, 803, 1992; G.I. Gregory P.W. Seale, W.K. Warburton, M.J. Wilson, *J.C.S. Perkin Trans 1*, **47**, 1973.

Publications

1. A.R. Mitchell, P.F. Pagoria, R.D. Schmidt, "Vicarious Nucleophilic Substitution using 4-amino-1,2,4-triazole, hydroxylamine or O-alkylhydroxylamine to prepare 1,3-diamino-2,4,6-triaminobenzene or 1,3,5-triamino-2,4,6-trinitrobenzene," U.S. Patent 5,633,406, May 27, 1997.
2. P. F. Pagoria, A.R. Mitchell, R.D. Schmidt, "Vicarious Nucleophilic Substitution to prepare 1,3-diamino-2,4,6-trinitrobenzene or 1,3,5-triamino-2,4,6-trinitrobenzene," U.S. Patent 5,569,783, Oct. 29, 1996.
3. P.F. Pagoria, A.R. Mitchell, R.D. Schmidt, and L.E. Fried, "Synthesis and Scale-up of New Explosives," Lawrence Livermore National Laboratory, UCRL-ID-125792, Jan. 15, 1997.
4. A. R. Mitchell, P. F Pagoria, and R. D Schmidt, "Amination of Electrophilic Aromatic Compounds by Vicarious Nucleophilic Substitution," Continuation-in-Part U.S. Patent Application (Nov. 10, 1997) claiming priority over International Application PCT/US96/06663 (May 10, 1996) filed by the same inventors.
5. P.F. Pagoria, A.R. Mitchell, R.D. Schmidt, G.A. Fox, T.F. Baumann, and L.E. Fried, "Synthesis and Scale-up of New Explosives," UCRL-ID-103482-97, p. II-3, January 15, 1998.

6. P.F. Pagoria, A.R. Mitchell, R.D. Schmidt, L.E. Fried, "Synthesis of New Explosives," C&MS Progress Report—FY96, UCID-20622-96, March, 1997.
7. A.R. Mitchell, P.F. Pagoria, R.D. Schmidt, "Recent Advances in the Chemical Conversion of Energetic Materials to Higher Value Products," UCRL-JC-127971, April 30, 1998.
8. A.R. Mitchell, M.D. Coburn, R.D. Schmidt, P.F. Pagoria, Chemical Conversion of Energetic Materials to Higher Value Products," UCRL-JC-113394, May 1, 1998.
9. R.D. Schmidt, A.R. Mitchell, P.F. Pagoria, New Synthesis of TATB Development Studies," UCRL-JC-130089, April 1, 1998.
10. P.F. Pagoria, A.R. Mitchell, R.D. Schmidt, R.L. Simpson, J.W. Forbes, R.W. Swansiger, D.M. Hofmann, "Scale-up, Synthesis and Characterization of 2,6-Diamino-3,5-dinitropyrazine-1-oxide (LLM-105)," UCRL-MI-130518.
11. P.F. Pagoria, A.R. Mitchell, and R.D. Schmidt, "Addressing a Cold War Legacy with a New Way to Produce TATB," *Science and Technology Review*, R. Upadhye, D. Wheatcraft, Eds., Nov. 1996.
12. "Transforming Explosive Art into Science," *Science and Technology Review*, R. Upadhye, D. Wheatcraft, Eds., June, 1997.
13. P. F. Pagoria, A.R. Mitchell, R.D. Schmidt, "1,1,1-Trimethylhydrazinium iodide: A Novel, Highly Reactive Reagent for Aromatic Amination via Vicarious Nucleophilic Substitution of Hydrogen," *J. Org. Chem.*, **61**, 2934, 1996.
14. P.F. Pagoria, A.R. Mitchell, R.D. Schmidt, and L.E. Fried, "Synthesis and Scale-up of New Explosives," UCRL-ID-125792, Jan. 15, 1997.
15. International PCT Patent Application (IL-9628 and IL-9686), A.R. Mitchell, P.F. Pagoria, R.D. Schmidt, "Amination of Electrophilic Aromatic Compounds by Vicarious Nucleophilic Substitution," May 1996.
16. A.R. Mitchell, R.D. Sanner, P.F. Pagoria, "Chemical Conversion of Energetic Materials to Higher Value Products," UCRL-JC-113394, May, 1996.
17. P.F. Pagoria, A.R. Mitchell, R.D. Schmidt, C.L. Coon, and E.S. Jessop, "New Nitration and Nitrolysis Procedures in the Synthesis of Energetic Materials," in *Nitration: Recent Laboratory and Industrial Developments*; Albright, L. F.; Carr, R. V. C.; Schmitt, R. J., eds.; ACS Symposium Series 623; American Chemical Society: Washington, D.C., 1996.
18. M.F. Foltz, D.L. Ornellas, P.F. Pagoria, A.R. Mitchell, "Recrystallization and Solubility of 1,3,5-Triamino-2,4,6-trinitrobenzene in Dimethyl Sulfoxide," *J. Mat. Sci.*, **31**, 1893–1901, 1996.
19. P. F. Pagoria, A.R. Mitchell, R.D. Schmidt, "Vicarious Amination of Nitroarenes with Trimethylhydrazinium Iodide," presented at the *211th American Chemical Society National Meeting, New Orleans, LA*, March 24–28, 1996.

New Formulations and Material Characterization

R. L. Simpson, R. W. Swansiger, J. W. Forbes, R. S. Lee, J. Cutting,
T. M. Tillotson, and L. W. Hrubesh
Lawrence Livermore National Laboratory
(925) 423-0379
simpson5@llnl.gov

Abstract

The energetic molecule LLM-105 has been found to be extremely insensitive to shock. This material falls between TATB and HMX in explosive power, and is predicted to have 153% of the metal acceleration of TNT. We also have begun the early stages of characterization work on the energetic molecule DADE. This explosive has twice the impact insensitivity of HMX in the drop hammer and is comparable to RDX in detonation performance. It has very complex thermal decomposition behavior. One-dimensional, time-to-explosion test results are reported. Finally, we describe some entirely different approaches to explosive formulation and processing that are based on sol-gel chemistry.

Introduction

In this effort, we are developing and characterizing new energetic materials. Materials produced elsewhere are also evaluated using Lawrence Livermore's experimental, theoretical, and modeling capabilities. The goals include increases in energy, power, precision, and safety. Reduced costs are sought as well.

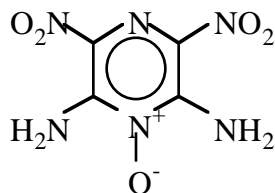
Two molecules were evaluated, LLM-105 and DADE. LLM-105 is an insensitive explosive with moderate energy and power. DADE is predicted to be somewhat higher in energy and power than LLM-105 but not as insensitive.

An entirely new process for making energetic materials is underway. The technology is based on sol-gel chemistry. Energetic material properties may be manipulated at the molecular level using low-cost bulk processing techniques. Potential applications include high explosives, propellants, and pyrotechnics.

Evaluation of the New Energetic Molecule LLM-105

Characterization of LLM-105

LLM-105 was synthesized in this energetic materials program. The formal name of the molecule is 2,6-diamino-3,5-dinitropyrazine-1-oxide; the structure is shown below. LLM-105 has excellent thermal stability. It is more thermally stable than 1,1'-(1,2-ethenediyl)bis-2,4,6-trinitrobenzene (a.k.a., HNS) and less stable than 1,3,5-triamino-2,4,6-trinitrobenzene (TATB). The material is very chemically stable. It also compares well in power and energy to RDX and HMX. The spectrum of properties of LLM-105 makes it a realistic candidate for future applications that require moderate performance and high insensitivity. In the following section "Evaluation of the New Energetic Molecule, DADE," we compare the performance properties of LLM-105 to other common materials and the Russian explosive DADE [1]. During FY98, the synthesis effort produced a larger quantity of LLM-105 to be characterized. Preliminary formulations have been made in this effort and larger scale characterization measurements made.



LLM-105

Figure 1 is a scanning electron micrograph of the LLM-105 crystals obtained in the synthesis of the material. These high surface area crystals have polymorphism characteristic of materials that can be used in initiation systems and devices requiring small failure diameters. Although desirable for some applications, this high surface area material would require other processing to obtain the desired rheological and processing properties appropriate for main charge applications. Crystal modifications have been attempted with some success. In Fig. 1, LLM-105 with a cubic habit can be seen amongst monoclinic needles. Although this crystal habit occurs to some small extent during standard recrystallization, it can be made to dominate in recrystallizations from nitric acid. However, we have not been able to make this cubic material in a chemically pure form. X-ray crystallography has shown it to be the same crystal polymorph. Fine, non-needle powders may also be produced through recrystallization.

We believe that particle morphology will not limit the utility of LLM-105 because we have demonstrated that it can be readily modified. The capability to easily produce high surface area material may be an advantage for some applications.

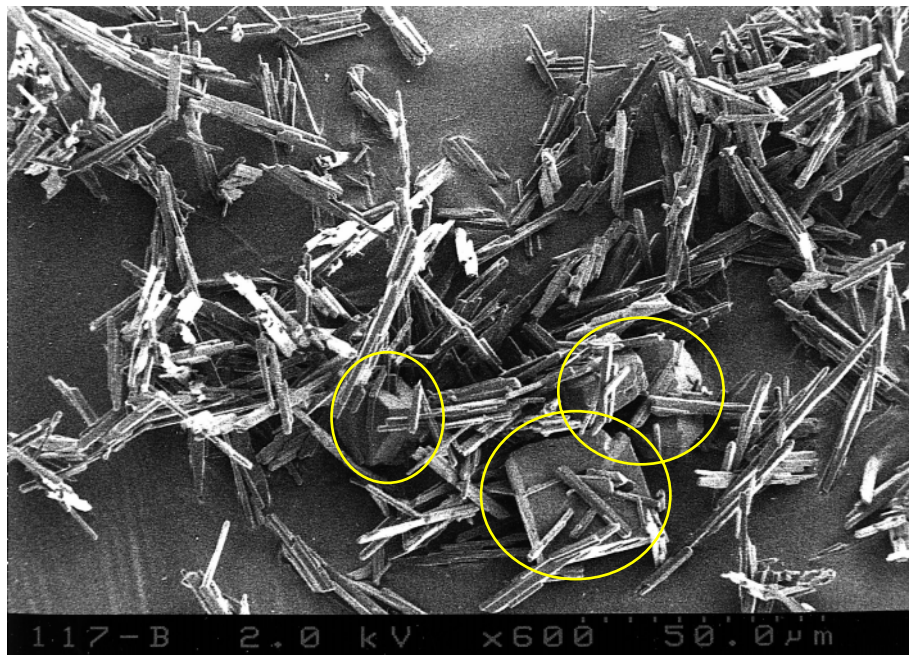


Figure 1. Scanning electron micrograph of LLM-105 showing long monoclinic needles. The cubic habits observed may be obtained through recrystallization in nitric acid.

Approximately 300 g of LLM-105 was formulated as a plastic bonded explosive for shock sensitivity experiments. This formulation, designated RX-55-AB, was made using the slurry process. It contained 7.59 wt% KelF-800, a high-density chlorofluorocarbon thermal plastic elastomer. RX-55-AB is a volumetric equivalent, with respect to explosive and binder content, to the extremely insensitive explosive LX-17-1 [2,3]. The particle distribution pictured in Fig. 1 was representative of the LLM-105 in the RX-55-AB formulation tested here. This molding powder was used to ram press samples for shock sensitivity studies. As expected, this simple prototype molding powder did not press well. At pressing conditions of 200 MPa and 105°C, part densities of only 93% of theoretical maximum were attained. Low density and high porosity increase the sensitivity to shock of explosives compared to the same materials near nominal press densities ($\geq 97\%$ of maximum density). Hence, this RX-55-AB was a material that was expected to be more sensitive to shock than could be expected for a formulation that went through a standard development cycle. In addition, high surface area explosives ingredients, such as those used in RX-55-AB, transition to detonation rapidly when shocked at moderate pressures. Therefore, in this explosive ingredient characterization effort, RX-55-AB was formulated counter to normal formulation practices, which seek to minimize shock sensitivity. The shock sensitivity of LLM-105 determined through these experiments should be considered greater than that which could be reasonably achieved in practical formulations.

Table 1 summarizes the small-scale safety test results for LLM-105 and RX-55-AB. All values are attractive from the insensitivity and stability points-of-view. One-dimension, time-to-explosion (ODTX) tests were carried out and were reported previously [4]. Those results showed LLM-105 to have times-explosions intermediate between those of HMX and the very stable explosive TATB. The reaction violence was low, similar to that exhibited by TATB.

Table 1. Small-scale safety test results of LLM-105 and RX-55-AB.

Material	Impact ^a (cm)	Friction ^b (kg)	Spark ^c	CRT ^d (cm ³ /g)
LLM-105 ^e	70–80	> 36	no reaction	n.a.
LLM-105 ^f	117	> 36	no reaction	0.056
RX-55-AB ^g	113	> 36	no reaction	0.032
PETN ref.	13–16	8.0	no reaction	0.4–0.56
HMX ref.	32	11.6	no reaction	≤0.1
LX-14	53	n.a.	no reaction	0.08

^a2.5-kg Type 12 tool with 35 mg pressed samples.

^bJulius-Peters-Berlin 21 friction machine; one reaction in ten tries.

^cTen tries at 1J with 510-W inline resistance.

^d22 h at 120°C under 1 atm He.

^eFirst 20-g batch; less pure.

^fFirst 100-g batch; more pure.

^gRX-55-AB is 92.41 wt% LLM-105 with 7.59% KeIF-800.

Shock Loading Experiments on RX-55-AB (LLM-105)

The sensitivity of RX-55-AB (LLM-105) to shock was evaluated using in situ pressure gauges in a series of three experiments. Figure 2 shows the experimental setup used. Eight manganin pressure gauges were assembled at four different positions within 50-mm-diam samples of RX-55-AB. Gauges were positioned at 0, 6.4, 12.7, and 19 mm in the explosive with 0 mm representing the point at which shock enters the sample. Shock loading was accomplished using a 102-mm smooth-bore powder gun. A 6061-T6 aluminum flier was used to impact the samples.

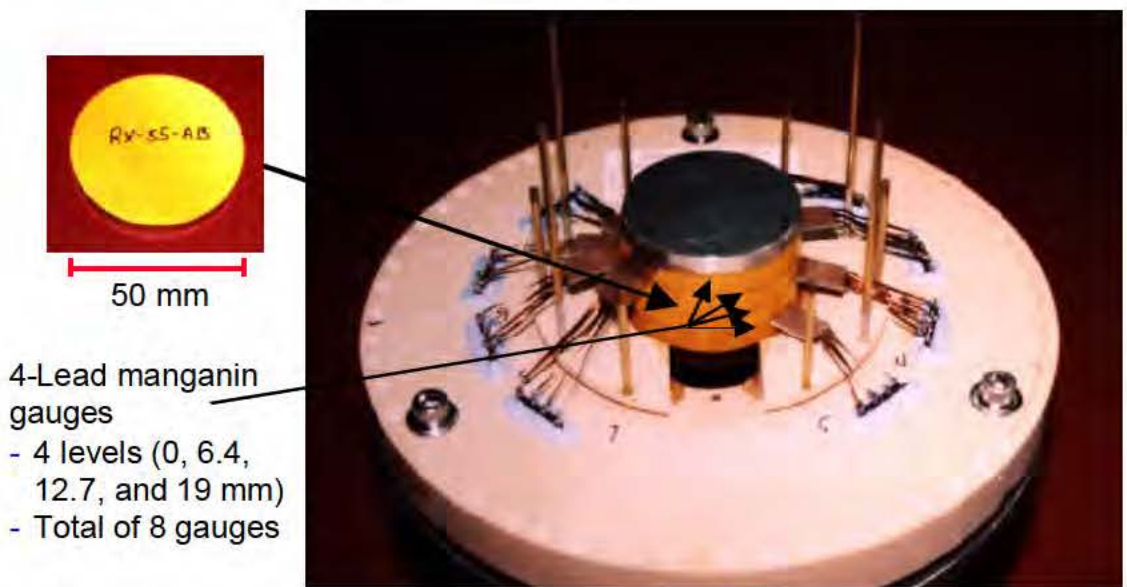


Figure 2. Target assembly used in the shock loading experiments.

The three experiments were carried out with initial shock strengths of 30, 42, and 58 kbar. The results observed at each gauge depth in the experiments are shown in Figs. 3–5. The measured shock velocities in the three regions between the four levels of gauges are listed in Table 2. Using the CHEETAH code, detonation properties were predicted at the initial RX-55-AB density of 93% theoretical maximum [5]. The predicted detonation velocity was 7.78 mm/ μ s. The Chapman-Jouguet pressure (i.e., the stress at the sonic plane) was calculated to be 253 kbar.

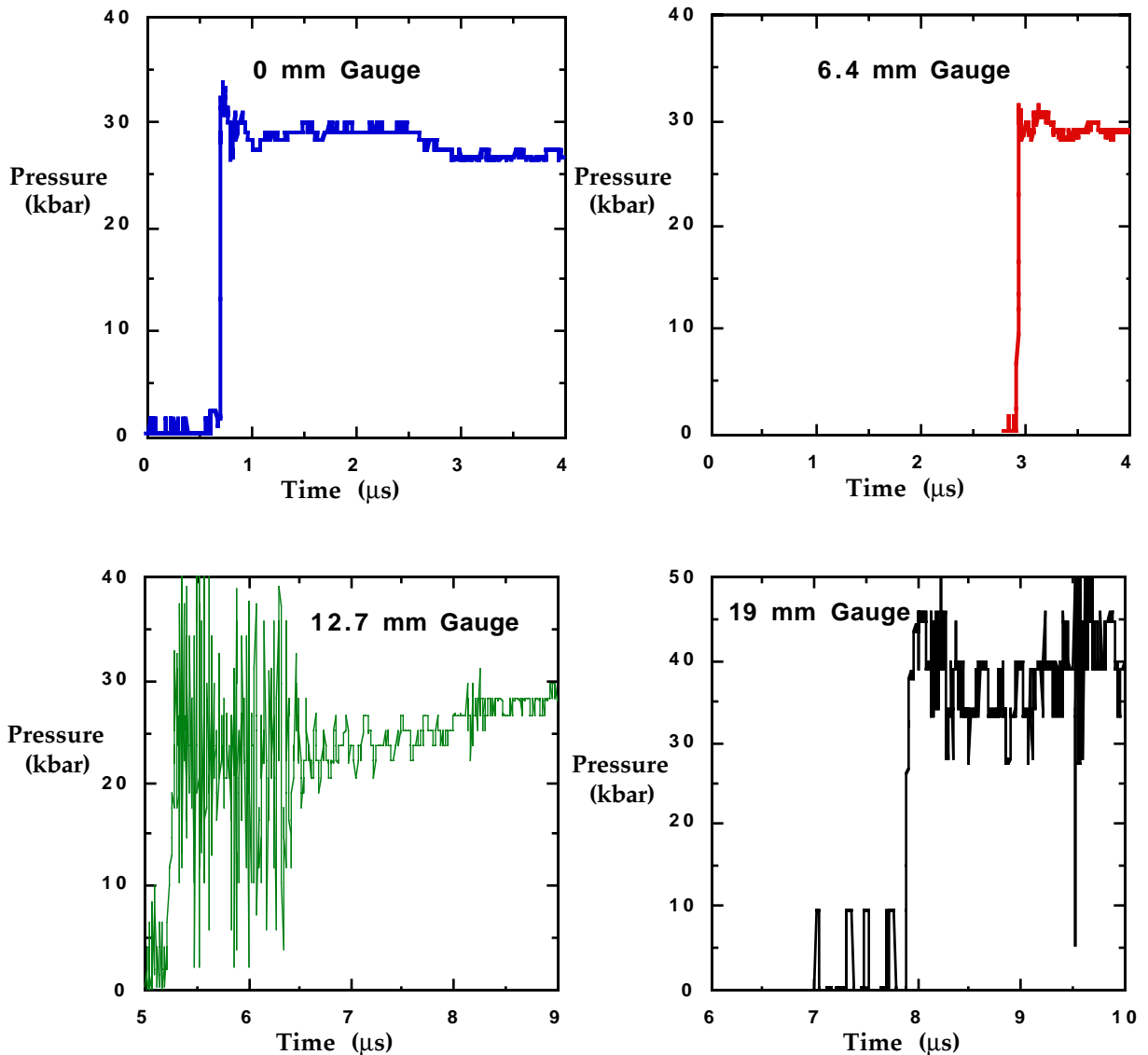


Figure 3. RX-55-AB shock loaded at 30 kbar. No build-up of chemical reaction was observed. Unreacted explosive material was recovered.

It can be seen in Fig. 3 that no reaction was observed at the moderate shock strength of 30 kbar. No buildup of shock velocity was observed either. Furthermore, unreacted explosive was recovered from the experiment. The absence of reaction in a porous explosive is unusual and a positive indication that LLM-105 is indeed an insensitive explosive.



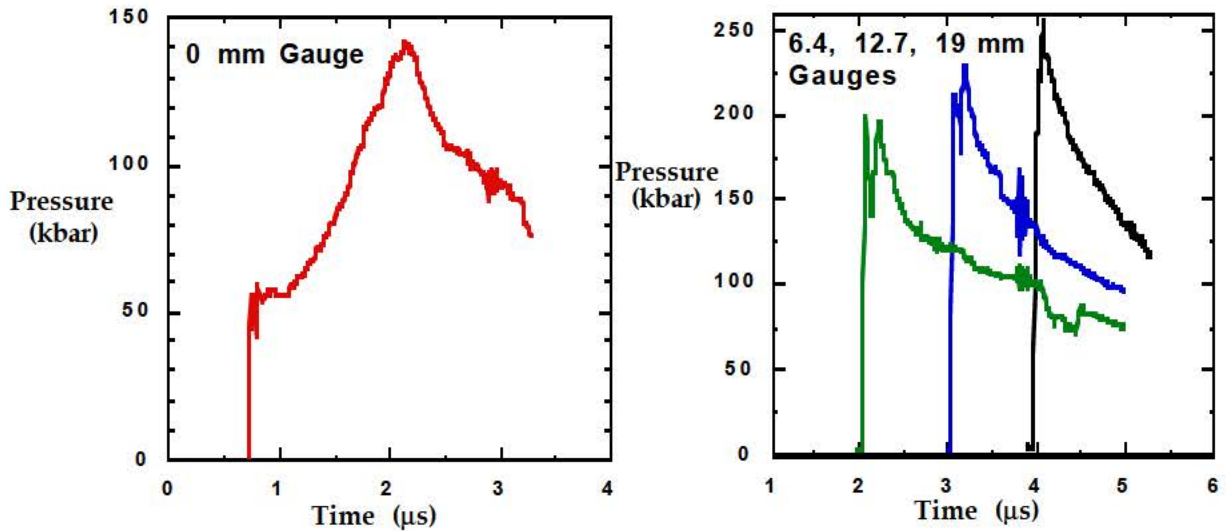


Figure 5. Experimental results with RX-55-AB shock loaded at 58 kbar. The peak shock pressure at the fourth gauge level is consistent with the predicted steady-state Chapman-Jouguet stress of 253 kbar.

At an initial shock strength of 42 kbar, a buildup of reaction was observed behind the shock front at the 0-mm and 6.4-mm gauge stations. Sharp shock fronts were measured at 12.7 mm and 19 mm, followed by relief waves. Analysis of the shock velocity indicated that steady-state detonation velocities were not achieved in any region (Table 2). The maximum velocity in Region 3 was 80% of the predicted value. The peak shock pressure at 19 mm into the flow was also only 80% that of the predicted value. Hence, we concluded that steady-state detonation was not reached within 19 mm.

Table 2. Measured shock velocities in in situ gauge experiments. The predicted steady-state detonation velocity was 7.78 mm/ μ s, 2.5% less than that observed in RX-55-AB.

Shock loading pressure (kbar)	Shock velocity (mm/ μ s)		
	Region 1 0.0–6.4 mm	Region 2 6.4–12.7 mm	Region 3 12.7–19.0 mm
30	2.96	3.00	\approx 2.87
42	3.48	4.57	6.24
58	5.01	6.73	7.98

In the third experiment, shown in Fig. 5, RX-55-AB was shocked to 58 kbar. In this case, sharp shocks followed by release waves were observed at all gauge stations except the first. The peak pressure increased at each depth within the flow indicating non-steady behavior. At 19 mm into the flow, the shock front pressure of \approx 250 kbar was in close agreement with the predicted value of 253 kbar. Analysis of the shock transit times showed the shock velocity to be increasing. A value of 7.98 mm/ μ s was measured in Region 3, which is 2.5% greater than that predicted.



(b)(3)

Figure 6 is a plot of run-distance-to-detonation versus shock loading strength of RX-55-AB and several other materials. The results are extremely encouraging in that LLM-105 was indeed found to be a very insensitive material. Figure 6 indicates that RX-55-AB is less sensitive than neat TATB at 88.5% density and approaches the insensitivity of LX-17.



(b)(3)

Conclusions from the Characterization of LLM-105

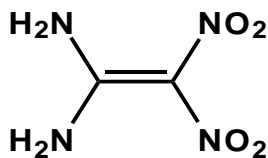
(b)(3)

In summary, LLM-105 appears to occupy an unusual region of property space in its combination of power, energy, sensitivity, and thermal and chemical stability. The synthesis of the material appears to be reasonable for large-scale production. High surface area material can be readily produced. Further developments are required to obtain particle morphologies for large charges. Possible uses for LLM-105 include applications where insensitivity or thermal and chemical stability are required. Munitions applications include insensitive detonators and boosters as well as bulk use in insensitive, high velocity, and hard target munitions.

Evaluation of the New Energetic Molecule DADE

Characterization of DADE

A recently identified molecule in the United States, 1,1-diamino-2,2-dinitroethylene (DADE), is now under characterization. This molecule was first synthesized in Russia. It has been pursued aggressively in Sweden, where they refer to it as FOX-7. As the Russians originated the material, and have not created their own designation, it is commonly referred by the IUPAC nomenclature-based acronym DADE.



1,1-diamino-2,2-dinitroethylene (DADE)

Table 3 tabulates the predicted performance properties of DADE and LLM-105 relative to other materials predicted using the CHEETAH code. (The confidence in the values is high as input data were measured and all materials have similar elemental structures). These calculations were based on measured heats of formation and densities. DADE is stoichiometrically equivalent to RDX and HMX ($C_xH_{2x}N_{2x}O_{2x}$). It is predicted to have nearly the performance of RDX. The lower performance is largely the result of DADE's lower density. DADE is predicted to have a detonation temperature ≈ 500 K lower than RDX and HMX. This characteristic may lead to slower reaction rates in composite explosives.

(b)(3)

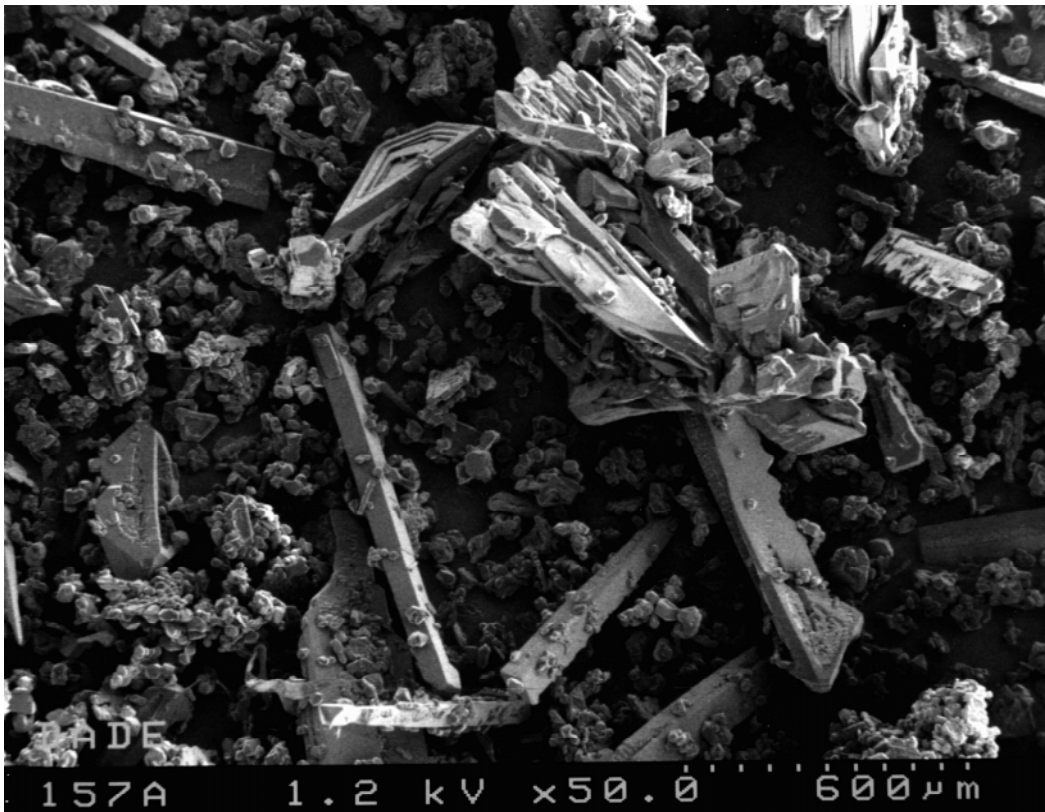


Figure 7. Scanning electron micrographs of DADE.

(b)(3)

Whether or not the first component of decomposition is dynamically coupled to the second decomposition step was examined. Figure 10 shows the result of heating DADE through the first exotherm, then cooling the material down to 100°C, and finally heating through complete decomposition. It can be seen that the second exotherm remains unchanged in character from that in a single sweep.

Samples of the DADE decomposition product were obtained by heating the material through the first exotherm and recooling to ambient conditions. Mass spectral analysis was done on both neat DADE and the decomposition product. When a thermal desorption probe was used, the mass spectra were the same for neat DADE and the decomposition product. It is likely that the thermal desorption analysis process resulted in the same decomposition process that was observed in the calorimetry. Further analysis is underway.

(b)(3)

(b)(3)

Thermal Cook-off: DADE

Our characterization strategy with larger quantities of materials was to measure the thermal response in the ODTX and then examine the detonation power [7]. In the ODTX test, a 1.27-cm sphere of explosive is rapidly inserted between two isothermal anvils at high temperature. The time to violent reaction is measured at a series of fixed temperatures.

The ODTX results for DADE, along with those for RDX and LX-10 (HMX), are given in Fig. 11. All reactions were mild explosions, except at intermediate temperatures where the violence of DADE approached that of RDX and HMX. Quantitation of the violence is in process. At high temperatures, the times-to-explosion were shorter than observed with the HMX-based LX-10. At lower temperatures, the times-to-explosion were longer.



(b)(3)

(b)(3)

Detonation Performance: DADE

Detonation front pressure measurements were made through a small-scale performance test [8]. The experimental configuration is shown in Fig. 14. A ≈ 300 -mg sample of neat DADE was initiated using a slapper detonator. The detonation wave then runs into a lithium fluoride crystal. The particle velocity at the DADE/LiF interface is monitored with a Fabry-Perot laser velocimeter. Shock velocities in the explosive are also measured. In the case of prompt initiation and steady-state detonation, the shock velocity equals the detonation velocity.



(b)(3)

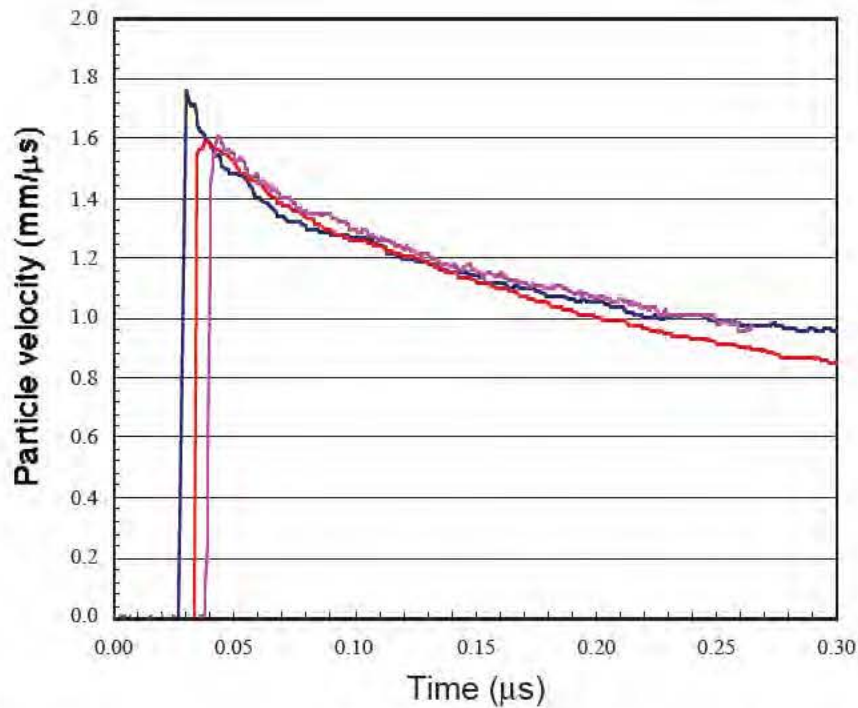


Figure 15. Particle velocity history at DADE/LiF interfaces taken at three sweep rates.

Conclusions from the Characterization of DADE

(b)(3)

Sol-gel Manufactured Energetic Materials

The properties of energetic materials are dramatically affected by their microstructure. Materials produced using sol-gel chemistry enable microstructural control to the nanometer scale. Potential applications include mass production of precision detonator pellets, net shape casting of initiating explosives, optical surface initiation, detonation wave shaping, initiation trains, detonation cord, high-power composite energetic materials (i.e.,

explosives, propellants, pyrotechnics), low-energy-density solid explosives, and desensitization of explosive powders. Basic scientific elements include initiation and detonation mechanisms in the nanometer range, mass transport and intramolecular reaction kinetics, and sol-gel chemistry.

Sol-gel chemistry produces high surface area, porous solids, which may be cast to near-net shape. The microstructure, comprising nanometer-sized pores and linked primary particles as well as the elemental composition, can be tailored and controlled by solution chemistry. Monomers are reacted in solution to produce small nanometer-size particles (i.e., a sol), which cross-link to form a 3D solid network with the remaining solution residing within open pores (the gel). Controlled extraction of the liquid phase in a gel results in a xerogel or aerogel.

Many problems in energetic materials may be addressed through this new chemical approach. In detonator materials, low manufacturing rates, difficulty in handling fine powders, and the inability to produce precise geometric shapes may be solved by this technique. Another current limitation is intimately mixing fuels and oxidizers. Using sol-gel chemistry, the intimacy of mixing may be controlled and dramatically improved over the current methods. A solid skeleton of a fuel with the oxidizer trapped within the pores has been made. An energetic materials goal is to create an explosive that has the energy density of a strategic propellant and the power of a monomolecular explosive. Sol-gel technology may be able to make energetic materials that have entirely new and desirable properties. A significant observation is that the presence of the gel structure dramatically decreases the impact sensitivity of an explosive.



(b)(3)

We were successful in developing the first solid loaded aerogels and xerogels. This is noteworthy because many applications for materials produced in this fashion have been identified. These materials are made by incorporating fine solids either during sol formation or the incipient gelation phase. Densities normally associated with aerogels can be made but materials approaching the theoretical maximum can also be made. Organic and inorganic solids, including metal, have been used successfully. In collaboration with the U.S. Navy (C. Johnson, NAWC, China Lake), crystalline aluminum, a fuel, has been made in the skeletal structures using in situ chemical processes.

Progress was made in creating an aerogel in which the skeletal structure itself is energetic using a number of organic monomers. In particular, an aerogel based on 1,3-diaminobenzene was made. This material has many chemical properties similar to those of explosives. It is the first non-resorcinol-based organic aerogel made at LLNL and the second in the world. Methods were identified that can produce aerogels using only organic liquids, a matter of general importance to the aerogel community.

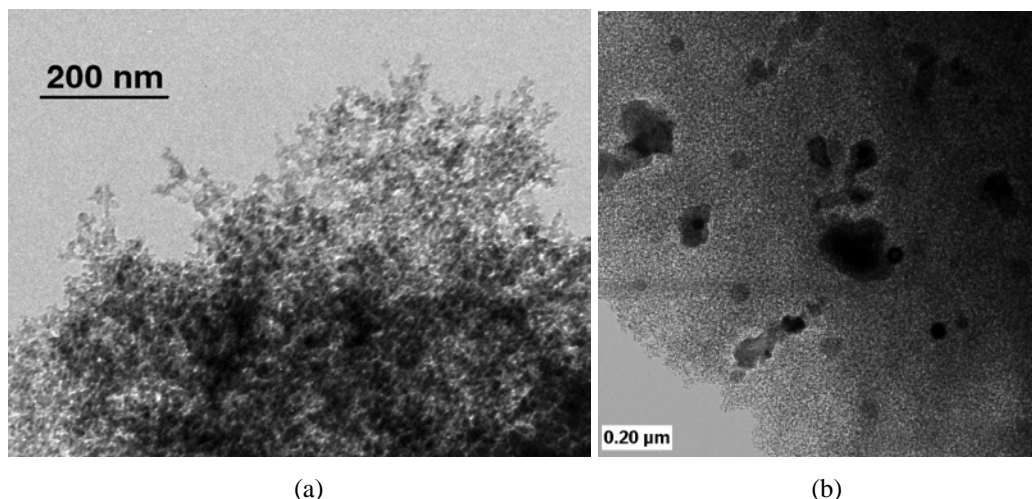


Figure 16. (a) AP-resorcinol nanocomposite; (b) crystalline aluminum (fuel) grown into an aerogel.

Summary: Sol-gel Chemistry

Sol-gel chemistry has promise in a broad range of important DOE and DoD applications. At this stage of basic research, it is too soon to predict the overall impact of this chemistry. Interactions with DoD investigators are being established to evaluate areas of potential impact more rapidly.

Conclusions

More extensive evaluation of LLM-105 has shown the material to be an excellent candidate as an insensitive, higher power explosive. Although it is premature to determine applications, the synthesis and characterization effort will help sustain new ingredient evaluation for hard target and related DoD/DOE applications.

The characterization work on DADE is still in the beginning stages. Its greatest virtue to date is its fairly good impact sensitivity. The thermal response may limit its applicability as an insensitive ingredient. Shock sensitivity needs to be studied. The thermal decomposition characteristics of DADE may produce important burn rate properties in propellants.

The combination of low volume, special materials needs, advanced material design tools, diagnostics, new molecules, and improvements in theory and modeling is leading to a new revolution in energetic materials. Although the work is preliminary, the sol-gel process may enable advanced materials to be made using low-cost bulk chemical processes. Future work needs to focus on material characterization of sol-gel materials already prototyped. Evaluation of the bulk material of the sol-gel nanocomposites at less than 10-nm resolution will be extremely challenging but it is essential if the work is to prove practical.

Acknowledgments

Much of the success of this effort is due to the dedicated synthesis work of P. Pagoria, A. Mitchell, R. Schmidt, and G. Lee. Without materials, the future of energetic materials is limited indeed. R. Hodgins assisted in carrying out the small-scale detonation performance tests. We wish to also thank L. Terminello for performing the x-ray microscopy on the sol-gel nanocomposite. M. Wall has provided outstanding transmission electron microscopy support in the sol-gel effort.

References

1. R.M. Doherty and R.L. Simpson, "A Comparative Evaluation of Several Insensitive High Explosives," Proceedings Institut Chemische Technologie Combustion and Detonation Meeting, Karlsruhe, Germany, June 24–27, 1997, pp. 32-1 to 32-23.
2. S.F. Rice and R.L. Simpson, "The Unusual Stability of TATB: A Review of the Scientific Literature," Lawrence Livermore National Laboratory, UCRL-LR-103683, July 4, 1990.
3. B.M. Dobratz, et al., "The Sensitivity of Triaminotrinitrobenzene (TATB) and TATB Formulations: Summary Report," Lawrence Livermore National Laboratory, UCID-17808, Sept. 15, 1978.

4. R.L. Simpson, et al., "Munitions Technology Development Program: FY97," Lawrence Livermore National Laboratory, UCRL-ID-103482-97, Jan. 15, 1998, pp. II-15 to II-32.
5. L.E. Fried, P.C. Souers, and M. Howard, CHEETAH 2.0 User's Manual, Lawrence Livermore National Laboratory, Livermore, CA, UCRL-MA-117541, Rev. 4, Oct. 1998.
6. B. Dobratz and P.C. Crawford, LLNL Explosives Handbook, Lawrence Livermore National Laboratory, UCRL-52997, 1985.
7. C.M. Tarver, R.R. McGuire, E.L. Lee, E.W. Wrenn, and K.R. Brein, "Thermal Decomposition of Explosives with Full Containment in One-Dimensional Geometries," Proc. 17th Combustion Symp., Leeds, United Kingdom, August 20–25, 1978.
8. R.S. Lee, J. L. Cutting, R. L. Hodgins, P. F. Pagoria, R. L. Simpson, and P. C. Souers, "Small-Scale Screening Tests for HE Performance as Applied to the New Explosive Molecule LLM-105," Proceedings of the Eleventh Symposium (International) on Detonation, Snowmass, CO, 1998, in press.
9. T.M. Tillotson, L.W. Hrubesh, R.L. Simpson, R.W. Lee, R.W. Swansiger, and L.R. Simpson, "Sol-Gel Processing of Energetic Materials," 5th International Symposium on Aerogels, Montpellier, France, Journal of Non-Crystalline Solids, Sept. 8–10, 1997 (accepted).
10. R.L. Simpson, R.S. Lee, T. Tillotson, G. Fox, R. Swansiger, and L. Hrubesh, "Sol-Gel Manufactured Energetic Materials," Patent applied for August 1997.

This page intentionally left blank

Equations of State for High Explosives

Choong-Shik Yoo and Hyunhae Cynn
Lawrence Livermore National Laboratory
(925) 422-5848
yoo1@llnl.gov

Abstract

The purpose of this study is to obtain the equations of state for high explosives and detonation products in an extended range of high pressures and temperatures. In FY98, we determined the isotherms of unreacted HMX, RDX, and PETN at quasi-hydrostatic high pressures below 45 GPa by using a diamond-anvil cell, angle-resolved synchrotron x-ray diffraction method. The equation-of-state parameters (bulk modulus B_0 and its derivatives B') are presented for the 3rd-order Birch-Murnaghan formula based on the measured isotherms. The evidence of shear-induced chemistry of HMX in non-hydrostatic conditions is presented. In this report, we also briefly describe the experiments planned for FY99.

Introduction

High-pressure equation-of-state (EOS) information for high explosives (HE) is fundamental to understanding intermolecular interactions of energetic molecules and is therefore needed for thermochemical descriptions of various energetic processes such as the detonation occurring in shock-compressed high explosives. These pressure-volume-time (PVT) relations of various forms of HE (including unreacted and reacting HE and detonation products) are also inputs to all hydrodynamics simulations of conventional and nuclear HE systems needed in every spatial and time step. The EOS data for unreacted high explosives (UHE) in particular are required to describe non-ideal detonation, to develop kinetic models, and to understand the safety and sensitivity of HE and HE systems in various aging stages.

High-pressure EOS data are typically developed from Hugoniot measurements in shock-wave experiments and/or isotherms in static high-pressure experiments at various temperatures. However, because of high reactivities of shock-compressed HE, it is difficult to obtain the EOS and structural information of unreacted high explosives at high pressures. In fact, it is not clear even at low pressures if there is any low level of chemical reaction occurring in shock-compressed HE. On the other hand, energetic molecules are mostly made of low-Z elements, such as hydrogen, carbon, nitrogen, and oxygen, which limits the application of conventional x-ray techniques to determine the PVT relation of HE in a small volume at high static pressures. For these reasons, there are very limited data available for unreacted systems, mostly at low pressures below 10 GPa [1].

Recent developments of diamond-anvil cell (DAC) technologies coupled with an intense μm -beam synchrotron x-ray are now capable of probing detailed crystal structural information from minute samples (less than 1 mg) of low-Z materials at high pressures and temperatures. Therefore, in this study we have developed a DAC angle-resolved x-ray diffraction technique using monochromatic synchrotron x-ray and highly sensitive image-plate detectors. This technique is capable of determining EOS and crystal structures of UHE at high pressures above Chapmann-Jouguet (CJ) conditions. In this paper, we present the EOS data of a few selected UHEs including HMX, RDX, and PETN, obtained by DAC angle-resolved synchrotron x-ray diffraction at the Stanford Synchrotron Radiation Laboratory.

Results of Experiments

Our main accomplishments in FY98 — determination of the isotherms of HMX, PETN, and RDX at high pressures — are discussed here:

Isotherms of HMX

HMX experiments were performed in both quasi-hydrostatic and non-hydrostatic conditions. Argon was used as a pressure medium in quasi-hydrostatic (“hydrostatic” hereafter for simplicity) experiments, whereas no pressure medium was used in non-hydrostatic experiments.

Figure 1 presents the compression curves of HMX to 42 GPa, showing a strong dependence on the stress conditions. In hydrostatic conditions, HMX can be compressed to 42 GPa, reversibly without any apparent chemical changes. There is some scattering in the data particularly above 15 GPa, which might be due to a phase transition. On the other hand, in non-hydrostatic conditions, HMX can be compressed only to 10 GPa, above which the compression data become unrealistic. The compression data below 10 GPa, however, are in good agreement with the previous measurements by Olinger et al. obtained using a WC-Bridgman anvil technique [1]. Those previous WC experiments were done in a methanol-ethanol pressure medium; however, it is still close to a non-hydrostatic condition in relative to a hydrostatic condition provided by using Ar pressure medium. For example, the bulk modulus (i.e., stiffness) of Ar is about 1.4 GPa, substantially smaller than that of methanol, ethanol, or any other covalently bonded hydrocarbons ranging from 10 to 20 GPa [2]. In fact, the stiffness of most HE is also within a similar range, 10–20 GPa. Consequently, the shear strength of Ar is also expected to be smaller, providing a better hydrostatic condition.

(b)(3)

The isotherms have been fitted to the 3rd-order Birch Murnaghan (BM) equation-of-state,

$$P \text{ (GPa)} = B_0^{3/2} [h^{-7/3} - h^{-5/3}][1 - 3(1 - B'/4)(h^{-2/3} - 1)]$$

where $h = V/V_0$ and B_0 and B' are respectively the bulk modulus and its pressure derivative. The best fits were obtained with

(b)(3)

This result is illustrated as the solid lines in Fig. 2. The fits are generally good at low pressures below 10 GPa for the non-hydrostatic data and 15 GPa for the hydrostatic data. The scattering in the hydrostatic data above 15 GPa might be due to a phase transition based on our Raman studies in HMX exhibiting an indication of a conformational phase transition above 15 GPa [3].

Note that at a given volume the hydrostatic pressure is lower than the non-hydrostatic pressure in Fig. 1. This is quite unusual, suggesting that the difference between the hydrostatic and non-hydrostatic results can not be explained in terms of a shear-induced compression change. This unusual compression behavior of HMX in non-hydrostatic conditions is probably due to chemical reaction occurring clearly above 10 GPa or likely even below. In fact, our Raman studies of HMX [3] indicate a similar irreversible spectral change and laser-induced fluorescence in non-hydrostatic conditions, even well below 10 GPa. In contrast, all the spectral changes of HMX in hydrostatic conditions are reversible and no fluorescence is apparent at all pressures to 45 GPa. Therefore, we conclude that the abnormal compression behavior in non-hydrostatic conditions is due to exothermic chemical reactions which should increase the pressure above the hydrostatic value at a given confined volume of unreacted HMX. Similar exothermic chemical reactions (i.e., “detonations”) have previously been observed in uniaxially compressed nitromethane [4] and cubanes [5] in DAC

experiments. It has also been suggested that the sensitivity of such a reaction is crystal-orientation-dependent with respect to the applied stress in a DAC.



(b)(3)

Isotherms of RDX

RDX experiments have been done only in hydrostatic Ar pressure medium. However, the results have been compared with the previous WC-anvil experiments, again, representing somewhat higher non-hydrostaticity. The diffraction patterns were indexed based on an orthorhombic structure by using more than 15 diffraction planes between 111 at $2\theta=5.5^\circ$ and 322 at 13° . It is well known that RDX-I (orthorhombic with *Pbca* space group) undergoes a phase transition to RDX-III at about 4 GPa [1]. This phase transition has been proposed to be conformational, which retains its basic crystallographic symmetry but alters its molecular structure. Therefore, in this study we have used the same orthorhombic symmetry to fit the data at all pressures.

The compression data are summarized in Fig. 2, together with the previous WC results. These compression data agree very well, clearly suggesting no stress dependent behavior of RDX. It is in contrast to the case of HMX, despite their chemical similarity. The differences in crystal structures and shear-plane interactions may result in such a difference in the compression curves of RDX and HMX.

The compression data have been fitted to the BM-EOS, resulting in B_0 and B' of



(b)(3)

These fits are extremely good as seen in Fig. 2. The results also yield a small, but apparent, discontinuous volume change at 4.2 GPa, which we attribute to the phase transition from RDX-I to RDX-III. The transition volume change is then found to be 1.5%. This is in very good agreement with the previous WC-result, 1.6% [1]. The consistency in compression data of two different phases and a small transition volume change support that the transition is indeed a conformational one. Furthermore, our preliminary Rietveld analysis also indicates that the structure of RDX-III is orthorhombic with a likely space group of $Pm2_1$ or $Pcca$. Detailed analysis of the crystal structure of RDX-III is currently underway and will be reported later.

Isotherms of PETN

PETN experiments were done in hydrostatic Ar pressure medium. By using an area detector, it is feasible to identify 10 diffraction planes of 201, 002, 221, 200, 201, 121, 220, 102, 301, 311, and to confirm the crystal structure of PETN to be orthorhombic with $P2_12_1$ space group consistent with the previous result [6]. The resulted volume data are presented in Fig. 3 (as solid circles with error bars), together with the previously reported Hugoniot data of PETN single crystals [7]. The solid and dotted lines represent the BM-EOS fits to this static and previous shock data, respectively. Clearly, these fits are in good agreement with the experiments, yielding

$$B_0 = 12.3 \text{ GPa}, \quad B' = 8.2 \quad (\text{Isotherm})$$

$$B_0 = 11.8 \text{ GPa}, \quad B' = 9.1 \quad (\text{Hugoniot})$$

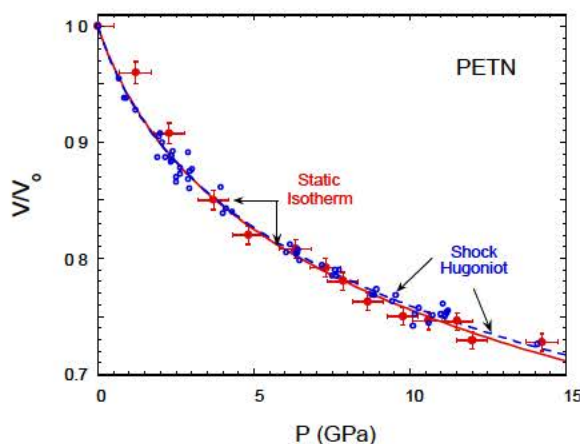


Figure 3. Static isotherm of PETN in Ar to 15 GPa at the ambient temperature in comparison with shock Hugoniot of single crystal PETN.

There is very good agreement between the static isotherm and the shock Hugoniot in Fig. 3. The difference is, in fact, smaller than the uncertainties of the fits or in the data. A slight increase in volume of shock Hugoniot above 10 GPa, however, may reflect a small temperature effect associated with shock compression, which remains small within the pressure range of this study.

Experiments Planned for FY99

Isotherms of Other High Explosives

We will continue to determine the equations of state of TATB, CL-20, and other high explosives important to DoD/DOE missions.

Studies of Shear-induced Chemical Reactions

The results of HMX experiments clearly indicate the importance of shear-induced chemical reaction in non-hydrostatic conditions. Further systematic studies are currently underway to correlate the shear-induced chemistry to the changes in HMX crystal structures at high pressures. We will also examine whether such a shear-induced exothermic reaction generally occurs in other non-hydrostatically compressed high explosives including PETN, which is well known to have extremely high crystal anisotropy.

Studies of Structure, Stability, and Equation-of-state for Detonation Products

Current detonation models assume high stability of detonation products, N_2, H_2O, CO_2, C , in a wide region of high pressures and temperatures. However their stabilities are not truly understood at high pressures and temperatures. Indeed, an increasing amount of experimental evidence contradicts the assumed stability of the molecular forms of these materials at high P-T conditions. Kinks in the Hugoniot of CO_2 and N_2 at 10 and 40 GPa, respectively, provide strong evidence that chemical reactions occur in these materials [8]. The electric conductivity of shocked H_2O substantially increases at 30 GPa, probably due to autoionization. Therefore, we will launch the experimental program to investigate the structure and stability of major detonation products at high pressures and temperatures by using an integrated technique of diamond-anvil cell, laser-heating, synchrotron x-ray diffraction, and various micro-probing spectroscopic methods.

Technology Transition

EOS data of high explosives will be fully incorporated into most advanced thermochemical codes (CHEETAH, CHEQ, etc.) and then to hydrodynamics codes used in DOE and DoD Laboratories. For example, HMX data obtained in this study have already been fully integrated into CHEETAH, resulting in improvements for the performance description of LX-17 and LX-14 [9]. In addition, all current and future work will be reported to energetic materials communities and defense programs via presentations and progress reports to the DoD/DOE Munitions Technology Program, and also be published in professional journals.

References

1. B. Olynik, B. Roof, and H. Cady, Proceedings of “*Du Symposium International Sur Le Comportement Des Milieux Denses Sous Hautes Pressions Dynamiques*” p. 3, (Commissariat a l’Energie Atomique, 1978, Paris).
2. E. Knittle, “Static Compression Measurements of Equation of State” in “*Mineral Physics and Crystallography, a Handbook of Physical Constants*” Ed., Ahrens, T., AGU, 1995, pp 98–142.
3. C. S. Yoo and H. Cynn, to be published.
4. G. J. Piermarini, S. Block, and P. J. Miller, *J. Phys. Chem.* **93**, 457 (1989).
5. G. J. Piermarini, S. Block, R. Damavarapu, and S. Iyer., *Propellants, Explosives, Pyrotechnics* **16**, 188 (1991).
6. A. D. Booth and S. J. Llewellyn, *J. Am. Chem. Soc.*, 837 (1947).
7. S. P. Marsh, *LASL Shock Hugoniot Data*, University of California, Berkeley, 1980.
8. A. C. Mitchell and W. J. Nellis., *J. Chem. Phys.* **76**, 6273 (1982).
9. C. S. Yoo, H. Cynn, M. Howard, and N. Holmes, “Equation of state of unreacted high explosives at high pressures,” *Proceedings of the 11th Detonation Symposium*, Aspen, Colorado, August (1998).

This page intentionally left blank

Kinetic Modeling of Non-Ideal Explosives with CHEETAH

Laurence E. Fried and W. Michael Howard
Lawrence Livermore National Laboratory
(925) 422-7796
lfried@llnl.gov

Abstract

We report a kinetic detonation model based on multi-species equations of state and multiple reaction rate laws. Finite rate laws are used for the slowest chemical reactions. Other reactions are given infinite rates and are kept in constant thermodynamic equilibrium. We model a wide range of ideal and non-ideal composite energetic materials. We find that we can replicate experimental detonation velocities to within a few percent, while obtaining good agreement with estimated reaction zone lengths. The detonation velocity as a function of charge radius is also correctly reproduced.

Introduction

The CHEETAH thermochemical code predicts the properties of detonating high explosives and other energetic materials. A primary problem for the Department of Defense (DoD) is the accurate prediction of detonation in composite energetic materials. Such materials often have high concentrations of slowly reacting binders, fuels such as Al, and oxidizers such as ammonium perchlorate. The slow reactions of composite energetic materials are poorly treated by traditional thermochemical codes, which are based on the assumption of instantaneous reaction. For the past two years, we have been developing a capability in the CHEETAH thermochemical code that treats slow chemical reactions in detonation on a scientifically sound footing. We show below that accurate predictions of detonation velocities in non-ideal explosives can be made with the present framework.

The new technology will be transferred to the over 300 users of the CHEETAH thermochemical code. Beta release versions of CHEETAH 2.0 have been extensively tested this year by DoD users. User feedback was also obtained through a CHEETAH user workshop held at LLNL in February 1998. In the discussion that follows, we present the detonation modeling capability implemented and validated against experiment in CHEETAH 2.0.

The detonation of an energetic material is the result of a complicated interplay between chemistry and hydrodynamics. While the detailed chemical kinetics of detonation in gases have been extensively studied, much less is known regarding chemical kinetic processes governing condensed energetic materials. The primary reason for this is the extreme pressure and temperature immediately behind the detonation wave: pressures of

400 kBar (40 GPa) and temperatures of 4000 K are common. The extreme conditions result in very broad spectroscopic features that make the identification of individual chemical species very difficult.

There is a continuing need in the energetic materials field for reliable predictions of detonation velocity and energy delivery. This has traditionally been accomplished through the means of Chapman-Jouget (C-J) thermodynamic detonation theory. The C-J detonation theory assumes that thermodynamic equilibrium of the detonation products is reached instantaneously.

For the purpose of this study, we define non-ideal explosives as those with a reaction zone of *one mm* or more. So-called “non-ideal” explosives are often poorly modeled by Chapman-Jouget theory. These materials have chemical reaction rates that are slow compared to hydrodynamic time scale of 10^{-6} s so that the C-J assumption of instantaneous thermodynamic equilibrium breaks down. For example, it is found experimentally that the detonation velocity of non-ideal explosives varies sharply from the C-J value and depends strongly on the charge radius.

We are therefore forced to consider the interaction of chemical kinetics with the detonation wave in order to reach an acceptable representation of detonation in non-ideal explosives. Wood and Kirkwood [1] (WK) proposed a two-dimensional, steady-state kinetic detonation theory that solves many of the limitations of Zeldovich, von Neumann, and Doering (ZND) theory. WK considered a cylindrical charge of infinite length. They solved the hydrodynamic Euler equations in the steady-state limit along the central streamline of the cylinder. Radial expansion was treated as a source term in the one-dimensional flow along the streamline.

The WK equations have been extensively analyzed by Erpenbeck [2] and co-workers. It is found that the detonation velocity depends on the interplay between chemical kinetics and radial expansion. In the limit of no radial expansion, the ZND plane wave result is obtained. When radial expansion is allowed however, the detonation velocity can vary from the C-J prediction. In the limit of strong radial expansion the detonation wave fails; no velocity is found which satisfies the steady-state equations. Bdzil has generalized WK theory to off-axis flow [3] and Stewart [4] and co-workers have studied the effect of kinetic rates on the decrease of detonation velocity with decreasing size and on curvature of the detonation wave.

In the present paper, we implement a model of detonation kinetics based on the identification of individual chemical species. The advantage of the present treatment is that the same equations of state and chemical rate laws can be used on a wide range of explosive mixtures. A mixture equation of state based on thermal, mechanical, and partial chemical equilibrium is used. The mixture model is implemented in the CHEETAH thermochemical code [5]. Small molecules that are gases at standard conditions are treated with the Beeker, Kistiakowski, and Wilson (BKW) [6] real gas equation of state. Solids are treated with a Murnaghan [7] equation of state. Simple pressure-dependent chemical reaction rates are employed. These rates represent the consumption of the energetic material by the detonation wave. Fast reaction rates (partial chemical equilibrium) are assumed for species other than the initial material.

The WK equations are solved numerically to find the steady-state detonation velocity. The radial expansion is derived from measured radii of curvature for the materials studied. We find good agreement with measured detonation velocities *using the same set of equations of state and rate laws for each composite*. Although our treatment of detonation is by no means exact, the ability to model a wide range of phenomena based on simple equations of state and rate laws is encouraging. We find that the inclusion of detonation kinetics yields a significant improvement in the predicted detonation velocity of materials with long estimated reaction zones. More importantly, we are able to reproduce the dependence of the detonation velocity on charge radius for several materials. For materials with short reaction zones, we recover the results of C-J thermochemistry.

Wood-Kirkwood Detonation Theory

WK theory starts with the hydrodynamic Euler equations coupled to chemical kinetics. The theory treats the detonation along the center of the cylinder. The Euler equations are reduced to their steady-state form. The result is a set of ordinary differential equations that describe hydrodynamic variables and chemical concentrations along the center of the cylinder.

The notation is as follows: we use cylindrical coordinates in a frame *moving with the shock velocity* D ; x is the axial coordinate, r is the radial coordinate, and u is the axial particle velocity in the moving frame (equal to $D-U$ in the lab frame). The radial velocity is called ω . Subscripts denote a spatial derivative.

$$\begin{aligned}
 u_x &= \psi/\eta \\
 \rho_x &= -(\rho/u)(u_x + 2\omega_r) \\
 E_x + p v_x &= 0 \\
 \mathbf{F}_x &= \mathbf{R}/u \\
 \omega_r &= [D - u(t=0)] / R_c
 \end{aligned}
 \tag{1}$$

where \mathbf{F} is the concentration vector, \mathbf{R} is the reaction rate vector and R_c is the radius of curvature. ρ is the density, p is the pressure, E is the specific energy and v is the specific volume. We take the form of these equations from Fickett and Davis (see Ref. 8, Equations 5.28 and 5.37). The expression for ω_r is an approximation that is strictly valid only at the initial jump off of the shock.

We define

$$\eta \equiv 1 - u^2/c^2
 \tag{2}$$

to be the sonic parameter, where c is the speed of sound. If the sonic parameter η is greater than zero, communication with the shock front is possible. If it is less than zero, the region cannot communicate with the shock front. Secondly, we will define the *pressure production* term

$$\psi = (fP/fF)_{v,E} \cdot \mathbf{R} / \rho c^2 - 2\omega_r \quad (3)$$

Chemical reactions that increase the pressure at constant v, E will increase the value of ψ . Radial expansion, however, decreases the pressure through the ω_r term.

Solution of the WK Equations

The initial conditions for the WK equations are the energy, density, and composition at the start of the shock front. We specify the initial composition to be the same as the unreacted material. The initial energy and density can be determined by specifying the detonation velocity; finding the intersection of the unreacted shock Hugoniot with the Rayleigh line yields the pressure and density at the shock front. This can be done if the shock velocity is specified. From this point on, the system visits a series of (p, v) states of different P with different chemical concentrations. A thermodynamic equilibration at fixed composition then determines the energy at the shock front. Note that the detonation velocity is treated as a *specified quantity* here.

As the equations are integrated, the shockwave structure is determined for positions behind the shock front. In practice, we use the ‘‘Lagrangian time’’ form of the WK equations, where the time variable is related to position by

$$dx = u dt \quad (4)$$

This choice of variables is most natural for the integration of kinetic laws.

The WK equations support a variety of solutions that have been discussed in great detail by Erpenbeck [2]. Let us consider the behavior of the equations as a function of the specified detonation velocity D . There are three qualitatively different solutions possible. For special detonation velocities, the solutions pass through the sonic plane, defined by $\eta = 0$. Points behind the sonic plane cannot communicate with the shock front. The WK equations are finite when $\eta = 0$ only if ψ also passes through zero. Therefore the sonic solutions are defined by the nonlinear equation

$$\psi(t, D) = \eta(t, D) = 0 \quad (5)$$

It is possible to think of this as the kinetic C-J condition. The next possibility is that η never passes through zero. These solutions are *overdriven*; that is the pressure increases with distance behind the shock front. These solutions correspond to a rear piston boundary condition that drives the shock front forward. Finally, if $\eta = 0$ when $\psi \neq 0$, the equations become infinite. This means that a steady-state flow cannot occur at the specified detonation velocity D .

Of all the solutions generated by the WK equations, only the sonic solutions have the pressure tend to zero as x becomes large. It is these solutions that correspond to steady-state self-propagating flow.

Mixture Equation-of-State Model

We now specify the equation of state used to model molecular mixtures. We treat the chemical equilibrium between N supercritical fluid or gaseous species and M condensed species. Condensed species i has C_i distinct phases. The Helmholtz free energy is a function of the system volume V , the temperature T , the molar concentrations of the fluid species \mathbf{x} and the molar concentrations of the condensed species \mathbf{X} . Since the gaseous and condensed species are assumed to be in separate phases, the Helmholtz free energy has the form:

$$A(\mathbf{x}, \mathbf{X}, V, T) = A^{\text{gas}}(\mathbf{x}, V_g, T) + A^{\text{cond}}(\mathbf{X}, V_c, T) \quad (6)$$

Here V_g is the volume of the gaseous phase and V_c is the volume of the condensed phase, so that $V_g + V_c = V$.

We now consider the condensed and gaseous contributions to the Helmholtz free energy separately. The gaseous free energy can be separated into an ideal gas contribution and an “excess” contribution:

$$A^{\text{gas}}(\mathbf{x}, V_g, T) = A^{\text{ideal}}(\mathbf{x}, V_g, T) + A^{\text{ex}}(\mathbf{x}, V_g, T) \quad (7)$$

For the ideal gas portion of the Helmholtz free energy, we use a polyatomic model including electronic, vibrational, and rotational states. Such a model can be conveniently expressed in terms of the heat of formation, standard entropy, and constant pressure heat capacity $C_p(T)$ of each species. The excess portion of the free energy comes from a real gas equation of state. In the present paper a BKW equation of state is used. The BKW parameters and covolumes are fitted *only to ideal explosives* and the resulting values are given in Table 1. We call this parameter set BKWC2.

We now turn to the condensed portion of the free energy. The i th condensed species has C_i condensed phases, which may possibly coexist in thermodynamic equilibrium. This yields the form:

$$A^{\text{cond}}(\mathbf{X}, V_c, T) = \sum \sum X_{i,j} A_{i,j}(P, T) \quad (8)$$

with a summation over all species and phases. Here, $X_{i,j}$ is the molar concentration of the j th phase of species i . $A_{i,j}(P, T)$ is the molar free energy of the j th phase of species i .

(b)(3)

The molar free energy $A_{i,j}$ is expressed as a “reference” part at standard pressure, and a part due to pressure:

$$A_{i,j}(P,T) = A_{i,j}^{\circ}(T) + \Delta A_{i,j}(P,T) \quad (9)$$

The reference part is determined through the Joint Army, Navy, Air Force (JANAF) compilations of thermochemical data at standard pressure. $\Delta A_{i,j}$ is determined by the condensed equation of state. We use a modified Murnaghan equation of state as follows:

$$V = V_0 [n \kappa P + \exp\{-\alpha (T-T_0)\}]^{-1/n} \quad (10)$$

V_0 is the molar volume when $P=0$ and $T=T_0$. κ is the inverse of the isothermal bulk modulus. T_0 is the temperature of the reference isotherm taken to be 298.15K. α is the volumetric coefficient of thermal expansion. n is the derivative $dB(P,T)/dP$. We have calibrated the

Murnaghan equation of state for the materials used in the present study to shock Hugoniot data [9] and other thermodynamic measurements. These parameters are given in Table 2.



(b)(3)

Application to Composite Energetic Materials

The detailed chemistry of composite energetic materials is very complicated. Very many chemical steps are involved in the decomposition of most large energetic material molecules into small simple product molecules. In general the composition reactions are not well characterized, especially at elevated temperatures. The situation is made more complicated by the heterogeneous composite nature of most energetic materials. Void collapse and shear dislocations can lead to so-called “hot spots” — regions of enhanced temperature behind the detonation front. These regions play an essential role in high explosive initiation. They preclude describing the energetic material with a single temperature, and complicate the use of even the simplest Arrhenius chemical kinetic schemes.

Most reactive flow models of high explosive initiation overcome these difficulties through the use of pressure-dependent rates. Pressure-dependent rate laws have been shown to be sufficiently flexible to model a variety of initiation and non-ideal detonation phenomena, while maintaining simplicity. The disadvantage of these rate laws is that they do

not explicitly treat the high explosive microstructure or the underlying activated chemical reaction rate laws.

We have inferred effective kinetic rates proportional to P^2 for a variety of ideal and non-ideal explosives and their composites. We find that this choice, while simpler than most reactive flow rate laws for high explosive initiation, is adequate to model steady-state detonation over the range of materials and diameters provided here. It has been noted that the detonation velocity size effect is sensitive to particle size. Many of the samples considered here are not fully characterized with regard to particle size, so we do not include dependence of kinetic rate laws on particle size.

We also predict sonic reaction zone widths. The sonic reaction zone width is the length of the zone behind the detonation wave for which the local velocity of sound is equal to or greater than the detonation velocity. This zone is where chemical reactions contribute to the detonation wave. Beyond this zone, chemical reactions do not contribute the detonation wave.

For the purposes of this study, we model the kinetic processes of the high explosives as being a single decomposition reaction into primary product constituents. The reaction products that we have assumed for the various high explosives, binders, and metal reactions are listed in Table 3. However, because we assume that all of the products are in thermochemical equilibrium, the results are independent of the assumed decomposition pathway. This would not be the case if reversible reactions were important.



(b)(3)

We assume that the kinetic rates are defined by the following equation:

$$d\lambda/dt = (1 - \lambda)RP^2 \quad (11)$$

where P is the pressure, R is the rate constant (see Table 3) and λ represents the amount of unburned reactant normalized to vary between 0 (all unburned) and 1 (all burned). In our kinetics scheme the concentrations of reactants are assumed to be controlled by the kinetic rate, while all of the products are assumed to be in thermochemical equilibrium.

For non-ideal explosives, the effects of equations of state are strongly coupled to the effects of kinetics and hydrodynamics. For the equations of state, the usual process is to fit the covolumes of the product gases to experimental detonation velocities of ideal and non-ideal explosives. For this study we have used a BKW equation of state for product gases *with parameters fit only to ideal explosives*. The modified Murnaghan EOS of Eq. 10 was fit to shock Hugoniot data for individual product species.

Results

The explosives mixtures studied here are composed of HMX, NM, RDX, PETN, TATB, TNT, and AP, along with a variety of binders. We also model Al combustion in composites. The composites and explosives that we consider are given in Table 4. In modeling these composites, we assume that each component material burns at a rate that is independent of the other components in the composite. We find that this simple approximation is adequate to describe the detonation velocity of the materials studied here. It should be noted that the approximation may fail for certain materials, most notably binary fuel/oxidizer mixtures, where the presence of one component dramatically accelerates the reaction of the other. Most of the composites contain a single high explosive and a binder. The composites with three or more components include IRX-3A, IRX-4 and PBXN-111. Each rate law was based on calculating the detonation velocity of several materials. The rate laws were adjusted to give the best fit to the experimental detonation velocity and where available the estimated reaction zone. The data for Table 4, as well as the experimental detonation velocities in Table 5, are taken from Ref. 10.

(b)(3)

A summary of our results is presented in Table 5. There are notable deficiencies in the C-J detonation velocity calculations when compared to experiment. In Figure 1, we compare detonation velocities calculated with C-J theory using the BKWC2 parameter set to experimental values. There is good agreement between theory and experiment for the

compounds with experimental detonation velocities greater than 8 km/s. These materials are predominantly high explosive with less than 10% binder by weight. The deviation between C-J theory and experiment is quite substantial for experimental detonation velocities less than 8 km/s. These materials are multi-component mixtures containing AP and Al. Generally there is more than 10% of the binder material present by weight.



(b)(3)

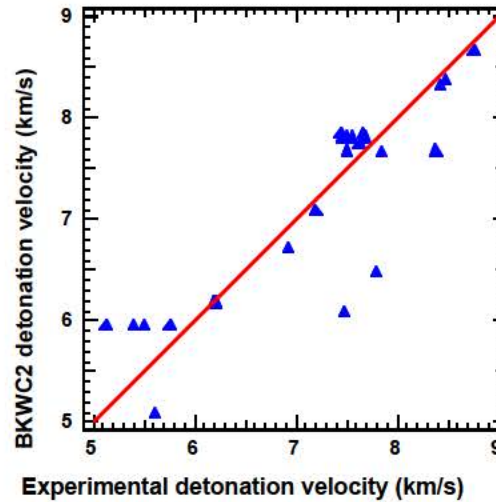


Figure 1. Detonation velocities (in km/s) as calculated with C-J theory and the BKWC2 equation-of-state parameter set.

We also performed C-J calculations with the larger BKWS [11] product set. The results are given in Table 5 and Figure 2. The BKWS predictions for the detonation velocity are accurate when the experimental detonation velocity is more than 7 km/s. Below this point, substantial deviations between theory and experiment remain. The BKWS product set predicts velocities more accurately than BKWC in the range of 7–8 km/s. This may be due to the calibration of BKWS, which was performed on a database of ideal and non-ideal explosives, while BKWC2 was calibrated solely to ideal explosives.

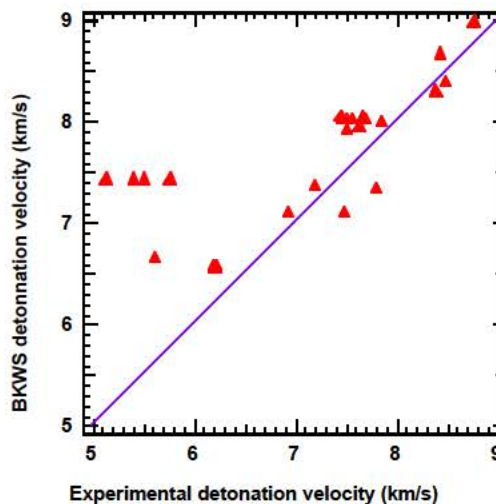


Figure 2. Detonation velocities (in km/s) as calculated with C-J theory and the BKWS equation-of-state parameter set.

In Figure 3, we plot detonation velocities obtained with WK detonation theory and the reactions given in Table 3. The kinetic calculations are nearly as accurate at detonation velocities around 5 km/s as they are at 8 km/s. Although the calculations are not exact, all the large deviations from experiment have been eliminated.

Some of the non-ideal explosives that we study have significant amounts of hydroxyl-terminated poly butiene (HTPB). These non-ideal composites include IRX1, IRX-3A, IRX4, PBXN-110, and PBXN-111. Table 5 gives the compositions of these composites. We find it interesting that the products of this binder are hydrocarbons such as CH_4 and C_2H_6 . For these cases the calculated detonation velocities are sensitive to the equations of state for these hydrocarbons. Unfortunately, there is only shock data for methane and not ethene or other hydrocarbons.

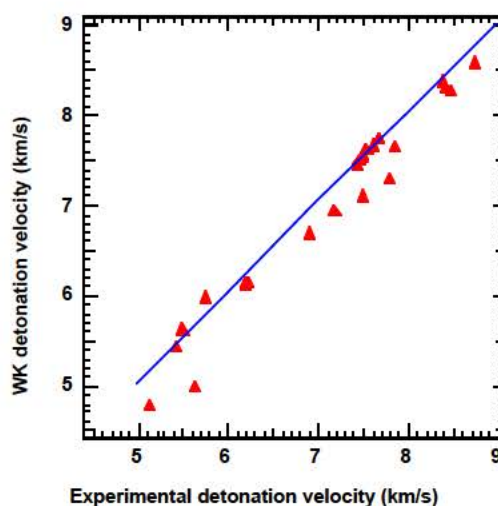


Figure 3. Detonation velocities (in km/s) as calculated with WK theory and the BKWC2 equation-of-state parameter set.

Figure 4 shows our results for PBXN-111. The solid circles are the experimental detonation velocity as a function of radius from Forbes and Lemar [12], while the open circles are our calculated values. Our calculated values reproduce the experimental values reasonably well, while using generic kinetic rates given in Table 3. The shape of the curve, however, is sensitive to the rates chosen for AP and Al. In addition, for PBXN-111 we find multi-valued solutions [4] for the detonation velocity. In such a case, we take the largest value.

At this point it is still difficult to differentiate some kinetic effects from equation-of-state effects. Take for example the case of HTPB. The three composites that we model with at least three components (see Table 6) contain HTPB, as well as Al and also ammonium perchlorate (except IRX-3A). It is interesting to notice that all of the explosive composites with the HTPB binder exhibit significant non-ideal behavior. In particular, we find that we must model HTPB to have a very slow kinetic rate (less than $0.1 \mu\text{s}^{-1}$). Kinetic rates for HTPB faster than $0.1 \mu\text{s}^{-1}$ have a significant effect on the calculated detonation velocity for these composites. Other explosives with significant amounts of binder also exhibit significant

non-ideal effects. In addition, TATB with only small amounts of binder (PBX-9502) also exhibits non-ideal behavior. The largest non-ideal effects in the detonation velocity exist for PBX-9502, PBXN-110, IRX-1, IRX-3A, PBXN-111 and IRX-4. For the most part these composites contain large amount of binder and/or metal. For all of the composites listed, there are radius of curvature measurements [10].



(b)(3)

Almost half of the composites (8 out of 16) listed in Table 4 exhibit significant non-ideal behavior. That is, the experimental detonation velocity is significantly different than the calculated C-J theory detonation velocity. The composites exhibiting significant non-ideal behavior include EDC-35, PBX-9502, PBXN-110, TATB, IRX-1, IRX-3A, PBXN-111 and IRX-4. Seven of these composites contain RDX or HMX, which should have similar kinetic properties. Among these seven composites, there is a correlation between the amount of binder and the percent deviation of the experimental detonation velocity from that predicted

by the C-J theory. The one exception to this correlation is IRX-4, which is a multi-component composite containing 24% AP and 16% Al. We have no explanation for this except to note that a multi-component composite may have complex interactions between the kinetic rates of its constituents.

It is also interesting to calculate the case for which there are data for the detonation velocity and radius of curvature for composites as a function of charge radius. There are three composite explosives for which we have data. These are PBXN-111, PBX-9502 and NITROMETHANE (NM). This is interesting because PBXN-111, and to a lesser extent PBX-9502 (which is 95% TATB by weight), exhibits significant non-ideal behavior. For PBXN-111 and PBX-9502, our calculated detonation velocities decrease faster with decreasing radius than the experimental detonation velocities.

Kennedy and Jones [13] have previously studied the non-ideal behavior of PBXN-111. Experiments with PBXN-111 have been performed from a charge radius of 50 cm down to the failure radius, which is less than 9.5 cm. Previous estimates of the equilibrium C-J detonation velocity of PBXN-111 by Kennedy and Jones range from 6.75 to 8.00 km/s. Our estimate of the equilibrium C-J detonation velocity of PBXN-111 is 5.97 km/s. A significant difference between our calculations and previous ones is that with our carbon equation of state, we predict all of the carbon is in the gas state at the C-J point, while Kennedy and Jones predict a significant amount of diamond is produced at that state.

In conclusion, we have developed a kinetic model for thermochemical detonations based on Wood-Kirkwood theory and the thermochemical CHEETAH code. We find that with a simple model for kinetic processes we are able to model many of the features of non-ideal explosives such as their detonation velocities and their sonic reaction zone widths. In the future, we plan to extend our kinetic modeling study to include more sophisticated temperature- and pressure-dependent rate laws. In this way, we can extend our model to more physically based rate laws and study more complex non-ideal detonation behavior such as shock initiation, hot spot formation, and failure processes.

References

1. W. W. Wood and J. G. Kirkwood, "Diameter Effect in Condensed Explosives," *J. Chem. Phys.*, **22**, pp. 1920–1924, 1954.
2. J. J. Erpenbeck, "The Stability of Idealized One Dimensional Detonations," *Phys. Fluids*, **7**, pp. 684–696, 1964.
3. J. B. Bdzil, "Steady-state Two-dimensional Detonation," *J. Fluid. Mech.*, **108**, pp. 195–206, 1981.
4. D. S. Stewart and J. Yao, "The Normal Detonation Shock Velocity Curvature Relationships for Materials with Non Ideal Equation of State and Multiple Turning Points," *Combustion and Flame*, **113**, pp. 224–235, 1998.

5. L. E. Fried, W. M. Howard, and P. C. Souers, "CHEETAH 2.0 User's Manual," Lawrence Livermore National Laboratory, UCRL-MA-117541 Rev. 5, 1998.
6. L. E. Fried and P. C. Souers, "BKWC: AN Emperical BKW Parameterization Based on Cylinder Test Data," *Propellants, Explosives, Pyrotechnics*, **21**, pp. 215–223, 1996.
7. F. D. Murnaghan, *Proc. Natl. Acad. Sci. (USA)*, **30**, pp. 244–247, 1944.
8. W. Fickett and W. C. Davis, "Detonation," University of California Press, Berkeley, Chapter 5, 1979.
9. S. P. Marsh, "LASL Shock Hugoniot Data," University of California Press, Berkeley, 1980; see also, Dobratz, B. M., and Crawford, P. C., "LLNL Explosives Handbook Properties of Chemical Explosives and Explosive Simulants," UCRL-52997 change 2, January 31, 1985.
10. P. C. Souers, "A Library of Prompt Detonation Reaction Zone Data," Lawrence Livermore National Laboratory, UCRL-ID-130055, Rev. 1, June, 1998.
11. M. L. Hobbs and M. R. Baer, "Calibrating the BKW-EOS with a Large Product Species Data Base and Measured C-J Properties," *Proceedings Tenth International Detonation Symposium*, Boston, MA, July 12–16, 1993, pp. 409–418, 1995.
12. J. W. Forbes and E. R. Lemar, "Detonation wave velocity and curvature of PBXN-111 as a function of size and confinement," submitted to *J. Appl. Phys.*, 1998.
13. D. L. Kennedy and D. A. Jones, "Modeling Shock Initiation and Detonation in the Non-ideal Explosive PBXW-115," *Proceeding of the 10th International Detonation Symposium*, Boston, MA, July 12–16, pp. 665–674, 1993.

Ignition and Initiation Phenomena: Cookoff Violence Prediction

Jon L. Maienschein and Albert L. Nichols III
Lawrence Livermore National Laboratory
(925) 423-1816
maienschein1@llnl.gov

Abstract

The Ignition and Initiation Phenomena program is focused on the prediction of the violence of cookoff response for energetic materials and their systems. To develop a predictive capability, we are measuring key response parameters for HMX-based energetic materials and developing analytical tools in the form of the ALE3D computer code. We report burn behavior for HMX-based explosives over a wide range of pressures and temperatures, and identify conditions and compositional ranges that lead to erratic rapid burning. We have begun measurement of mechanical properties of HMX-based explosives at high temperatures. We have also begun a series of scaled thermal explosion experiments, designed to provide a database of violence of thermal response over a carefully controlled parameter space. Results from the first two experiments are included here. We present data showing that temperature-driven sensitization of HMX-based explosives to shock is largely independent of physical confinement. Many of the responses can be related to the HMX $\beta \rightarrow \delta$ phase transition that occurs around 433 K. ALE3D, our parallel, fully coupled thermal-chemical-mechanical hydrocode, incorporates all these processes during the relatively slow heating of the energetic material and also during the rapid ensuing reaction wherein the degree of violence is determined. We describe the status of ALE3D development and show modeling results using ALE3D for a spherical explosive deflagration.

Introduction

The focus of this program is achieving a predictive capability for the violence of thermal explosions (i.e., slow and fast cookoff) for systems containing energetic materials. This requires that we understand the fundamental thermal response of energetic materials and that we develop the necessary calculational tools to apply this knowledge to the prediction of violence. It also requires a database of thermal explosion tests with which we can test and refine our predictive methods. Currently we (and others) can predict the time of reaction for a specific time-temperature profile, but reliable prediction of violence is not feasible. To properly assess the hazards from an event involving heating, we need to predict the violence of thermal response. This issue is of interest in the Department of Defense (DoD) and Department of Energy (DOE) communities. Dr. Thomas Boggs at NAWC-China Lake and Dr. Ruth Doherty at NSWC-Indian Head have shown particular interest in this work.

HMX-based explosives are the focus of our effort because they are of mutual interest to DOE and DoD. However, techniques developed in the study of HMX are being applied to other energetic materials.

The violence of thermal response of an energetic material is largely controlled by the balance between heat release by exothermic deflagration reactions and heat dissipation by thermal diffusion. In addition, the physical properties of energetic materials under cookoff conditions will strongly affect the violence of reaction. To characterize the fundamental thermal response of energetic materials, we are measuring the burn rate (i.e., rate of heat release) of pristine and thermally degraded energetic materials at high temperatures and pressures, as well as mechanical properties at high temperatures. We are also conducting experiments to measure the violence of thermal explosions under carefully controlled conditions to provide a database that we can use to develop and test our predictive code. In addition, we continue development of ALE3D as a fully coupled thermal-chemical-mechanical hydrocode to handle the physical and chemical processes in thermal explosions that occur over widely varying time scales. We are applying ALE3D to the analysis of our thermal explosion tests.

In our burn rate measurements, we approach as closely as possible the conditions that exist during cookoff of energetic materials, with pressure of thousands of atmospheres and temperatures of several hundred degrees Celsius. Here we present data from previously unreported HMX formulations that offer insight into the controlling factors in the burn behavior of these explosives. We also present our first stress-to-failure data for HMX formulations at high temperatures. We conducted two thermal explosion experiments in our series of planned tests. Finally, we report on ongoing work on a related safety topic, the increase in shock sensitivity of HMX explosives when heated, which is relevant to considerations of sympathetic detonation following an initial thermal explosion.

To develop calculational tools for predicting thermal response violence, we must consider very different characteristics than those of traditional shock initiation and propagation. First, the time scales associated with the response range from hours to minutes to milliseconds to microseconds. Second, the mechanism of energy transfer is by thermal transfer instead of shock propagation. Third, the change in composition is directly a function of the temperature and must be modeled as such, instead of modeling it as either a predefined reaction rate or a pressure driven reaction. Fourth, the process can be relatively slow so that the energetic material and its containment are subject to deformation in the elastic regime for the major portion of the response, instead of very quickly transitioning to plastic modes. Fifth, because the reactions occur slowly, the composition of the energetic material is a mixture of reactants, intermediates, and final products throughout the duration of the calculation. This is very different from detonation modeling where material is either fully unreacted or fully reacted in all but a small region of space and time. Therefore, it is more important to model the properties of the material mixture.

We continue to develop ALE3D as a fully coupled thermal-chemical-mechanical hydrocode to handle the above characteristics and allow prediction of the violence of thermal events. It offers arbitrary Lagrangian-Eulerian treatment of problems for optimum analysis and includes fully coupled thermal transport and generalized, fully coupled chemical reactions. We incorporated into ALE3D the capability for implicit and explicit time stepping, with automatic switching from one to the other. This allows calculation of very slow thermal events and very fast hydrodynamic events, just as occur in a cookoff, in one code. ALE3D offers the ability to integrate all aspects of the thermal response problem because each aspect may control the overall reaction rate under different conditions. ALE3D therefore offers the potential to treat the entire cookoff problem, including hydrodynamic violence of the reaction, in one calculation. We are applying ALE3D to a range of problems to support its development as well as to gain understanding of the different problems.

Burn Rate Measurement Experimental Work

Burn Rate Apparatus

The hybrid strand burner/closed bomb system, shown in Fig. 1, combines the features of a traditional closed-bomb burner with those of a traditional strand burner. In a standard closed-bomb burner, pressure in the combustion chamber is the only measurement, with no measure of the surface regression rate to check combustion uniformity. With this design the data from samples that burn erratically are particularly hard to interpret. The standard strand burner provides direct measurement of the surface regression rate in a large volume at constant pressure, giving only one data point of rate vs. pressure in each experiment; further, the large volume required for isobaric operation means that operation at high pressures is generally not practical. In contrast, our hybrid strand burner/closed bomb system burns a sample in a small constant-volume, high-pressure chamber whose volume is approximately 70 cm³ with pressures up to 400 MPa initial to >1 GPa final pressure. The temporal pressure data and burn front time-of-arrival data provide surface regression and mass regression data for a range of pressures in one experiment.

The burn sample, 64 mm long and 6.4 mm in diameter, is generally formed by stacking nine pellets end-to-end, with 75- μ m-diam silver burn wires between each pair of pellets and at top and bottom. The stack is coated with an epoxy (Epon 82 with Versamid 140 catalyst) on its cylindrical surface to restrict combustion to the end of the sample. The ignition system at the sample top is a hot wire embedded in boron potassium nitrate, which then lights a thin HNS pellet.

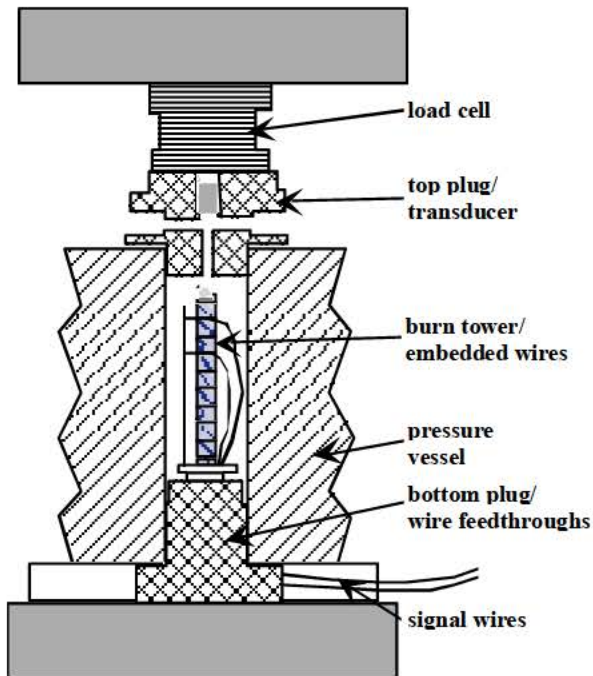


Figure 1. Schematic of hybrid strand burner.

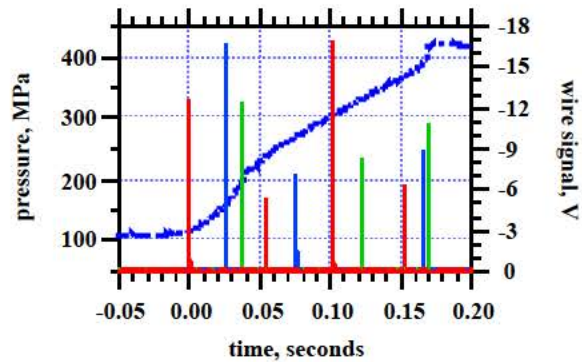


Figure 2. Typical pressure and wire data from the strand burner.

The strand burner is pre-pressurized, generally with argon, to the desired starting pressure before igniting the burn; this initial pressure can range from 5–400 MPa. During the burn, we use a load cell and/or a pressure transducer to measure the temporal pressure in the bomb; because of the small bomb volume, the pressure increases 3- to 6-fold during a burn. We detect the arrival of the burn front by the burning through of wires embedded in the sample. A high-speed digitizer captures the data for subsequent analysis. Burn wires are recorded in a way that we can unambiguously assign each signal to a particular wire; occasionally a wire will report out of sequence if it is broken by debris in the bomb chamber. Typical data are shown in Fig. 2, along with the pressure signal. Faster-burning segments can be seen in both the pressure and wire data, providing confirmation that the apparent non-uniform burning rate is real and not an artifact of the experiment. The burn wire electronics provide a well defined signal, with rise time less than 40 microseconds. The wires burn through reproducibly, with wires mounted at the same location in the sample showing a standard deviation of about 2 milliseconds. The wires do take several milliseconds to burn through; however, this time is essentially independent of initial pressure and temperature conditions and therefore does not affect the burn rate calculation made by differences in times-of-arrival. The burn wire at the bottom of the stack does not burn through unless enough energetic material is placed below it to provide several milliseconds of burning once the flame front has passed.

We calculate burn rate using the location-time data from the wires. We calculate the burn rate from the elapsed time to burn each pair of pellets, and the associated average pressure, to smooth the data somewhat. We do not calculate the burn rate from the pressure-time record. We thereby avoid the uncertainties in the equation of state of the combustion products and heat loss to the vessel walls. This is particularly important for pre-pressurized experiments because the equation of state of argon at 200–400 MPa is not modeled well in conventional thermochemical packages [1]. We do use the pressure data to confirm observations from the wire data.

Experimental Plan for Burn Rates

To study the burning behavior of HMX-based explosives, we start with the baseline explosive LX-04 and then investigate variations, as shown in Fig. 3. The baseline LX-04 contains fine-particle HMX with a large quantity (15 wt%) of Viton A binder, and shows smooth regular burning behavior over a wide range of conditions. The presence of less binder and/or larger particles generally leads to more erratic burning [2,3] and we seek to quantify this effect. We also are studying the effect of damage from pressure cycling or thermal treatment on the burn rate, and plan to look at different binders. Our pressed pellets have densities ranging from 98.0–99.3% of theoretical maximum density.

Ideally, we would also measure the burn rate of pure HMX at high temperature and pressure. However, it is not practical to make pellets of pure HMX that will burn uniformly. To get uniform planar burn down the length of the sample, the sample must contain small-particle HMX in a low-porosity pellet. The presence of voids in the sample also leads to irregular burning as the flames propagate through the voids. Unfortunately, pure small-particle HMX cannot be pressed into high-density, void-free pellets.

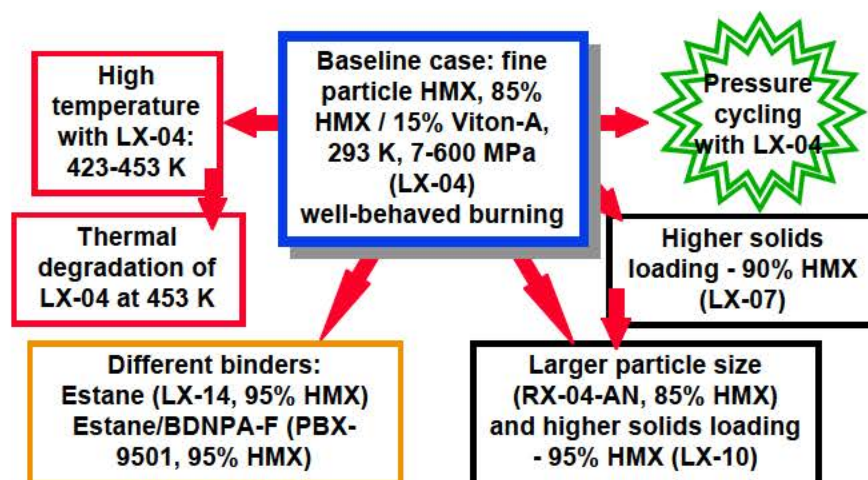


Figure 3. Plan for study of behavior of HMX-based explosives. We study effect of binder quantity and type, particle size, and damage from pressure cycling or high temperature. RX-04-AN has the composition of LX-04 but a particle size distribution like that of LX-10 or LX-14.

Results and Discussion of Burn Rate Experiments

Baseline Data—LX-04

Our baseline explosive, LX-04, contains 85 wt% HMX and 15 wt% Viton-A with fine particle “LX-04 grade” HMX (no particles $\geq 300 \mu\text{m}$, 90% $\leq 100 \mu\text{m}$, and 35–50% $< 44 \mu\text{m}$). Pellets were uniaxially pressed to 98–99% of TMD. The combination of fine particle size and high binder content results in a smoothly burning formulation over all pressure conditions at ambient temperature. Burn rate data for LX-04 at 300 K initial temperature are shown in Fig. 4. Two sets of data are included, with pressure measured either by load cell or by pressure transducer. The pressure error bars indicate that the load cell is less precise than the pressure transducer, so when possible the load cell is not used; currently we are limited to the load cell for runs at elevated temperature or with materials with corrosive products. For LX-04, both sets of data are consistent and give a burn rate linear in pressure over the pressure range 10–500 MPa. The burn rate error bars show that the error is larger at fast burn rates; there is an inherent noise of $\approx 1\text{--}2$ millisecond in the wire time to burn and, at the faster burn rates, this becomes a significant contribution to the error.



(b)(3)

In Fig. 4, we show a linear fit of burn rate to pressure with the error envelope as dashed lines. If we allowed the pressure exponent to vary, the best value was 0.95, not significantly different from 1.0, so we chose to use the linear description. The data in Fig. 4 are compared with literature data [4,6] for the pure HMX (crystals and pressed powder) burn rate in Fig. 5. We see that the LX-04 burns somewhat slower, as would be expected with its 15% inert binder. However, the overall agreement demonstrates the validity of this measurement technique.

Effect of Binder Content and Particle Size

Variations in formulations allowed us to determine the effect of binder content and particle size on burn behavior. The formulation LX-07 contains 90 wt% HMX and 10 wt%

Viton-A, with fine-particle “LX-04 grade” HMX. Its burn behavior, shown in Fig. 6, is the same as LX-04 at low pressure but is very rapid and erratic at high pressures (>100 MPa). This deconsolidative burning has been reported in the literature [4,7,8] and is apparently the result of physical failure of the sample at high pressure leading to increased surface area and faster burn rate. Deconsolidative burning is seen at lower pressures with binderless HMX pressed powder samples [4–7]; thus, it is reasonable to expect it at higher pressures for plastic-bonded explosives that are more physically robust.

The effect of particle size was determined using formulation RX-04-AN, with 85 wt% HMX and 15 wt% Viton-A. This has the same composition as LX-04 but contains larger-particle “LX-10 grade” HMX ($\approx 6\%$ >300 μm , $\approx 30\%$ 125–300 μm , $\approx 40\%$ 44–125 μm , and $\approx 24\%$ <44 μm). As shown in Fig. 7, this formulation burns smoothly over the entire pressure range with no deconsolidative behavior. The burn rate of RX-04-AN was lower than that of LX-04. This is consistent with the particle size difference—we would expect that larger-particle material would burn more slowly with its reduced HMX surface area per unit volume of explosive.



(b)(3)

The data in Figs. 6 and 7 allow us to conclude that, at least for formulations containing HMX and Viton-A, a low binder content (≤ 10 wt%) will lead to erratic deconsolidative burning with rates increased up to 100-fold. However, the presence of large-particle HMX alone does not lead to deconsolidative burning. One possible cause of deconsolidative burning, the fracture of large HMX particles with increasing pressure leading to increased surface area, does not seem to be operative in RX-04-AN.

We also made burn rate measurements on two HMX formulations with large particles and ≈ 5 wt% binder. LX-10-1 is 94.5 wt% HMX and 5.5 wt% Viton-A, with the same particle size distribution as RX-04-AN. PBX-9501 is 95 wt% HMX, 2.5 wt% Estane, and 2.5 wt% BDNPA/F, with a similar particle size distribution (8% > 300 μm , $\approx 37\%$ 125–300 μm , $\approx 30\%$ 44–125 μm , and $\approx 25\%$ <44 μm). Burn rate data for these formulations are shown in Figs. 8 and 9. Both formulations show the onset of deconsolidative burning at ≈ 150 MPa, with the

burn rates increasing almost 1000-fold. At pressures below the onset of deconsolidation, the LX-10 and PBX-9501 burn rates are essentially the same as that of LX-04, in contrast to the slower rate of RX-04-AN with a similar particle size distribution. One plausible explanation is that the reduction in burn rate by larger particles is offset by an increase in burn rate with reduced binder content and hence increased combustion energy. We did not observe such an effect in comparing 15 wt% and 10 wt% binder (LX-04 and LX-07), but the relative increase in combustion energy is much higher for the 5 wt% binder formulations.



(b)(3)

Implications of Observed Burn Behavior for Thermal Response

In the data reported here and the data reported last year for heated LX-04 and pressure-cycled LX-04 [9,10] we have quantified the burn rate at ambient temperature for several formulations with Viton A binder and Estane binders. More importantly, we have identified conditions (e.g., low binder content or heating > 430 K at low pressure) that lead to a 10-1000 fold increase in burn rate. Low binder content presumably results in physical failure of the sample with a concomitant increase in surface area and burn rate. As reported last year [9], heating over 430 K at low pressure causes the HMX $\beta \rightarrow \delta$ phase transition, which physically disrupts the sample with the 8% density decrease. The combustion gases apparently propagate through the defects and again result in a very fast burn. Both of these mechanisms are physical in nature, not chemical, but both will certainly play a significant role in the overall violence of a thermal reaction.

To predict the violence of a thermal reaction, the burn rate of the explosive must be accurately understood and described. The data reported here indicate areas where further work is needed, but do not necessarily represent thorough understanding of the phenomena involved. In particular, the behavior of heated explosives requires further study before we can quantify it sufficiently to allow meaningful prediction of violence.

We can draw one conclusion from this work. The violence of thermal response of HMX-based formulations will be strongly affected by the binder content. Formulations with 5 to 10 wt% binder are expected to give much more violent explosions than those containing higher levels of binder.

Future Plans for Burn Rate Measurements

There are many more burn rate measurements that will be informative. LX-04 is a good baseline material because it burns uniformly under all pressure conditions. We previously reported some measurements with heated LX-04 [9] but more data are needed at different pressure and temperature conditions. We also plan to evaluate aged LX-04 to determine any effects of aging. We then will turn to other HMX-based formulations such as PBX-9501, which have not been characterized at high temperatures. We also wish to study directly the effect of HMX phase on burn behavior, to aid in interpretation of the high-temperature burn results. Other aspects to study include measurement of flame spread rates, burning in cracks or slots, and determination of burn temperatures.

Mechanical Property Measurement Experimental Work

We need material models over a wide of conditions to accurately model the coupled thermal-chemical-mechanical response of explosives. Although mechanical properties of many explosives have been measured over temperature ranges of normal operation, there are essentially no data on mechanical properties at higher temperatures, and therefore any material models that may have been developed are essentially arbitrary. We have established a capability for mechanical property measurements, initially in the form of stress-strain-strain rate data in tension and compression, over a wide range of conditions. In our laboratory, shown in Fig. 10, we have creep frames for very low strain rates, two hydraulic testers for intermediate strain rates of $0.01\text{--}100\text{ s}^{-1}$, and a split Hopkinson bar for very high strain rates of $1000\text{--}3000\text{ s}^{-1}$. The samples in the creep and hydraulic testers are held in sealed containers (Fig. 11), which allow us to control the atmosphere present over the explosive. Details of the sample container are shown in Fig. 12. The containers can be heated or cooled over a wide range of temperatures. We can handle 20 creep samples at a time, since they may run for weeks.

Currently the hydraulic units for moderate strain rates are being used while the creep frames and Hopkinson split bar are undergoing final activation. Here we show results for LX-04 from those units at a variety of temperatures. Figure 13 shows tension data for LX-04 at a strain rate of $\approx 10^{-5}\text{ /s}$ at temperatures ranging from -223 K to 373 K . The strain data are not calibrated (due to problems with the sensor), so the primary data is the stress to failure. This value increases steadily as the temperature decreases, with the largest changes occurring at 248 K and below. This is consistent with the glass transition temperature of about 246 K for the binder Viton-A. Figure 14 shows similar data for LX-4 in compression where again a significant change occurs when the temperature goes below the glass transition temperature of the binder. The data in Fig. 14 are extended to even higher temperatures in Fig. 15 where we see that LX-04 retains some compressive strength even at 443 K .

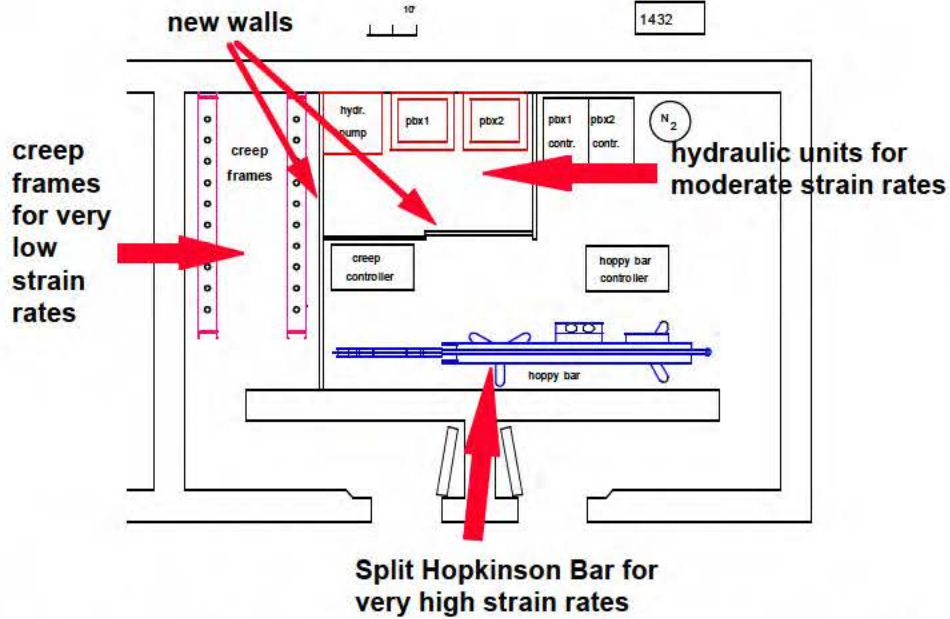


Figure 10. Laboratory arrangement at LLNL for mechanical property measurement over a wide range of strain rates and temperatures. Lab was activated in January 1998.

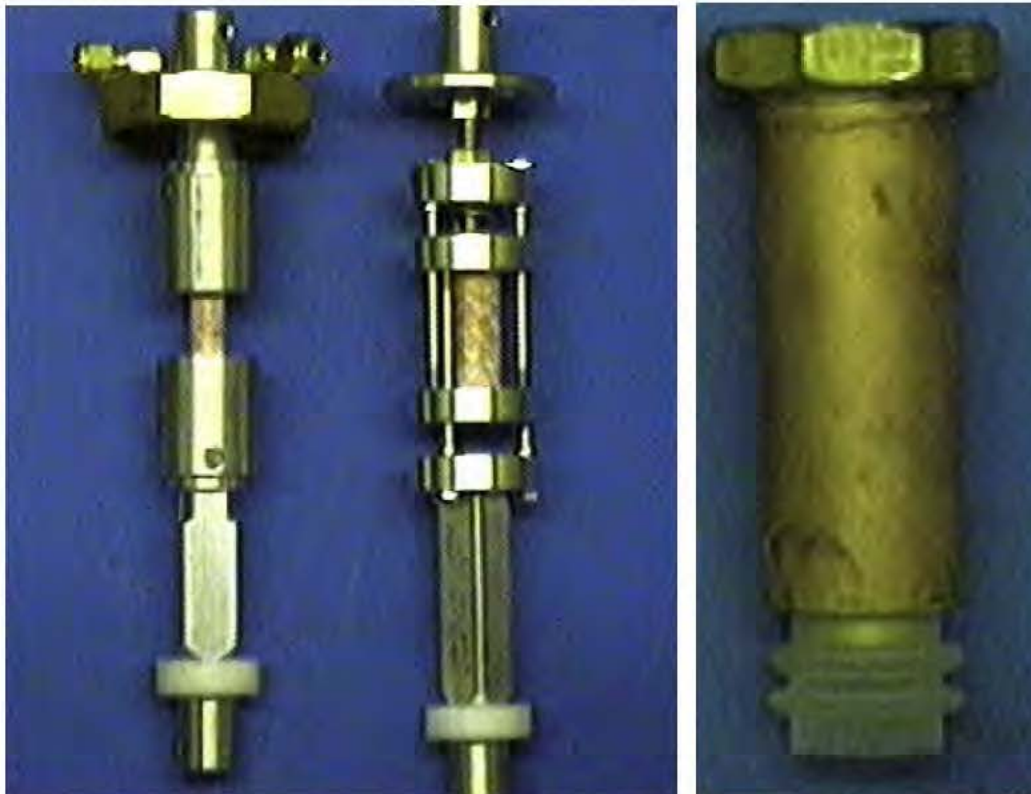


Figure 11. Left: Sample configuration for tension (left) and compression (right) testing. Right: Outer container provides capture of sample fragments and allows control of atmosphere surrounding sample.

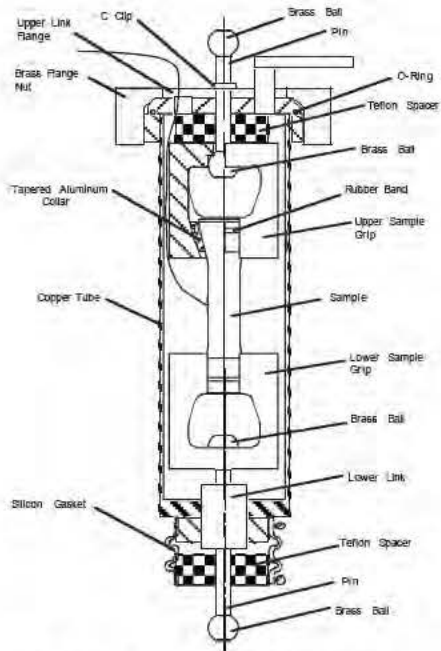


Figure 12. Detailed schematic of sample container for mechanical property testing.

(b)(3)

(b)(3)

The data reported here are a start on the measurement of mechanical properties at high temperatures, but much remains to be done. We must accurately measure stress/strain in addition to strain-to-failure over a wide range of temperatures and after some prolonged exposure to high temperature. We also need to check the relationship between the HMX $\beta \rightarrow \delta$ phase transition and mechanical properties at high temperature. Finally, additional formulations beyond LX-04 must be tested.

Scaled Thermal Explosion Experimental Work

We have begun a series of scaled thermal explosion experiments, with the goal of generating a database of thermal explosion violence as a function of several parameters such as dimension, confinement, explosive type, and thermal history. By carefully scaling dimensions and heating rates, we can cover a wide range of well-defined conditions. By keeping the tests as simple as possible, we plan to do many to cover as wide a range as possible. Quantification of reaction violence is the major diagnostic in these tests. We note that the outcome of each test will be a combination of the factors listed above (as well as others). As such, these tests are not well suited for development of physical parameters describing the explosives, but will provide a good methodology for testing and refining our predictive models and codes. One goal of this series of tests is to move us beyond engineering cookoff tests to give us a scientifically designed database of thermal reaction violence.

The planned test series has three levels of physical confinement (0.5, 1, and 2 kbar rupture strength), and three dimensions (1-, 2-, and 4-in.-diam with L/D of 4 in all cases). A typical vessel design is shown in Fig. 16. The high-strength steel cylinder wall is designed to the desired rupture strength, while the end closures are sufficiently stiff that they will not deform during the test. Initially, we are focusing on very slow heating rates to achieve uniform heating of the sample; we expect that the ensuing thermal reaction will propagate from the center of the cylinder (for 2-in. diameter, this requires a heating rate of 1 K/h). Radiant heaters are used for the cylinder to eliminate the extra confinement presented by band heaters; band heaters are used on the end caps. We measure temperatures on the exterior, and in some cases in the interior of the vessel. Violence of the thermal explosion is quantified by micropower impulse radar, which was developed for these tests and reported last year. Three radar units monitor wall motion, as shown in Fig. 17.

We used computer simulation extensively in the design of the experiment. The physical behavior of the confinement was modeled to ensure that rupture occurred at the desired pressure and near the center of the cylindrical portion of the vessel. The end caps were designed so that they would not yield at the maximum pressure; this ensures that the gas-tight seals remain intact. Calculation of the temperature profile across the explosive under different heating rates showed that a very slow heating rate is required to cause the reaction to initiate in the center of the explosive, from which we expect the most violent reaction. For the 2-in.-diam test, a heating rate of 1 K/h is required for the thermal runaway to take place at the center. A rate of 2 K/h causes the calculated ignition point to move 80% of the way to the edge of the sample. This effect is shown graphically in Fig. 18, where the scaled location of ignition is shown as a function of scaled heating rate.

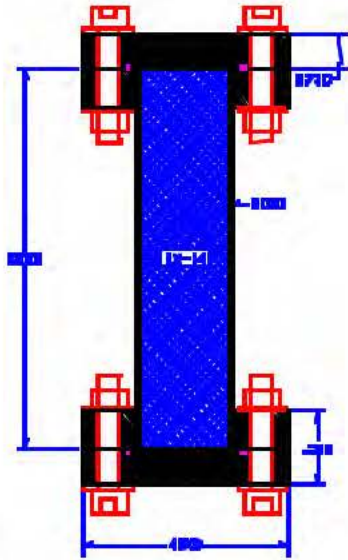


Figure 16. Vessel design for scaled thermal explosion test.

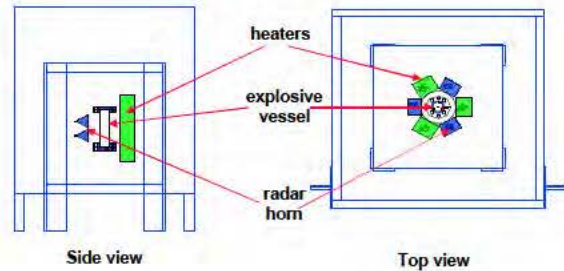


Figure 17. Schematic arrangement of explosive vessel, heaters, and radar horns in scaled thermal explosion tests.

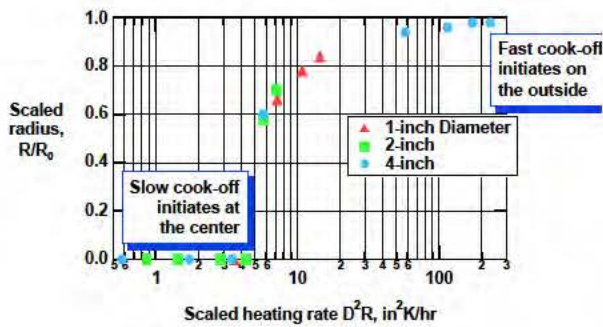


Figure 18. Simulation results showing the radial location of ignition as a function of heating rate. Very slow heating rates are required for ignition at the center with large radius tests.

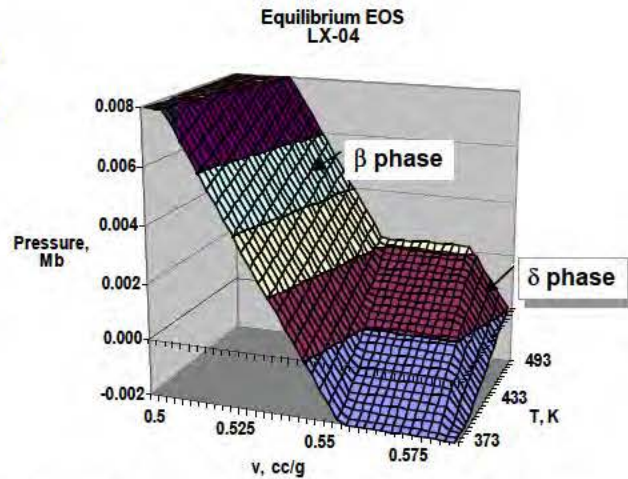


Figure 19. Approximate $\beta \rightarrow \delta$ phase diagram for HMX, based on literature data [11–18]. Further dependencies on particle size and formulation are not included.

Another key consideration in design and simulation is the $\beta \rightarrow \delta$ phase transition in HMX that occurs at about 440 K at atmospheric pressure [11–18]. We expect the HMX response to be quite different for the two phases, as we saw with the burn rate data; therefore, we need to know the phase state of the HMX at the time of thermal runaway, and would like to control which phase is present. An approximate $\beta \rightarrow \delta$ phase diagram for HMX is shown in

Fig. 19, derived from the above-cited references. We see from this diagram that a pressure of 2 kbar should be sufficient to prevent the conversion of β -phase HMX to δ -phase, whereas at lower pressures the phase conversion will take place. This means that the phase conversion will occur with our 0.5- and 1-kbar confinement cases. However, if we combine 2 kbar confinement with diametral dimensions selected so the explosive comes snug with the steel container prior to the onset of the phase change, we can prevent the phase change and determine the thermal response of β -phase HMX. We simulated the effect of phase change by calculating the explosive response first with the measured laminar burn rate of pristine LX-04, and then with a laminar burn rate 100 times faster in accord with our strand burner measurements with phase-converted LX-04 (reported last year) [9]. As shown in Fig. 20, the calculated violence, given by cylinder wall velocity, is about 100 times higher for the case with laminar burn velocity that is consistent with that of LX-04 with δ -phase HMX.



(b)(3)

The phase conversion in HMX is kinetically limited. To provide data on the phase composition of the explosive during the experiment, we equipped the steel cylinder with strain gauges to measure the hoop and axial strain in the cylinder wall. Our simulations show that monitoring the strain will show the phase change, as shown in Fig. 21. Several different behaviors can be seen in this figure. There is initially a gap between the steel cylinder and the explosive, and the first strain is simply the thermal expansion of the steel. Since the explosive thermal expansion is much greater than that of steel, it will eventually come up snug with the steel. At this time, the explosive expansion drives the steel, and the strain rate increases. When the phase conversion starts, the strain and strain rate increases greatly from the $\approx 6\%$ volume expansion. Finally, the strain rate becomes that of δ -phase HMX (assumed the same as β -phase in Fig. 21). The details of the strain signal depend on the initial gap, but by selection of the gap we should be able to monitor the phase of the HMX during the experiment.

We have conducted two tests in the series of scaled thermal explosions, one with LX-04 at a confinement of about 0.25 kbar (vessel had a flaw that was not detected prior to test), and one with PBX-9501 at 0.5 kbar confinement. Both vessels were hardened 4340 steel with a wall thickness of 1 mm (0.040 in.).

Results from the first test with LX-04 are shown in Figs. 22–28. The explosive comprised two stacked cylinders, each 1.95 in. in diameter and 3.9 in. long. The temperature data in Fig. 22 clearly show the endothermic phase conversion starting about 163°C. The temperature data in Fig. 23, just before the explosion occurred, show the spread in external temperatures due to differences in instrumentation and heater output. They also show the expected damping of temperature fluctuations at the center of the explosive. The temperature in the center of the LX-04 at runaway was 173-174°C, about 10° lower than we predicted based on One-Dimensional Time-to-Explosion (ODTX) data for LX-04. The ODTX data were taken under isothermal conditions where reactions took place in seconds to a few hours—clearly with the very long durations of heating present in this experiment, we have conditions that are not well-replicated by the ODTX test.



(b)(3)

(b)(3)

The strain data are shown in Figs. 24 and 25. The hoop and axial strain results in Fig. 24 show the rapid increase in strain at 165°C, as expected from the HMX phase conversion. The strain behavior prior to the phase conversion is not quantitative, as a consequence of the way the strain gauges were installed. Comparison of strain and internal temperature, in Fig. 25, corroborates the identification of the dip in internal temperature at 48–51 hours as the phase change because this dip and the onset of high strain coincide completely. We infer the existence of a flaw in the vessel giving a rupture strength of 0.25 kbar from these strain data. If the pressure had risen to the expected 0.5 kbar, the strain would have been significantly higher than we observed—the observed strain corresponds to an internal pressure of about 0.25 kbar.

The raw radar data show motion in only one radar unit. The other two showed no signal, as seen in Fig. 26. When analyzed in Fig. 27, the data show the wall velocity to be about 13 m/s, a very mild explosion. This is consistent with the appearance of the steel containment vessel after the test, which shows a simple rupture (Fig. 28). The physical confinement in this test was less than we had desired, but the test showed that LX-04 with 0.25 kbar confinement does not violently explode, even after undergoing the HMX $\beta \rightarrow \delta$ phase conversion.

(b)(3)

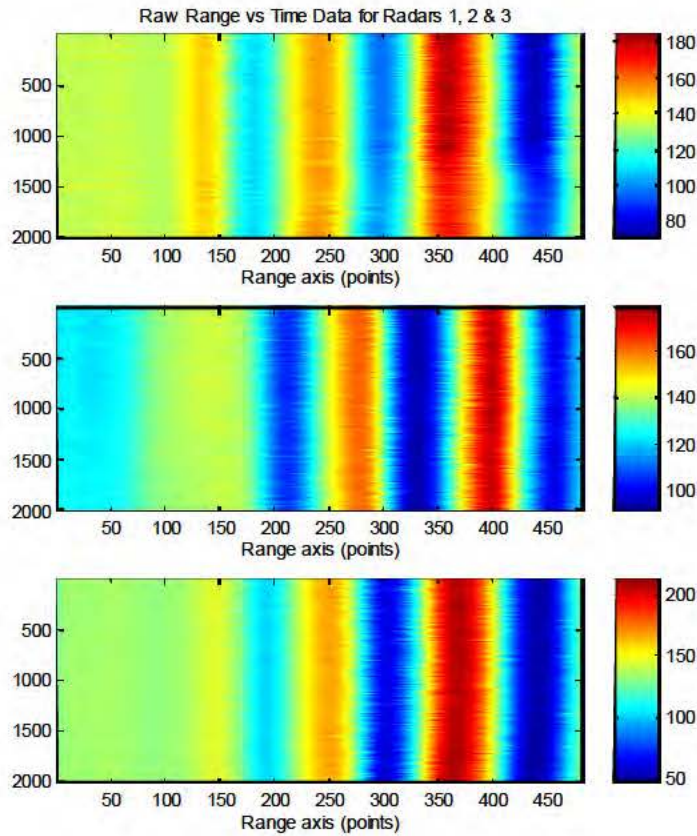


Figure 26. Micropower impulse radar raw data from scaled thermal explosion test with LX-04 with 0.25 kbar confinement. Second and third radar units show no measured motion, while the first unit shows slight motion about half-way through the test. The abscissa is distance, and the ordinate is time.

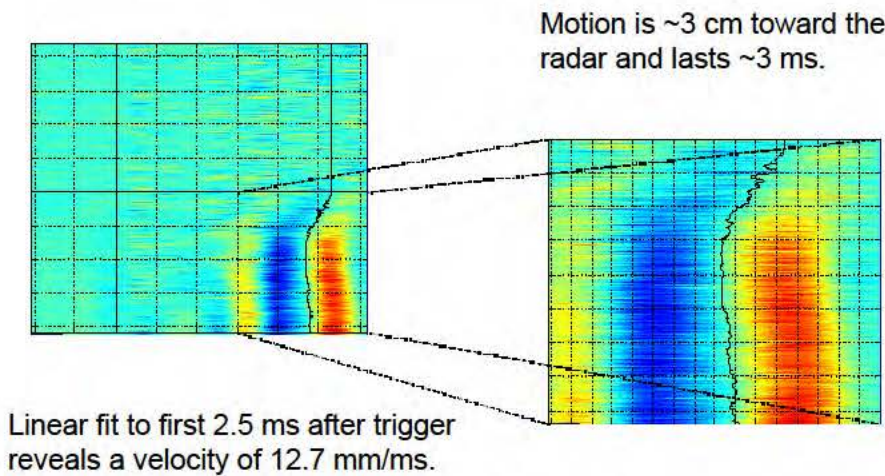


Figure 27. Data from first radar unit during thermal explosion event. The measured wall velocity is about 13 m/s, a very mild event.



Figure 28. Aftermath of thermal explosion with LX-04 with 0.25 kbar confinement. The rupture was very mild, consistent with the radar data in Figure 27. One radar horn can be seen in the left of the photo, with the ruptured cylinder adjacent to it.

We made a few changes in the configuration of the second test before we identified the cause of the low rupture pressure as a flaw in the metal. We were initially uncertain if the internal thermocouple played a role in the unexpected vessel failure with LX-04, so we eliminated internal thermocouples. We also thought that the gap between the two LX-04 pellets at mid-height might have given a pathway for hot reaction gases to flow to the cylinder wall and heat it sufficiently to prematurely reduce its strength. We therefore used three stacked cylinders to give a solid piece of explosive at the mid-height location where ignition was expected. The explosive tested was PBX-9501. Otherwise the second test was essentially the same as the first. The vessel was free of flaws (as shown by dye penetrant testing), so the physical confinement was the intended 0.5 kbar.

Results from the PBX-9501 test are shown in Figs. 29–34. The temperature data in Fig. 29 show that the reaction occurred at 170°C, somewhat lower than with LX-04. The strain data in Fig. 30 show the rapid increase in strain corresponding to the HMX phase conversion. Because the thermal explosion occurred 3° lower, and hence 3 hours earlier, there was less separation between the onset of phase conversion and the explosion, and the strain data are not as clear as those with LX-04. We also cannot match the onset of rapid strain with the internal endotherm since we did not have internal thermocouples.

(b)(3)

The raw radar data are shown in Fig. 31. All three radar units recorded motion, with units 1 and 3 showing early motion before failing and unit 2 reporting later motion. The analysis of these data is shown in Fig. 32, where the initial wall velocity was measured at 130 m/s for units 1 and 3, and 60 m/s for unit 2. Interpretation of these data is aided by inspection of the video images from the test (Fig. 33) and the vessel configuration after the test (Fig. 34). In Fig. 33, we see an eruption of flame away from the camera view in the middle frame. In the following frame ($\approx 1/60$ th of a second later), the flame is extinguished, although a fire restarts in following frames and burns brightly for another few 30th seconds

(followed by several seconds of burning of the radar-absorbing cloth enveloping the shot). In Fig. 34, we see that the vessel is split open and off of the end flanges, and is essentially folded back on itself. The configuration of the apparatus was such that the flame was directed between radar units 1 and 3. We conclude, therefore, that the vessel ruptured in between the view of radar units 1 and 3, so that these units saw the motion of the wall towards them immediately after rupture before being damaged by the hot flame. Radar 2 did not detect motion until the vessel wall wrapped far enough around itself to come into its field of view. This motion was also slower, since the wall was essentially coasting at that point. This thermal explosion with PBX-9501 at 0.5 kbar was fairly mild, given that the vessel remained more or less in one piece, but was much more violent than the thermal explosion of LX-04 at 0.25 kbar confinement.

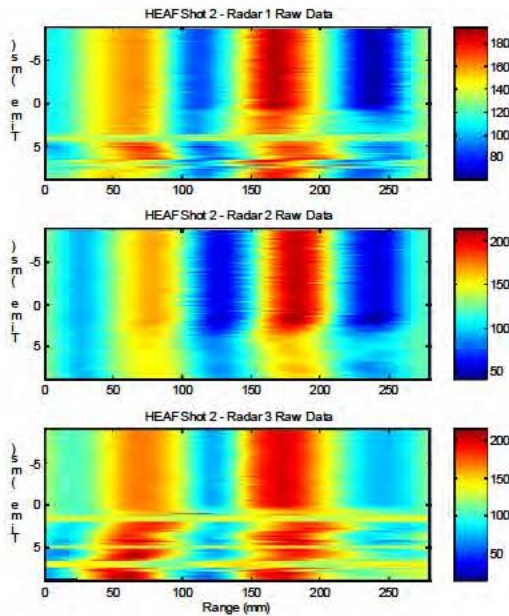


Figure 31. Micropower impulse radar raw data from scaled thermal explosion test with PBX-9501 with 0.5 kbar confinement. All radar units show motion, with unit 2 reporting motion later than the others. The abscissa is distance, and the ordinate is time.

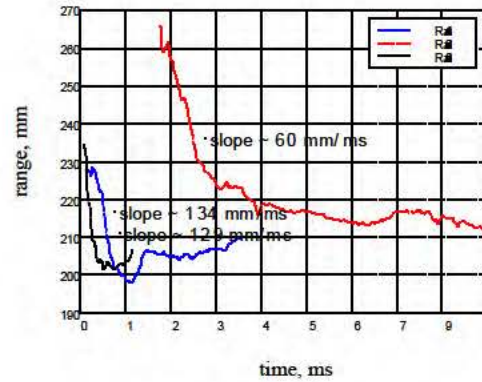


Figure 32. Analysis of radar data. Units 1 and 3 report wall velocities of about 130 m/s before being destroyed in blast. Unit 2 reported later, with lower velocity.

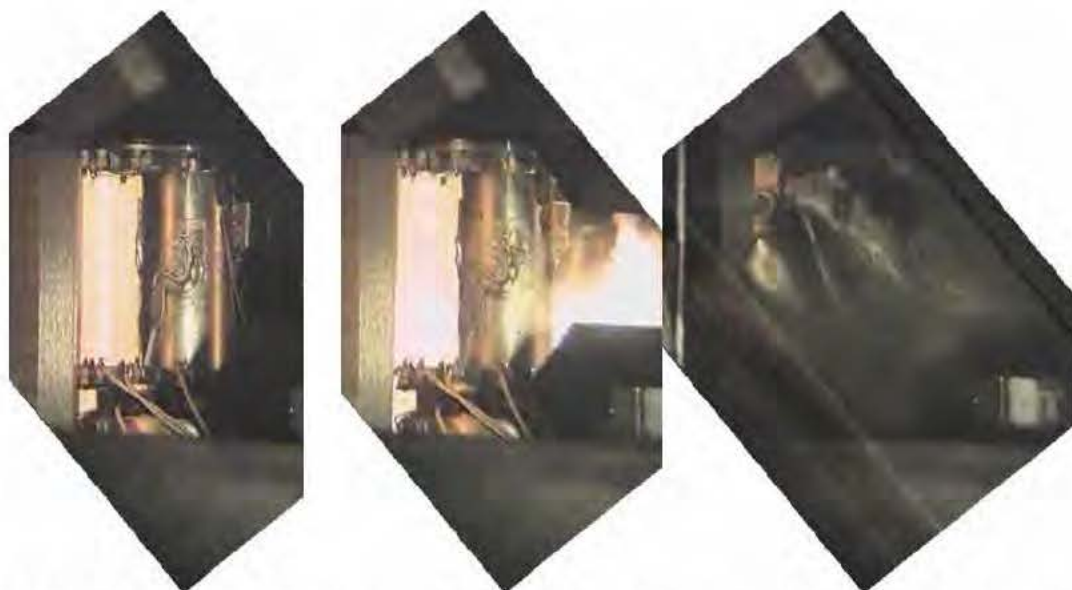


Figure 33. Still images from conventional video, $\sim 1/60$ th of a second intervals, showing (left-to-right) before reaction, flame erupting away from view, and ruptured vessel with no flame.



Figure 34. Ruptured vessel following PBX-9501 thermal explosion with 0.5-kbar confinement. Cylinder wall has been split and folded back on itself, but remains in one piece.

Future Plans for Scaled Thermal Explosion Experiments

We have just begun the series of scaled thermal explosion tests. We defined an extensive parameter set as part of the test series description (e.g., explosive type, dimension, confinement, and temporal thermal profile) and we will test with the extremes of the parameters and then fill in as appropriate. Quantification of the violence through wall velocity measurement remains the key diagnostic. These tests will be conducted as resources permit over the next few years.

Effect of High Temperature on Shock Sensitivity of HMX-Based Explosives

In analyzing thermal response of explosives, we must consider sympathetic detonation, where even a relatively mild explosion may propel fragments or shock into a nearby system, causing it to detonate. If the nearby system has been sensitized by heating, then the likelihood of sympathetic detonation increases. Therefore, part of understanding the thermal response of explosives is knowing how heating changes shock sensitivity.

In last year's report, we showed that an HMX-based explosive, LX-04, is sensitized by heating to 443 K (past the $\beta \rightarrow \delta$ phase transition) when unconfined [9]. This year, we studied the same material under heavy physical confinement. The test configuration is shown in Fig. 35. Six manganin gauges record the pressure histories at various depths in the sample. The front steel plate was 9 mm thick and was fastened to the 9-mm-thick rear steel plate with several steel bolts. Each disc of explosive was radially contained by a close fitting, 10-mm-thick steel rings of the same height as the explosive disc. The gauge packages contained both thermocouples and manganin pressure gauges between two discs of 0.13-mm-thick Teflon armor. The leads for the gauges and thermocouples were brought out the sides between the steel rings. A 1-mm-thick aluminum plate was placed between the front steel plate and the explosive to distribute the heat faster and more uniformly than the steel plate could do. A flat spiral ribbon heater was placed between the steel plate and the aluminum plate. The same heater configuration was placed at the back of the target assembly. Piezoelectric pins were placed flush with the face of the target to measure tilt, and pins were also placed a nominal 15 mm in front of target face to measure projectile velocity. Flash x-rays were also used to give a second measure of projectile velocity. Additional details are given by Forbes [19].

A total of five shots were fired with heavily confined, heated LX-04 at 443 K with impact velocities ranging from 0.535 to 0.828 km/s. Typical gauge data are shown in Fig. 36 along with results from reactive flow calculations; for complete data, see Forbes [19]. The buildup of reaction and eventual transition to detonation are clearly seen.

The change in shock sensitivity of LX-04 is shown in the Pop plot in Fig. 37, where the response of heated LX-04 (confined and unconfined) is compared with that of room temperature LX-04 and PBX-9404. This latter explosive contains 94 wt% HMX, 3 wt% nitrocellulose, and 3 wt% tris- β -chloroethylphosphate; it is considered to be fairly shock sensitive. As reported last year [9], the shock sensitivity of unconfined LX-04 is significantly increased when heated, and reaches the sensitivity of PBX-9404. The presence of confinement has very little effect on shock sensitivity as displayed in the Pop plot, with the behavior essentially unchanged. Detailed comparison of the pressure histories from confined and unconfined shots shows that the heated, confined LX-04 is slightly less sensitive than heated, unconfined LX-04. This difference can be modeled with reactive flow but, from Fig. 37, we see the effect is very small.

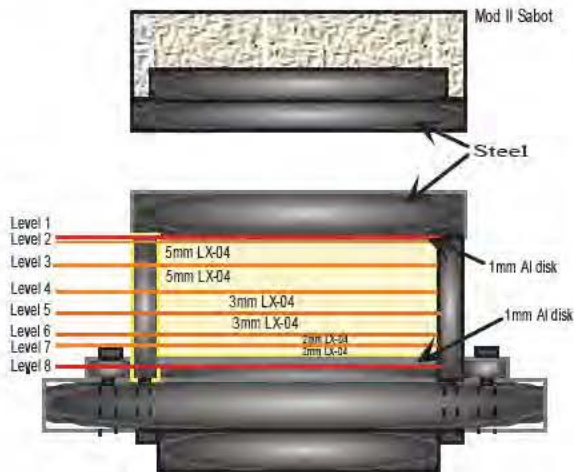
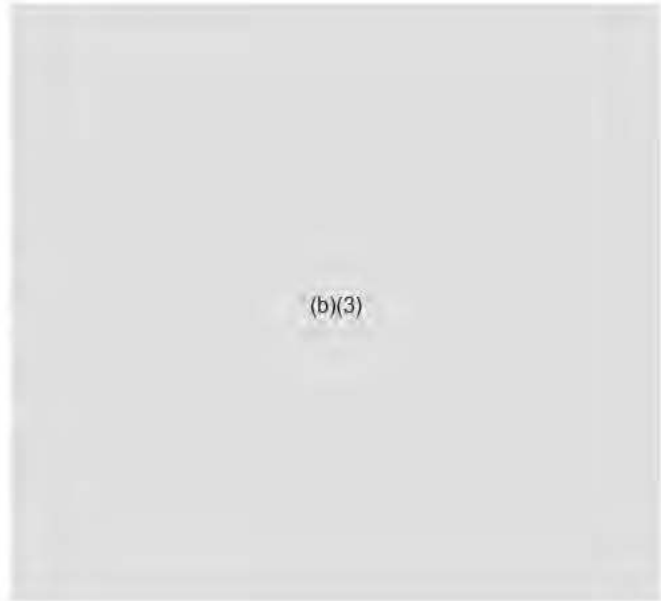


Figure 35. Geometry of the heated and confined shock initiation experiments with LX-04. Manganin gauges were used to measure *in-situ* pressure. Confinement was 304 stainless steel.



In all of the LX-04 tests to date, the LX-04 was heated above the transition temperature for the $\beta \rightarrow \delta$ phase transition. We think that this phase transition plays the key role in LX-04 shock sensitization. Because of the volume increase in going from β to δ , the presence of physical confinement should retard the phase transition. However, from Brill's data on the pressure dependence of the phase transition temperature [16,17], it is unlikely that the degree of physical confinement in these experiments could completely prevent the phase transition from occurring. Therefore, to further observe the effect of the phase transition, we plan to make further measurements in the coming year at slightly lower temperatures below the phase transition temperature.

Future Plans for Characterizing the Effect of High Temperature on Shock Sensitivity

As mentioned above, the $\beta \rightarrow \delta$ phase transition appears to be a key factor in shock sensitization of HMX-based explosives. We plan to test this more definitively by making measurements at a temperature slightly below that of the phase transition. The definition of further tests depends on the outcome of these tests, although study of other HMX-based explosives will probably be undertaken as well.

Development and Application of ALE3D

Introduction

In order to understand the hazards associated with a weapon system, it is necessary to model the response of the system to a variety of conditions. The response associated with shock initiation has been well modeled with explicit hydrodynamics codes. One particular area that has not been well characterized is the response of energetic materials to an unusual thermal environment, such as a fire.

In a typical fire scenario, radiation and convection transport the heat from the fire to the exterior of the explosive device. From there, it is conducted through the outer case and then to the explosive, which begins the process of thermal decomposition. This decomposition gradually alters the material properties of the explosive, which range from changes in heat capacities and thermal conductivities, to changes in shear modulus, yield strength and bulk moduli, to phase changes. The change from a solid to a gas induces mass motion in the explosive confinement. Depending on the strength of that confinement, the decomposition can be either slow, leading to a benign overall system response, or very fast, leading to a catastrophic event.

The characteristics of the thermal hazard environment and the type of modeling required are significantly different from those of shock initiation and propagation. First, the time scales associated with the response range from minutes to days instead of micro- to milliseconds. Second, the mechanism of energy transfer is thermal transport instead of shock propagation. Third, the change in composition is directly a function of the temperature and must be modeled as such, instead of modeling it as either a *fait accompli* or as a pressure-driven reaction. Fourth, the process can be accompanied by relatively slow motion so that the energetic material and its confinement are subject to deformation in the elastic regime for the major portion of the response, instead of very quickly transitioning to plastic modes. Fifth, because the reactions occur slowly, the composition of the energetic material is a mixture of reactants, intermediates, and final products throughout the duration of the calculation. This is very different from detonation modeling where material is either fully unreacted or fully reacted in all but a small region of space and time. Therefore, it is more important to model the properties of the material mixture, because it is no longer the exception but rather the rule.

To achieve these characteristics, we have developed ALE3D into a 3D coupled thermal-chemical-mechanical code. It offers arbitrary Lagrangian-Eulerian treatment of problems for optimum analysis and includes fully coupled thermal transport and generalized, fully coupled chemical reactions. We have incorporated into ALE3D the capability for implicit and explicit time stepping in hydrodynamic calculations, with automatic switching from one to the other. This allows calculation of very slow thermal events and very fast hydrodynamic events, just as occur in a cookoff, in one code. ALE3D also includes thermally driven reactions, models for both the thermal and mechanical properties of chemical mixtures, and second-order species advection. We have reported on the development of ALE3D in previous annual reports [9,20,21] and in recent literature [22].

Current Progress

Development of ALE3D during the past year has been largely focused on conversion of the original single-processor version into a code to run on massively parallel computers. This is necessary to be able to run large three-dimensional problems, and safety analyses usually require full 3D treatment for accurate simulations. We have made much progress on this formidable problem, and will soon be able to run ALE3D in massively parallel computations.

In addition, three new capabilities were added to ALE3D: material history variables, additional material models, and a burn front propagation model. The first, the material history variables, increases computational efficiency by reducing memory requirements. Each material model requires extra state variables (e.g., extent of chemical reaction, chemical composition, or degree of fracture). The use of material history variables results in storage of these state variables only where the material exists in the mesh, instead of throughout the entire simulation. This significantly reduces memory needs and allows the use of more scientifically rigorous material models.

The second new capability, additional material models, extends previously-developed gas-solid mixture models for equation of state from ideal-gas/elastic solid components to arbitrary user-defined gas and solid models. In addition, the constitutive model for gas-solid mixtures developed previously has been extended. The original model used a combination of elastic solid elements with a strength cutoff when the gas volume reached 40%. The new model incorporates plastic yield coefficients into the solid component model.

The third significant capability is the incorporation of a burn front propagation model. In a calculation, we could compute deflagration after ignition by direct numerical simulation. This would require very fine zoning and much better chemical kinetic models than we currently have available. Instead of a direct numerical simulation, we have added a front propagating capability based on level set models. To propagate the burn front with these models, one creates a field ψ that is zero at the point of ignition, and monotonically increasing away from it. One then solves:

$$\frac{\partial \psi}{\partial t} = -c(P, T, \{N_i\}) |\nabla \psi| \quad (1)$$

which is a reformulation of the wave equation. Here c is the experimentally determined burn speed of the high explosive under the appropriate conditions, as measured for example by the high pressure strand burner. This model therefore provides a direct connection between the laboratory measurement of burn rates at various conditions and the inclusion of the data in ALE3D simulations. The burn front is determined by finding the location where the field goes through zero. This method is similar to methods used to calculate the detonation front like the DSD [23] and WBL [24] models. It differs in that those models may be run as a preprocessor step because the waves they are tracking are supersonic, while this model must be run during the deflagration because the deflagration is subsonic. At this stage, we are not including any of the boundary condition effects that are common in the DSD and WBL approaches.

We apply our new burn front propagation model in the sample calculation shown in Fig. 38. The initial configuration is a pressure vessel consisting of a 1-cm spherical shell of aluminum surrounding a 2-cm spherical shell of HE surrounding a 1-cm spherical shell of aluminum. The pristine HE in this hypothetical system has the material properties of aluminum, and the reaction products are treated as a gamma-law gas. A point in the middle of the explosive is ignited with a high initial temperature. This triggers the burn propagation criteria to in turn propagate the remainder of the user-defined burn rate. For this example, we chose a burn rate for the explosive of $0.1 * P^{78}$ where P is in Mbar. The system starts at an initial pressure of one atmosphere.

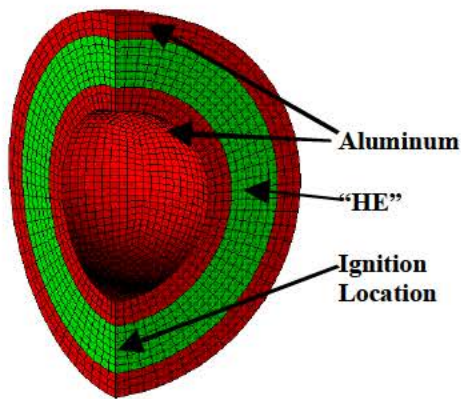


Figure 38. Initial configuration of calculation using burn front propagation model.

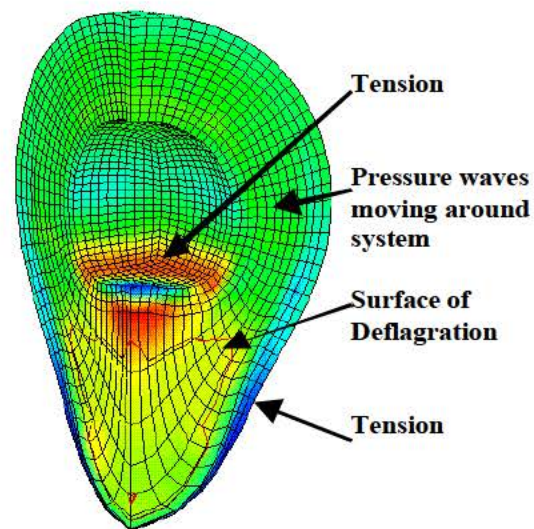


Figure 39. Late time configuration of deflagrating system. Pressure waves have time to move throughout the system.

We show the results of our calculation in Fig. 39. In this system, the configuration remains unchanged for roughly 200 microseconds as the explosive burns very slowly under low pressure. As more of the explosive burns, the pressure in the vessel increases, causing the burn rate to increase according to the burn rate law. The burn rate is sufficiently slow that there is time for signals from the burning explosive to move around the entire vessel. After roughly 200 microseconds, the pressure in the vessel is sufficiently high that the burn is too rapid for the pressure to equilibrate inside the vessel. This allows the explosive burn rate to bootstrap up. Also affecting this is the strength of the explosive material. With this particular model, the partially degraded explosive material has enough strength to resist the pressure of the decomposing explosive.

We continue to apply ALE3D to other safety-related problems of interest. Calculations are underway to simulate the scaled thermal explosion tests. Results are not available for this progress report, so will be included in the next report.

Discussion of ALE3D Approach

The features of ALE3D are designed to allow calculation of the response of an energetic material to thermal stimulus. We have chosen the route of completely coupling all of the various effects together. Although this may appear complicated, most fundamental effects are relatively simple and do not require special consideration. However, when multiple effects are simultaneous, the effects may combine to produce interesting and unanticipated results. It is precisely this type of response that is missed in other approaches, wherein a suite of separate codes is used to examine the behavior in different physical regimes. The separate-code methodology is appropriate when the major responses are well separated in both time and effect, but this is often not the case in safety problems.

We must do more work on the material models associated with the chemically reacting mixture material. The strength of the explosive in the partially decomposed state can have a profound effect on the ensuing reaction. The higher the strength of the explosive, the more it will resist the expansion of the decomposition products. This will increase the rate at which the explosive burns, turning what could have been a benign event into a catastrophic one. Our example problem of deflagration in a spherical vessel illustrates this effect. In addition, the implicit hydrodynamics option is essential to model the fully coupled, very-long-time response of the explosive system to thermal events. Execution of the implicit scheme with massively parallel computation is a major technical challenge, but we have made significant progress this year on solving this.

Future Plans for ALE3D Development and Application

The primary task in ALE3D development is realization of the full capability of the code while running on massively parallel computers. This includes accurate treatment of all coupled effects as well as successful implementation of the implicit calculational scheme for slow events. Other areas of ongoing work include improved material models (especially for mixtures), and implementation of chemical species diffusion and incompressible fluid flow.

Along with these improvements, we seek to make the code more accessible and useful to potential users. As part of this effort, we are aggressively applying ALE3D to a variety of problems. We are also increasing the user base in DOE and DoD by wider distribution of the code and training users onsite at LLNL. This will result in a more robust code as different users exercise different capabilities and it will provide the user with an analysis of previously intractable problems. This year, we trained new ALE3D users from the U.S. Navy, Indian Head, and the U.K. Atomic Weapons Establishment.

Conclusions

The Ignition and Initiation Phenomena program is focused on the prediction of cookoff violence of explosives. This program features tightly integrated efforts in model and code development and in experimental characterization of explosive properties and responses. The proper connections between theoretical and experimental elements are required to direct both efforts in the most effective manner, and the work at LLNL is designed with this in mind.

We are developing the fully-coupled thermal-chemical-mechanical hydrocode ALE3D to provide the capability to incorporate many physical and chemical processes into cookoff modeling. We also can treat the entire problem in one calculation, as required for accurate simulation. We are measuring key thermal response parameters of explosives that will be incorporated into models in the ALE3D code. From the theoretical and experimental work, we are gaining an understanding of the effect of high temperature on HMX. Our overall goal is development of a predictive capability for the violence of thermal response of energetic materials and systems containing them, with our initial focus on HMX as a material of mutual interest to the DoD and DOE.

Acknowledgments

We thank the following people for their excellent work in support of different areas of the program: Strand Burner—Jeff Chandler, Dan Greenwood, Jeff Wardell, Rich Simpson, and Lonnie Daniels; Mechanical Properties—Bruce Cunningham, Scott Groves, Ing Chiu, Henry Andreski; Thermal Explosion Tests—Craig Tarver, Ed Lee, LeRoy Green, John Reaugh, Jeff Wardell, Dan Greenwood, Don Hansen, Paul Marples, Pat McMaster, Ernie Urquidez, Robert Gray, Gary Steinhour; Micropower Radar—Tom Rosenbury and Doug Poland; Shock Sensitivity—Jerry Forbes, Paul Urtiew, Frank Garcia, Dan Greenwood, and Paul Marples; ALE3D Development—John Reaugh, and the ALE3D development team headed by Richard Sharp.

References

1. L. E. Fried, "CHEETAH 1.39 User's Manual," Lawrence Livermore National Laboratory, UCRL-MA-117541 Rev. 3 (March 19, 1996).
2. W. C. Tao, M. S. Costantino and D. L. Ornellas, "Burning mechanism and regression rate of RX-35-AU and RX-35-AV as a function of HMX particle size measured by the hybrid closed bomb-strand burner," in *Proceedings of 1990 JANNAF Propulsion Systems Hazards Subcommittee Meeting*, Johns Hopkins University, Laurel, MD, Chemical Propulsion Information Agency, Laurel, MD (1990).
3. W. C. Tao, M. S. Costantino, D. L. Ornellas, L. G. Green, and E. S. Jessop, "The effects of HMX particle size and binder stiffness on the burning mechanism and regression rate of a series of fast burning propellants," Lawrence Livermore National Laboratory, UCRL-JC-104515 (June 3, 1991).
4. T. L. Boggs, "Thermal Behavior of Cyclotrimethylenetrinitramine(RDX) and Cyclotetramethylenetetranitramine (HMX)," in *Fundamentals of Solid-Propellant Combustion*, K.S. Kuo and M. Summerfield, eds., American Institute of Aeronautics and Astronautics, New York (1984).
5. R. L. Derr, T. L. Boggs, D. E. Zurn, and E. J. Dibble, "The Combustion Characteristics of HMX," in *Proceedings of 11th JANNAF Combustion Meeting*, Pasadena, CA, CPIA, p. 231 (1974).
6. M. Herrmann, W. Engel, and N. Eisenreich, "Thermal Expansion, Transitions, Sensitivities and Burning Rates of HMX," *Propellants, Explosives, Pyrotechnics*, **17**, 190 (1992).
7. R. A. Fifer and J. E. Cole, "Transitions from Laminar Burning for Porous Crystalline Explosives," in *Proceedings of the Seventh Symposium (International) of Detonation*, Annapolis, MD, Office of Naval Research, NSWC MP-82-334, p. 164 (1981).
8. W. C. Tao, M. S. Costantino, and D. L. Ornellas, "Burning Rates of Two Cast Nitramine Explosives Using a Hybrid Closed Bomb-Strand Burner," in *Proceedings of the Ninth Symposium (International) of Detonation*, Portland, OR, Office of the Chief of Naval Research, OCNR 113291-7, p. 1310 (1989).
9. J. L. Maienschein and A. L. Nichols III, *Joint DoD/DOE Munitions Technology Development Program FY-97 Progress Report*, pp. II-61-84, "Ignition and Initiation Phenomena: Cookoff Violence Prediction," Lawrence Livermore National Laboratory, UCRL-ID-103482-97 (January 15, 1998).
10. J. L. Maienschein and J. B. Chandler, "Burn Rates of Pristine and Degraded Explosives at Elevated Pressures and Temperatures," in *Proceedings of 11th International Detonation Symposium*, Snowmass, CO, Office of Naval Research (1998).
11. H. H. Cady, "Studies on the Polymorphs of HMX," Los Alamos Scientific Laboratory, LAMS-2652 (October 18, 1961).

12. R. E. Cobble Dick and R. W. H. Small, "The Crystal Structure of the δ -form of 1, 3, 5, 6 - Tetranitro-1, 3, 5, 7-tetraazacyclooctane (δ -HMX)," *Acta Cryst.*, **B30**, 1918 (1974).
13. A. S. Teetsov and W. C. McCrone, "The Microscopical Study of Polymorph Stability Diagrams," *Microscop. Cryst. Front.*, **15**, 13 (1965).
14. W. C. McCrone, "Crystallographic Data: Cyclotetramethylene Tetranitramine (HMX)," *Analytical Chem.*, **22**, 1225 (1950).
15. M. Herrmann, W. Engel, and N. Eisenreich, "Phase Transitions of HMX and their Significance for the Sensitivity of Explosives," in *Proceedings of Proceedings of the Technical Meeting of Specialists MWDDEA AF-71-F/G-7304 - Physics of Explosives*, p. 12 (1990).
16. R. J. Karpowicz and T. B. Brill, "The β — δ Transformation of HMX: Its Thermal Analysis and Relationship to Propellants," *AIAA Journal*, **20**, 1586 (1982).
17. R. J. Karpowicz, L. S. Gelfand, and T. B. Brill, "Application of Solid-Phase Transition Kinetics to the Properties of HMX," *AIAA Journal*, (1982).
18. A. G. Landers and T. B. Brill, "Pressure-Temperature Dependence of the β — δ Polymorph Interconversion in Octahydro-1,3,5,7-tetranitro-1,3,5,7-tetrazocine," *J. Phys. Chem*, **84**, 3573 (1980).
19. J. W. Forbes, C. M. Tarver, P. A. Urtiew, and F. Garcia, "The Effects of Confinement and Temperature on the Shock Sensitivity of Solid Explosives," in *Proceedings of 11th International Detonation Symposium*, Snowmass, CA, Office of Naval Research (1998).
20. J. L. Maienschein, A. L. Nichols III, and C. G. Lee, *Joint DoD/DOE Munitions Technology Development Program FY-95 Progress Report*, pp. 173–192, "Ignition and Initiation Phenomena: Cookoff Violence Prediction," Lawrence Livermore National Laboratory, UCRL-ID-103482-95 (January 15, 1996).
21. J. L. Maienschein and A. L. Nichols III, *Joint DoD/DOE Munitions Technology Development Program FY-96 Progress Report*, pp. 173-192, "Ignition and Initiation Phenomena: Cookoff Violence Prediction," Lawrence Livermore National Laboratory, UCRL-ID-103482-96 (January 15, 1997).
22. A. L. Nichols III, R. Couch, R. C. McCallen, I. Otero, and R. Sharp, "Modeling Thermally Driven Energetic Response of High Explosive," in *Proceedings of 11th International Detonation Symposium*, Snowmass, CO, Office of Naval Research (1998).
23. J. B. Bdzil et al., "Level Set Techniques Applied to Unsteady Detonation Propagation," in *Proceedings of Mathematical Modeling & Combustion Science Conference*, Hawaii (1994).
24. B. D. Lambourn and D. C. Swift, "Application of Whitham's Shock Dynamics Theory to the Propagation of Divergent Detonation Waves," in *Proceedings of the Ninth Symposium (International) of Detonation*, Portland, Oregon, Office of Naval Research, p. 784 (1989).

This page intentionally left blank

Gun Propellants

John E. Reaugh
Lawrence Livermore National Laboratory
(925) 422-7206
jreaugh@llnl.gov

Abstract

The pressure dependence of the laminar burn rate of gun propellants plays a role in the design and behavior of high-performance guns. We have begun a program to investigate the effects of processing variables on the laminar burn rates, using our high-pressure strand burner to measure these rates at pressures exceeding 700 MPa. We have burned JA2 and M43 propellant samples, provided by Arpad Juhasz, Army Research Laboratory (ARL), from propellant lots previously used in round-robin tests. Our results at room temperature are in accord with other measurements, although the measured burn rates of M43 are erratic. In addition, we present results measured for propellant that has been preheated to 50°C before burning. We received more recently formulated EX-99 propellant, similar to M43, from Indian Head, and have begun preparation for burn-rate testing with that material. We received samples of energetic binder monomers and polymers from Aerojet at the beginning of FY99 for heat of formation determination.

Program Objectives

The program objectives are: (1) to measure the laminar burn rate of various advanced-propellant formulations over the pressure range experienced in gun applications, and to measure the effects of composition, additives, and particle size on that burn rate; and (2) to determine the heats of formation of the components used in advanced, high-impetus propellants, including energetic binders. The burn-rate measurements will take advantage of the unique high-pressure strand burner at this laboratory. The pressure range of that apparatus, up to 1 GPa, will extend the pressure range for burning-rate measurements to exceed the normal operating range of fielded and experimental guns.

Interaction with DoD Laboratories

The principal Department of Defense (DoD) contacts have been Arpad Juhasz, ARL Aberdeen, and Susan Peters, Naval Surface Warfare Center (NSWC), Indian Head. We have been in frequent contact during the reporting period. In addition, Alice Atwood, NSWC China Lake, has made measurements of the burn of our M43 material.

Work Performed to Date

JA2 Burn-rate Measurements

We confirmed the experimental techniques we use in the high-pressure strand burner by comparing the accepted burn rate of JA2 as a function of pressure at both ambient and elevated temperature (50°C). The results, shown in Figs. 1 and 2, are in accord with accepted values of the laminar burn rate. The error analysis described by Maienschein in this volume shows that the main contribution to uncertainty in the laminar burn rate at high pressure is the uncertainty in the burn-wire reporting time. Low-pressure experiments with replicated wires between two pellets showed an average difference in reporting time of 2.5 ms. It is uncertain whether the same difference will be observed at high pressure. The experimental results for the elevated temperature burn-rate (Fig. 2) show significantly less scatter at high pressure than the error bars indicate. This suggests that our estimates of uncertainty in the measured burn rate may be too generous.

There does appear to be a systematic difference in the low-pressure burn rates. Our data are noticeably faster than nominal at both ambient and elevated temperature. The cause of this discrepancy is uncertain.



(b)(3)

(b)(3)

M43 Burn Rate

Our measurement of the M43 burn rate shows significant scatter that is much larger than our apparently generous estimates of the uncertainty (Figs. 3 and 4). The previous data, taken in FY97, were made on pellets that had been cut with a diamond saw, and then stacked to give a more-or-less vertical tower. The extruded propellant sticks (Fig. 5) exhibit significant curvature. As a result, the cut cylinders were not right-circular ones. The present data were taken on pellets that had been cut, and then machined to be smaller-diameter right-circular cylinders, so that straight towers could be assembled. The scatter is not noticeably different.

We examined the pressure histories from the Kistler gauge mounted in the strand-burner volume. We observe that the irregular burn rate measured by the break wires is also seen as an irregular pressurization rate (Fig. 6). This irregularity is not observed for JA2 (Fig. 7).

We examined the pellets with dye penetrant before and after machining, and before and after a pressurization cycle. If cracks were present, they could be seen, and were observed to extend after a pressurization cycle. Only one pellet was observed to have a crack. The propellant does not have noticeable defects, and pressurization does not cause hidden defects to reach the surface.

(b)(3)

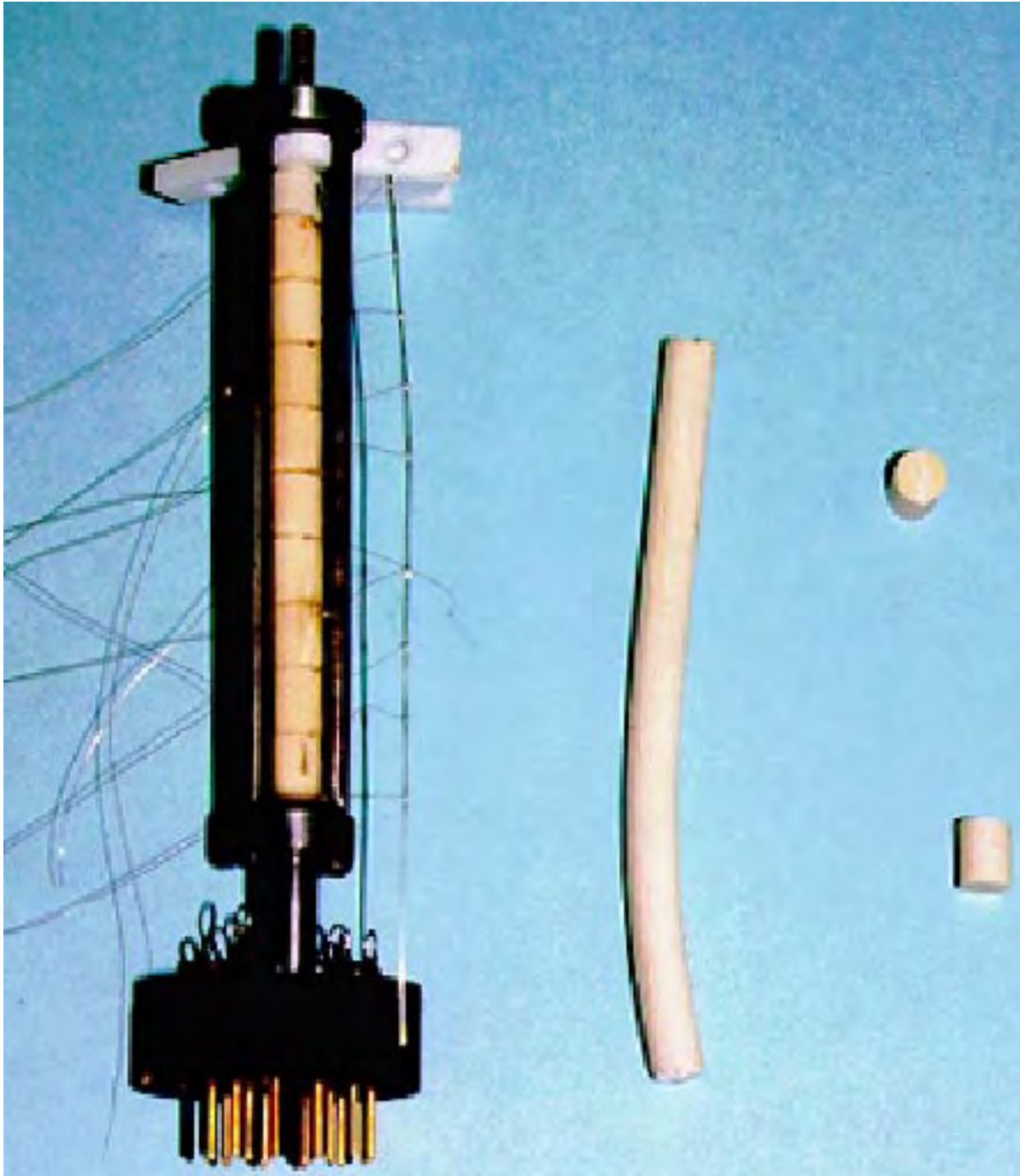


Figure 5. Extruded stick of M43 propellant showing stick curvature, cut pellets, and a tower.

(b)(3)

We thought to burn a constructed tower at one atmosphere without pressurization, and record the progress of the burn with a video camera. We placed the tower on an electronic balance, so that we could also record the mass loss as a function of time. The JA2 showed a regular, steady advance of the burn front and mass loss consistent with the break-wire speed of 0.7 mm/s, which is also consistent with the low-pressure strand burner data of Miller and others. Of the five tests of M43, only two of them burned to near completion. The others stopped burning midway through the tower, typically stopping in the middle of a pellet. The two complete burns showed mass loss consistent with a burn speed of 0.3 mm/s, a little higher than the above referenced low-pressure data.

Conclusions

It is our assessment that the laminar burn speeds can be measured with the high-pressure strand burner. The behavior of M43 is puzzling. The videos of the one atmosphere burn by us, and of higher pressure burns by Atwood, show a burn front that does not advance as a laminar flow. Instead the flame front is not normal to the advance direction, and progresses erratically, sometimes tilted to one side and then, later in the burn, tilted to the other side.

Further Work

Xerogel Process

We are examining the xerogel process, described by Simpson in this volume, to make an RDX-based propellant with different RDX particle sizes. We plan to measure the detonation critical diameter and the laminar burn rate of these materials.

EX-99 Propellant

We received five lots of EX-99 propellant, similar in composition to M43, from Susan Peters, NSWC-IH in August. They are described in Table 1, below. We will perform burn rate tests on these materials, which were made much more recently than the previous batch of material. As a consequence, we will be examining the effects of RDX particle size and other process variables on the laminar burn rate.

(b)(3)

Energetic Binders

We received samples of energetic binder polymers and monomers from Aerojet in November. We will measure the heats of combustion and density to determine the heats of formation for these materials.

Acknowledgments

We are grateful for the enthusiastic support of Arpad Juhasz, ARL. Susan Peters, NSWC, Indian Head, supplied the EX-99 propellant samples, and Ruth Doherty helped break the logjam that had delayed shipment of the material. Gerry Manser, Aerojet, supplied samples of the energetic binder materials, and helped to expedite getting the samples to us.

Metastable Solid Phase High Energy Density Materials

Hector E. Lorenzana and William Evans
Lawrence Livermore National Laboratory
(925) 422-8982
hlorenzana@llnl.gov

Abstract

Radical advances in the development of high energy density materials (HEDM) are critical to the realization of the next generation of munitions featuring enhanced compactness, delivery, and power. This project pursues the synthesis and characterization of a radically new class of energetic materials predicted to have an energy density per unit volume of up to 3 times that of HMX. Conventional energetic materials are characterized by strong intramolecular bonds within molecules and weak intermolecular bonds between molecules, leading to large equilibrium volumes for the liquid and solid phases. In contrast, the class of novel energetic materials we are investigating achieve an unprecedented enhancement in energy density by replacing weak intermolecular interactions with highly energetic covalent bonds. These novel materials, known as extended solids, represent the analog of infinitely large, energetic molecules. We have pursued experiments aimed at the synthesis of extended solid versions of nitrogen and boron-hydride. It is our strong belief that we have successfully synthesized an extended solid HEDM, namely the high pressure conversion of molecular carbon monoxide (CO) to a polymeric form. This novel polymer is recoverable at ambient conditions. In order to better understand and evaluate these new materials, we have been developing enhanced material property characterization tools, with particular focus on energetic content measurements. Ultimately, synthesis of bulk quantity samples will be required for conventional performance tests and large-scale production. To address this need, we have pursued the development of large volume press techniques.

Introduction

The need for conventional weapons incorporating maximum performance, effectiveness, and efficiency continues within the context of an increasingly budget-limited political environment [1]. A key avenue for enhancing conventional weapons is the development and utilization of high energy density materials. Energetic materials that exhibit a reduction in weight or volume will enable new capabilities in munitions, delivery systems, and other applications. Calculations performed at Lawrence Livermore National Laboratory (LLNL) predict the existence of materials with dramatically enhanced energy densities (E/V) of about three times that of HMX [2]. These novel materials constitute a new class of materials, largely unexplored, that can be synthesized using high pressure methodologies available at LLNL. These new phases represent normally gaseous systems that have been transformed into fully interconnected, covalently bonded, three-dimensional solids.

These extended solids are predicted to be recoverable at ambient conditions [3]. The goal of our project is to identify and to synthesize such novel materials, characterize their properties, and investigate technologically viable pathways for bulk characterization and synthesis.

Conventional explosives and propellants store energy in covalent bonds within the constituent molecules. The most energetic materials are, therefore, derived from first and second row elements, which characteristically have the strongest covalent bonds, such as H, B, C, N, and O. Weak van der Waals interactions, which play no role in energy storage, cause these molecules to condense into liquids or solids; these energetic materials are characterized by relatively large equilibrium volumes. In contrast, the new HEDMs proposed here eliminate the weak, external van der Waals bonds and replace them with strong, energetic, covalent bonds, as illustrated in Fig. 1. The elimination of weak bonds leads to new solid phases of matter that are three-dimensionally bonded networks [4] with significantly smaller equilibrium volumes and enhanced energy densities. Theoretical calculations for such candidate systems have been performed. Examples include a polymeric form of nitrogen [2,5,6]; an aluminum-like, body-centered tetragonal (bct) phase of boron [7], a distorted tetrahedrally coordinated form of carbon (bc8 C) [8,9] and the long-sought monatomic phase of hydrogen [10]. Calculated stored energy densities are 34, 26, and 21 kJ/cm³ for the nitrogen, boron, and carbon phases, respectively, in contrast to 12 kJ/cm³ for HMX. Though the energy per bond is approximately the same as in conventional energetic materials, the novel extended solids contain dramatically more energy per volume. Conventional chemical or non-equilibrium techniques are capable of generating energetic species in metastable states—configurations that are energetically unfavorable but nevertheless stable—because of kinetic barriers imposed by large activation energies. The metastability of the proposed novel materials also relies on the expected existence of large activation energy barriers, some which have been calculated [2,3]. The theoretical basis for the existence of extended solid HEDMs is well founded [11], and suggests experimentally accessible synthesis conditions. These quantum mechanical calculations based on the local-density functional approximation are in remarkable agreement with experimentally observed phase transitions. For example, in the group III, IV, and V elements, there are approximately 44 experimentally observed solid phases [12]. More than half of these phases have been investigated theoretically with almost perfect agreement with regard to phase identification [12]. Such a track record for the theory lends a high level of confidence that the predicted extended solids indeed can be synthesized at high pressures. Experimentally observed trends in the behavior of the elements also support the idea that the desired new phases should be thermodynamically stable at high pressures [13]. Therefore, the natural synthesis route is to apply sufficiently high pressures and high temperatures to induce the desired transformation, pressure quench, and recover the energetic phase at ambient conditions. The pressure-temperature (PT) conditions required to induce these transformations are well within the experimentally accessible range.

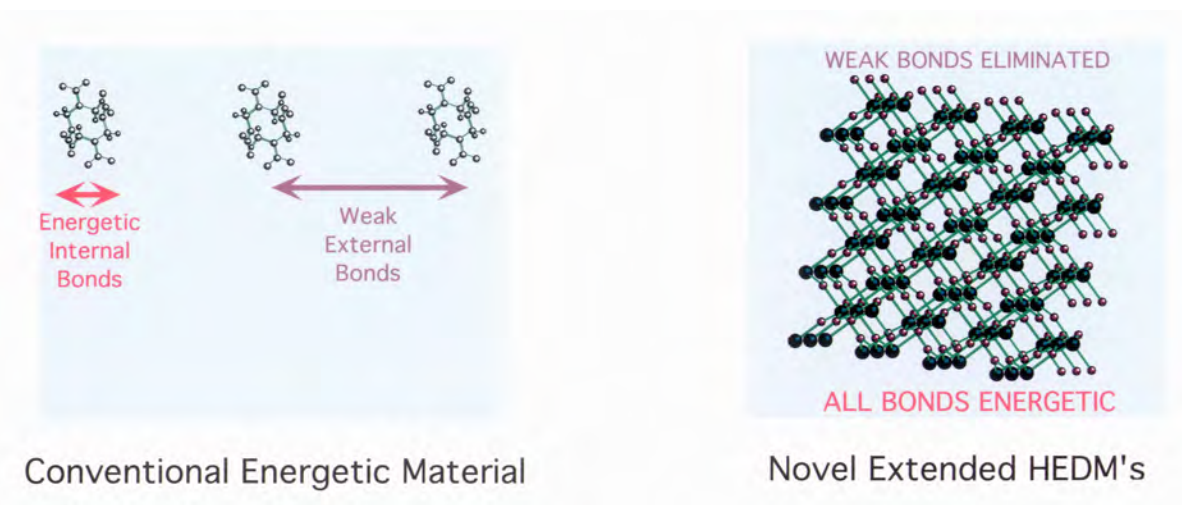


Figure 1. Concept of an extended solid HEDM. Conventional energetic systems store energy *within* molecules. The proposed novel HEDMs eliminate weak intermolecular bonds and replace them with energetic covalent bonds. Thus, dramatically higher energy per unit volume is achieved.

Our success at synthesizing a CO-derived extended solid [14] led us to expand the scope of our experimental work beyond proof-of-existence synthesis to include a strong emphasis on implementing energetic content methods and bulk quantity synthesis methodologies. In this report, we present our continued synthesis studies as well as development of synthesis and bulk quantity characterization tools. Although the size of our current samples places particularly severe requirements upon the characterization techniques, these challenges have been largely overcome.

Until now, our effort has concentrated on proof-of-principle studies primarily utilizing diamond anvil cell (DAC) techniques, which are perfectly suited for rapid, scientific studies at high pressures and temperatures. However, the samples typically synthesized in a DAC are small, with masses on the order of micrograms. While spectroscopic measurements are well suited to characterize sub-microgram samples, many important conventional analytical techniques of interest require larger quantities of material. We have sought to measure one key property, the energy content of the candidate CO-derived HEDM. We describe preliminary measurements using microcalorimetric techniques developed to accommodate a small DAC sample. The progress we have made in developing large volume press (LVP) synthesis capabilities is also discussed.

Experimental Techniques

High pressure research and technology have advanced dramatically in the last two decades. These advances are in large part due to the advent and continued development of the DAC. It is now possible for scientists to vary the thermodynamic variable, pressure, in a fashion similar to the routine manipulation of temperature. This new frontier of pressure and temperature has and will certainly continue to lead to discoveries of new materials and

phenomena [15,16]. In the area of material synthesis, this largely unexplored capability is predicted to lead to a broad range of radically new materials, including dramatically enhanced energetic solids.

The DAC serves as a near ideal instrument for pressurizing and probing materials at ultra-high pressures. The DAC operates on the principle of applying a moderate force over a large area and concentrating it to a small area, thus generating exceedingly high pressures of the same magnitude as those at the center of the earth, ~ 3 Mbars. The anvil material is diamond, the hardest substance known, used as a pair in an opposing geometry to pressurize samples between the two tips (Fig. 2a). For soft samples, such as those studied here, a gasket is used to contain the sample between the anvils. We are fortunate that diamonds are transparent over a wide range of the electromagnetic spectrum, permitting powerful *in situ* characterizations of materials using visible, infrared, or x-ray spectroscopy. Combined with laser heating techniques, it is possible to reach temperatures of approximately 6000 K at these pressures [17]. We have a well-established competency in high-pressure DAC methodologies at LLNL. Experimental capabilities include visible and infrared absorption, Raman scattering, photoluminescence, x-ray determinations, and cryogenic and laser heating techniques, all of which are useful in phase characterizations (Fig. 2) [14,18,19].

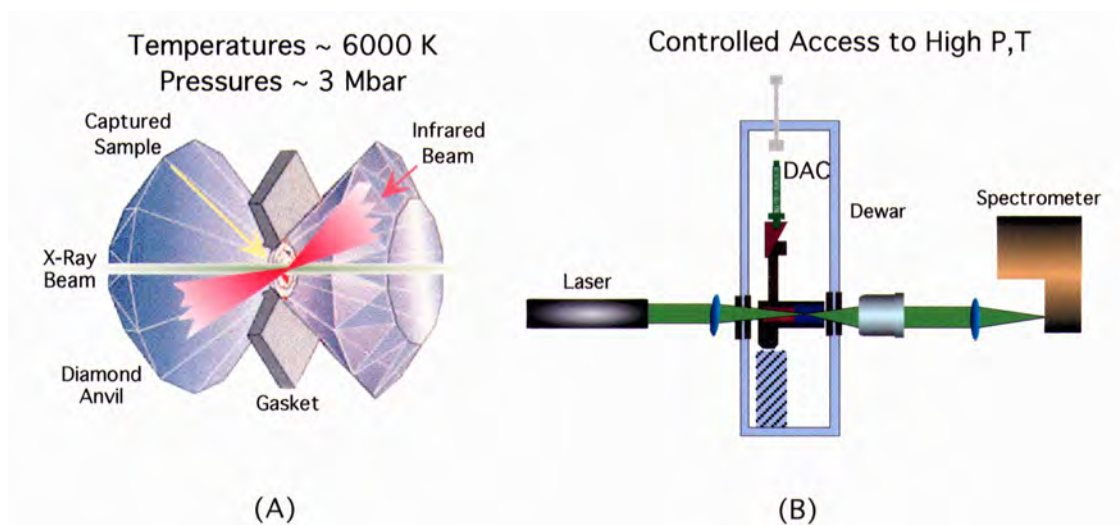


Figure 2. *In situ* high pressure experiments. The concept of a diamond anvil cell illustrated in (a). Force concentrated by small tips generates pressures of over 3 Mbars. Gasket confines soft samples under pressure (yellow chamber). Samples are studied *in situ* through a combination of cryogenic, resistive heating, x-ray, and laser heating techniques. Access to temperatures from 2–6000 K.

Experimentally, high pressures have been observed to induce tremendous changes in material properties, specifically crystalline states, electronic structure, and bonding characteristics. Because large activation energy barriers must be overcome in the synthesis of the extended solids at high pressures, heating is crucial to coaxing the strong chemical bonds into rearranging. We now have access to several methodologies for accomplishing the heating using conventional resistive and laser heating techniques. In particular, we have both YAG and CO₂ infrared laser systems that allow important studies of phase transformations.

In this reporting period, we established a pulsed Nd:YAG laser facility, including both the laser system and high power steering and focusing optics. This system is capable of delivering up to 1.2 J of energy focused down to a ~100- μm spot in a 10-ns pulse, or equivalently delivering a peak power of 100 MW. This formidable capability greatly extends our ability to heat materials and overcome kinetically impeded transitions.

Results

In addition to investigating the synthesis of new extended solid HEDMs, we made a strong effort to extend our material property characterization tools beyond spectroscopic probes; in particular, to determine energetic content. This was a two-pronged effort to develop (1) instrumentation and techniques suited to small, microgram-sized DAC samples (~1 μg) and (2) large volume press capability to enable synthesis of bulk quantities. These parallel efforts have both progressed successfully, and the results are described below.

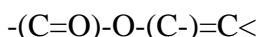
Extended Solid HEDMs—Results

We continued proof-of-existence experiments in nitrogen-rich and hydrogen-rich systems. We established the viability of the high pressure synthesis technique by synthesizing and then completing a spectroscopic analysis of a CO-derived extended solid [14]. Capitalizing on this success, we proceeded to other potential HEDM systems.

Carbon Monoxide

A brief summary of our continuing work on the characterization of the CO-derived extended solid follows. Carbon monoxide is one of the most fundamental heteronuclear molecules. As in most molecular systems, solid CO is characterized by a strong intramolecular bond and weak intermolecular van der Waals links between the CO molecules, leading to large equilibrium volumes for the molecular phases. At pressures above about 50 kbar, CO can be transformed by a photoreaction to a dark red solid that can be recovered at ambient conditions [14,24]. Spectroscopic measurements indicate that the dark red substance has lost its diatomic molecular character and is believed to be a polymer, though its exact nature is unknown [14]. This type of transformation is expected to be hampered by large activation energy barriers that can be overcome by the application of high pressures and high temperatures. We performed a wide range of optical investigations of the red high-pressure CO-derived solid, seeking to understand the character of this material (Fig. 3).

The optical measurements allowed us to probe the various characteristics of the high-pressure transformed sample. We have inferred that the sample is a heterogeneous material. Our measurements indicate that the transformed system is a mixture of graphitic-like carbon, carbon dioxide, and an extended solid. Based on these spectroscopic measurements, we propose that the extended solid is a network of C_3O_2 vinyl-ester-like monomer units:



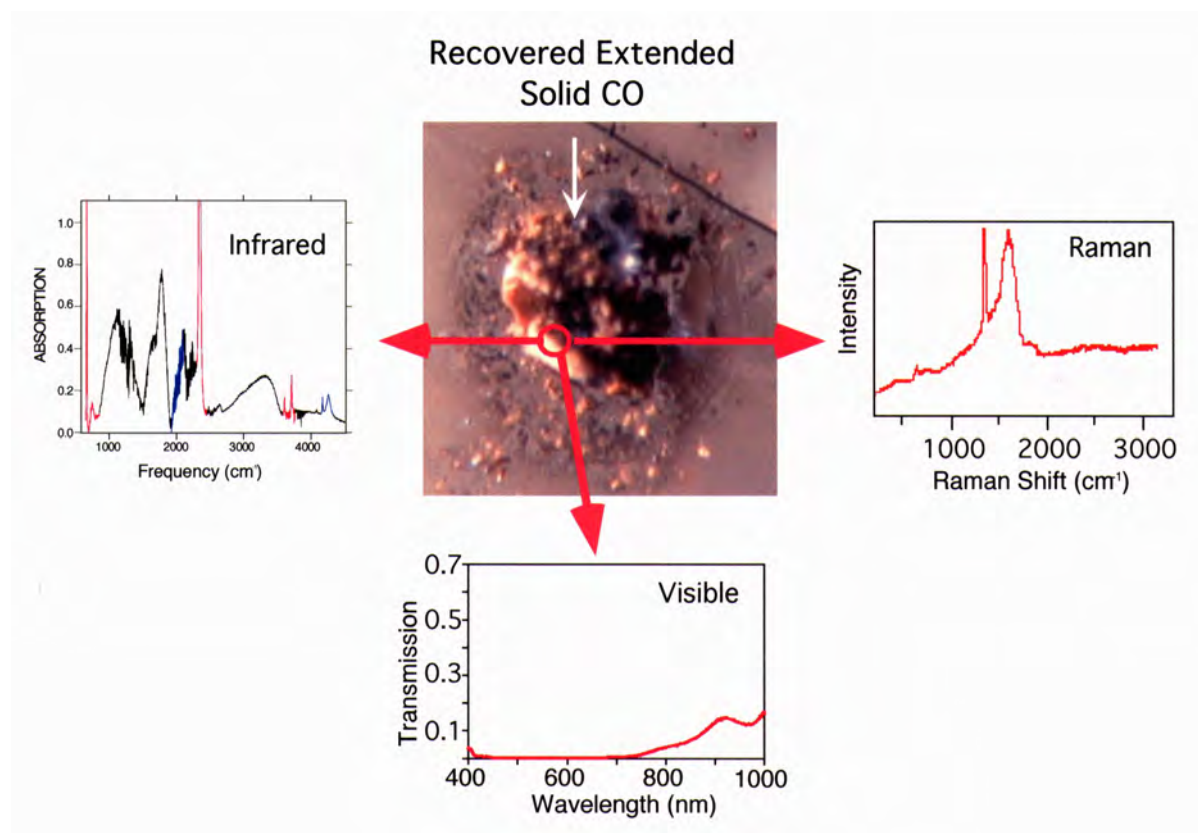


Figure 3. Recovered extended solid carbon monoxide. Extensive optical characterization has been performed.

One of our principal activities in the past reporting period was the measurement of the energetic content of the CO-derived extended solid. This proved to be an extremely challenging task, which we discuss in detail in a later section.

Boron Hydride

Initial studies of hydrogen were pursued in order to establish necessary instrumentation and baseline data for synthesizing and studying boron hydride extended solids. Theoretical studies of boron trihydride, BH_3 , indicate that an extended solid phase, stable at high pressures and possibly recoverable, stores 2.6 times more hydrogen per unit volume than cryogenic liquid H_2 itself [7,20].

In order to pursue this synthesis project, we established the necessary experimental infrastructure (e.g., cryogenic loading facilities) and started baseline measurements on pure hydrogen. The general synthesis approach is to react a sample of elemental boron or a boron hydride intermediary in the presence of hydrogen. Thus, knowledge of the properties of molecular hydrogen will be important in discerning the behavior of the boron hydride extended solid in both the extended solid synthesis reaction and ambient pressure recovery (Fig. 4). Our measurements of the high-pressure behavior of hydrogen include equation-of-state and dielectric properties [21], shown in Fig. 5.

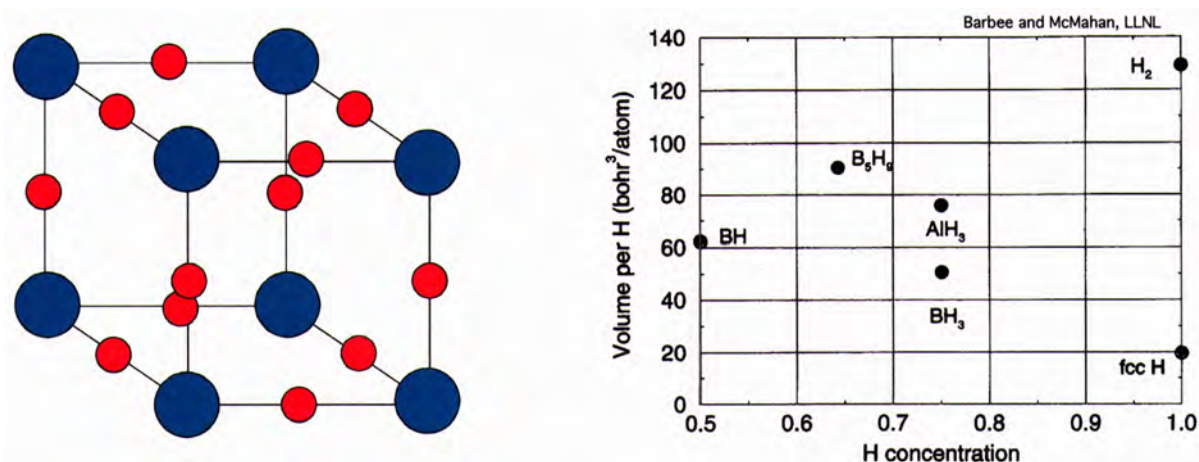


Figure 4. Structure of extended solid BH_3 and a comparison of the volume occupied by hydrogen atoms in select compounds.

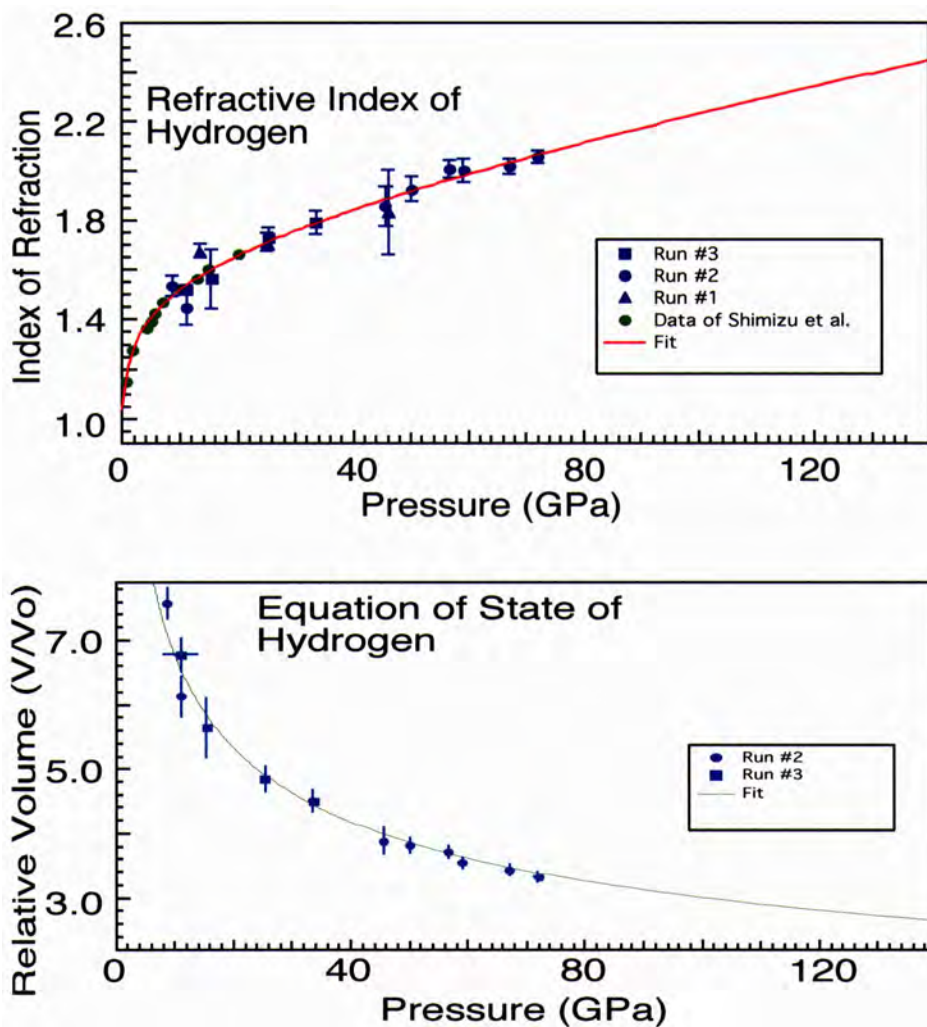


Figure 5. Baseline measurements of the properties of hydrogen. Hydrogen is one of the reactants in the synthesis of the proposed HEDM BH_3 . Thus hydrogen's properties are important in order to refine possible synthesis routes.

Nitrogen-rich Compounds

We also targeted the synthesis of nitrogen-rich energetic materials. In an attempt to circumvent the difficulty of breaking the bond in molecular nitrogen, we used energetic nitrogen-rich materials as precursors for our novel HEDM synthesis experiments. These “dirty” nitrogen systems do not have the strong nitrogen triple bond, and we expect that modifying their bonding character may be easier than for pure molecular nitrogen. We studied bond changes in some of these systems with increasing pressure and are systematically investigating the changes that occur when they transform at high pressures and temperatures. The ability to react these materials at high pressures and temperatures is very encouraging because the most difficult issue in transforming nitrogen at high pressures and temperatures has been modifying the exceedingly strong bond of the nitrogen molecule. The ultimate goal of these experiments is to create a metastable product that can be recovered at ambient conditions.

Enhanced Characterization Developments

The need for enhanced characterization techniques and synthesis of bulk quantities of sample is critical to the development of this program. The DAC has been demonstrated as an excellent proof-of-existence tool, specifically in the case of the CO-derived extended solid. However, the microscopic nature of this very example ($\sim 10^{-7}$ cc or $\sim 10^{14}$ atoms) has brought to the fore the need for enhanced characterization tools and ultimately bulk sample synthesis capabilities. A typical DAC sample is mere micrograms of material. This limitation severely strains conventional techniques, necessitating the development of novel characterization techniques. Even with the successes we have had at making measurements of microgram quantities of material, performance tests (e.g., detonation velocity) will require bulk samples. We are actively addressing these needs by developing novel measurement techniques and pushing existing technologies to the limits of their sensitivity. We are also developing LVP capabilities that will ultimately address the need for bulk quantities of extended solid energetic materials.

Energetic Content

A property of key importance for any novel HEDM is its energy content. Conventional energetic content measurements are made using a detonation calorimeter [22]. Such a measurement typically requires tens of grams of material. Because this quantity is several orders of magnitude beyond our current synthesis capability, we have been developing and pursuing alternate approaches.

We have made significant investments of effort in developing mass and density measurement diagnostics. The parameters necessary to determine the energetic content are the amount of energy evolved and the quantity of material. To address the sample quantity issue, we acquired a microbalance with a precision of 0.1 μg and a capacity of grams. We also obtained access to the x-ray diffraction beam at the Stanford Synchrotron Radiation Laboratory. These capabilities allow us to determine both the density and mass of our microgram-sized DAC samples.

In collaboration with Prof. Frances Hellman at UC San Diego, we started the development of a microcalorimeter that is fabricated using semiconductor technology and photolithography techniques at UC Berkeley [23]. A picture of one of these devices is shown in Fig. 6. The sample to be measured is placed on the SiN membrane of a device. Two devices, with and without a sample, are then simultaneously raised in temperature in a controlled environment chamber. When the sample releases its stored energy, the SiN membrane upon which it rests rises in temperature dramatically because of the membrane's small heat capacity. Therefore, the two thermometers, one on the membrane and the other on the Si substrate, will read very different temperatures. With appropriate calibrations, the energy content of the material being studied can be evaluated. The devices are remarkably robust and can operate over a temperature range of 1.5 to 1000 K [23]. The sensitivity has been measured to be 4×10^{-6} J/K, which is estimated to be adequate to measure the larger DAC samples.

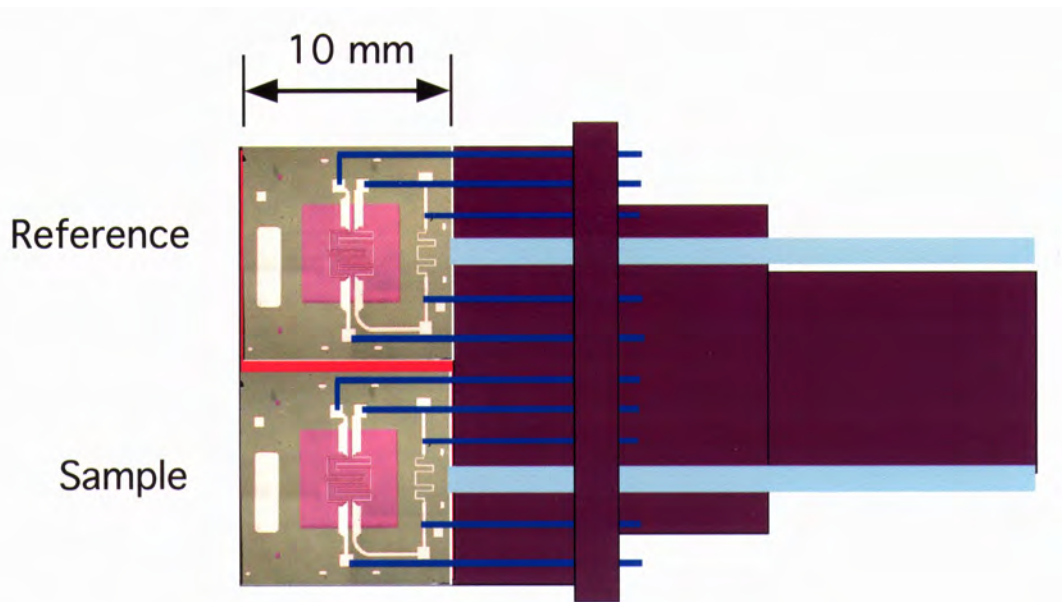


Figure 6. Microfabricated thin film microcalorimeter. State-of-the-art in sensitivity is needed to obtain meaningful energetic content measurements from diamond anvil cell samples. Devices developed through a collaboration with Frances Hellman, UC San Diego.

Having demonstrated the feasibility of the thin film microcalorimeter technique, we are now aiming to couple our samples to these devices. Remaining technical issues include fabricating metal foils on the devices to fold the sample, and handling issues to address the delicate nature of these devices.

Finally, we are pursuing two techniques that are based on standard differential scanning calorimetry. In the first approach, we have simply been probing the ultimate sensitivity limits of a standard, commercially available, differential scanning calorimeter. Using known energetic materials, we have been able to detect heat of detonation exotherms from quantities as small as 6 μ g. While this is very encouraging, the importance of maintaining a pristine work environment is critical because a contaminant such as a piece of

dust can alter the mass measurement. A modification of this technique was developed at Los Alamos National Laboratory by Dr. Joe Martin. The HEDM energy release is initiated by a short-duration laser pulse rather than by slowly raising the temperature as in the previously described technique. If the sample couples to the initiating laser pulse, this technique achieves immediate release of the entire energetic content. Thus, the sensitivity requirements on the DSC instrument are not as severe as in the standard operating scenario, and extremely accurate baseline determinations are not necessary. However, this technique does not yield information on kinetic issues, such as the rate of energy release and the decomposition temperature. These commercial devices are ultimately less sensitive than the thin film microcalorimeter; however, they have the advantage of being readily available.

Bulk Quantity Synthesis

The need for generating larger samples is clear. Bulk quantities of sample are absolutely necessary for conventional characterization of the recovered novel HEDMs (e.g., detonation velocity, initiation sensitivity, etc.). We have engaged in the development of large volume press technologies for generating high pressures. LVP technologies are very mature and are used in the synthesis of over 250 metric tons of industrial-grade diamond each year. Concerns include simplicity of operation in a cryogenic environment, cost, availability, and maximum attainable pressures. Before making a commitment to a specific technological implementation, we are conducting experiments using a Bridgeman-type, large volume press at UCLA in collaboration with Prof. Richard Kaner (Fig. 7). The aims are two-fold: (1) refine the LVP technique in its application to loading condensed gases, and (2) explore alternate synthesis pathways that optimize the ease of synthesis for the HEDM materials of interest.

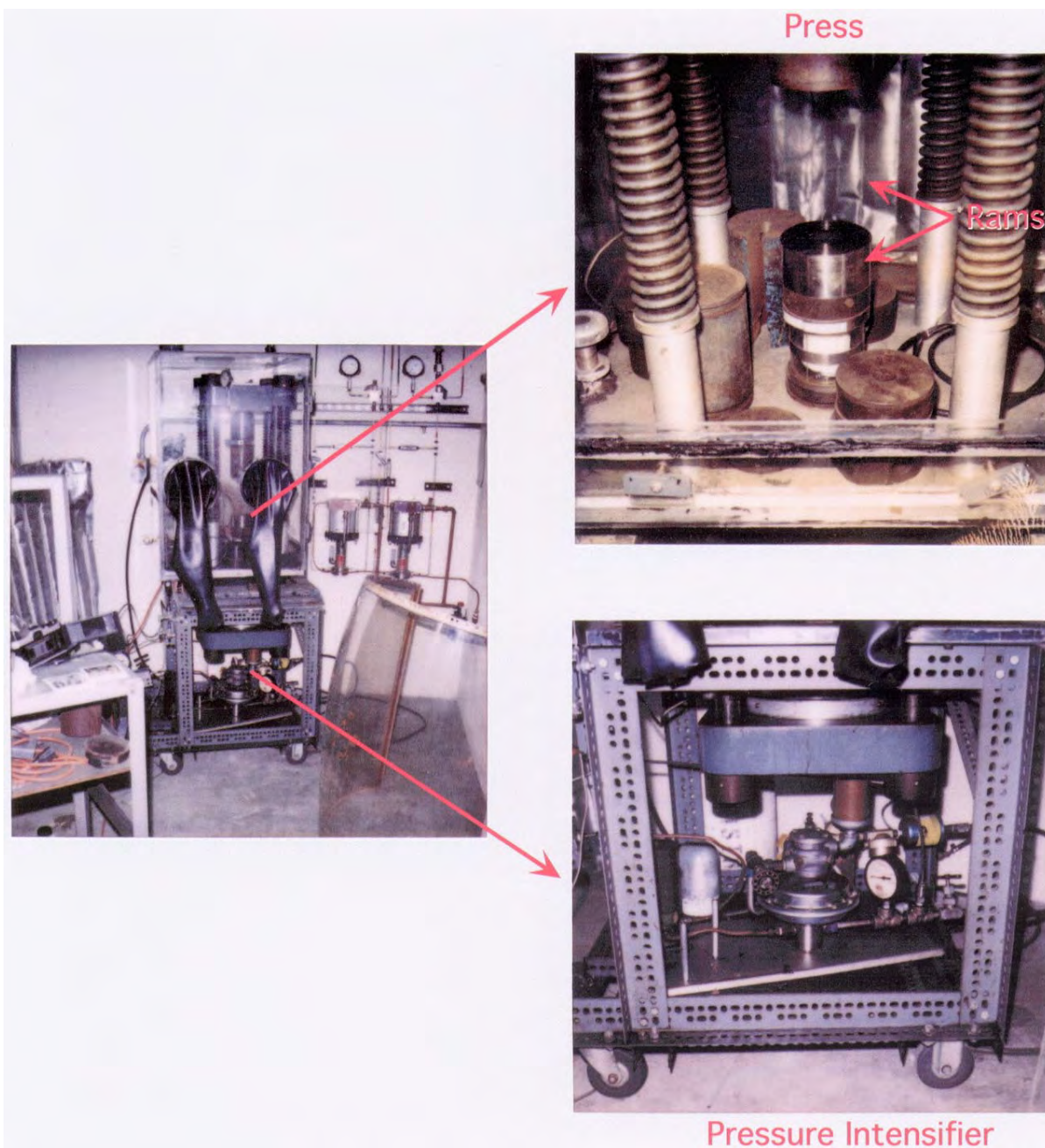


Figure 7. Large Volume Press (LVP at UCLA). Samples can be approximately 1 cm³ at pressures up to 300 kbar, several orders of magnitude larger than DAC specimens.

Conclusion/Summary

The focus of this work has been to synthesize and characterize materials of a new class of HEDMs with an energy density up to 300% that of HMX. This year, we continued studying the CO-derived extended solid we synthesized previously, and began attempting the synthesis of other potential extended solid HEDMs.

We also devoted efforts to develop diagnostics and bulk synthesis capabilities attuned to measuring performance characteristics of the extended solid HEDMs. The techniques have demonstrated the sensitivity to make meaningful measurements of the quantities of material that we are currently synthesizing. In the near term, we expect to be able to apply these techniques to our synthesis products to obtain heat-of-detonation measurements. Additional diagnostics are being developed to measure energetic content of the $\int PdV$ work contained in these materials. Our continued efforts in large volume press experiments are crucial to the ultimate exploration of bulk production of these new materials.

Our experimental results demonstrate significant progress in synthesizing new extended solid HEDMs and evaluating their performance characteristics. The synthesis technique of hot pressing using a DAC has been definitively demonstrated and applied to several promising extended solid HEDM candidate systems. The resultant novel materials still require additional characterization and evaluation, particularly in regard to their energetic content. We are confident that our continued studies and characterizations will firmly establish the existence of this new class of HEDMs, and provide firm evaluations of their viability as the next generation of high performance explosives.

References

1. Naval Warfare Innovation Concept Team Reports: Chief of Naval Operations, Strategic Studies Group XVI, (Naval War College, Newport, RI, June 1997).
2. C. Mailhot, L. H. Yang, and A. K. McMahan, *Phys. Rev. B* **46**, 14419 (1992).
3. T. W. Barbee III, *Phys. Rev. B* **48** 9327 (1993).
4. F. J. DiSalvo, *Science* **247**, 649 (1990).
5. A. K. McMahan and R. LeSar, *Phys. Rev. Lett.* **54**, 1929 (1985).
6. R. M. Martin and R. J. Needs, *Phys. Rev. B* **34**, 5082 (1986).
7. C. Mailhot, J. B. Grant and A. K. McMahan, *Phys. Rev. B* **42**, 9033 (1990).
8. C. Mailhot and A. K. McMahan, *Phys. Rev. B* **44**, 11578 (1991).
9. D. B. Boercker, *Phys. Rev. B* **44**, 11592 (1991).
10. I. F. Silvera, in *Simple Molecular Systems at Very High Density*, Ed., A. Polian, P. Loubeyre, and N. Boccara (Plenum, New York, 1989).
11. G. P. Srivastava and D. Weaire, *Advances in Physics* **36**, 463 (1987).
12. D. A. Young, *Phase Diagrams of the Elements* (University of California Press, Berkeley, 1991).
13. A. K. McMahan, *Physica* **139&140B**, 31 (1986).

14. M. J. Lipp, W. J. Evans, V. G. Baonza, and H. Lorenzana, *J. Low Temp. Phys.*, **111**, 247 (1998).
15. R. J. Hemley and N. W. Ashcroft, *Physics Today*, **51**, 26 (1998).
16. C.-M. Sung, *High Temperatures - High Pressures*, **29**, 253 (1997).
17. C. S. Yoo, J. Akella, and C. Ruddle, *EOS Trans. Amer. Geophys. Union* **64**, (1992).
18. H. E. Lorenzana, J. E. Klepeis, M. J. Lipp, W. J. Evans, and H. B. Radousky, *Phys. Rev. B* **56**, 543(1997).
19. M. J. Lipp, V. Garcia-Baonza, W. J. Evans, H. E. Lorenzana, *Phys. Rev. B* **56**, 5978 (1997).
20. T. W. Barbee III, A. K. McMahan, J. E. Klepeis, M. van Schilfgaarde, *Phys. Rev. B* **56**, 5148 (1997).
21. W. J. Evans, I. F. Silvera, *Phys. Rev. B* **57**, 14105 (1997).
22. B. M. Dobratz, P. C. Crawford, *LLNL Explosives Handbook: Properties of Chemical Explosives and Explosive Simulants*, UCRL-52997-Chg.2, Lawrence Livermore National Laboratory, Livermore, CA.
23. D. W. Denlinger, E. N. Abarra, K. Allen, P.W. Rooney et al., *Rev. Sci. Instr* **65**, 946 (1994).
24. R. L. Mills, D. Schiferl, A. I. Katz, and B. W. Olinger, *J. Phys. (Paris) Colloq.* C-8, 187 (1984)

This page intentionally left blank

III. Life Cycle Technology Overview

The Life Cycle Technology section includes technology for destruction and demilitarization of munitions, Resource Recovery and Reuse (R³), and studies aimed at understanding how energetic materials are changing in the aging stockpile. Four programs were funded during FY98.

This was the final year for funding of the Molten Salt Destruction (MSD) project under the Joint DoD/DOE Program. MSD technology was evaluated at bench scale and demonstrated at pilot scale, and is now being transitioned to users. A pilot unit was built and tested at LLNL and subsequently shipped to Eglin Air Force Base. There it has been installed and will be used to further optimize and develop a feed system. A larger demonstration unit was built at LLNL for the Blue Grass Army Depot, and is currently being readied for operation. Another production unit is being designed for the Republic of Korea. These programs are directly funded by the U.S. Army. There are also ongoing discussions with an industrial partner to transition the MSD technology. This is a successful conclusion to a Joint DoD/DOE project—the fundamental work was performed and processes developed under the Joint Program, and the technology transitioned to the DoD sponsor and an industrial partner for further implementation.

The “Femtosecond Laser Cutting” project was initiated in FY98. This project broadens the technology mix we are developing to address the pressing requirements in a munition’s life cycle. These requirements include the need for processes that are safe, flexible, environmentally benign, and economical during the manufacturing, storage, and demilitarization of munitions. The femtosecond laser beam can cut through any material with near-zero heat transfer, minimal wastes, and without chemically altering the cut surfaces. Using this laser to cut explosives, explosives components, and munitions potentially translates to unprecedented safety, precision, and flexibility during the manufacturing, surveillance, and demilitarization process. The continuing work in the Femtosecond Laser Cutting project will focus on understanding the parameters of safe operation, optimizing laser operation for the various applications, and demonstrating its utility on actual munition systems.

The project for Resource Recovery and Reuse of Explosives by Conversion to Higher-Value Products focused on using Explosive D as a raw material for industrial processes to produce higher value products. Explosive D was successfully converted to picramide, an important industrial chemical, and to the insensitive explosive, TATB. Explosive D is particularly difficult to destroy by open burning/open detonation because it is not a particularly efficient explosive. As a result, significant quantities of uncombusted Explosive D residues contaminate open burning/open detonation sites causing potential environmental insults to soil and water.

In the past year, in the Direct Chemical Oxidization project, we developed and tested procedures, and documented the complete destruction of explosives residue on metal parts. This technology uses peroxydisulfate to completely convert toxic organic materials to carbon

dioxide and other nonhazardous materials. The resulting mineralized residue is not hazardous and may be disposed of as industrial waste. One of the major problems facing demilitarization sites is proving that metal scrap is explosives free and may be recycled. This technology was also successfully used to mineralize the hazardous components of pink water and red water, two EPA listed wastes.

Femtosecond Laser Cutting of Energetic Materials

Frank Roeske, Paul Banks, Rick Cross, Ron Lee, and Brent Stuart
Lawrence Livermore National Laboratory
(925) 422-1394
roeske1@llnl.gov

Ed Roos
Allied Signal, Inc., Kansas City, MO

Abstract

Using small-scale testing, we demonstrated that a high-power, femtosecond (fs) laser beam can cut explosive materials and explosives in contact with metal without transferring heat to the explosive. We have cut through samples where metal is in direct contact with explosive both from the metal side and the explosive side. These cuts showed no signs of heating or any reaction in the explosives. We have also successfully sectioned a detonator and have dissected other weapons components, such as a header and bridge wire, and detonator cable. In addition, we drilled holes of less than 50- μm diameter through centimeter-thick samples of high explosive. These tests demonstrate that the fs laser is an attractive tool for use in demilitarization operations. Attributes such as precision material removal rate and cutting without altering the morphology of the surface make this technique very useful for enhanced surveillance activities as well as explosive and component machining for the purpose of manufacturing novel new explosive components, such as detonators.

All of this initial demonstration work has been accomplished using an existing experimental fs laser located in a non-explosive area at LLNL. This location has severely limited what we can accomplish in terms of the amount and type of high explosive (HE) we can work with and the type of experiments we can carry out. To alleviate this problem, we initiated a program to build a femtosecond laser and laboratory in the explosive facility in Building 191 at LLNL. The laser will be portable so we can take advantage of the 10-kg firing tank already in existence in the building to cut much larger amounts of explosive and ordnance or ordnance mockups. We will be able to determine quantitatively important parameters involving cutting rates, limitation, and safety margins in this laboratory as well as demonstrating cutting operations on large-scale assemblies and components.

Introduction

To safely dispose of munitions containing high explosives and other hazardous materials, it is necessary to gain access to the interior of the munition so that the contents may be removed. A safe method is needed to cut open munition casings and components that are likely to be in contact or close proximity to HE or other energetic materials. Using conventional machining techniques, there may be a significant risk of an explosive reaction. Other techniques have been developed which may safely cut the explosive but produce an undesirable hazardous waste stream.

Ablation of energetic material by fs laser pulses is potentially an attractive alternative to conventional machining [1,2]. Absorption of these ultra-short laser pulses occurs on such a short time scale that the material is ablated with virtually no heat transfer to the surrounding material [3], resulting in a “cold” laser cutting process and, hence, a safe process. In contrast, laser cutting techniques that use laser pulses longer than ~10 ps first melt, then vaporize, the material with significant heat transfer to material outside of the cutting region. When cutting with laser pulses on the order of ~100–150 fs, multiphoton ionization and plasma formation occur on a time scale on the order of the lattice vibrational period of the explosive. Because this time is so short, energy cannot be effectively coupled into the lattice of the material and is carried away from the surface by hydrodynamic expansion and cooling of the plasma.

Each laser pulse removes only a few microns of material. For explosives, the resultant products are mostly carbon and benign gases. The laser footprint can be made very small, on the order of tens of microns, so that very little material is removed during the cut. This combination—mostly benign material and very little of it in the cutting by-products—makes the technique very clean relative to other methods used. The small laser footprint also makes it an attractive tool when precision cutting operations are needed.

The fs laser cutting process does not alter the morphology of the surface of the material. This attribute, along with the precision removal of material, makes this tool very valuable for use in surveillance studies of weapons and their components.

Summary of Work to Date

Work was begun in the latter part of FY97 with Department of Energy (DOE) funding. In FY98, DOE and the Department of Defense (DoD) Memorandum of Understanding (MOU) jointly funded work. To date, we do not have a femtosecond laser in our explosive facility, HEAF, and have done all work in a non-explosive work area in the laser laboratory in Building 298. A special Operational Safety Procedure was written to allow this work to proceed using a small firing chamber and explosive samples of less than 500 mg.

We have so far demonstrated the following:

(b)(3)

(b)(3)

Figures 1 and 2 show some examples of these accomplishments.

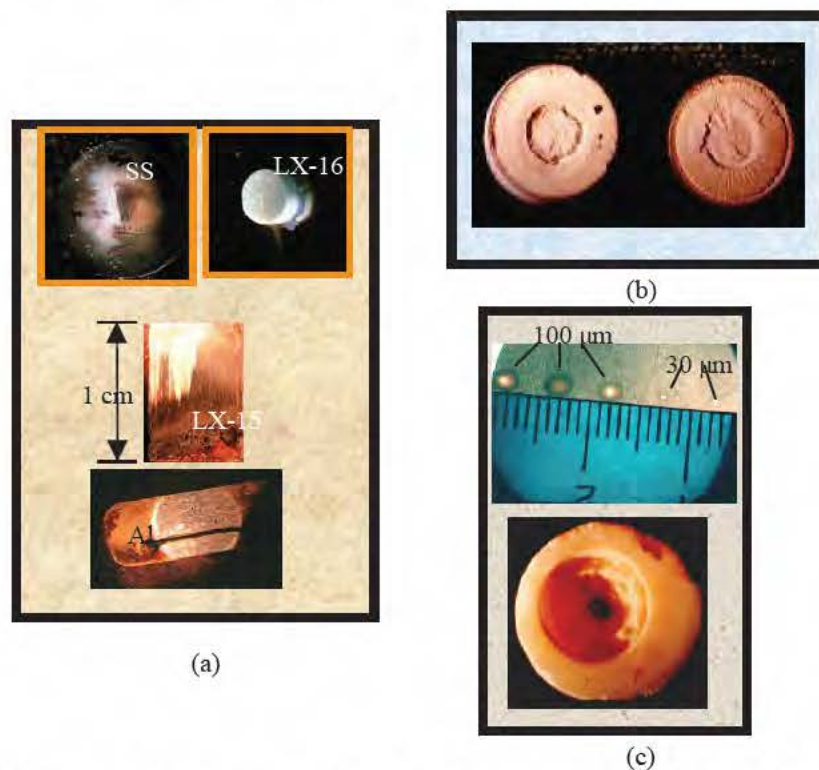


Figure 1. (a) Top: laser cut through 1.2 mm of stainless steel and 2 mm of LX-16. (a) Bottom: cut through 1 cm of LX-15 and 0.5 mm of aluminum; (b) Sectioned hemispherical detonator consisting of an Al shell, PBX-9407, and a PETN center; (c) Top: Several holes drilled through PBX-9407. (c) Bottom: a 3-mm-diameter cavity machined in TNT.

The cutting of metals and explosives combinations without any reaction taking place and the sectioning of the hemispherical detonator shows a great deal of promise for the fs laser cutting technique in the arena of demilitarization. Our demonstrations of sectioning detonator components and cables show the tremendous potential in the area of advanced surveillance. The machining and hole drilling demonstration opens the door for use of this technique in the development and experimental science involved in creating new and improved detonators and explosive related components. We have already put this technique to work in cutting a novel shaped piece of high-surface area PETN for use in the prototype demonstration of a potential new DOE detonator.

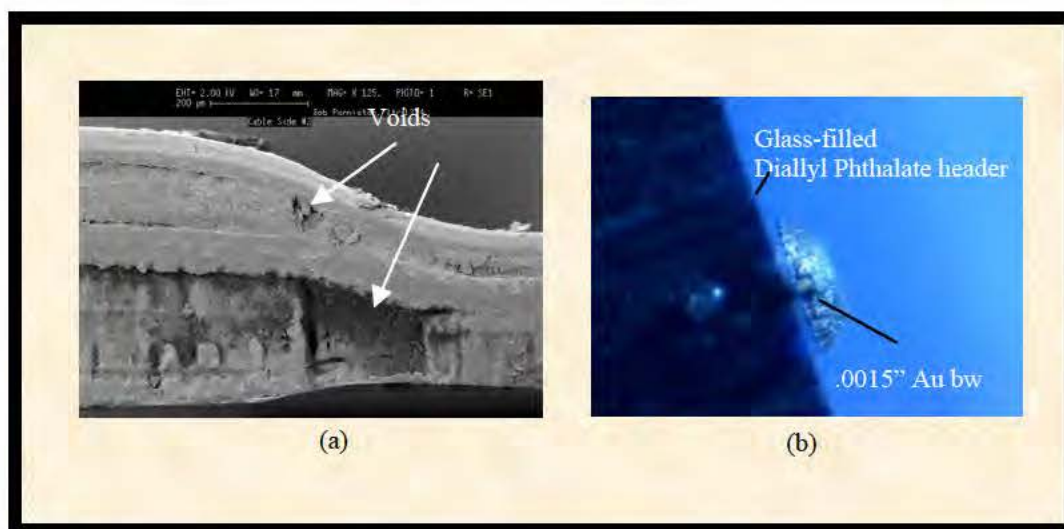


Figure 2. (a) Sectioning of a detonator cable shows voids. (b) Slicing a EBW header nicely shows a cross section of the 15-mil bridgewire.

Current Work

Funds received for FY99 from the DoD MOU and matching Advanced Design and Production Technologies (ADAPT) funding is earmarked for use in constructing a laser laboratory and a 4- to 6-W average power, fs laser in Building 191 at Livermore. The laser will be on a portable laser table so that it can be taken a short distance from the laser laboratory to the 10-kg spherical shot tank.

Having the laser in an explosive approved area will allow us to make many tests that were not possible to perform in Building 298. It is vital that we obtain quantitative data in the following areas:

- Establish optimum cutting parameters for HE and ordnance systems and components. This involves many small-scale and a few large-scale tests involving laser power, spot size, laser rep rate, focus, beam profile, etc.
- Establish machining rates for various materials and processes.

- Find safety limits for various explosives. These studies will investigate safely cutting explosives as a function of parameters such as power density, laser pulse length, materials being cut, chamber pressure, geometry, cutting thresholds, laser rep rate, etc.
- Establish size, material or geometry limits, if any.

The laser is currently being constructed in Building 298 (since we do not yet have the laser lab in Building 191) and is expected to be complete by July 1999. Figure 3 shows a cartoon representation of the laser and a picture of a similar laser that has been constructed for use at Y-12, Oak Ridge National Laboratory.

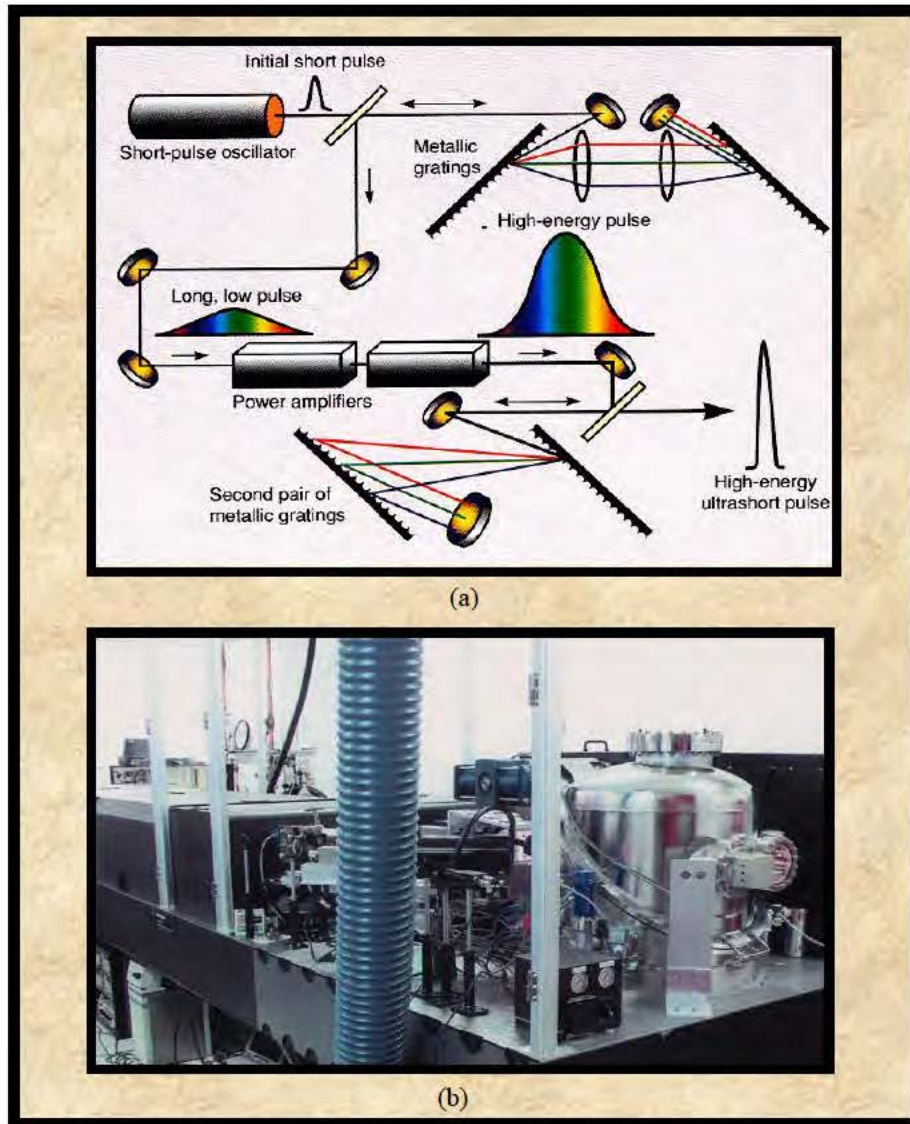


Figure 3. (a) Cartoon depicting the principles behind the high-powered, femtosecond laser and (b) a similar laser constructed to be used at Oak Ridge National Laboratory.

In parallel with the laser construction, a laboratory (Fig. 4, 1711 A) is being prepared in the explosive work area of Building 191. This laboratory will house the laser and associated support and diagnostic equipment necessary to run the laser and conduct experiments. An explosive work area (1711B) located adjacent to the lab will provide an efficient area for sample preparation and study after the cutting has taken place.

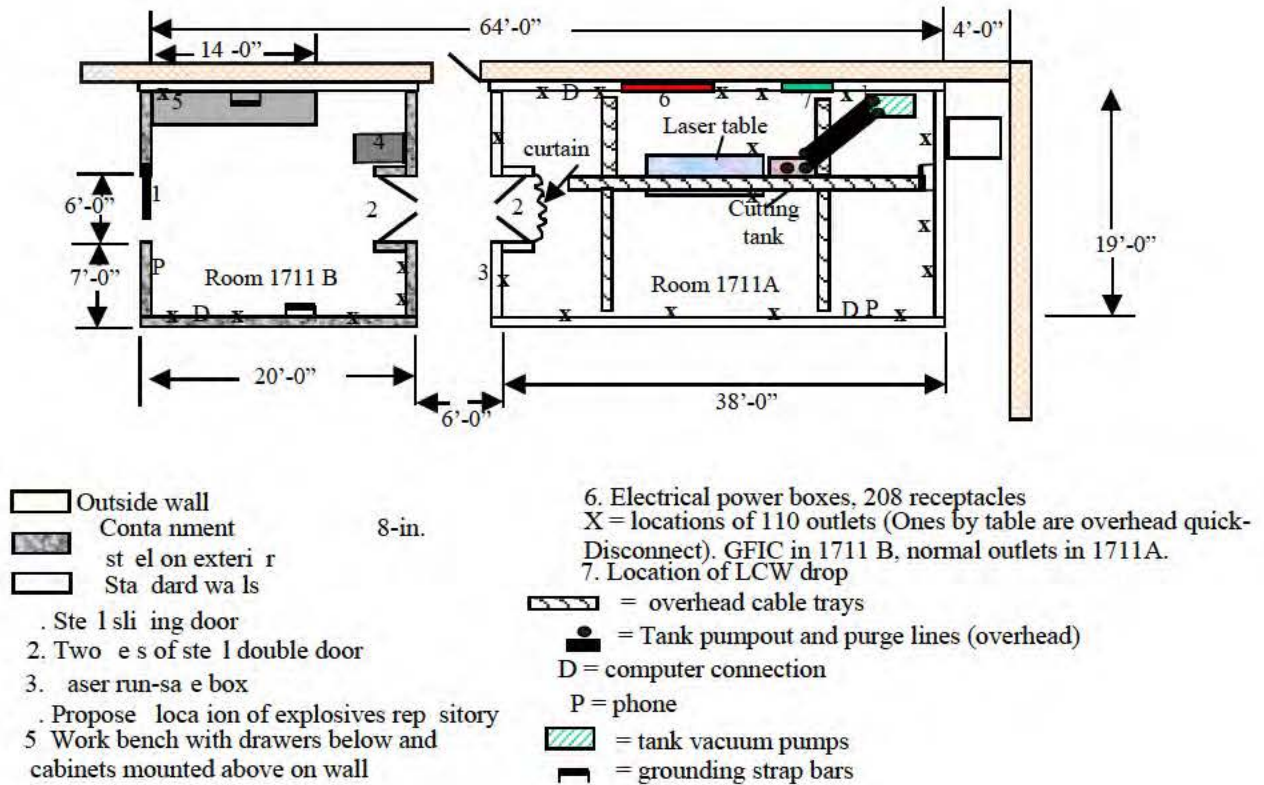


Figure 4. Femtosecond laser lab to be constructed in Building 191 in FY99.

Our Plant Engineering Department is currently preparing engineering drawings for construction of this laboratory. The laser laboratory is scheduled for completion in June of 1999.

The cutting chamber for the laser laboratory will be a modified existing tank shown in Fig. 5. This tank, when modified, will be rated at 5 grams of explosive while laser personnel work in the area. This improvement gives us 10 times the limits we were forced to work with in Building 298. In addition, the tank is much larger. It will allow us to cut more efficiently by installing the appropriate plume collection equipment in the tank, thus protecting our windows from attaining a coating of condensed material from the cutting process. We need to do some work to determine the optimum method to do this. We are currently considering apertures, magnets, electrostatic fields, differential pumping, or a combination of the above. The tank must be reconfigured, tested, and approved by the explosive safety team at HEAF.

Also shown in Fig. 5 is the 10-kg tank located about 50 meters from the femtosecond laser lab. This is where we intend to cut larger assemblies containing explosives up to 10 kg in weight.

The laser and laboratory construction is presently on schedule; we expect them to be completed so that we can have a functional laser laboratory by the end of FY99. Funding is very tight and we may not be able to complete the necessary modifications to the cutting tank this year without supplementary funds.

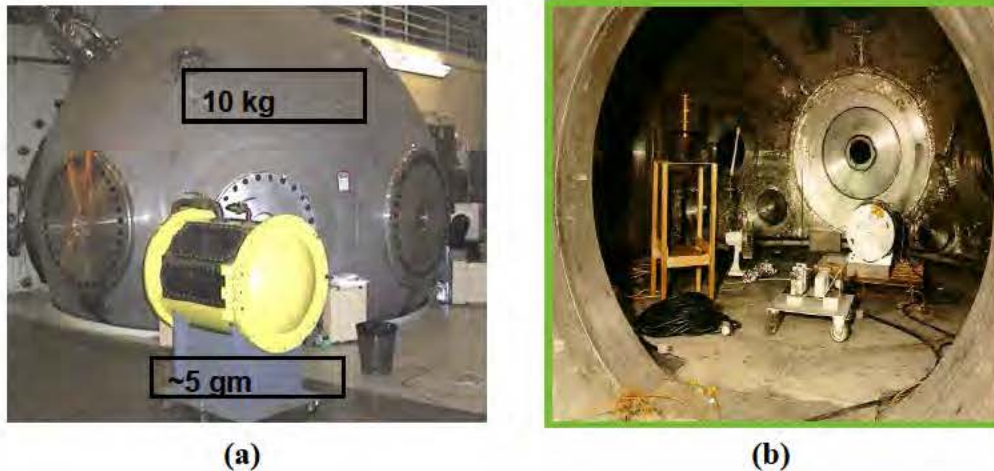


Figure 5. (a) Small-scale tests will be performed in the 5-g tank in the laser lab. Larger-scale experiments will be performed in the 10-kg tank. The 5-g tank is shown in front of the 10-kg tank here for reference. (b) The interior of the 10-kg tank allows installation of shrapnel shielding for tests on real munitions.

To use the 10-kg tank, we must convert it to a vacuum capability. Pump lines from a pump room to the tank are already in place. We are currently evaluating a pair of pumps previously used in LLNL's Magnetic Fusion Program for use as the pumps for this tank. This is being done with LLNL funds and, if the pumps will meet our criteria, will save a considerable amount of money in bringing the 10-kg tank up to our specifications.

Future Work

We will bring the 10-kg tank to vacuum capability and design a transport system to bring the laser beam into the tank and meet the explosive safety requirements. This work will continue next year with plans to have the capability to perform large-scale tests in the 10-kg tank by the start of the following year.

We are also to continue small-scale testing in Building 298 while our lab and laser are being constructed. These tests would consist of

- Engineering tests to determine the best system for beam transport and window protection for our 5-g laboratory chamber

- Cutting specified ordnance components as specified by the army (such as removing grenade fuses, for example)
- Small amount of work on surveillance projects as funds from those interested in such activities materialize.

Figure 6 summarizes the future plans over the next few years. In addition to the activities mentioned earlier in this report, we plan to initiate modeling studies for the interaction of the laser plasma with the HE. Because we have not been able to make any of our samples detonate to date, the modeling may become very important in calculating where safety limits actually fall and how far away from those limits our operating parameters lie.

Finally, when we thoroughly understand the cutting capabilities and have the safe, efficient cutting parameters mapped out, we intend the transfer this technology to DoD and DOE facilities interested in using this tool on a regular basis. Our laboratory will continue to serve as a test bed for those organizations to work out specific problems and new techniques before they are implemented in a production system.

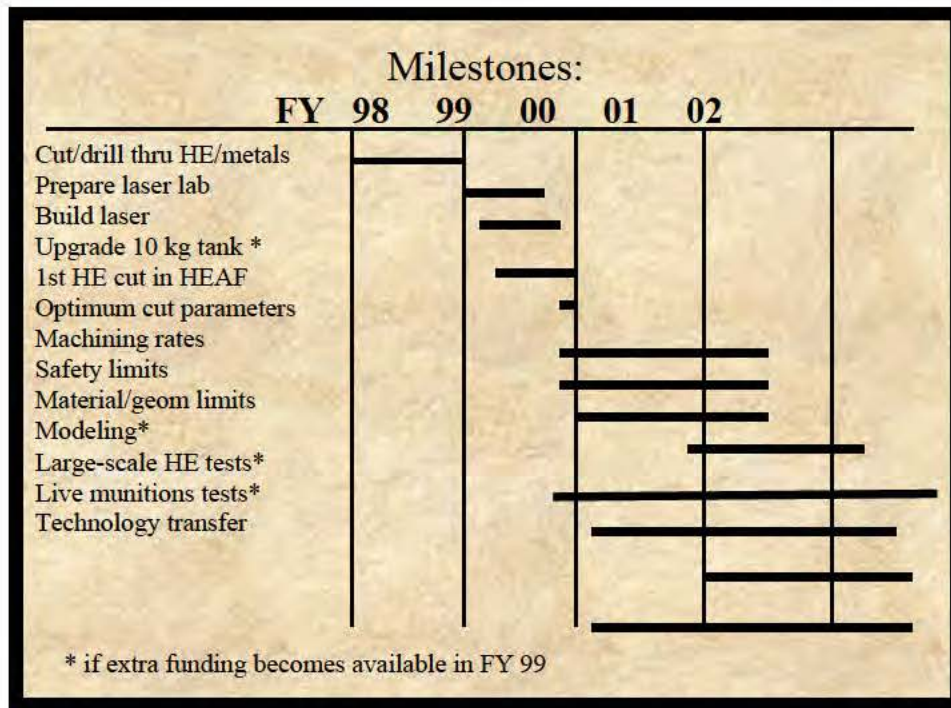


Figure 6. Future plans for femtosecond laser cutting.

Conclusions

We have shown that the fs laser is a viable tool for use in areas that are of importance to the DoD, such as demilitarization, surveillance, and the creation of new ordnance components. Femtosecond laser cutting is expected to be a technique that can be used to disassemble munitions that are difficult to disassemble by other means without safety concerns or the generation of an unacceptable waste stream. The clean, precision cut made by the fs laser makes it an attractive candidate for many surveillance operations. Finally, novel new shapes of explosives, which can be cut with relative ease with the femtosecond laser, will make possible the development of new weapons system components.

Our initial work had proven the viability of the ultra-short, high-powered laser-cutting technique. Now we are constructing a laboratory in an explosive work area where we can obtain good, quantitative data to optimize the cutting procedure while assuring that we are well within sensible safety margins. The new laser will be located near a 10-kg firing tank that will allow us to cut large HE assemblies and actual ordnance. Thus, the new laboratory will serve not only to develop the science of femtosecond cutting of explosives but also to serve as a test bed for future ideas in this area.

We have developed a workable plan to meet the goals outlined in this report and expect to have a workable system and the knowledge to transfer this technology to those facilities that have an interest in the production use of this technique.

References

1. F. Roeske, J. P. Armstrong, P. S. Banks, M. D. Feit, R. S. Lee, M. D. Perry, and B.C. Stuart, "Laser Cutting of Pressed Explosives," *Energetic Materials, Production, Processing and Characterization*, Germany: Fraunhofer-Institut fur Chemische Technologie, pp 104-1–104-14, 1998.
2. Franklin Roeske, Jr., P. S. Banks, J. P. Armstrong, M. D. Feit, R. S. Lee, M. D. Perry, and B. C. Stuart, "Laser Cutting of Pressed Explosives," *Proceedings of 1998 Life Cycles of Energetic Materials*, pp. 344-347, 1998.
3. B. C. Stuart, M. D. Feit, S. Herman, A. M. Rubenchik, B. W. Shore, and M. D. Perry, "Optical ablation by high-power short-pulse lasers," *J. of the Optical Society of America B*, pp. 459-468, 1996.

This page intentionally left blank

Characterization of NO_x Emission from Molten Salt Destruction of Explosives

Henrik Wallman, Martyn Adamson, Peter Hsu, César Pruneda, and Bruce Watkins
Lawrence Livermore National Laboratory
(925) 423-1522
wallman1@llnl.gov

Abstract

Pilot-plant runs have been conducted for the purpose of characterizing and mitigating NO_x emissions from the oxidation of explosives in an aerated molten salt bed. To allow experiments to be performed in facilities not approved to handle explosives, non-explosive surrogate feedstocks were used. These feedstocks contained nitrogen with different oxidation states.

The nitrogen-containing liquid feedstocks produced NO_x emissions in the primary offgas that were above EPA's new source performance standards. Hence, a DeNO_x unit is a necessary processing step for the destruction of many explosives. Interestingly, a nitrogen-containing solid material yielded much lower primary NO_x emissions than the other, liquid feedstocks. Some analysis of this difference is given in this report.

Introduction

The Lawrence Livermore National Laboratory is developing a molten salt destruction (MSD) process for the demilitarization of excess explosives such as TNT and Composition B (a mixture of TNT and RDX). The process is based on oxidation in a molten salt bed by means of injected air. The MSD process shown in Fig. 1 also represents the pilot plant used in this study. The figure includes the nominal feed rate and the associated mass balance for TNT as feedstock although the pilot plant runs so far have been limited to non-energetic feedstocks. In the plant, TNT will be converted to oxidation products that exit the process through the stack diluted by steam (from the slurry medium) and nitrogen from the feed air. The process is composed of three main units: the MSD bed nominally at 950°C for the decomposition of TNT, the Hot-Gas Filter nominally at 500°C for the collection of entrained bed particles, and the catalytic DeNO_x unit nominally at 300°C for the reduction of NO_x to molecular nitrogen by means of injected ammonia.

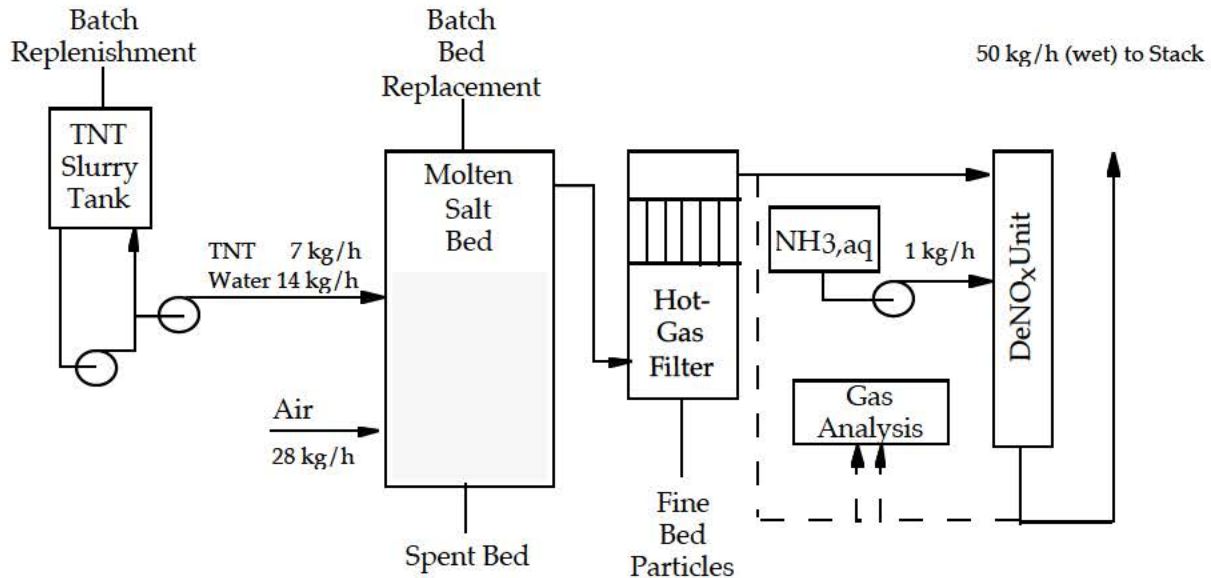


Figure 1. Molten salt process for the destruction of explosives.

The MSD bed is contained in a 1/2-in.-thick Inconel vessel provided with a proprietary feed injector for the slurry and air feeds. Electric heaters surrounding the vessel are used for startup and temperature control of the bed. The reactor vessel has auxiliary equipment for batch replacement of bed material. Inorganic contaminants in the feed alter the bed material slowly over time, which forces a bed replacement from time to time. The bed can deteriorate physically (increased viscosity, for example) from mineral components in the feed, as well as chemically from reactive compounds such as acid gases (e.g., HCl, HF, and SO₂). The initial molten salt bed is a mixture of Na₂CO₃ and K₂CO₃. This material reacts with acid gases and forms the corresponding neutral salt while releasing CO₂.

The Hot-Gas Filter consists of two ceramic filter units with automatic cleanup cycle equipment. The two units cycle between an on-line filtering mode and an off-line cleanup mode. The cleanup mode uses a high-pressure air pulse to dislodge the filter cake. The Hot-Gas Filter allows the DeNO_x unit to function better by removing traces of sodium/potassium carbonate dust from the offgas prior to entry into the DeNO_x unit.

The DeNO_x unit is an electrically heated vessel holding a packed bed of a noble-metal based catalyst. The vessel is provided with a port for introduction of gaseous ammonia into the gas stream. The rate of ammonia injection is based on the measured NH₃ concentration in the stack gas (maximum unreacted ammonia slip of 20 ppm).

This report describes experiments that have been performed in this pilot plant for the purpose of determining the NO_x emissions from molten salt oxidation of energetic materials containing high levels of nitrogen.

Results from MSD Pilot-plant Test Runs

The pilot-plant runs were conducted with the following nitrogen-containing feedstocks: pyridine, nitromethane, urea, and ABS plastic pellets. The first three were diluted by suitable solvents and fed as liquids while the plastic pellets were fed as dry solids (conveyed pneumatically by air). Total fuel feed to the pilot plant was around 2 kg/h and the excess air was around 30% in these runs. Temperature in the bed was 950°C. Each run lasted for several hours during which the offgas was monitored for O_2 , CO_2 , CO, NO_x and total hydrocarbon content. Constancy of the offgas concentrations implied steady-state conditions. The steady-state offgas concentrations were the primary results of this study.

NO_x Results

The measured NO_x gas concentrations in the four runs are assembled in Table 1. The primary NO_x concentration in the offgas from the MSD bed is given both in terms of the ppm measured and in terms of the conversion of feed nitrogen to NO_x . The final stackgas concentration (after the catalytic converter) is also reported in the table but in this case the conversion is based on the formation of N_2 relative to the NO_x fed to the converter. (This is the customary definition for catalytic converters).

Table 1. NO_x results in MSD pilot plant runs with different feedstocks.

Feedstock	NO_x After MSD Bed		NO_x After SCR Catalyst	
	ppm	Conversion of Fuel N to NO_x (%)	ppm	Conversion of Flue Gas NO_x to N_2 (%)
Pyridine in Toluene (3.5wt%N)	1800	44	70	96
Nitromethane in Glycol (2.3wt%N)	1990	34	40	98
Urea in Alcohol (1.6wt%N)	860	31	20	98
ABS Plastic Pellets (2.9wt%N)	310	5	SCR not in Service	

The main conclusion from the results in Table 1 is that the nitrogen contained in liquid MSD feed is converted to NO_x in the range of 31–44%. This conversion level is too high for direct discharge of the MSD offgas to the atmosphere. Hence, these results imply that a De NO_x process is required for explosives destruction in the molten salt bed. Interestingly, the amide-type nitrogen yields somewhat less NO_x than nitrogroup-type nitrogen, which in turn yields less than the aromatic ring-type nitrogen of pyridine. We speculate that urea in a primary decomposition step produces ammonia and similar compounds that react with secondary NO to form N_2 . A NO destruction path must also exist

for the nitromethane and pyridine cases because more than half of the total nitrogen in the feed is converted to molecular N_2 (small amounts of N_2O could be present, but this component was not measured in these runs).

Thermal NO_x (formed by oxidation of molecular N_2) is inferred to be a minor component of total NO_x . This has been shown by Adamson [1] by experiments with pure toluene yielding NO_x levels of about 100 ppm at conditions corresponding to the conditions used here.

NO_x conversion efficiency in the catalytic converter was found to be at least 95% or nearly two orders of magnitude. This is more than adequate because federal NO_x standards for the case at hand mandate a maximum NO_x concentration of about 400 ppm (based on 0.45 lb NO_x /million Btu in accordance with new source performance standards for boilers).

The run with plastic pellet feed produced very favorable NO_x results. In this run only 5% of the feed nitrogen was converted to NO_x (and by inference, 95% converted to N_2) in the molten salt bed. The interpretation is that the NO destruction pathway is more favorable in the case of this solid feed of 1- to 3-mm particles. Because the particles oxidize slowly, the steady-state bed concentration of plastic particles is high, and consequently there is a large carbonaceous surface present in the bed. Such a surface provides sites for NO reduction as shown by Wallman [2]. Hence, a De NO_x unit is not an absolute necessity with this particular feedstock.

Although TNT is a solid at room temperature, it behaves as a liquid because of its low melting point. Hence, the favorable result obtained with plastic pellets cannot be directly applied to TNT. However, Lacchia [3] has shown that TNT decomposition in molten salt beds leads to soot formation. These soot particles may provide reaction surfaces for the favorable NO reduction to occur, and consequently, TNT-based NO_x results may be significantly better than the nitromethane results in Table 1.

A process consequence of these NO_2 results is that a molten salt destruction process for explosives with high N content must include a De NO_x process so as to yield an acceptable stack gas emission level. The catalytic De NO_x process used in the pilot plant runs is well established commercial technology. Another option is to use the original thermal De NO_x process developed by Exxon in the 1970s [4]. This process, which uses ammonia reductant at a temperature of about 900°C with no catalyst, is more robust because catalyst deactivation is not an issue. As shown by Wallman [5], the thermal process works well with dilute aqueous ammonia, and a conversion efficiency of 80% can easily be obtained.

MSD Process Scale-Up

With the addition of a De NO_x unit, the overall MSD process is ready for validation with real explosive feedstock. Such a run will be conducted with TNT sludge in early 1999.

The concept of using the MSD process to treat explosives was initially developed under the DoD/DOE memorandum of understanding. Success in the program has resulted in continued research and emerging commercialization. Operating units are being installed at Eglin Air Force Base in Florida and at the Blue Grass Army Depot in Kentucky. An MSD plant is also included in the designs for a demil complex at a U.S. Army base in South Korea.

References

1. M. G. Adamson, P. C. Hsu, D. L. Hipple, K. G. Foster, R. W. Hopper, and T. D. Ford, "Organic Waste Processing Using Molten Salt Oxidation," *1998 Euchem Conference on Molten Salts*, Porquerolles, France, June 27–July 3, 1998. Also LLNL publication UCRL-JC-129946.
2. P. H. Wallman, R. C. J. Carlsson, and B. Leckner, "NO $_x$ Reduction in Pressurized Fluidized-Bed Combustion," *Proc., 1993 Internat. Conference on Fluidized Bed Combustion*, The American Soc. of Mech. Engineers, pp.789–794.
3. M. B. Lacchia and B. Shaw, "Decomposition of DNT in Molten Salt," *Proc. 15th Internat. Conference of Incineration and Thermal Treatment Technologies*, Savannah, GA, May 6–10, 1996.
4. K. Lyon, *Internat. J. Chem. Kinetics* **8**, pp. 315–319, 1976.
5. P. H. Wallman and R. C. J. Carlsson, "NO $_x$ Reduction by Ammonia," *Fuel* **72**, pp. 187–192, 1993.

This page intentionally left blank

Resource Recovery and Reuse (R³) of Explosives by Conversion to Higher Value Products

Alexander R. Mitchell
Lawrence Livermore National Laboratory
(925) 422-7994
mitchell4@llnl.gov

Abstract

Five million pounds of Explosive D (ammonium picrate) are available from demilitarization inventories for use in Resource Recovery and Reuse (R³) activities. Investigations on the direct conversion of Explosive D to picramide (2,4,6-trinitroaniline) are described. Studies leading to improved conversions of picramide to TATB (1,3,5-triamino-2,4,6-trinitrobenzene) using Vicarious Nucleophilic Substitution (VNS) chemistry are reported.

Introduction

The general objective of this project is to develop new and innovative solutions for the disposal of surplus energetic materials. Disposal through open burning/open detonation (OB/OD) is less attractive today due to environmental, cost and safety concerns. We are examining the use of military high explosives as raw materials for the production of higher value products useful in civilian and military applications [1,2]. Five million pounds of Explosive D (ammonium picrate), a surplus military explosive, have been mandated for disposal (demilitarization). The development of a safe and economic conversion of Explosive D to picramide will allow access to a variety of higher value products (Fig. 1) including TATB (DOE's benchmark insensitive main-charge explosive) [3,4].

Our specific goal is to couple the demilitarization of Explosive D to a cleaner, "greener" and cheaper production of TATB. The two-stage conversion of Explosive D to TATB that we are investigating is outlined in Fig. 2. Picramide is usually prepared by first reacting picric acid (2,4,6-trinitrophenol) with thionyl chloride to provide picryl chloride, which is then reacted with ammonia to provide picramide. The use of Explosive D in place of picric acid should also furnish picramide (Fig. 2). Unfortunately, this process is not environmentally friendly as the use of thionyl chloride produces sulfur dioxide and hydrogen chloride. The evaluation of direct pathways from Explosive D to picramide and advances in the production of TATB using VNS chemistry are described in subsequent sections of this report.

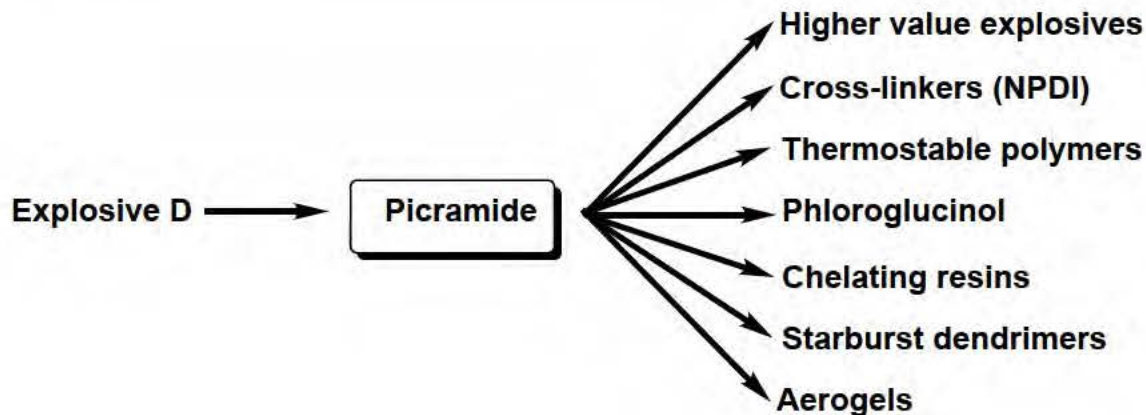


Figure 1. Picramide provides access to a variety of higher value products.

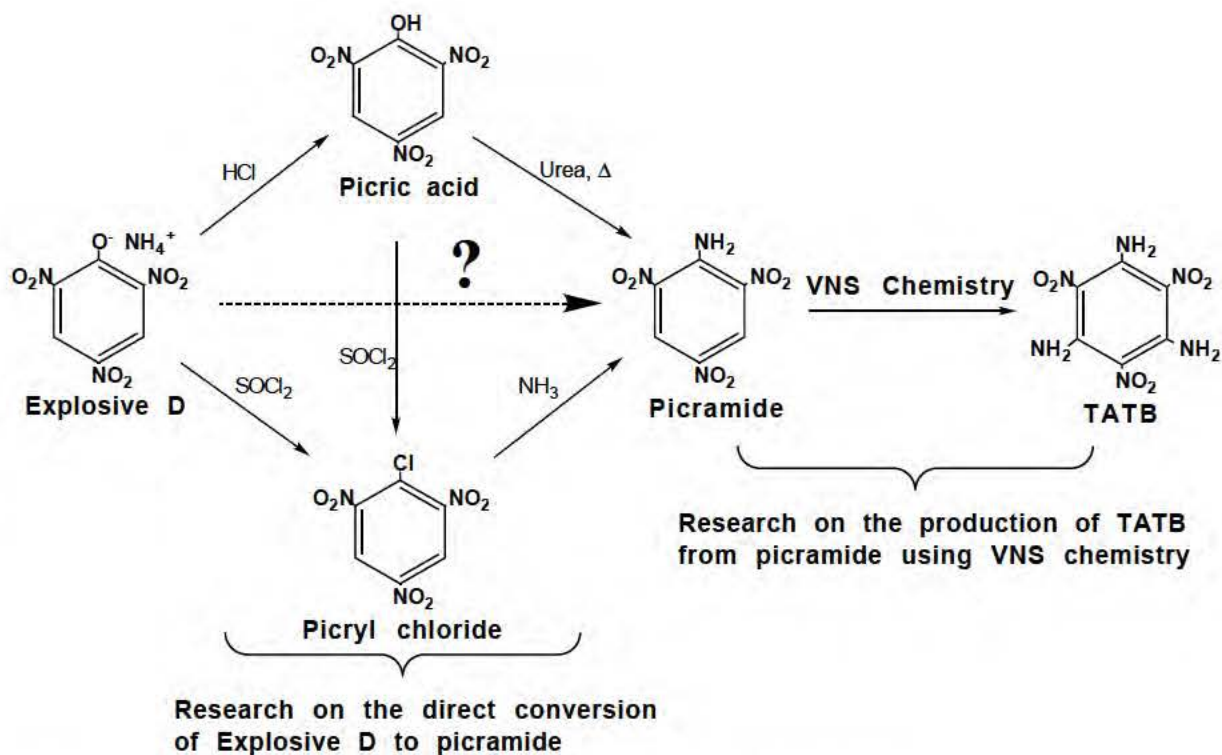


Figure 2. Conversion of Explosive D to picramide and TATB production.

Experimental Work

Description of Problem

Conversion of Explosive D to Picramide

There is one report that describes the direct conversion of picric acid to picramide [5]. Molten picric acid and urea were heated at 173°C for 36 hours to produce a mixture of picramide, urea, and cyanuric acid. Removal of the urea and cyanuric acid by extractions with the appropriate solvents (water, acetone) afforded picramide in 88% yield (Fig. 3).

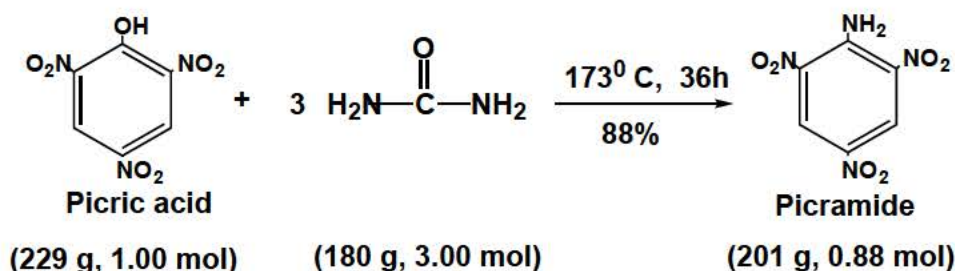


Figure 3. Direct conversion of picric acid to picramide.

This procedure has major drawbacks. Molten picric acid, especially at such an elevated temperature (173°C), is a recognized hazard. Furthermore, the picramide is produced as a solid glass product which cannot be safely and efficiently removed from an industrial scale reactor. So we asked the question: “What about the direct conversion of Explosive D to picramide (Fig. 4)?”

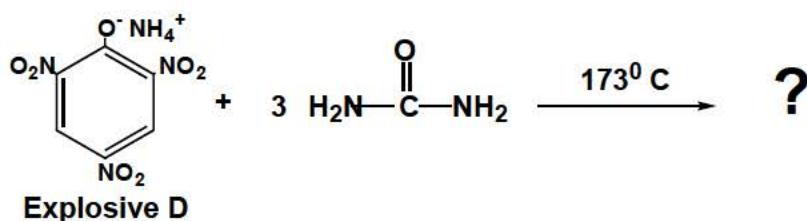


Figure 4. Direct conversion of picric acid to picramide.

We have not found any reports in the chemical literature describing such a conversion. There are suggestions, however, that the reaction of Explosive D with urea at elevated temperature has been attempted and little or no picramide was produced [6]. Since inexpensive picramide is key to our R^3 activities, we investigated the conversion of Explosive D to picramide in collaboration with Dr. Michael D. Coburn (LLNL consultant and guest investigator at LANL). Some of our findings are described under Experimental Results.

Conversion of Picramide to TATB

We are addressing a DOE requirement for a less expensive and more environmentally benign production of TATB. Current production techniques for making TATB are expensive and rely on environmentally hazardous reagents and relatively harsh conditions [7,8]. We have developed a novel approach to the synthesis of TATB that utilizes potentially inexpensive starting materials and mild reaction conditions (Fig. 5) [9–11]. This new process relies on amination of nitroaromatic starting materials using a reaction known as Vicarious Nucleophilic Substitution (VNS) of hydrogen [12].

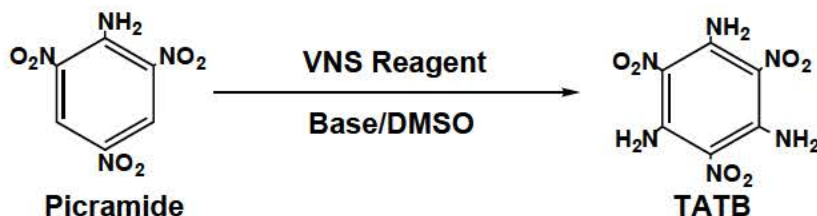


Figure 5. VNS synthesis of TATB from picramide.

We have been working on the scale-up of this new synthesis with the goal of developing a new production of TATB. We have been studying the influence of VNS aminating reagent, base, solvent, temperature, quenching and other variables on the yield, purity, and morphology of TATB product. These studies are described under Experimental Results.

Experimental Results

Conversion of Explosive D to Picramide

The procedure described for the conversion of molten picric acid to picramide (Fig. 3) [5] was repeated on a smaller scale and gave a clean preparation of picramide in less than 20 hours reaction time. The reaction was then studied using solutions of picric acid and urea prepared from a variety of solvents. A preferred solvent was discovered and the reaction was repeated using Explosive D in place of picric acid. Good yields (>90%) were obtained irrespective of the starting material. In each case, however, cyanuric acid was present as an unwanted by-product formed from excess urea in the reaction mixture.

The use of other compounds to replace urea was investigated and conditions were found where Explosive D was converted to picramide (80%) without the concomitant formation of cyanuric acid (Fig. 6). A Record of Invention [13] has been filed with LLNL and we are continuing to optimize the reaction. Our complete findings will be detailed upon submission of a patent application.

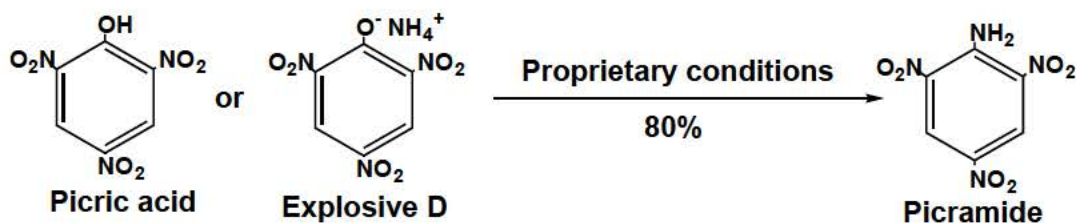


Figure 6. Conversion of picric acid or Explosive D to picramide.

Conversion of Picramide to TATB

VNS Amination Reagents

We have documented the use of three reagents for the amination of picramide to TATB by the VNS of hydrogen [9–11]. The reagents in order of increasing reactivity, as well as increasing cost, are hydroxylamine, 4-amino-1,2,4-triazole (ATA) and 1,1,1-trimethylhydrazinium iodide (TMHI) (Fig. 7).

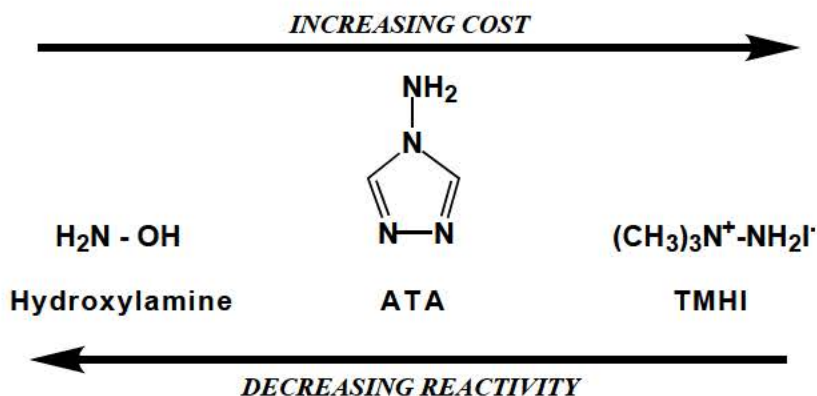


Figure 7. VNS amination reagents.

Hydroxylamine is an inexpensive chemical obtained in bulk quantities as the hydrochloride or sulfate salt. ATA is obtained from formylhydrazide, which is prepared from relatively inexpensive hydrazine and ethyl formate [14]. TMHI is prepared from reaction of the more expensive 1,1-dimethylhydrazine and methyl iodide [9]. Each reagent has advantages and disadvantages that will be discussed in subsequent sections.

Reaction Condition Studies

TMHI is the most efficient aminating reagent available for the synthesis of TATB [9,10]. Picramide, TMHI, and base (sodium alkoxide or hydroxide) react in DMSO to provide TATB in 80–90% yield (Fig. 8). The reaction is conducted at room temperature and is complete in less than 3 hours. The major expected impurity is 1,3-diamino-2,4,6-trinitrobenzene (DATB), which results from incomplete amination. Under these reaction

conditions no DATB (0.5%) is detected by FTIR spectroscopy or direct insertion solids probe mass spectroscopy (DIP-MS). The largest scale attempted thus far has been at the 50-gram level. The reaction appears to scale linearly to afford TATB in 82% yield at >99% purity.

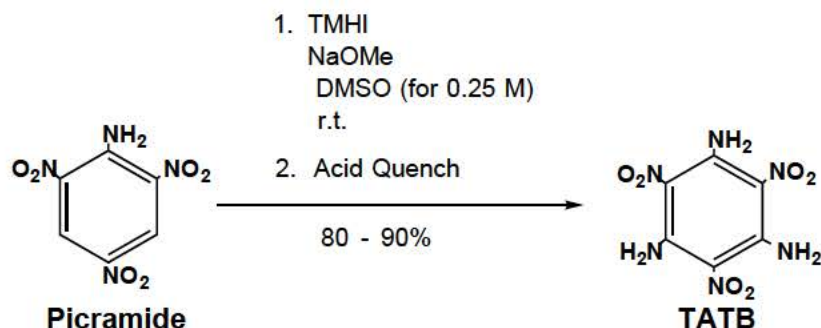


Figure 8. VNS synthesis of TATB using TMHI.

While TMHI is very reactive and efficiently produces TATB, there are several disadvantages to its use. The reagents used to generate TMHI (UDMH and methyl iodide) are toxic and relatively expensive. In addition, the by-product of amination using TMHI is trimethylamine, a volatile and noxious gas which must be scrubbed from the reaction exhaust system. In contrast, hydroxylamine is much cheaper, less toxic and does not release gaseous products. The VNS amination of picramide proceeds poorly at room temperature to furnish predominantly DATB [11]. Elevated temperature (65–90°C) forces the reaction nearly to completion and provides TATB in 50–74% yield with about 97% purity (Fig. 9) [15].

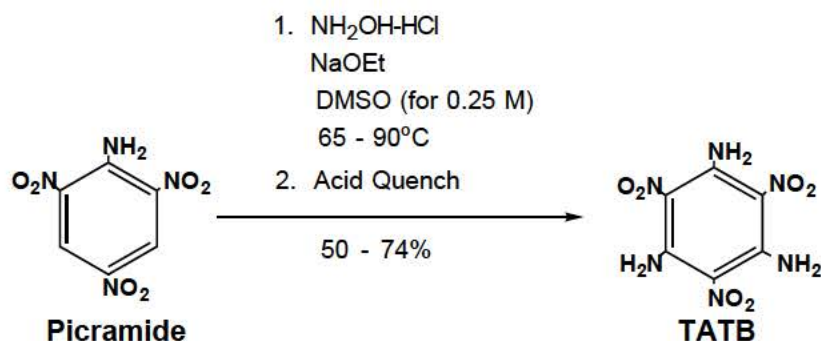


Figure 9. VNS synthesis of TATB using hydroxylamine hydrochloride.

The first VNS synthesis of TATB was accomplished at LLNL in 1994 using 4-amino-1,2,4-triazole (ATA) as the VNS amination reagent [11]. ATA is less reactive than TMHI and more reactive than hydroxylamine (Fig. 7). The use of elevated temperature (60–70°C), however, does make ATA equivalent to TMHI in VNS aminations with respect to yield of TATB. Our use of ATA was discontinued after the more reactive TMHI was discovered and evaluated in VNS aminations [9,10]. We are now reinvestigating the use of ATA in light of the quality of TATB produced with TMHI and hydroxylamine (See Product Analysis).

Product Analysis

TATB prepared from the VNS process will have to satisfy purity and testing profiles (DSC, CRT, DH_{50} , spark and friction tests, etc.) established for conventionally prepared TATB [4,7,8]. FTIR and DIP-MS show TATB using TMHI and ATA is chemically >99% pure while the use of hydroxylamine gives TATB that is typically >97% pure. DSC (differential scanning calorimetry) values are 10–20°C low for TATB prepared with hydroxylamine or TMHI. In addition, hydroxylamine or TMHI furnish TATB preparations that are tan to dark brown in color while TATB is typically yellow.

In contrast, TATB prepared with ATA has good color and higher DSC values. In addition, recent experiments indicate that VNS aminations using ATA can be run at double the concentrations required with hydroxylamine or TMHI. The use of more concentrated reactions (lower solvent volumes) is significant from a cost perspective when the process is taken to an industrial scale.

Reaction Quenching and Particle Size

VNS reactions employ a strong base (sodium alkoxide) and are quenched with acid or by dilution with water. Our initial quenching studies on VNS reactions employed aqueous mineral acids or water that precipitated TATB particles in a size range of 0.2–2 μm . The use of weak organic acids in the absence of water was explored. Citric acid monohydrate in DMSO produced TATB particles in the 1–10 μm range. Larger particles (20–30 μm) have been obtained using salicylic acid.

Summary of Experimental Work and Plans for Next Year

The first direct conversion of Explosive D to picramide has been demonstrated (Fig. 6). The optimization of this reaction is under investigation. The evaluation of TMHI, ATA, and hydroxylamine as VNS aminating reagents for the production of TATB continues. ATA is emerging as a reagent of choice with respect to cost and quality of TATB produced. Our plans for next year are summarized in Fig. 10.

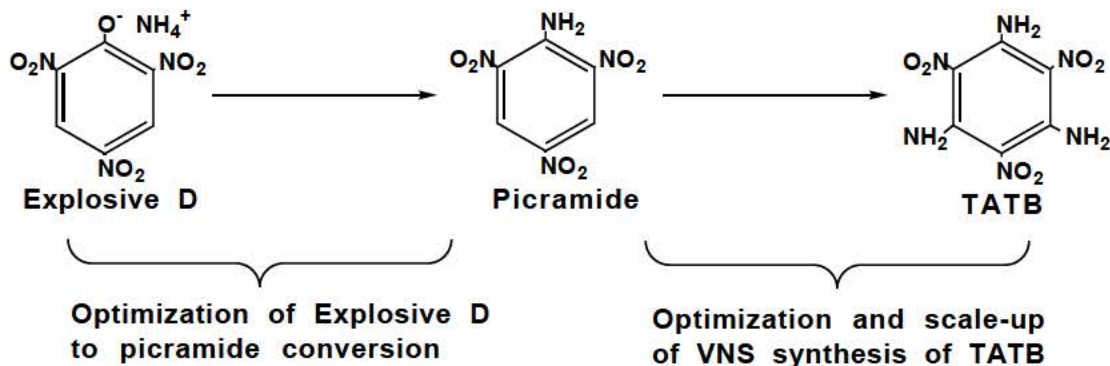


Figure 10. Continuing studies on the conversion of Explosive D to TATB.

Conclusions

The first direct conversion of Explosive D to picramide, an important precursor for a variety of higher value products, has been accomplished. The optimization of this reaction is underway. Improved conversions of picramide to TATB using Vicarious Nucleophilic Substitution (VNS) chemistry have been developed. Studies on the scale-up of TATB production are in progress.

Acknowledgments

The continuing interest and support by James Q. Wheeler (Defense Ammunition Center, US Army, McAlester, OK) and Dan Burch (Naval Surface Warfare Center, Crane, IN) are gratefully acknowledged.

References

1. A. R. Mitchell and R. D. Sanner, "Chemical Conversion of Energetic Materials to Higher Value Products," in *Energetic Materials- Insensitivity and Environmental Awareness, Proc. 24th Intl. Annual Conference of ICT*, H. Ebeling, Ed., Karlsruhe, Germany, 1993, p. 38.
2. A. R. Mitchell, P. F. Pagoria, and R. D Schmidt, "A New Synthesis of TATB Using Inexpensive Starting Materials and Mild Reaction Conditions," in *Energetic Materials- Technology, Manufacturing and Processing*, T. Keicher, Ed., Proc. 27th Int. Annual Conf. of ICT. Karlsruhe, Germany 1996, p. 29.
3. S. F. Rice and R. L. Simpson, "The Unusual Stability of TATB: A Review of the Scientific Literature," Lawrence Livermore National Laboratory, Livermore, CA, UCRL-LR-103683 (July, 1990).
4. B. M. Dobratz, "The Insensitive High Explosive Triaminotrinitrobenzene (TATB): Development and Characterization—1888 to 1994," Los Alamos Scientific Laboratory, Los Alamos, NM, Report LA-13014-H, (August, 1995).
5. E. Y. Spencer and G. F. Wright, "Preparation of Picramide," *Can. J. Research*, **24B**, 204 (1946).
6. Joint Explosives Processing Committee Meeting, October 18-20, 1994, Amarillo, Texas.
7. T. M. Benziger, "Manufacture of Triaminotrinitrobenzene," in *Chemical and Mechanical Technologies of Propellants and Explosives, Proc. 1981 Intl. Annual Conference of ICT*, Karlsruhe, Germany, 1981, p. 491.
8. T. M. Benziger, "Method for the Production of High-Purity Triaminotrinitrobenzene," *US Patent 4,032,377* (1977).

9. P. F. Pagoria, A. R. Mitchell, and R. D. Schmidt, "1,1,1-Trimethylhydrazinium Iodide (TMHI): A Novel, Highly Reactive Reagent for Aromatic Amination via Vicarious Nucleophilic Substitution (VNS)," *J. Org. Chem.*, **61**, 2934 (1996).
10. A. R. Mitchell, P. F. Pagoria, and R. D. Schmidt, "Vicarious Nucleophilic Substitution to Prepare 1,3-Diamino-2,4,6-trinitrobenzene or 1,3,5-Triamino-2,4,6-trinitrobenzene," *US Patent* 5,569,783 (1996).
11. A. R. Mitchell, P. F. Pagoria and R. D. Schmidt, "Vicarious Nucleophilic Substitution Using 4-Amino-1,2,4-triazole, Hydroxylamine or O-Alkylhydroxyl-amine to Prepare 1,3-Diamino-2,4,6-trinitrobenzene or 1,3,5-Triamino-2,4,6-trinitrobenzene," *US Patent* 5,633,406 (1997).
12. M. Makosza and J. Winiarski, "Vicarious Nucleophilic Substitution of Hydrogen", *Acc. Chem. Res.*, **20**, 282 (1987).
13. A.R. Mitchell and M.D. Coburn, "Conversion of Picric Acid and Its Salts to Picramide," Record of Invention (IL-10388) filed with LLNL Patent Group, August 13, 1998.
14. C. F. H. Allen and A. Bell, "4-Amino-4H-1,2,4-triazole," *Organic Syntheses*, **24**, 12 (1944).
15. A. R. Mitchell, P. F. Pagoria, and R. D. Schmidt, "Amination of Electrophilic Aromatic Compounds by Vicarious Nucleophilic Substitution," Continuation-in-Part U.S. Patent Application (Nov. 10, 1997) claiming priority over International Application PCT/US96/06663 (May 10, 1996) filed by the same inventors.

This page intentionally left blank

IV. Fuzing Overview

Safe, Arm, and Fuze Technology is a continuing project that is managed under the High Explosives and Initiation Systems Thrust Program. In this work, the design of an insensitive fuze train was derived from LLNL's experience in initiating our LX-17 explosive. This project also demonstrates the valuable synergy developed by this Memorandum of Understanding (MOU). The Department of Defense (DoD) requires a safer, more insensitive explosive in its ordnance, which presents initiation challenges; the Department of Energy (DOE) will receive the benefits of the state-of-the-art initiation technology for its own insensitive high explosive requirements.

We continued our work in several areas of safe, arm, and fuze technology this year. We have worked with Kaman Aerospace Corporation, Raymond Engineering Operations (Raymond Engineering) to evaluate the performance of a second generation of their R&D detonators. Tests on the first production run had shown very interesting performance, and we ordered and received additional detonators for testing. We used a Fabry-Perot velocimeter to measure slapper velocity-time histories and performed threshold testing using high-specific-surface-area PETN and HNS initiating pellets. The new production run showed even better performance than the first run.

We continued to use our new, small-scale, high explosive (HE) performance test, which allows us to measure the shock-wave pressure profile transmitted into a lithium fluoride (LiF) crystal by the detonating HE. We performed many experiments on explosives in common use at LLNL to demonstrate the reproducibility of the results and to establish a database for determination of the equation-of-state of these explosives.

We reported to the Fuzing TCG on a DOE project that tests detonator firing cables for aging-induced changes with a technique called partial discharge testing.

A new computer code is up and running that models the operation of slapper detonators by combining an electrical circuit model and an electrical model of the exploding bridgefoil into a 1D hydrodynamic code. We are presently working on the determination of appropriate model parameters and the development of a more convenient user interface for providing the input parameters to the code.

At the request of DoD colleagues, we coordinated safety and characterization tests on various energetic materials of interest. We also performed experiments on cutting HE with a short pulse laser. The laser work is a separate project, reported to the Demilitarization TCG; however, because it has numerous fuzing applications, we have reported it to the TCG on fuzing as well.

This page intentionally left blank

Safe, Arm, and Fuze Technology

R. S. Lee, J. L. Cutting, R. Druce, A. M. Frank, C. Gillespie, F. Roeske, and P. Watts
Lawrence Livermore National Laboratory
(925) 423-5081
lee35@llnl.gov

Abstract

This year, we continued our efforts in several areas of safe, arm, and fuze technology. We worked with Kaman Aerospace Corporation, Raymond Engineering Operations (Raymond Engineering), to evaluate the performance of a second generation of their R&D detonators. Because tests on the first production run had shown very interesting performance, we ordered and received additional detonators for testing. We used a Fabry-Perot velocimeter to measure slapper velocity-time histories and performed threshold testing using high-specific-surface-area PETN and HNS initiating pellets. We continued to use our new, small-scale, high explosive (HE) performance test, which allows us to measure the shock-wave pressure profile transmitted into a lithium fluoride (LiF) crystal by the detonating HE. We performed many experiments on explosives in common use at LLNL to demonstrate the reproducibility of the results and to establish a database for determination of the equation of state (EOS) of these explosives. Our work on a new Department of Energy (DOE) project for testing detonator firing cables for aging-induced changes, called partial discharge testing, is also reported here. A new computer code is up and running; it models the operation of slapper detonators by combining an electrical circuit model and an electrical model of the exploding bridgefoil into a 1D hydrodynamic code. We are presently working on appropriate model parameters and a more convenient user interface for providing the input parameters to the code. At the request of Department of Defense (DoD) colleagues, we coordinated safety and characterization tests on various energetic materials of interest. We performed experiments on cutting HE with a short pulse laser. The laser work is a separate project, discussed elsewhere in this Annual Report, but some of the applications to fuze technology are briefly mentioned here.

Introduction

This report describes continuing work on developing technology that can be used in generic fuze train designs, with special attention to the problem of initiating insensitive high explosive (IHE) main charges. This work has two major objectives: (1) to investigate and optimize generic fuze train designs, including materials, detonator design and fabrication, detonation transfer, and diagnostics, all of which are areas of past and continuing investigations; and (2) to develop thermal and performance models that can characterize generic and specific fuze train designs. In pursuit of this second objective, we performed one-dimensional-time-to explosion (ODTX) tests, developed new thermal characterization tests,

and developed computer simulations of how fuze trains and components perform and respond to normal and abnormal environments. The goals of the work are to (1) develop simple, generic fuze train designs that meet insensitive munition (IM) requirements and give predictable responses in abnormal environments, and (2) optimize the performance of fuze trains and components.

Background

Weapon vulnerability and safety in extreme abnormal environments have always been matters of great concern to the DoD. A great deal of attention is now focused on the use of insensitive materials in new weapons in order to greatly enhance weapon safety in abnormal environments. Fuzes designed for insensitive munitions must reliably initiate insensitive main charge HEs with large critical diameters without compromising the safety of the insensitive main charge. Designing an initiation train that will meet such requirements requires a judicious choice of initiating and booster HEs, experimentation, and a good modeling capability.

In past work, we developed a generic design for an IM fuze and demonstrated that the design can be scaled to initiate an IHE of any critical diameter. Our initial IM fuze train design relied on a very conservative choice of initiating and booster HE materials, which we have already used for DOE applications. Some applications may demand higher performance materials — e.g., higher-energy booster HEs. Fitting new insensitive fuze designs into the geometry of existing fuzes will require innovative designs and careful attention to design margins for reliable fuzing.

Modeling is extremely important in optimizing fuze train designs. We are developing thermal models for HE materials of interest, which can be used in modeling system response to abnormal thermal environments. Data for these thermal models are obtained from ODTX tests. We are also interested in modeling the transfer of detonation between explosive components in a fuze train. We are developing a new computer code to model the operation of slapper detonators that incorporates an electrical circuit model and an electrical model of the exploding bridgefoil into a 1D hydrodynamic model. The new code will enable us to model the performance of the entire initiation train from the electrical current into the slapper bridgefoil to the output of the booster into the main charge. As a long-range goal, we also plan to use the hydrodynamic part of this code to model detonation transfer between HE components.

We have continued to work with Raymond Engineering on evaluating the performance of some of their R&D detonators. Tests on the first production run showed very interesting performance and we ordered and received additional detonators for testing. We also measured slapper velocity-time histories and performed threshold testing using high-specific-surface-area PETN initiating pellets. We have material transfer and non-disclosure agreements with Kaman Aerospace Corporation, Raymond Engineering Operations, to conduct this performance testing. This work is of mutual benefit, enabling us to explore this

technology without the burden of developing the process, while it gives Raymond Engineering access to our detonator diagnostic capabilities.

We developed a new, small-scale, HE performance test that allows us to measure the shock-wave pressure profile transmitted into a LiF crystal by the detonating HE. With this test, we can evaluate the performance of HE formulations with only a few grams of material. This test is not a replacement for the cylinder test, which has become a standard for HE performance testing, but it allows us to screen new materials without the expense of having to formulate kilogram quantities of explosive. The new test does give EOS information at high pressures that cannot be obtained from the cylinder test.

We strive to facilitate the transfer of DOE technology to DoD applications. The material transfer agreement with Raymond Engineering is an example of our work in this area.

Work with Raymond Engineering

Work with Raymond Engineering has consisted of evaluating the second-generation slappers, which they fabricated. The new slappers were fabricated using the same process but with variations in the bridge and slapper thickness. The design will not be discussed here; the reader is directed to the classified part of the FY97 final report [1] for details of the Raymond design. The performance was consistent with that reported for the first generation slappers and, with the design variations, will be useful in optimizing the design. Details of the results were reported at the May, 1998, Technical Coordinating Group (TCG) meeting, but the results are classified, and therefore, not reported here.

Small-scale Performance Test

It is expensive and time-consuming to scale up the processing of a new explosive material or formulation to produce a quantity of material sufficient to perform a cylinder test to characterize the performance. Calculated performance does not always correspond with measured performance, so there is also a concern that the time and resources expended in firing a cylinder test on a new material may not be justified by the outcome. We have developed a small-scale test to give a preliminary characterization of the performance of a new explosive using only a few grams of material. The new test is also proving to be useful in studying the EOS of explosives in the high-pressure region close to the detonation front. We have studied several explosives in common use and compared the experimental results with calculations which use equations of state (EOSs) that have been measured in cylinder tests. The test fixture, which was discussed in detail in the FY97 report [1], is shown in Fig. 1.

Experimental results for the explosive LX-10 (95% HMX/5% Viton A binder) are shown in Fig. 2. The experimental interface velocity data, shown as gray lines, are from six different shots and the scatter in the curves shows the excellent reproducibility of the measurement. The solid black line is a calculation using the CALE hydrocode [2] and a JWL equation of state [3], determined from cylinder tests. The agreement is good except near the

peak at the shock arrival. The fact that the measured peak velocity is larger than the calculated peak velocity may be due to the Von Neumann spike, which has not been completely attenuated in its passage through the 0.13-mm Al foil. There is also more scatter in the experimental data near the shock jump, due to difficulties that will be discussed below.



(b)(3)

Figure 3 shows an experimental streak record of fringes from the laser velocimeter record as the detonation wave collides with 13- μm Al foil, which forms the interface between the HE and the LiF crystal. The interface velocity is determined from the spacing between the fringes, and at the shock jump, the error is greater than the 1% error we estimate for the bulk of the record. This is because the fringe spacing is decreasing rapidly after the shock jump which, coupled with the finite width of the fringes, makes the peak value very difficult to read. This difficulty can be overcome by streaking faster, so the slope of the fringes is reduced.

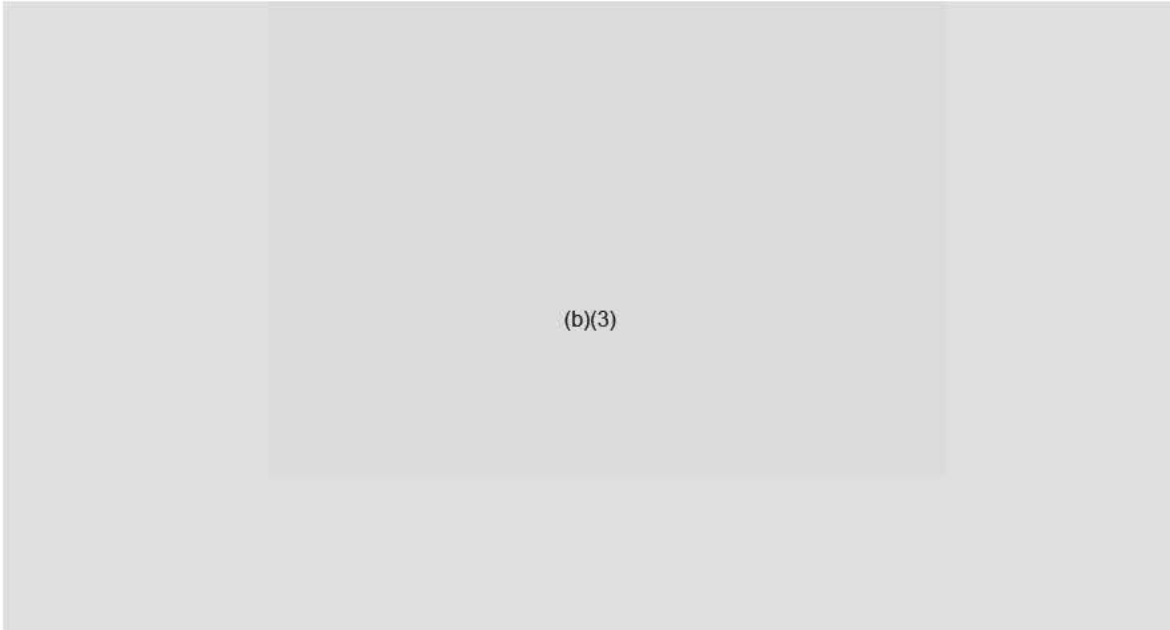


Figure 4 shows the six experimental records from Fig. 3 separated in time. The first two records were recorded at a 2- μs sweep rate and the last four at 1 μs . There is a consistent trend for the faster sweeps to give higher peaks. At the time of the experiments we were limited to a 1- μs sweep because we did not have a comb generator that would generate time marks faster than every 100 ns. This meant that at sweeps faster than 1 μs , we could not generate an accurate time fiducial to give us cross timing with the digitizer records of the electrical signals. In future work, we will use a faster comb generator and, for some experiments, plan to use a much thinner aluminum reflector in conjunction with a sub-nanosecond-time-resolution VISAR velocimeter.

Finally, in Fig. 5, we show a comparison of calculation with experimental data for LX-17 (92.5% TATB/7.5% Kel-F 800 binder), a very non-ideal explosive that is known to have a large reaction zone. The LX-17 could not be initiated directly by the aluminum flyer, so an additional booster of LX-10 was used. The simulation of this experiment included the LX-10 booster. The experimental curves lie above the calculated curve for more than 0.1 μs , consistent with the existence of a large reaction zone.

(b)(3)

(b)(3)

(b)(3)

The agreement between the data and the CALE simulations for nearly ideal explosives like LX-10 shows that our test gives a good representation of the performance of an explosive in the high-pressure region near the Chapman-Jouguet state. At the detonation front, the simulation usually gives a lower interface velocity than is measured; this is probably a result of the Von Neumann spike, which is not accounted for in the simulations. There is also some experimental uncertainty in the measurement of the shock jump, but this can be alleviated by a faster sweep rate on the camera that records the velocimeter data.

Agreement between experiment and simulation for the non-ideal explosive, LX-17, was much poorer. LX-17 has a very large reaction zone, which would lead to a wide Von Neumann spike and an under-prediction by the simulation near the detonation front. It is likely that the LX-17 detonation has not yet reached steady state, and one would not expect agreement with the simulation in such a case.

The test results may be useful in understanding the performance of booster explosives. In all of the explosives we tested, except for LX-16 (96% PETN/4% FPC 461 binder), the maximum measured interface velocity exceeded the calculated maximum interface velocity, indicating the presence of significant reaction zones in some of the explosives. We can use this test to quantitatively determine whether reaction zone thickness can play a role in detonation transfer.

Partial Discharge Testing

We have been studying partial discharge testing of detonator cables, which is funded as part of the DOE enhanced surveillance program. The partial discharge (PD) work is of interest for DoD firing systems as well, so we will briefly report on it here. The goal of the program is to perform partial discharge testing on detonator cables that have been subjected to aging in order to be able to detect changes in the dielectric strength of the cables, and possibly to make end-of-life predictions for the cables. The detonators had already been fired on the cables we tested. The aged cables came to us with the end cut off, so we needed to be able to prepare the end of the cable to prevent breakdown during testing. Figure 6 is a photo of the cable end after encapsulation in Stycast epoxy. Partial discharge testing of these cables, after encapsulation of the end, showed that activity occurred away from the encapsulation, confirming that this is a viable method of preparing cables for analysis. Once we demonstrated that cables could be prepared successfully, we concentrated efforts on comparing analysis of new cables with aged cables. Figure 7 is a time-to-inception comparison of new cables with cables stored in two different aging environments. The aged cables were treated as in Fig. 6 to ensure a valid test. Many of the cables analyzed did not exhibit activity right away. To establish a consistent test procedure, a standard voltage was applied to the cable and held there until a PD signature was observed. The time between voltage application and first PD signature is recorded as time to inception. The conditions of this test were 7.07 kV rms AC applied to each cable until partial discharge activity was observed. It can be seen from Fig. 7 that the new cables have a significantly longer time to inception than either aged set. There were 15 cables in the set of new cables. The aged group #1 consisted of 5 cables. The aged group #2 consisted of a sample of 2 cables. It can be seen that this is a very small sample size — particularly for the aged group #2. With the small

sample size in mind, we observe that the older cables appear to be less robust than the new cables. The reader must, however, remember that none of these cables broke down. The point of the partial discharge activity is to provide an early warning for problems that may occur in the future. We plan to continue this work in 1999 to include interactions of the cable conductors with a ground-plane.

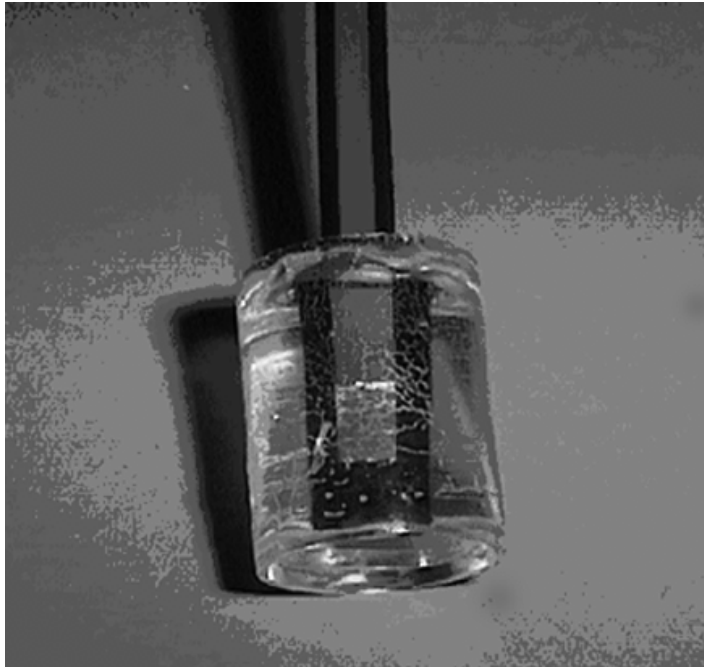


Figure 6. Photo of typical cable-end after preparation for analysis. The casting material is Stycast epoxy.

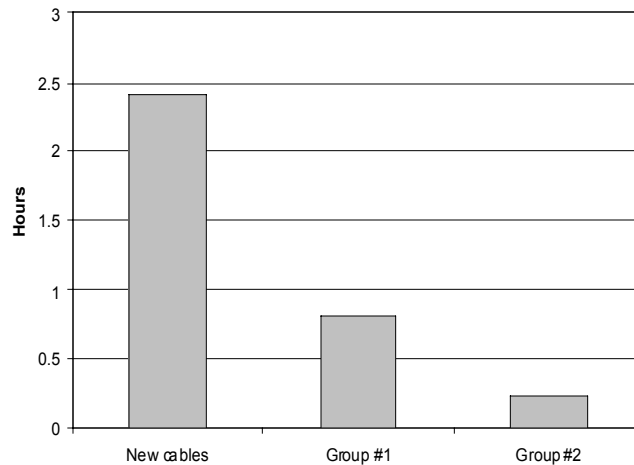


Figure 7. Plot of the average time to inception of partial discharges with the cable held at 7.07 kV AC voltage until inception occurred. The sample for Group #2 contains only two cables, which is probably statistically insignificant.

New Code for Initiation Train Performance Modeling

Len Haselman of LLNL [4] wrote a new 1D hydrocode, KOWIN. KOWIN is written in C++ and operates with Microsoft Windows 95. On a Pentium processor, it easily runs problems with several hundred zones in a few minutes. An EOS database is included, which supports JWL, 5-term-polynomial, 7-term-polynomial, 28-term-polynomial, Grüneisen, linear Us-Up, gamma-law, and table-lookup forms. EOS data can be added to the database with a text editor. KOWIN, which runs in an interactive mode and is easy to use, has been extremely useful for modeling impact and HE burn experiments. Professor Kenneth Carpenter of Kansas State University is working with us to incorporate an electrical circuit model and a bridgefoil resistance model into KOWIN. This will allow us to model the operation of an initiation train, from the onset of current flow to the initiation of a main charge explosive by a booster.

Modeling the electrically exploded bridgefoil requires a model for the bridgefoil resistance as a function of time or some other progress variable. Two models were incorporated into the new code. One model, developed by Lee [5], the FIRESET model, expresses the resistance as a function of specific action through the bridge. The other model, used by Furnberg [6], expresses the resistance as a function of energy deposited in the bridge. In work done during FY98, both models were tested against experimental data to determine the functional form that best fits the widest range of experimental data.

It was determined that specific action was a more useful progress variable for the resistivity model because it is easily measured and because it appears to yield more accurate results. A hybrid model, utilizing some features from both the FIRESET and Furnberg model, gave the best results. Figure 8 compares resistivity curves generated by the FIRESET model and two versions of the hybrid model with an experimental resistivity curve generated by measuring the current and voltage drop for an exploding bridge conductor. All three models give reasonable simulations of the experimental resistivity up until the peak of the curve (burst) but after burst, the hybrid model is clearly superior (the FIRESET model was never intended to give an accurate representation of post-burst resistivity). Figure 9 compares experimental data with current and voltage waveforms calculated using the model parameters of the exponential-start hybrid model of Fig. 8. The agreement with experiment is excellent.

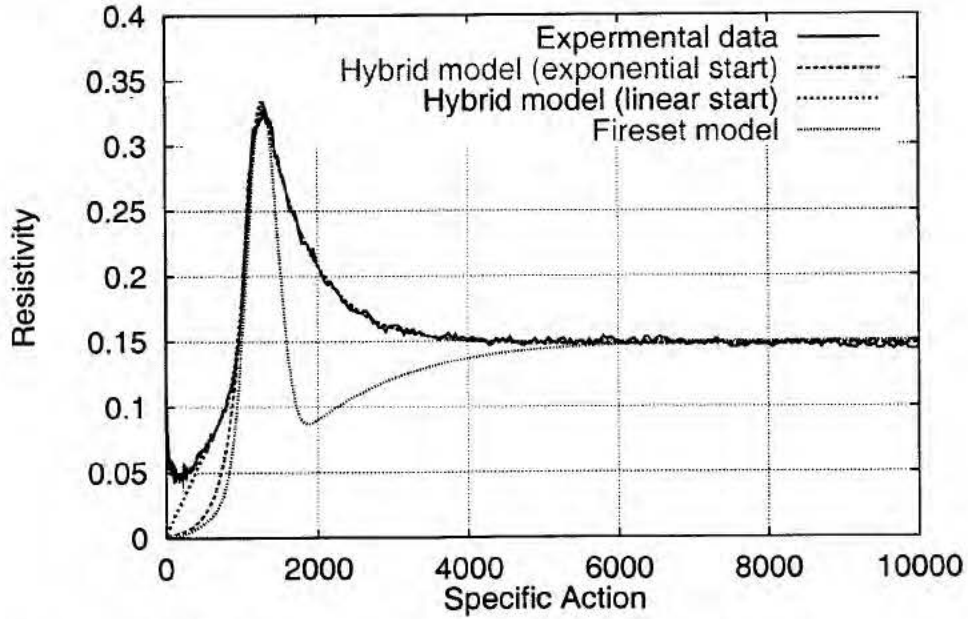


Figure 8. Comparison of various resistivity models for electrically exploded conductors.

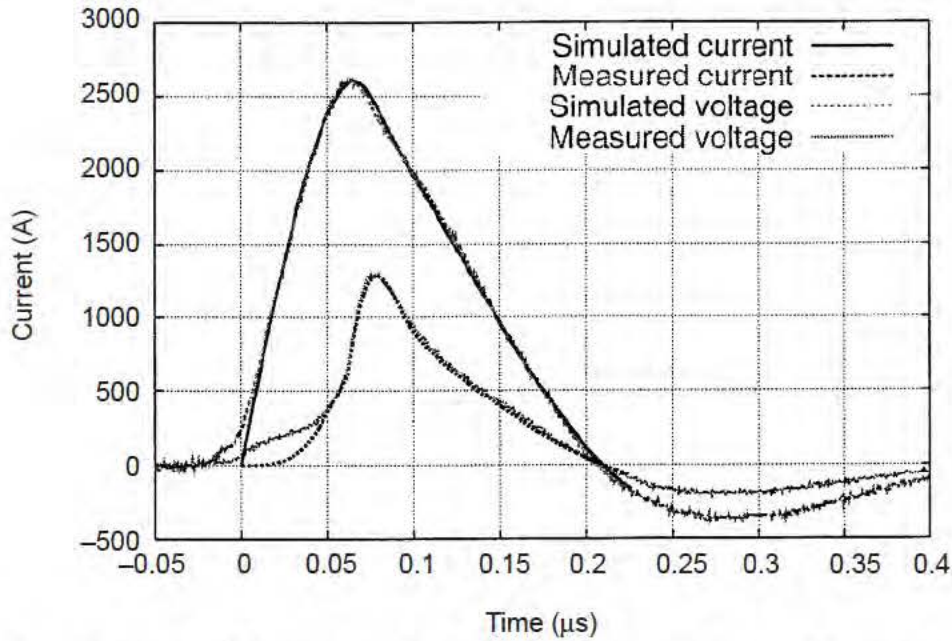


Figure 9. Experimental data compared with simulations using the model parameters from the exponential-start hybrid model of Fig. 8.

The electrical energy deposited in the bridgefoil is the link between the electrical part of the code and KOWIN. At each time step in the calculation, the calculated increment in electrical energy is added to the zones, which represent the bridgefoil in the hydrodynamic part of the code. The EOS of the bridgefoil material is expressed in the γ -law form:

$$E - E_0 = pv/(\gamma - 1), \quad (1)$$

where $E - E_0$ is the specific internal energy, p is the pressure, and v is the relative volume of the bridgefoil material. E_0 and γ are parameters that can be adjusted to make the calculations fit the experimental data. At the beginning of the calculation, E is zero, making $E - E_0$ negative, and in the hydrodynamic calculation we hold the pressure P at zero until $E - E_0$ becomes positive. We have also found it necessary to make a gradual transition when the pressure term is turned on, otherwise a strong shock develops in the zones representing the exploding bridge conductor and the acceleration is too violent. We also include a term that approximates the effect of the magnetic pressure. Figure 10 compares experimentally measured velocity with a simulation using KOWIN and the model parameters of Figs. 8 and 9. The simulation shows more early motion than is observed, but fits the experimental curve quite well at later times. The simulation also shows some shock reverberations that result from energy being deposited too rapidly in the conductor. Such reverberations are sometimes observed experimentally when the slapper is being driven hard by a fast-rising current.

Work at the present time is concentrating on developing realistic model parameters that give good simulations over a wide range of circuit parameters and bridge geometries. We also plan to develop a more friendly user interface to facilitate use of the code by those who are not familiar with the intricacies of hydrocodes.

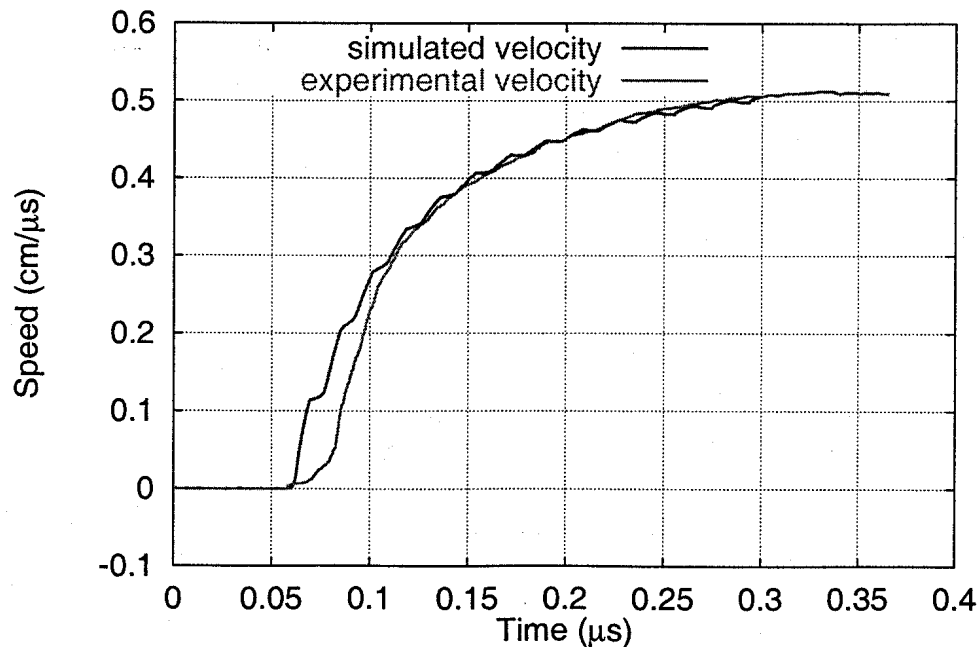


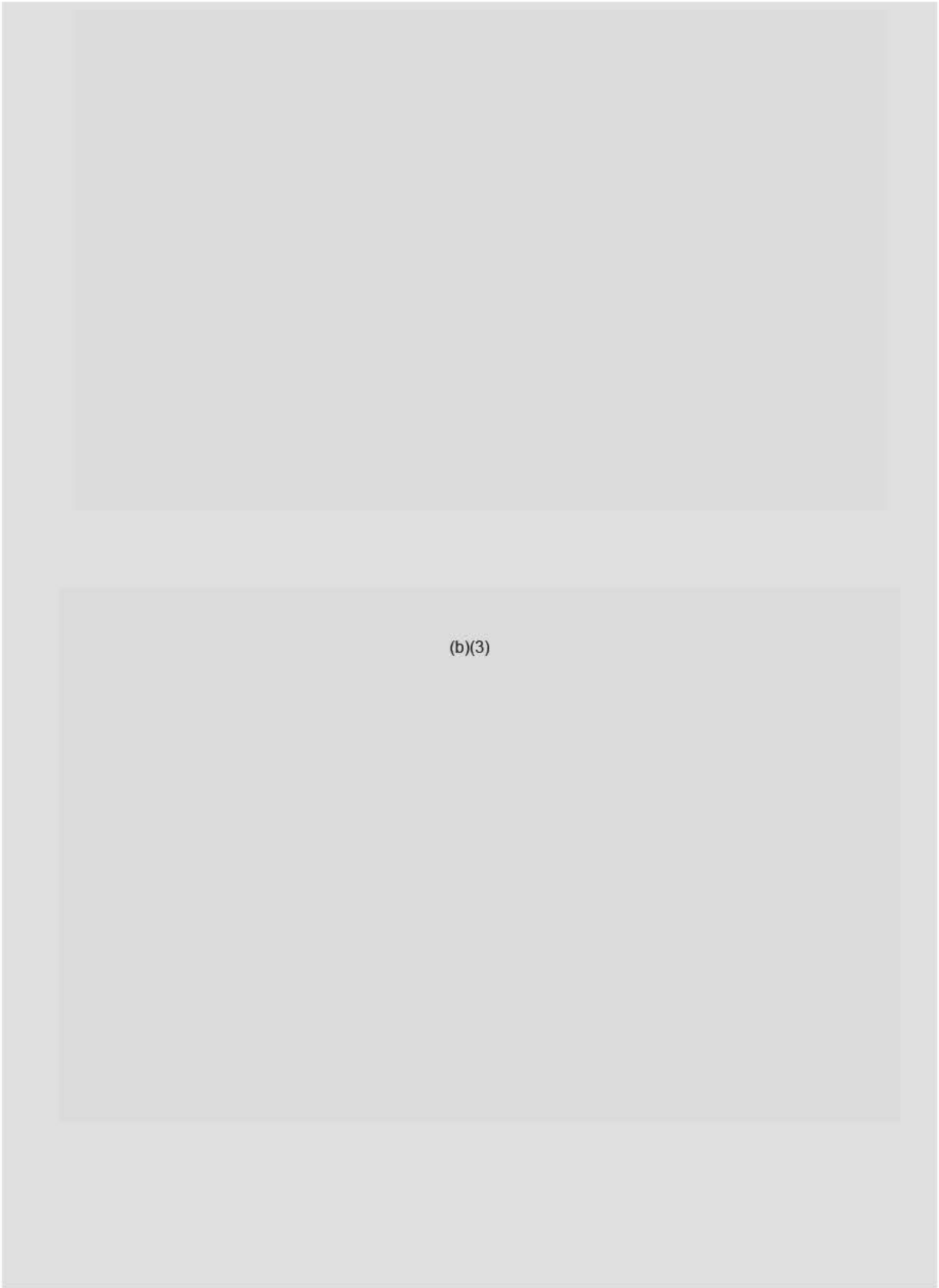
Figure 10. Experimental velocity-time curve compared with a simulation. The simulation is the curve with the shock reverberations (stair-step feature).

Thermal and Safety Tests on HE

At the request of TCG members, we performed small-scale safety tests on several explosives [7]. These included DAAF, HNS-IV manufactured at Pantex, HNS with 2% Kel-F binder from Reynolds Industries Systems, Inc. (RISI), and high-surface-area HNS with 2% Kel-F binder manufactured at Pantex. The results of some of these tests are summarized in Table 1. Differential scanning calorimetry results for DAAF are shown in Fig. 11 and the results of DSC tests on HNS-IV and HNS with 2% Kel F binder are shown in Fig. 12. Figure 13 shows the results of ODTX testing on DAAF.



(b)(3)



(b)(3)

Femtosecond Laser Cutting of HE

In a project that is partially funded by the Memorandum of Understanding (MOU) Program, we used a femtosecond laser beam to make cuts through small pressed pellets of six common high explosives. More details are provided in a separate section in this Annual Report, but a brief synopsis is given here along with a discussion of possible applications to fuze technology. The laser system produced 100- to 150-fs pulses of 820-nm light at a repetition rate of 1 kHz. Maximum energy per pulse was 3.5 mJ. The samples were 6.35-mm-diam, 2-mm-thick, pressed pellets of various explosives mounted on stainless-steel substrates whose thickness ranged from 0.1–1.2 mm. Various cutting rates were used with average power varying from 0.1W to 3W. The HE was easily cut at low power levels. At 0.5 W average power, one or two sweeps sufficed to cut most of the pellets. Experiments were also performed where we cut through both the HE pellet and the stainless-steel substrate from either direction. Explosives that were cut included high-surface-area PETN, LX-16 (96%PETN/4% FPC 461 binder), LX-14 (95.5% HMX/4.5% Estane), LX-15 (95% HNS/5% Kel-F), LX-17 (92.5% TATB/7.5% Kel-F), PBX-9407 (94% RDX/6% Exon 461), and pressed TNT. Absorption of such short pulses transfers virtually no heat to the material being cut; no evidence of HE burning or decomposition was observed on the cut surfaces. Numerous applications appear feasible for the processing of energetic materials, including HE machining and demilitarization operations.

In FY99, we expect to construct such a laser, along with an associated laboratory in the High Explosives Applications Facility (HEAF) that we anticipate will be very useful in our fuze technology work. The first application will probably be in the preparation of micro-wedges and very thin samples of initiating explosives to study the shock-to-detonation transition in initiating explosives. Laser cutting may be feasible for cutting initiating pellets out of a slab of pressed material, or in machining complex shapes. Another possibility is fabrication of precision barrels for slappers.

Summary and Conclusions

We continued our work in several areas of safe, arm, and fuze technology. The second generation R&D detonators from Kaman Aerospace Corporation continue to show very interesting performance. We used a Fabry-Perot velocimeter to measure slapper velocity-time histories and performed threshold testing using high-specific-surface-area PETN and HNS initiating pellets.

We continued to use our new, small-scale, HE performance test to measure the shock-wave pressure profile transmitted into a lithium fluoride (LiF) crystal by the detonating HE. This test is giving results that agree with calculations using accepted cylinder test data. We have performed many experiments on explosives in common use at LLNL to demonstrate the reproducibility of the results and to establish a database for determination of the equation of state of these explosives. We report briefly on a DOE project for testing detonator firing cables for aging-induced changes, called partial discharge testing. A new computer code is up and running that models the operation of slapper detonators by combining an electrical circuit model and an electrical model of the exploding bridgefoil into a 1D hydrodynamic

code. We are presently working on determination of appropriate model parameters and on developing a more convenient user interface for providing the input parameters to the code. At the request of DoD colleagues, we have coordinated safety and characterization tests on various energetic materials of interest. In thermal tests, the Reynolds HNS gave almost identical results to the Pantex HNS-IV.

Future Work

We plan to address the following tasks:

1. *Slapper detonator development.* We will continue working on technology for low-energy slapper detonators. This may include further work with Raymond Engineering on evaluation of their detonators. We also hope to bring some sub-nanosecond diagnostics to bear on evaluating the performance of these slappers.
2. *New slapper detonator models.* We will determine appropriate electrical model parameters for Cu and Al bridges and for Cu and Al equations of state. We also plan to improve the user interface for the code and hope to have a version we can distribute for beta testing by the end of FY99.
3. *Performance studies/new HEs.* We will continue to develop a database of HE performance using our small-scale test. We also plan to characterize new explosives that will be made by sol-gel processing and to investigate desensitization of explosives by sol-gel processing.
4. *Laser cutting/machining.* We have begun work on cutting and machining of HEs by high-power femtosecond laser pulses with very encouraging results. This work will receive Office of Munitions support during FY98, and we will continue our investigations on applications of this technology to fuze applications.

References

1. R. S. Lee and co-workers, "Safe, Arm, and Fuze Technology," *Munitions Technology Program Progress Report*, UCRL-ID-103482-97, Lawrence Livermore National Laboratory, Livermore, CA (1998).
2. Robert Tipton, *Modeling flux compression generators with a 2D ALE code*, UCRL-99900, Lawrence Livermore National Laboratory, Livermore, CA (1988).
3. J. W. Kury and co-workers, "Metal acceleration by chemical explosives," *Proc. 4th Symp. (Int.) on Detonation*, Naval Ordnance Laboratory, ACR-126, pp. 3–13 (1965).
4. L. C. Haselman, private communication, Lawrence Livermore National Laboratory, Livermore, CA (1996).
5. Ronald S. Lee, *FIRESET*, UCID-21322, Lawrence Livermore National Laboratory, Livermore, CA (1988).

6. Carlton M. Furnberg, private communication, Sandia National Laboratories, Livermore, CA.
7. Jack Cutting and co-workers, *LLNL characterization of HNS-IV with 2% Kel-F 800 binder for the Department of Defense Explosive hazard classification*, UCRL-ID-132711, Lawrence Livermore National Laboratory, Livermore, CA (1998).

V. Simulation Overview

ALE3D is a finite element code with Arbitrary Lagrange-Eulerian capabilities. It is being used for a variety of multidisciplinary simulations. It couples fluids and structures as well as providing thermal transport and chemical evolution. Much of the current effort is directed toward improving the user interface and documentation, adding or improving physical algorithms, and bringing the parallel version of the code to a state at which it can be distributed to external agencies. Progress this year includes additional material models and boundary conditions to treat special cases and further validation of code performance for specific classes of applications, particularly those requiring thermo-mechanical treatments. The parallel version of the code is now installed at one Department of Defense (DoD) facility.

The Dynamic Material Properties project currently has two thrust areas, both associated with the mechanical behavior of metals subject to high pressure shock loading and high deformation as a result of explosive loading. This is a topic of ongoing interest within both DoD and Department of Energy (DOE) programs. The first thrust area deals with the effects of strong shocks on the post-shock constitutive and failure behavior of metals. Copper has been selected as the initial material of choice because it is representative of the entire class of fcc materials and because it is commonly used as a shaped-charge liner material. The second thrust area is associated with the constitutive behavior of tantalum (Ta) and Ta-W alloys, materials used in explosively formed projectiles. Tantalum is also the material selected for study under a multiscale modeling Strategic Initiative at LLNL.

The effects of strong shocks on the post-shock constitutive behavior of metals are, by and large, unexplored technology. Based on preliminary results of our experimental work, we do know that strong shock can cause significant changes in the microstructure of copper, which in turn can significantly affect post-shock mechanical behavior. For example, shock pressures in the vicinity of 600 kbar and above have resulted in large amounts of mechanical twinning. We are conducting a series of shock recovery experiments to evaluate the effects of strong shock on post-shock constitutive behavior with emphasis on the evaluation of the effects of shock-induced changes in microstructure. We are also performing experiments to examine the effects of high heating rates (similar to those encountered in explosive deformation) on the high-strain-rate tensile rupture of copper and other materials. This effort is coupled with the work of Adam J. Schwartz (see Sec. I, Warhead Technology: "Liner Processing/Microstructural Effects") on the effects of microstructure and impurities on the ductile properties of highly shocked and deformed copper, as evaluated by its breakup behavior in a shaped-charge jet.

The constitutive behavior of polycrystalline Ta and Ta-W alloys has been an ongoing thrust area for this project. Recently, we showed that the constitutive response and failure behavior of Ta-W alloys is superior to that of unalloyed Ta. Unalloyed Ta is plagued by non-uniformities in microstructure that lead to erratic and unpredictable deformation and failure modes. We are now focusing on the constitutive response of single crystal Ta and Ta-W alloys. The overall goal of this work is to provide experimental data on yield and

work-hardening behavior of single crystals. This data will be used in the crystal plasticity modeling work of Dr. Scott Schoenfeld (ARL) and LLNL staff associated with the LLNL multiscale modeling program. We expect that crystal plasticity modeling will provide predictive capabilities needed to better understand the erratic behavior of unalloyed polycrystalline Ta. Gains in fundamental knowledge of the effects of microstructure on mechanical behavior will then form the basis for the development of new alloys.

ALE Hydrocode Development

Richard Couch, Richard Sharp, Ivan Otero, Juliana Hsu
Rob Neely, Scott Futral, Evi Dube, Tim Pierce
Rose McCallen, John Dolaghan, Brad Wallin, Albert Nichols
Lawrence Livermore National Laboratory
(925) 422-1655
couch1@llnl.gov

Introduction

Numerical simulation software utilizing arbitrary-Lagrangian-Eulerian (ALE) techniques have been under development for application to problems of direct interest to the DoD. The software is intended for both internal and external use. Emphasis has been placed on portability so that the coding can be run on a variety of hardware platforms and made available to the broadest spectrum of users.

The 3D ALE code ALE3D has been distributed to a number of DoD facilities and DoD contractors. Feedback from that community continues to define the development path for ALE3D. The initial focus during early stages of development was on efficient methods for performing analyses related to armor/anti-armor issues. Soon after distribution to DoD agencies began, the response from users made it apparent that the arenas in which a code with the features of ALE3D could make the greatest contribution were in the general area of fluid structure interactions. This category of applications includes blast loading of structures, underwater explosion effects, aero-structural interactions, weapon system vulnerability and lethality, and weapon design issues. A major effect of this guidance was to put greater emphasis on providing a robust structural analysis capability. The interest in vulnerability and lethality issues made it desirable to have available a thermal transport capability with reaction chemistry and an implicit dynamic solver.

The development of 3D simulation tools at LLNL in the areas of structural, fluid, and thermal analysis has followed the traditional path of first developing capabilities limited to the particular topic. DYNA3D is the culmination of two decades of research in structural analysis. TOPAZ3D is the equivalent tool for use in static-geometry, thermal transport simulations. CALE, a 2D finite-difference ALE code, provides the heritage for a fluid mechanics capability. ALE3D has been developed as a means of merging many of the capabilities developed in the individual technology areas. ALE3D was developed from a version of DYNA3D. It utilized the basic Lagrangian finite element techniques developed there, but has not maintained an identical set of algorithms as the two code efforts evolved along different paths. The treatment of solid elements, where fluid dynamics is treated, has been completely rewritten. The coding and the available models for treating beam and shell elements have been kept consistent with the equivalent DYNA3D models, although only a subset are currently available. Fluid mechanics and ALE techniques from CALE were

modified for application to unstructured meshes and incorporated into ALE3D. A version of TOPAZ3D has been incorporated into ALE3D to provide a thermal transport capability. The TOPAZ3D package has been enhanced by the inclusion of a reaction chemistry module. These capabilities are utilized in a split operator mode whereby the operator can be applied at a time interval that is appropriate for thermal effects and need not be consistent with the time step for the dynamics. Thermal and structural analysis techniques are generally developed first in DYNA3D and TOPAZ3D, then migrated to ALE3D as required. In addition, an implicit dynamic solution scheme is being specifically developed for ALE3D.

ALE3D is a finite element code that treats fluid and elastic-plastic response on an unstructured grid. The grid may consist of arbitrarily connected hexahedral, shell and beam elements. There is currently no allowance for tetrahedra or wedge shaped elements. The mesh can be constructed from disjoint blocks of elements that interact at the boundaries via slide surfaces or other types of boundary conditions. Nodes can be designated as relax nodes, and ALE3D will adjust their position relative to the material in order to relieve distortion or to improve accuracy or efficiency. This relaxation process can allow nodes to cross material boundaries and create mixed or multi-material elements.

The interaction at slide surfaces can consist of pure sliding in which there are no tangential forces on interface nodes, or the nodes may be tied to inhibit sliding entirely, a coulomb friction algorithm can be used, or turbulence models can be applied. Voids may open or close between the surfaces depending on the dynamics of the problem, and there is an option to allow a block to fold back on itself (single-sided sliding). Where no void is present, as is the case in most fluid/structure interactions, the forces on either side of the slide surface are accumulated and used to produce a net acceleration of the nodes on the surface consistent with the center-of-mass motion. In this manner the dynamics of both the fluid and structure are treated in a consistent manner. No advection is allowed across slide surfaces.

The basic computational step consists of a Lagrangian step followed by an advection, or remap step. This combination of operations is formally equivalent to an Eulerian solution while providing increased flexibility and, in some cases, greater accuracy. In the Lagrangian phase, nodal forces are accumulated and an updated nodal acceleration is computed. Following DYNA3D, the stress gradients and strain rates are evaluated by a lowest order finite element method. A diagonal mass matrix is used. Second-order accuracy is obtained with a grid that is staggered in both space and time. The stress tensor for the elastic-plastic material strength model is integrated by an incremental strain method. The Jauman rate derivative is used for the stress tensor, and the von Mises yield condition is applied.

At the end of the Lagrangian phase of the cycle, the velocities and nodal positions are updated. At this point several options are available. If the user wishes to run the code in a pure-Lagrangian mode, no further action is taken and the code proceeds to the next time step. If a pure-Eulerian calculation is desired, the nodes are placed back in their original positions. This nodal motion or relaxation generates inter-element fluxes that must be used to update velocities, masses, energies, stresses, and other constitutive properties. This re-mapping process is referred to as advection. Second-order-accurate schemes are required to perform this operation with sufficient accuracy. In addition, it is not generally adequate to allow

advection only within material boundaries. ALE3D has the ability to treat multi-material elements, thus allowing relaxation to take place across material boundaries.

The full potential of the ALE approach is realized when the code user has options available to tailor the evolution of the mesh to maximize either efficiency or accuracy. In the simplest implementation, the code is instructed to relax nodes as required to eliminate distortions in the mesh. A more powerful approach has the code relax nodes on the basis of an optimization scheme. To this purpose ALE3D utilizes a finite-element-based equipotential method developed by R. Tipton. This method accommodates weighting functions that can be used to optimize the mesh based on some defined criterion. ALE3D currently allows weighting by pressure, by artificial viscosity, by plastic strain, by material number, and along designated slip surfaces. The solution will result in a more highly resolved mesh in the volumes containing the highest weights. This provides a form of dynamic mesh refinement. This technique has proved useful in improving the effective resolution in shock tracking simulations. There are also a number of options available for selecting predetermined or dynamically programmed mesh evolution in cases where that is appropriate.

ALE3D Activity in FY98

Tabular EOS with Compaction

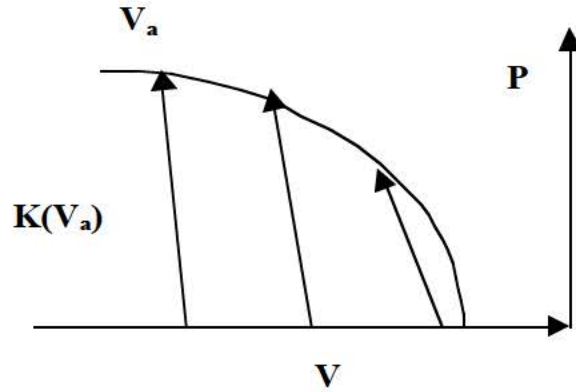
This model provides an equation of state that can be used to represent crushable materials such as foams and other porous media. It reproduces the functionality of EOS 8 in DYNA3D; however its implementation differs somewhat. In DYNA3D, the model parameters are input as functions of the volumetric strain; in ALE3D, the representation is in terms of the relative volume. Two representations of a constitutive model are available to represent strength of materials. This model can be used to reproduce much of the functionality of the DYNA3D model 5 by inputting a table of yield strength versus pressure. If this table has not been entered, the code assumes a model that is identical to the bilinear yield strength provided by material model 12.

The pressure along an initial loading curve is defined by

$$p = C(V) + \gamma T(V)E \quad (1)$$

where $C(V)$ and $T(V)$ are tables of value versus relative volume. E is the internal energy and γ is a constant. The code stores the minimum relative volume attained by an element. If the relative volume exceeds the minimum attained value, the material in the element unloads with a bulk modulus obtained from the table for $K(V)$.

The value of K , the bulk modulus is obtained by interpolating in the table with the minimum attained relative volume. The material will reload with this same bulk modulus until it reaches the minimum relative volume, at which point it again loads using the expression for the initial loading curve. This behavior is represented in the following diagram.



The constitutive model that is identical to that of model 12 produces a bilinear elastic plastic response of the form

$$\sigma = \sigma_0 + E_p \varepsilon \quad (2)$$

where the plastic hardening modulus is given by

$$E_p = \left(\frac{EE_T}{E - E_T} \right) \quad (3)$$

where E is Young's modulus, E_T is the tangent modulus, ε is the effective plastic strain, and σ_0 is the initial yield stress.

Navier-Stokes Viscosity

A Navier-Stokes viscosity treatment is available in ALE3D. This feature is occasionally referred to as “real” viscosity, in order to differentiate it from the “artificial” viscosity used in shock hydrodynamics. The values of the viscosity coefficients are associated with materials and are input for each material for which the viscous treatment is desired.

The current implementation allows the user to define the temperature dependence for only the shear coefficient. Three temperature dependent models are available:

$$\mu = \mu_0 \left(\frac{T}{T_0} \right)^n \quad , \quad (4)$$

$$\mu = \mu_0 \frac{\left(\frac{T}{T_0} \right)^{\frac{3}{2}} (T_0 + S)}{T + S} \quad , \text{ and} \quad (5)$$

$$\mu = \mu_0 \exp \left[a + b \left(\frac{T_0}{T} \right) + c \left(\frac{T_0}{T} \right)^2 \right] \quad . \quad (6)$$

If viscosity is requested, the code will place the viscous stress components in the stress deviator fields for plotting purposes. An array called “visc” is created to hold the net zonal viscosities. This array is available for plotting. No versus time plots are currently available. Mixed zones are treated by volume weighting the component viscosities in the mixed zone. The viscous heating terms are apportioned to the components in a mixed zone by volume weighting.

This model has been used for a number of fluid flow simulations. It can be used in concert with all other features in the code including slide surface treatments and heat transfer.

3D Simulation of Shaped Charges

(b)(3)

Such a simulation is illustrated in Figures 1–3. In this case, a three-dimensional perturbation was purposely imposed on the geometry in order to evaluate the effect on jet shape. Figure 1 illustrates the material boundaries at the initial configuration. Figure 2 illustrates the shape of the jet when it is fully formed. A comparison between the calculated and experimental jet aspect ratios is shown in Figure 3.



Figure 2. A material plot illustrating the jet in its fully formed stage.

(b)(3)

Web Site Development

The user documentation for ALE3D is being recast into a form more consistent with on-line, browsable information. The original user's manual was written in the traditional "book" format. It became a massive document in which it was difficult to find the needed information. It was adequate for providing information on available parameters, but light on providing guidance on how and when to use them. The new version is broken into a number of files, each covering a specific topic that is explained in greater detail than previously. These files are then organized into functional families and converted to HTML format. The final product is accessible with readily available browsers. Approximately 95% of the code features have been documented in this format.

While not yet complete, the documentation is sufficient to allow useful access by the ALE3D collaboration community. The documentation is available at the web address: www.llnl.gov/bdiv/ale3d. A search feature has also been provided. The next step is to make the minor corrections required to produce the equivalent set of documentation in a form consistent with the parallel version of ALE3D. Once the documentation is complete, the next phase will focus on providing access to examples of classes of simulations with sample input files and graphical demonstrations of simulations.

Parallel Code Development

The parallel version of ALE3D is being written in C at the highest levels. Most of the lower level computational models can be incorporated essentially unchanged in their existing FORTRAN versions or written in C. Code modularity has been improved to facilitate development activities by our collaborators. Mesh decomposition, parallel I/O, and graphic rendering continue to be areas in which research is required. A significant component of our strategy is to utilize the concept of domain overloading. There need not be a one-to-one correlation between domains and processors. If one allows for multiple domains on a single processor, one can choose a domain size that optimizes computational efficiency for the processor/memory characteristics of a given platform. Having multiple domains on a single processor will also provide savings in overall memory usage.

Much of this year's activities have been devoted to development of the parallel version of the code. Beam and shell elements are not currently available, and a few material models have not yet been ported from the serial version of the code. General distribution of the parallel code will not be made until these deficiencies are remedied and the documentation is more complete. However, we will begin to release to code gradually to select users who are in a position to make use of it in the current state. The first release is scheduled for January, 1999.

Distribution

ALE3D has been provided to approximately 30 facilities. Most copies have gone to service laboratories and defense contractors, the rest to commercial industries or universities. The serial code is being run on several CRAY platforms, and on SGI, SUN, IBM, HP, and DEC workstations. It had not been available on PC platforms because of compiler limitations. Those limitations have recently been eliminated making a port to PC systems feasible, provided a Unix-like operating system is used. The parallel version has not been distributed yet.

ALE3D Activity — FY99

The focus in the coming year will be on continuing to improve the capabilities in the area of fluid/structure interactions. This includes better methods for treating structural response, with particular emphasis on development of a more complete set of material models consistent with the types of materials being encountered. The models for some materials must include failure criteria and the ability to track failure evolution. Thermo-mechanical modeling with reactive chemistry will continue to be a major focus area for application to a number of problems involving energetic materials. In the coming year, the transition to the parallel version of the code will continue to take place, eventually making the parallel version the sole vehicle for development.

Electron-Beam Heated Dynamic Tensile Experiments

David H. Lassila and Mary M. LeBlanc
Lawrence Livermore National Laboratory
(925) 423-9537
lassila1@llnl.gov



(b)(3)

(b)(3)

Experimental

Test Sample Preparation

Thin tensile samples (0.35 mm thick) were cut using wire electrical discharge machining (WEDM) from the copper study material. The geometry of the sample is shown in Fig. 2. The samples were then heat treated to develop either a 10- μm or 85- μm grain size. Photographs of the resulting microstructures are shown in Fig. 3.

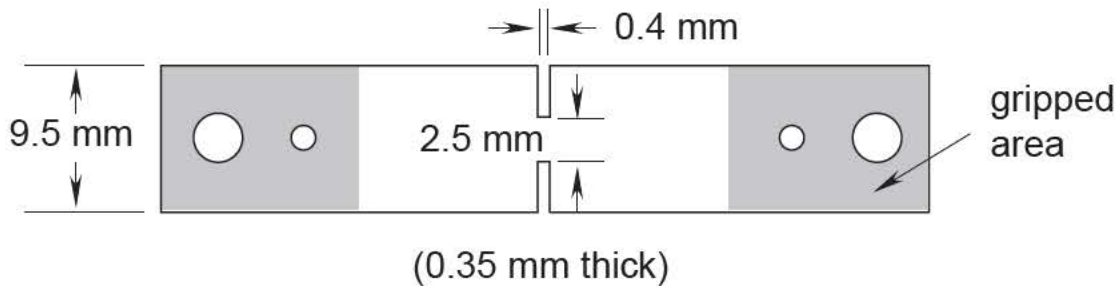


Figure 2. Test sample geometry. Foil tabs, 0.012 mm thick, were bonded to the sample in the gripping area to increase the sample thickness.

After heat treatment, the sample faces were mechanically abraded to reduce the WEDM surface roughness and to prepare the surfaces for bonding. Foil tabs were glued to the sample ends to increase the thickness in the gripping regions. Gas fusion (LECO) analyses were performed to determine the interstitial content of the materials, as shown in Table 1.

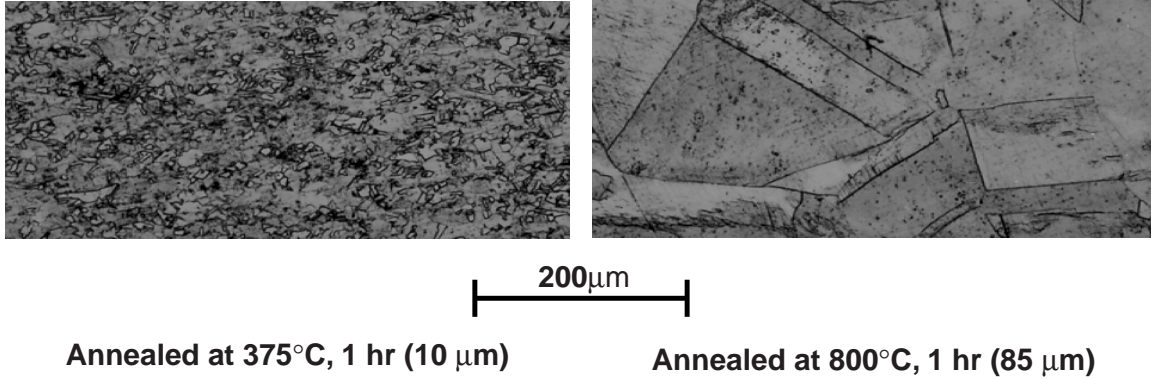


Figure 3. Micrographs of the test materials. Average grain size is 10 μm (left) and 85 μm (right).

Table 1. Interstitial content of test samples, as determined by LECO analyses.

Grain size (μm)	O (ppm)	N (ppm)	C (ppm)	S (ppm)
10	3.6	19	27	3
85	2.8	12	21	2

The samples were instrumented with two 0.003-in. diameter Type K thermocouples. One thermocouple was mounted on the front of the sample to one side of the gauge section. The second was mounted on the rear of the sample on the other side of the gauge section. In order to attach the thermocouples to the sample, a small pad of nickel-based powder braze alloy was wet to the surface using a Nd-YAG laser. The thermocouple wires were then individually laser-brazed to the pad. A photograph showing the installation is shown in Fig. 4.



Figure 4. Photograph of test sample showing a 0.003-in.-diam thermocouple attached at the lower right corner of the sample gauge section.

Portable Tensile Hopkinson Bar and Electron Beam

A portable Hopkinson bar apparatus was developed to subject the samples to rapid tensile loading. A schematic of the apparatus is shown in Fig. 5. The test sample is fastened in serrated-faced grips between the incident and transmitter bars. The section of the incident bar between the clamp and the end of the reaction tube is stretched using a portable hydraulic cylinder and hand pump. The locking nut on the end of the incident bar is then tightened to hold the elastic strain in the bar. To release the elastic energy, a second hydraulic cylinder is used to fracture a notched bolt in the clamp. The clamp opens, allowing the elastic strain to propagate down the incident bar to the test sample. The maximum duration of loading for this system is about 300 μs .

A pair of strain gauges mounted on the incident bar between the clamp and sample is used to detect the strain as it propagates toward the sample. This signal is used to trigger the electron beam that heats the sample. The time between heating and the onset of loading varies between 0 μs and 10 μs , depending upon how cleanly the clamp opens.

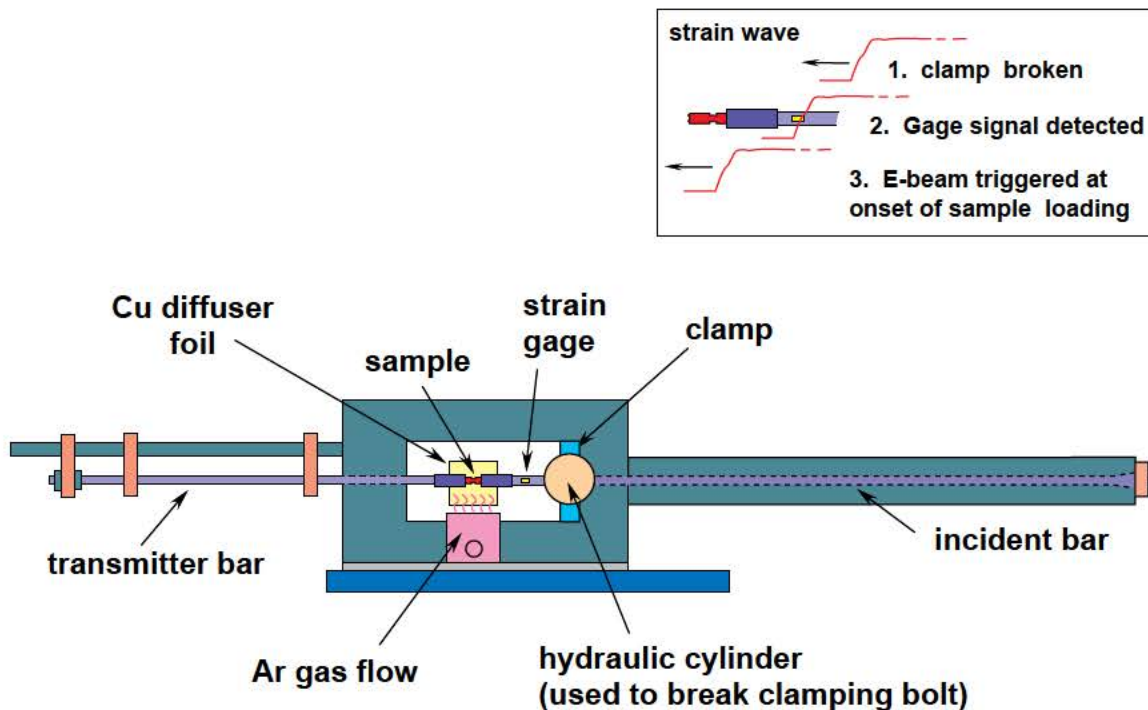


Figure 5. Schematic of the apparatus used for tensile loading.

The Troll accelerator [6] at the Sandia National Laboratories, Albuquerque, was used to heat the samples for these experiments. The Troll uses a Marx generator to drive a multi-microsecond electron beam diode. The Troll operates at 3 MV and 1.3 kA with a characteristic discharge duration of 6 μs . The pulse duration can be shortened to approximately 1 μs by triggering a diverter switch that shorts the generator output to ground (Fig. 6). A DC coil located outside the diode tank is used to focus and position the beam. The beam diameter at the location of the test sample is on the order of 1 cm.

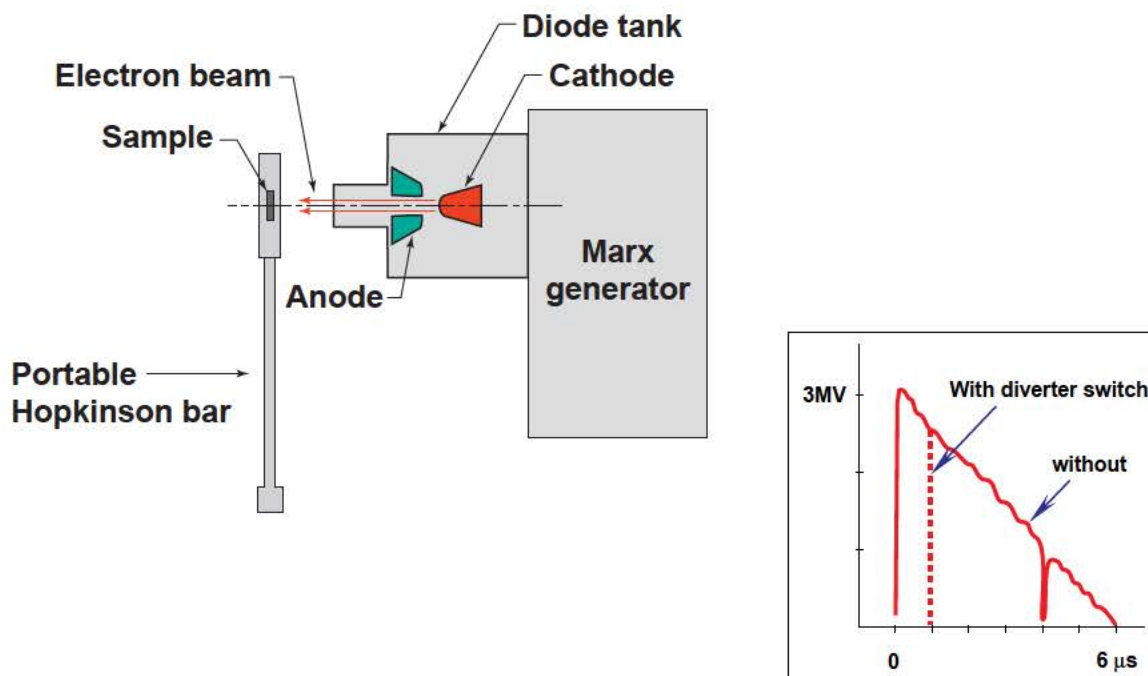


Figure 6. Schematic of the portable Hopkinson bar with beam energy/voltage vs. time (insert). The operation of the diverter switch results in a more uniform beam energy, and consequently more uniform heating of the test sample.

Layers of copper foil tape 0.2 mm to 0.3 mm thick were placed in front of the sample to attempt to attenuate the less energetic portion of the beam, thereby improving the temperature distribution through the sample thickness.

The test samples were subjected to flowing argon gas during prior to heating and during the period of time after fracture, primarily to reduce the amount of oxide formation on the fracture surfaces.

A total of 10 samples were successfully tested (5 each of the 85- μm and 10- μm grain size). The output of the incident bar gauges was recorded to determine the time from heating to onset of deformation. The output of the thermocouples attached to the sample was also recorded, which indicated that the heating of the samples in the gauge section is not uniform. A typical result is shown in Fig. 7. Lateral differences occurred due to changes in the beam position from shot to shot. Temperature differences through the thickness are likely caused by variation in energy deposition in the sample with depth. In instances where the diverter switch failed to operate and the entire 6- μs pulse was directed at the sample, spall and melt of the front of the sample frequently occurred. Using the diverter switch resulted in a 1- μs pulse duration and the front thermocouple recorded a higher temperature at the time of deformation than the rear thermocouple. The difference in temperature front to back was estimated to be as much as 250°C at the time of fracture.

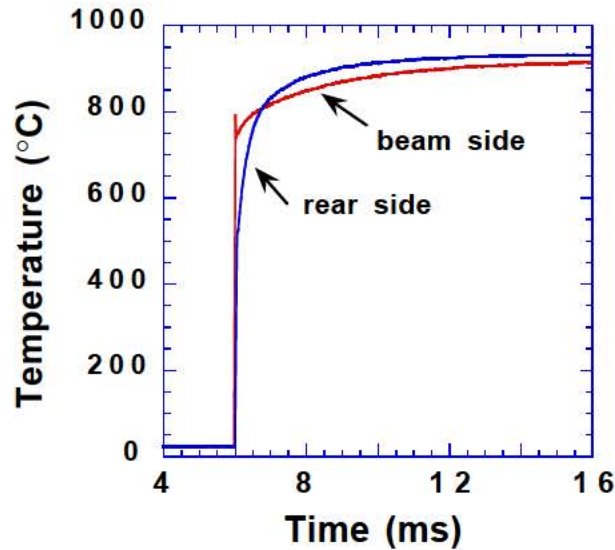


Figure 7. Temperatures measured on the front (beam) and rear sides of an 85- μm grain size sample.

Fracture Behavior and Discussion

After the test, the sample ends (fracture surfaces) were examined and photographed using scanning electron microscopy (SEM) to determine the reduction in area at the fracture surface morphology. The reduction in area as a function of temperature (taken as the average of the maximum front and rear temperature measurements) is shown in Fig. 8. A significant drop in ductility in the large grain size material at approximately 850°C was found to be a result of grain boundary failure, as illustrated in the micrographs shown in Fig. 9. The fracture behavior of both large- and small-grain size materials at a test temperature of 925°C is compared in Fig. 10. This comparison clearly shows the relative reduction in ductility of the large grain size material due to the intergranular fracture mode. However, upon close inspection using higher magnification, the fracture behavior of the small grain size copper also appeared to have a “brittle” appearance, although no discernible grain boundaries were observed (Fig. 11).

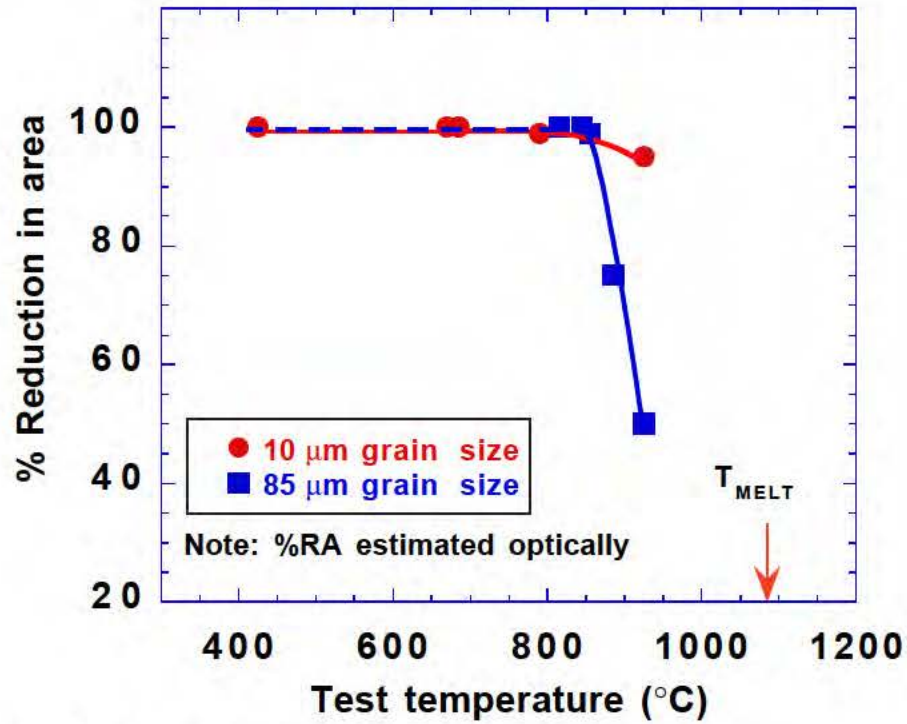


Figure 8. Change in fracture mode with temperature.

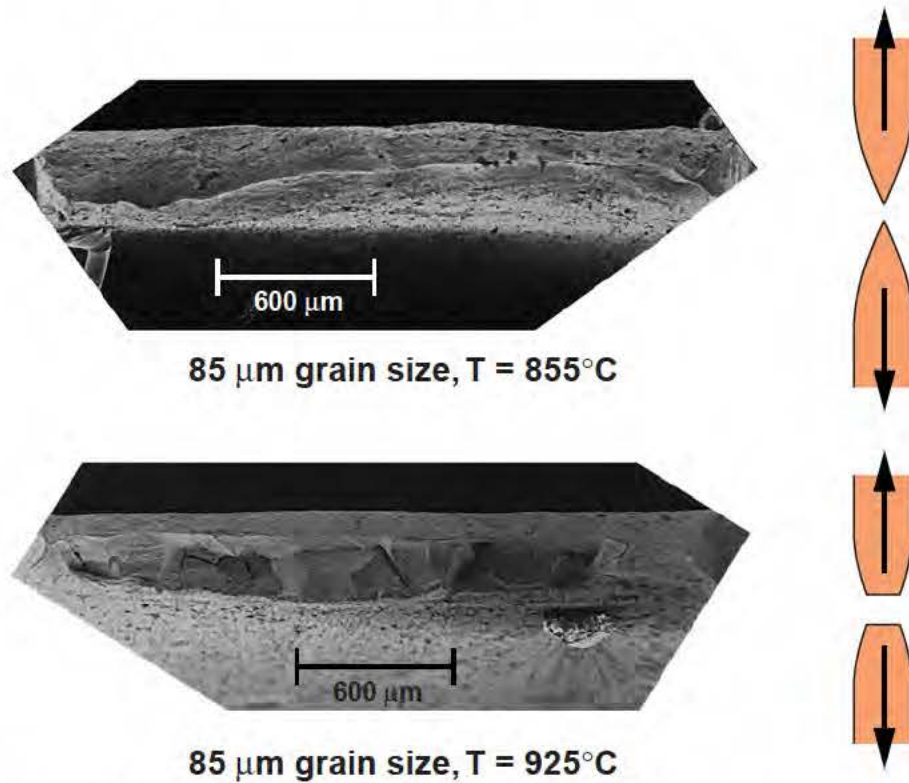
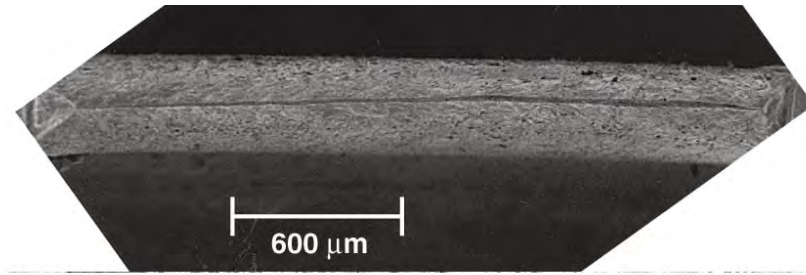
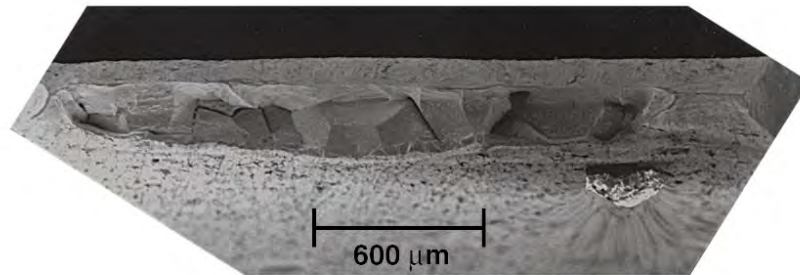


Figure 9. Fracture modes of 85-μm grain size copper. At a test temperature of 855°C, the fracture was a completely ductile process. In contrast, the fracture at 925°C was dominated by an intergranular fracture mode.



10 μm grain size, $T = 925^\circ\text{C}$



85 μm grain size, $T = 925^\circ\text{C}$

Figure 10. Comparison of the fracture behavior of small and large grain size materials, both tested at 925°C. The intergranular fracture mode dominated the fracture process of the large grain size material.

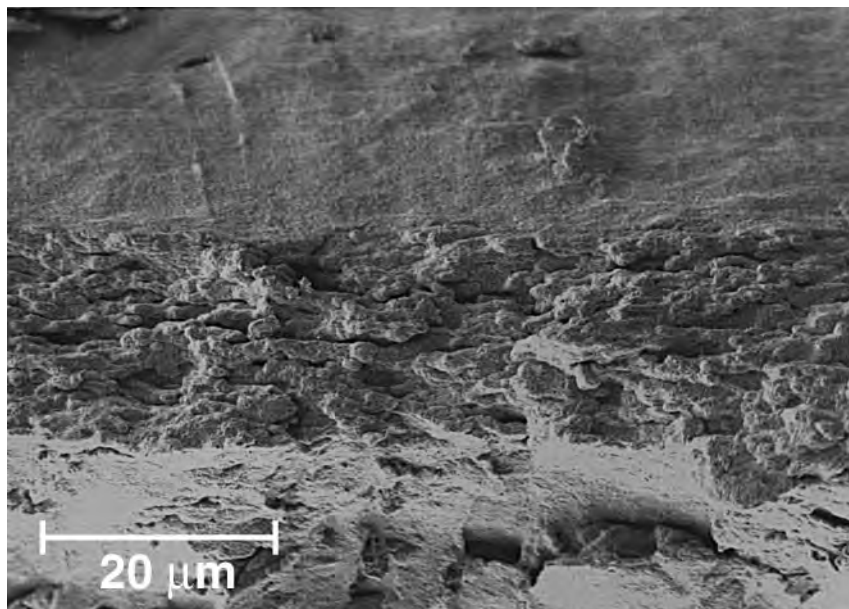


Figure 11. High magnification SEM image of a small grain size fracture surface (test temperature = 925°C). Although the reduction of area was large, there is clearly a “brittle nature” to the fracture surface.

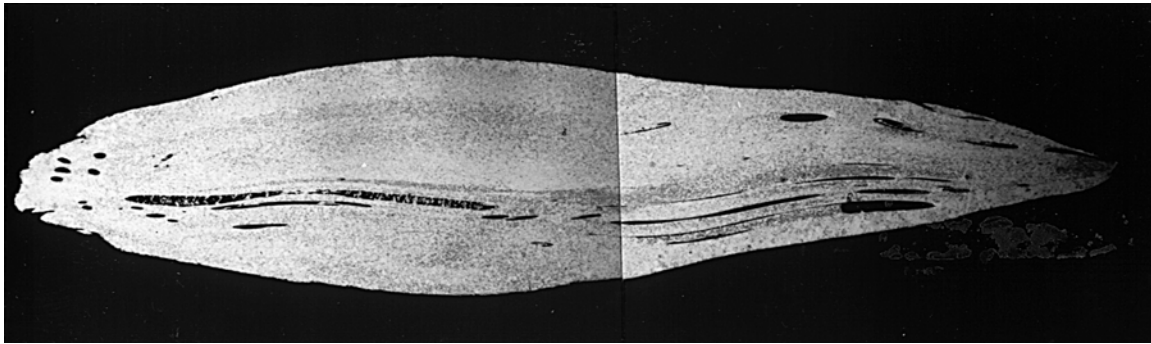
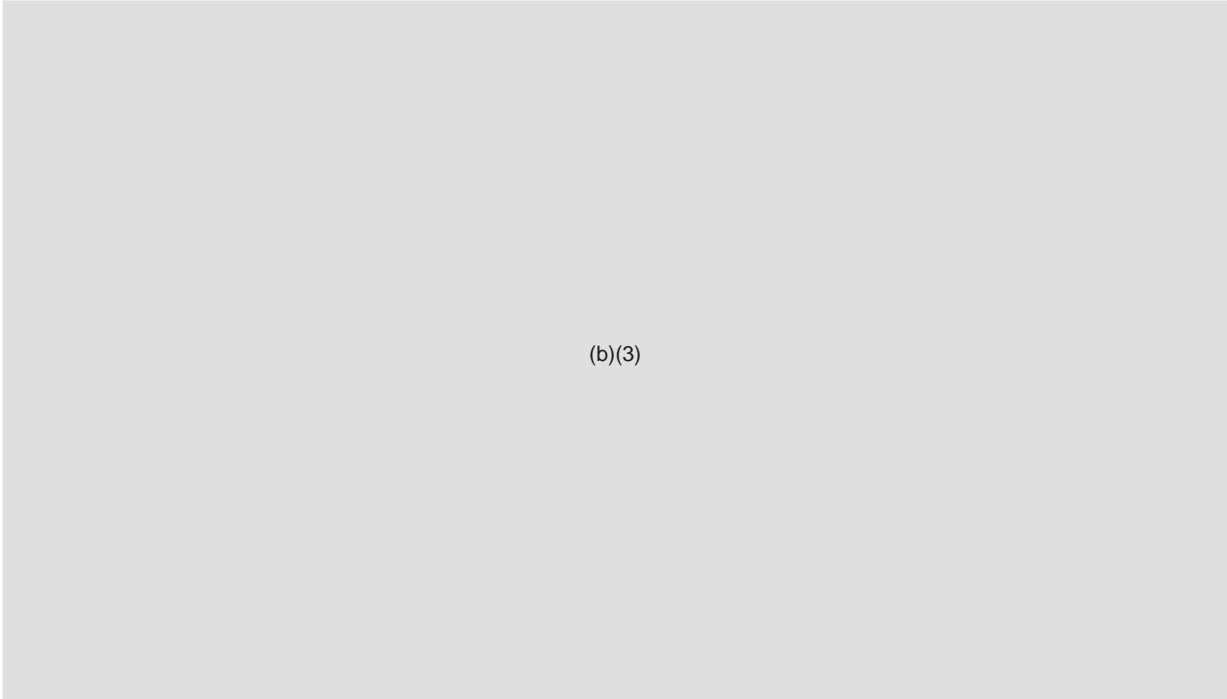


Figure 12. Micrograph of a recovered OFE copper jet particle.

Acknowledgments

The authors gratefully acknowledge the following individuals for their contributions to this work: Bob Turman and Isidro Molina for the reconstruction and operation of the Troll accelerator at SNLA, Carl Westrich and Eric Ziebarth for the laser brazing operations, James Ferriera for the SEM work, Robert Kershaw for the metallographic examinations, and Daniel Greenwood for instrumentation support.

The DoD contacts for this thrust area are E. J. Baker and James Pearson, ARDEC.

References

1. W. G. VonHolle and J. J. Trimble, "Shaped Charge Temperature Measurement," *6th International Symposium on Detonation*, Naval Surface Weapons Center ACR-221 ONR (1976).
2. D. J. Nikkel and D. H. Lassila, "Effect of Pressure-Dependent Constitutive Behavior on the Calculated Temperature of Shaped Charge Jets," *Proceedings of the APS Topical Conference on Shock Compression of Condensed Matter*, Colorado, American Institute of Physics, New York (1994).
3. A. Lichtenberger, "Some Criteria for the Choice of Shaped Charge Copper Liners," *Proceedings of the 11th International Symposium on Ballistics*, Vol. II, Brussels, Belgium (1989).
4. D. H. Lassila, E. L. Baker, D. K. Chan, W. E. King, and A. J. Schwartz, "Effect of Sulfur on the Ductility of Copper Shaped Charge Jets," *16th International Symposium on Ballistics*, September 23, 1996.
5. A. J. Schwartz, D. H. Lassila, and E. L. Baker, "Analysis of Intergranular Impurity Concentration and the Effects on the Ductility of Copper Shaped Charge Jets," *Proceedings of the 17th International Symposium on Ballistics*, Midrand, South Africa, March 23 - 27, 1998, Ed., C. Van Niekerk, International Ballistics Committee, Vol. 2, pp. 439-446 (1998).
6. R. S. Clark, M. T. Buttram, J. V. Poukey, and T. R. Lockner, "A Multi-Megavolt, Two Microsecond Electron Beam Diode," *6th IEEE Pulsed Power Conference*, Washington, D.C., June 1987.
7. D. H. Lassila, "Material Characteristics Related to the Fracture and Particulation of Electrodeposited-Copper Shaped Charge Jets," *International Conference on Shock-Wave and High-Strain-Rate Phenomena in Materials (EXPLOMET '90)*, San Diego, CA, August 12-17, 1990.
8. D. H. Lassila, "Correlations Between Shaped Charge Jet Breakup and Grain Boundary Impurity Concentrations," *13th International Ballistic Symposium*, Stockholm, Sweden, June 1-3, 1992.
9. D. H. Lassila, W. Walters, D. Nikkel, and R. Kershaw, "Metallurgical Examination of Recovered Copper Jet Particles," internal ARL report, Lawrence Livermore National Laboratory, 1995.

Shock Induced Plastic Deformation of Tantalum

Peter S. Fiske, Neil Holmes, and David Lassila
Lawrence Livermore National Laboratory
(925) 422-7489
fiske1@llnl.gov

Introduction

Accurate modeling of many phenomena related to dynamic deformation and failure requires a precise understanding of material behavior at strain rates on the order of 10^5 s^{-1} . This is a typical plastic strain rate when metals are shock loading in the “weak shock regime.” The weak shock regime is defined as the range of intermediate pressures in which a material is shocked above its Hugoniot elastic limit (HEL) but below the pressure in which a single strong shock wave is developed in the material. The elastic “precursor” wave propagates at a higher velocity than the plastic deformational wave (which may or may not be steady). In a recent study of the dynamic properties of Ta in the weak shock regime, Furnish et al. noted a discrepancy in the relative timing of the elastic and plastic waves predicted by calculation and as measured using VISAR [1]. We carried out a series of experiments and calculations to verify this discrepancy and evaluate the possible influence of crystallographic texture on elastic and plastic wave speeds in Ta. Ultimately, the data from these experiments will be used to both develop and validate material models for polycrystal bcc metals, such as the Steinberg-Guinen-Lund rate dependent model. The principal goal of the single crystal studies is to support single crystal plasticity models in use at the Army Research Laboratory by Dr. Scott Shoenfeld for Taylor theory analyses and other homogenization schemes. This work is also of interest to Dr. Joe Foster at Eglin AFB.

This year, we completed design and construction of new experimental facilities that allow us to carry out controlled impact experiments in the velocity range of 200–1200 m/s. Specific achievements include:

- Design and installation of a new gas breech system for low-velocity launch
- Design and fabrication of a new target and alignment system
- Installation and testing of a new VISAR system.

Using this system, we carried out shock compression experiments on polycrystalline Ta in both the spall and release configuration. We compared these results to computer calculations. Specific scientific achievements include:

- Impact experiments on polycrystalline Ta in the spall and release configuration
- Modeling of shock wave profiles using an explicit 1D computer code
- Analysis of discrepancies between experiment and calculation.

Procedures, Results, and Discussion

Disks of polycrystalline Ta ($3 \text{ mm} \times 30 \text{ mm}$) were cut from known materials and polished to remove surface damage. Acoustical properties were measured using the Papadakis technique. Rolled Ta plate is known to exhibit significant textural anisotropy that leads to non-uniform strain during mechanical testing [2]. Acoustical tests detected slight shear wave echoes caused by reflections within the sample, indicating possible crystallographic banding.

Samples were shock-loaded to pressures in the range of 4–11 GPa using Lexan and sapphire impactors. Shock wave profiles were measured using a VISAR system and wave speeds were independently timed using piezoelectric signal pins.

The experiments shown in Fig. 1 were carried out in both a spall configuration (free rear surface) and release configuration (with a window on the rear surface).

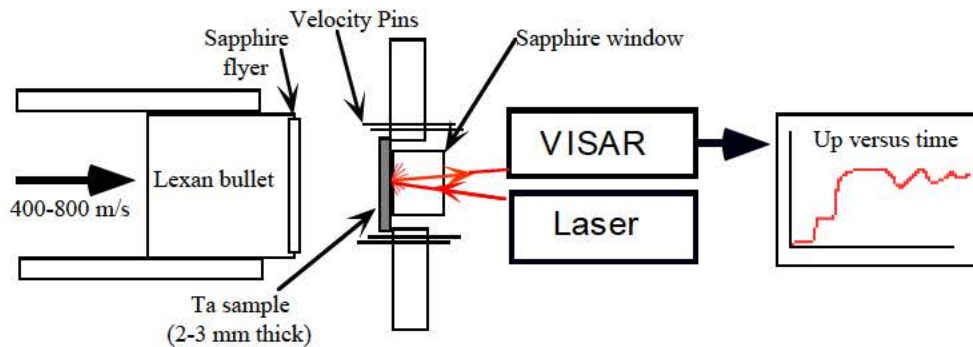


Figure 1. Diagram of experimental configuration.

Figure 2 shows the discrepancy in the relative timing of the elastic and plastic waves predicted by calculation and as measured using VISAR in previous studies of the dynamic properties of Ta by Furnish et al.

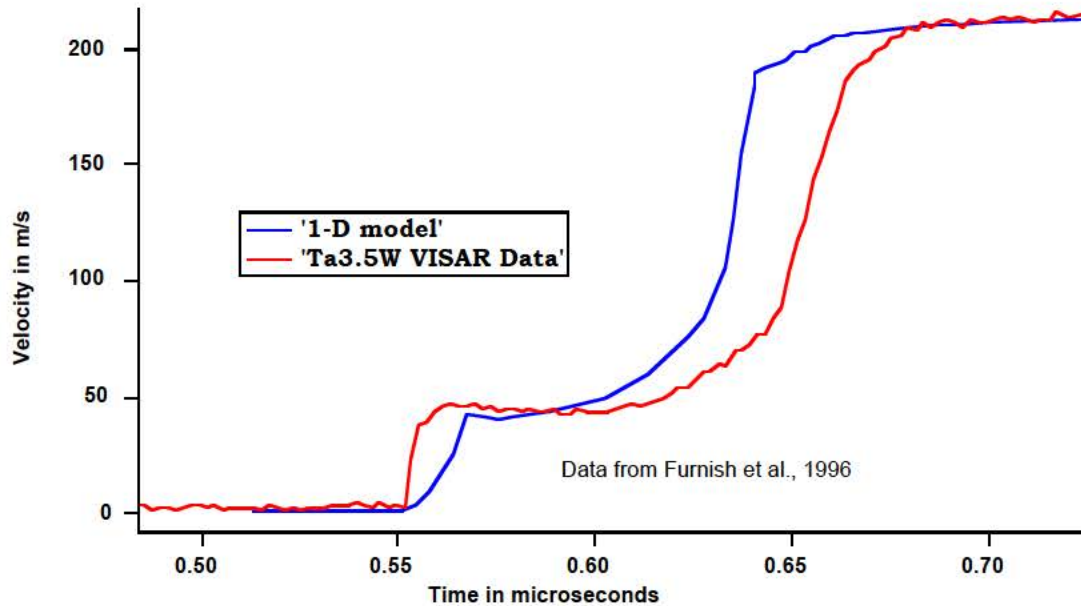


Figure 2. 1D calculation and VISAR measurement of plastic wave offset in Ta3.5%W alloy differ significantly [1].

Our preliminary results on polycrystalline Ta confirm the reported discrepancy with the plastic wave arriving later, and rising more gradually, than predicted by calculation (Fig. 3).

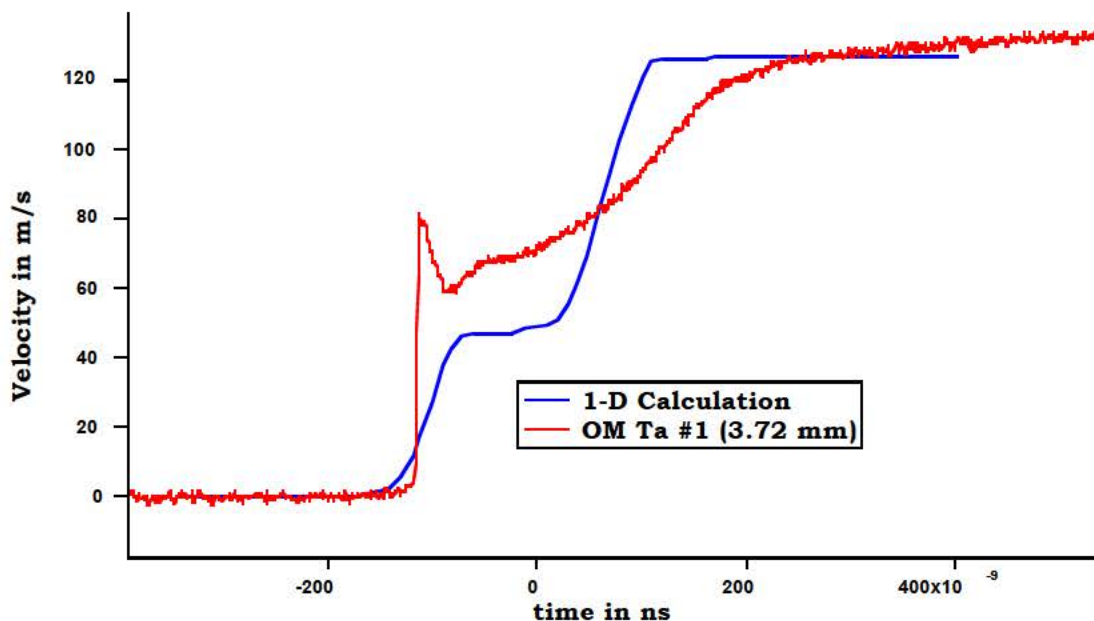


Figure 3. Comparison of shock wave profiles in Ta measured with VISAR and calculated using an explicit 1D code.

Goals for FY99

We will continue our study of dynamic deformation of Ta with a series of shock experiments on oriented, single-crystal Ta. We will use these data to constrain orientational effects on plasticity, work hardening, and spall strength. We will also carry out a study of the effect of temperature on the plasticity and yield of polycrystalline Ta. Using 1D and possibly 3D computer code calculations, we will simulate these results and further test strength and plasticity models.

References

1. M. D. Furnish, D. H. Lassila, L. C. Chhabildas, and D. J. Steinberg, "High Pressure Science and Technology—1995," S. C. Schmidt and W. C. Tao, Eds., pp. 527–530, AIP, Washington, D.C. (1996).
2. A. J. Schwartz, D. H. Lassila, and M. M. LeBlanc, *Mat. Sci. Eng.*, **A244**, 178 (1998).

Mechanical Behavior of Orientated, Single Crystal Tantalum

Adam J. Schwartz, W. E. King, G. H. Campbell, Mary M. LeBlanc, and David H. Lassila
Lawrence Livermore National Laboratory
(925) 423-3454
schwartz6@llnl.gov

Introduction

There is an increased interest in using single-crystal constitutive behavior in continuum computer code to predict the macroscopic plastic properties of polycrystal metal. This involves the use of homogenization schemes such as Taylor theory, Sacks theory, and the so-called self-consistent theory. Work at the Army Research Laboratory (ARL) under the direction of Dr. Scott Schoenfeld is currently using this approach to examine the effects of the crystallographic texture of the non-axisymmetric formation of explosively formed penetrator (efp) and shaped-charge jets.

The use of Taylor and other homogenization theories to predict the plastic properties of polycrystals requires a constitutive model for the plastic properties of the constituent single-crystal metal that comprises the polycrystal material. The development of a single-crystal constitutive model in turn requires mechanical test data, just as polycrystalline constitutive models do. The work described in this report is the beginning of the LLNL effort to support the database used to construct and validate single-crystal constitutive models. A more detailed account of this work, and of the OIM results in particular, will be published in the Proceedings of the fall 1998 meeting of the Materials Research Society [1]. Advance copies of the MRS paper can be obtained by contacting Dr. A. Schwartz at LLNL.

We report on deformation experiments on tantalum (Ta) single-crystal cylinders oriented with $[011]$ parallel to the cylinder axis. The samples were deformed 10%, 20%, and 30% in compression, and took on an ellipsoidal shape during testing, elongated along the $[100]$ direction with almost no dimensional change along $[0\bar{1}1]$. Orientation Imaging Microscopy (OIM) data were collected on a transverse section of the deformed materials. OIM reveals patterns of alternating crystal rotations that develop as a function of strain and exhibit evolving length scales. The spacing and magnitude of these alternating misorientations increase in number density and decrease in spacing with increasing strain; they are believed to be related to the evolution of dislocation substructure.

Experiment

Single Crystal Preparation

The single-crystal Ta was grown at the Institute for Solid State Physics (ISSP) in Chernogolovka, Russia, from “ballistic grade” polycrystalline Ta (Cabot Corporation). Single crystals with various orientations were produced by a standard float zone technique, whereby the molten zone was created by electron beam heating. During crystal growth, the stock Ta was purified with respect to substitutional elements by virtue of zone refining inherent in the process. The crystals produced were approximately 18 mm in diameter and 200 mm in length. Each slice for compression testing was oriented using Laue back-reflection x-ray diffraction. After alignment on the Laue camera, the sample and mounting fixture were transferred as a single unit, and slices were sectioned approximately 5.1 mm thick using wire electrical discharge machining (WEDM). Compression cylinders approximately 5.47 mm in diameter \times 4.65 mm long were cut by WEDM from the single-crystal disks, and then machine turned to near final length and diameter. The diameters were polished with 1200 grit SiC paper followed by Super Blau metallputz paste. The ends were lapped flat and parallel using 1200-grit paper to within 0.01 mm.

The relevant interstitial impurities in Ta (H, C, N, O, and perhaps He) were present in the as-grown single crystals at levels between 10 and 100 ppm by weight. It is well established that the mechanical behavior of bcc metals such as Ta is significantly affected by interstitial impurities at levels both higher and lower. Our first strategy was to reduce the interstitial impurities to gain a more fundamental understanding of the mechanical response of orientated Ta single crystals. Attempts were made to purify the single-crystal Ta by decarburization using an oxygen environment and subsequent outgasing by an ultra-high vacuum (UHV) anneal. However, gas fusion analyses (LECO) confirmed that these attempts were not successful and the interstitial content of the gas impurities remained on the order of 10–100 ppm by weight after purification attempts. On the bright side, these are the levels of these impurities in typical ballistic grade polycrystal Ta. Because of this, the mechanical test data is particularly relevant in the evaluation and validation of crystal plasticity models used to model ballistic grade Ta.

Mechanical Testing

A series of mechanical tests aimed at understanding the deformation behavior of high-purity tantalum single crystals was undertaken. Quasistatic compression tests were performed using an Instron 1127 short frame test machine in a subpress with tungsten carbide platens and an MTS 7.6-mm extensometer was used to measure the relative motion of the platens. Teflon tape was preloaded to 2045 kg for use as a lubricant. All of the results described here pertain to samples tested at room temperature at a strain rate of 10^{-3}s^{-1} .

The engineering and true stress-strain response of three [011] single-crystal compression samples is shown in Fig. 1. These purified specimens exhibit a minor yield drop, followed by a nearly linear region of hardening. At approximately 20% true strain, the stress-strain response begins to turn up and is believed to be due to platen friction [1].

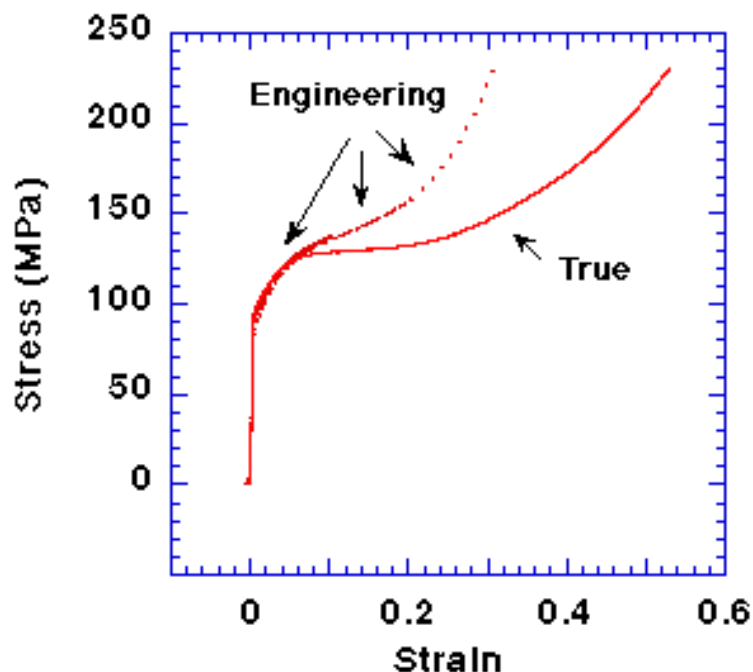


Figure 1. Room temperature stress-strain response of Ta [011] single crystals at a strain rate of 10^{-3}s^{-1} .

Orientation Imaging Microscopy

The objective of the OIM analysis was to explore the variations in local lattice rotations as a function of position in the sample and strain. The ovoid samples were sectioned along the plane containing [011] and [100] to reveal the longitudinal view. The unused half was again sectioned to reveal the transverse plane which contains $[0\bar{1}1]$ and [011]. These specimens were mounted in conductive epoxy and prepared for OIM examination using careful lapping procedures. Up to five individual OIM scans were required to cover the longitudinal section and two for the transverse section. Each individual scan was analyzed separately and plotted in terms of in-plane and out-of-plane rotation angles. These overlapping maps were then aligned to assemble an overall collage.

Figure 2 illustrates the measured lattice rotations of the [011] specimen compressed 10% with a misorientation scale of 0 to 5 degrees. These three scans have step sizes between 13 and 15 microns. In the longitudinal plane, rather sharp changes in crystal orientation ($\sim 1^\circ$) are observed that appear to be geometric in nature and emanate at 45° from the top and bottom corners. These features, which do not appear to correspond to the traces of either the {110} or {112} slip planes, appear early in deformation and persist throughout. We observed a second type of contrast feature lying roughly perpendicular to the above features. This feature is characterized by relatively smaller changes in orientation ($\sim 0.5^\circ$). Of particular interest are the alternating orientation changes observed upon crossing several of these features. They suggest the existence of networks of dislocations with net alternating sign in order to accommodate the observed rotations. Essentially all of the rotations measured with OIM are about the $[0\bar{1}1]$ axis.

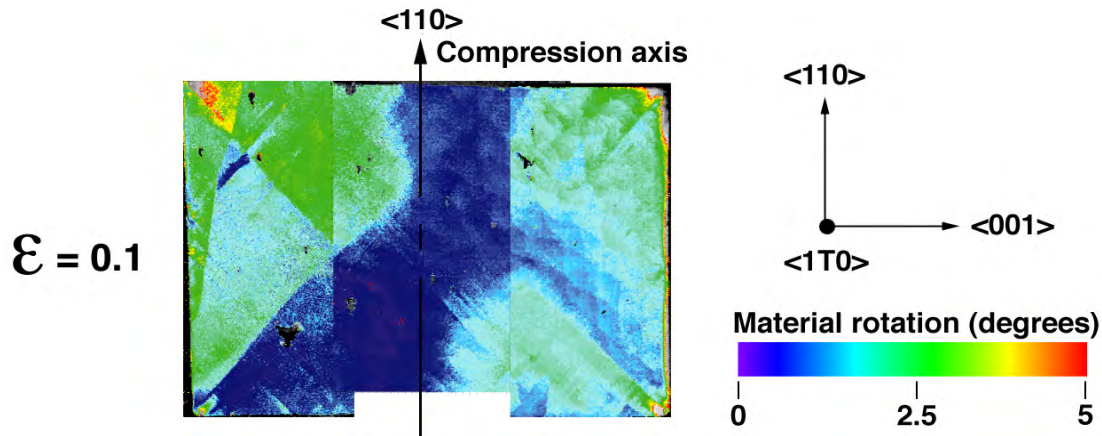


Figure 2. Misorientation collage of the 10% compressed sample, longitudinal view. Rather sharp changes in crystal orientation ($\sim 1^\circ$) are observed that appear to be geometric in nature and emanate at 45° from the top and bottom corners.

Figure 3 represents a collage of the four scans required to cover the 20% compressed specimen plotted on the misorientation scale from 0 to 10 degrees. The rotations are all about the $[0\bar{1}1]$ axis with the largest lattice rotations occurring in the corners and prominent misorientation features emanating from the corners. The finer scale contrast features normal to these are more pronounced than the 10% compressed specimen. In addition, the spacing of these alternating misorientations is becoming smaller.

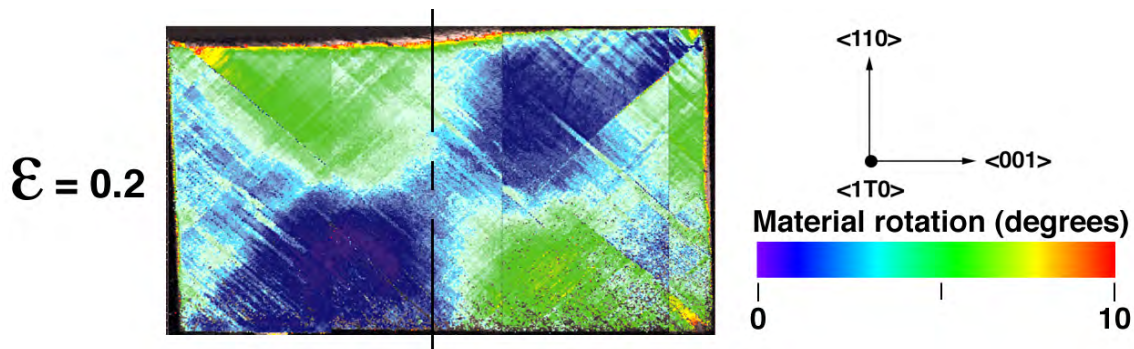


Figure 3. Misorientation collage of the 20% compressed sample, longitudinal view. The rotations are all about the $[0\bar{1}1]$ axis with the largest lattice rotations occurring in the corners and prominent misorientation features emanating from the corners.

Figure 4 reveals the longitudinal section of all but the final 300 microns on the right side of the specimen compressed 30%. This image spans a misorientation scale from 0 to 15 degrees. Greater than 15-degree rotations occur in the corners as well as at the ends of the horizontal midplane. Severe orientation changes are observed throughout this figure. Of particular interest is the approximately 5-degree alternating misorientations with width on the order of 70 microns. The spacing, magnitude, and angles of the alternating misorientations are observed to increase in number density and decrease in spacing with strain. Specifically, at 10% compression, the angle between primary bands is approximately 95 degrees. This decreases to 85 degrees and then to 80 degrees as the specimen is compressed to 20% and 30% deformation, respectively [2]. Observed rotations are about the $[0\bar{1}1]$ axis.

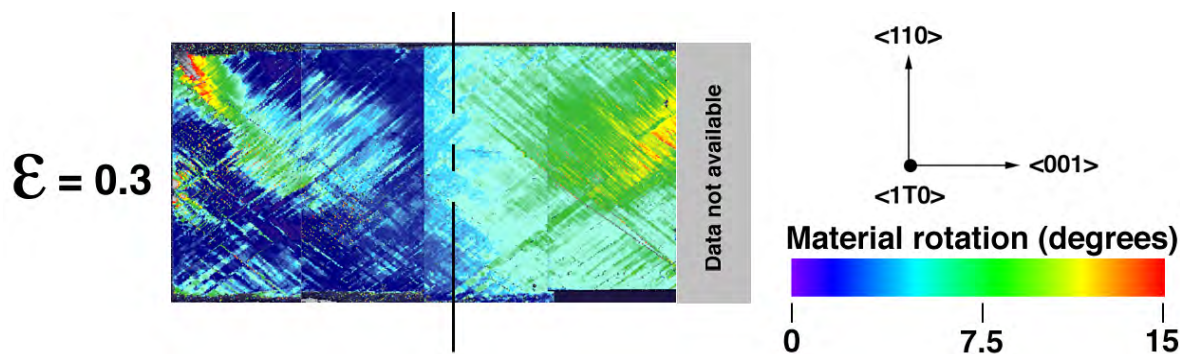


Figure 4. Misorientation collage of the 30% compressed sample, longitudinal view. Greater than 15-degree rotations occur in the corners as well as at the ends of the horizontal midplane. Severe orientation changes are observed throughout this figure. Of particular interest is the approximately 5-degree alternating misorientations with width on the order of 70 microns. Observed rotations are about the $[0\bar{1}1]$ axis.

Summary

We report on the beginning of an in-depth study of the mechanical behavior of Ta single crystals with purity levels approximately equal to that of ballistic grade Ta. This work is in support of the Ta crystal plasticity model in use at ARL and LLNL. The OIM data clearly suggest the single-crystal nature of the axial compressive deformation of $\langle 110 \rangle$ orientated samples. In addition, the OIM reveals lattice rotations that suggest a dislocation substructure evolution. These lattice rotations may directly relate to the observed work hardening in the stress-strain response.

Acknowledgments

The authors thank Robert K. Kershaw for performing the metallographic analyses.

References

1. A. J. Schwartz, J. S. Stölken, W. E. King, G. H. Campbell, D. H. Lassila, S. Sun, and B. L. Adams, "Analysis of Compression Behavior of a $[011]$ Ta Single Crystal with Orientation Imaging Microscopy and Crystal Plasticity," *Materials Research Society*, Boston, MA, Nov. 30–Dec. 4, 1998, in press.
2. A. J. Schwartz, W. E. King, G. H. Campbell, J. S. Stölken, D. H. Lassila, S. Sun, and B. L. Adams, "Orientation Imaging Microscopy Investigation of the Compression Deformation of a $[110]$ Ta Single Crystal," *Journal of Engineering Materials and Technology* **121**, (April 1999).

Internal Distribution

Adamson, M.	L-276
Banks, P.	L-439
Baumann, T. F.	L-370
Baum, D. W.	L-170
Bookless, B.	L-160
Boyd, P.	L-663
Campbell, G. H.	L-356
Christensen, R. M.	L-355
Clough, R.	L-160
Couch, R.	L-170
Cross, R.	L-474
Cutting, J.	L-281
Cynn, H.	L-174
DeTeresa, S. J.	L-338
Dolaghan, J.	L-170
Druce, R.	L-281
Dube, E.	L-170
Evans, W. J.	L-050
Fiske, P.	L-045
Forbes, J. W.	L-282
Fox, G. A.	L-092
Frank, A. M.	L-281
Fried, L. E.	L-282
Futral, S. W.	L-170
Gillespie, C.	L-281
Goldstein, B.	L-051
Goodwin, B.	L-170
Groves, S. E.	L-342
Holmes, N.	L-045
Howard, W. M.	L-043
Hrubesh, L. W.	L-092
Hsu, J.	L-312
Hsu, P.	L-276
Iantuono, A.	L-160
Johnson, K.	L-160
Kass, J.	L-125
King, W. E.	L-356
Lassila, D. H.	L-170
LeBlanc, M.	L-346
Lee, R. S.	L-281
Lorenzana, H. E.	L-050
Maienschein, J. L.	L-282
Mara, G.	L-125
McCallen, R.	L-170
McCoy, M.	L-068

Mitchell, A. R.	L-282
Murphy, M. J.	L-282
Nattrass, L.	L-149
Neely, R.	L-170
Nichols III, A. L.	L-282
Nowak, D.	L-066
Null, L.	L-164
Otero, I. J.	L-170
Pagoria, P. F.	L-282
Pierce, T.	L-561
Poulsen, P.	L-170
Pruneda, C. O.	L-282
Reaugh, J. E.	L-321
Roeske, Jr., F.	L-281
Roos, Ed.	L-281
Sanchez, R. J.	L-346
Schmidt, R. D.	L-282
Schwartz, A. J.	L-355
Sefcik, J.	L-359
Sharp, R.	L-170
Simonson, S. C.	L-170
Simpson, R. L.	L-282
Stuart, B.	L-439
Swansiger, R. W.	L-282
Tillotson, T. M.	L-092
Tyler, J.	L-160
Verdon, C.	L-030
Wallin, B.	L-170
Wallman, H.	L-282
Ward, R.	L-013
Watkins, B. E.	L-282
Watts, P.	L-284
Yoo, C.-S.	L-045
TID (3 Copies)	L-658

External Distribution

Bharat Agrawal
US Department of Energy
DP 16 (Room B306)
19901 Germantown Rd.
Germantown, MD 20874-1290

John Appel
Headquarter, Department of the Army
ATTN: SARD-TT
103 Army, Pentagon
Washington, D.C. 20301-0103

Celedon Aragon
U.S. Dept. of Energy
STTD, Albuquerque Operations Office
P.O. Box 5400
Albuquerque, NM 87185-5400

Dave Belk
Air Force Research Laboratory
ATTN: AFRL/MNAC
101 W. Eglin Blvd., Suite 337
Eglin AFB, Florida 32542-6810

Danny Brunson
Naval Surface Warfare Center,
Dahlgren Div.
Attn: NAVSURFWARCENDIV,
Code G02
17320 Dahlgren Rd.
Dahlgren, VA 22448-5100

Bruce Burns
US Army Research Laboratory
ATTN: AMSRL-WT-TC
Aberdeen Proving Ground MD 21005-
5066

James Chew
Department of the Navy
ONR 351
800 North Quincy St
Arlington, VA 22217-5660

Randy Cope
Naval Air Warfare Center-Weapons
Division
Code C2743
China Lake CA 93555-6001

Ruth Doherty
Naval Surface Warfare Center, Indian
Head Division
ATTN: Code 90B
101 Strauss Ave.
Indian Head, MD 20640-5035

Thomas Erickson
US Army Aviation and Missile
Command
ATTN: AMSAM-RD-QA-RA
Redstone Arsenal AL 35898-5290

Rick Fellerhoff
Sandia National Laboratories, MS 0501
P.O. Box 5800
Albuquerque NM 87185-0501

Steve Fowler
Naval Air Warfare Center, Weapons Div.
Code 478000D
1 Administration Circle
China Lake, CA 93555-6001

Joe Foster
Air Force Research Laboratory
ATTN: AFRL/MNMW
101 West Eglin Blvd, Suite 239
Eglin AFB, FL 32542-6810

Robert Garrett
Naval Surface Weapons Center, Indian
Head Division
Code 420C6
101 Strauss Ave
Indian Head, MD, 20640-5035

John Hedderich
U.S. Army ARDEC
ATTN: AMSTA-AR-TDC
Picatinny Arsenal, NJ 07806-5000

Tom Hitchcock
OUSD(A&T)/S&TS/Mun
3090 Defense Pentagon, Room 3B1060
Washington, DC 20301-3090

William Holt
Naval Surface Warfare Center
Code G22
Dahlgren VA 22448-5000

Paul Jacobs
US Army Aviation & Missile Command
ATTN: AMSAM-RD
Redstone Arsenal, AL 35898-5240

David Jerome
Air Force Research Laboratory
ATTN: AFRL/MNMW
101 West Eglin Blvd, Suite 239
Eglin Air Force Base, FL 32542-6810

Sam Lambert
Air Force Research Laboratory
Laboratory
ATTN: AFRL/MNGS
101 West Eglin Blvd, Suite 214
Eglin AFB, FL 32542-6810

Ingo May
US Army Research Laboratory
ATTN: AMSRL-WM-T
Aberdeen Proving Ground, MD 21005-5066

Tony Melita
OUSD(A&T)/S&TS/Mun
3060 Defense Pentagon, Room 3B1060
Washington, D.C. 20301-3090

Dennis Miotla
U.S. Dept. of Energy
DP-16
19901 Germantown Road
Germantown, MD 29874-1290

Kurt Mueller
Naval Surface Warfare Center, Indian
Head Division
ATTN: Code 90
101 Strauss Ave.
Indian Head, MD 20640-5035

James Pearson
US Army ARDEC
ATTN: SMCAR-AEE-WW
Picatinny Arsenal NJ 07806-5000

Steve Percy
U.S. Army ARDEC
ATTN: SMCAR-FSP
Picatinny Arsenal NJ 07806-5000

Steve Newfield
Los Alamos National Laboratory
Mailstop MS A133
P.O. Box 1663
Los Alamos, NM 87545

Arunachalam Rajendran
US Army Research Laboratory
ATTN: AMSRL-WM-MF
Aberdeen Proving Ground MD
21005-5066

John Robbins
Naval Air Warfare Center, Weapons Div.
Code 47C000D
1 Administration Circle
China Lake, CA 93555-6001

Michael Schexnayder
US Army Aviation & Missile Command
ATTN: AMSAM-RD
Redstone Arsenal, AL 35898-5240

George Ullrich
OUSD(A&T)/DDRE/WS
1777 N. Kent St., Suite 9030
Arlington, VA 22209

David Vaughn
US Marine Corps Systems Command
ATTN:MARCORSYSCOM
2033 Barnett Ave, Suite 315
Quantico, VA 22134-5010

Frank Wattenbarger
US Special Operations Command
MacDill AFB, FL 33608-6001

James Wheeler
Defense Ammunition Center
ATTN: SIOAV-TD
1C Tree Road
McAlister, OK 74501-9053